

Nanoscience and Technology

Daniela Dragoman  
Mircea Dragoman

# Bionanoelectronics

Bioinquiring and Bioinspired Devices

 Springer

# NANOSCIENCE AND TECHNOLOGY

---

# NANO SCIENCE AND TECHNOLOGY

---

*Series Editors:*

P. Avouris B. Bhushan D. Bimberg K. von Klitzing H. Sakaki R. Wiesendanger

The series NanoScience and Technology is focused on the fascinating nano-world, mesoscopic physics, analysis with atomic resolution, nano and quantum-effect devices, nanomechanics and atomic-scale processes. All the basic aspects and technology-oriented developments in this emerging discipline are covered by comprehensive and timely books. The series constitutes a survey of the relevant special topics, which are presented by leading experts in the field. These books will appeal to researchers, engineers, and advanced students.

Please view available titles in *NanoScience and Technology* on series homepage  
<http://www.springer.com/series/3705/>

Daniela Dragoman  
Mircea Dragoman

# Bionanoelectronics

Bioinquiring and Bioinspired Devices

With 201 Figures

 Springer

Professor Daniela Dragoman  
Univ. Bucharest, Physics Dept., P.O. Box MG-11  
077125 Bucharest-Magurele, Romania

Professor Mircea Dragoman  
National Research and Development Institute in Microtechnology, Str. Erou Iancu  
Nicolae 126 A, 077190 Bucharest-Voluntari, Romania

*Series Editors:*

Professor Dr. Phaedon Avouris  
IBM Research Division  
Nanometer Scale Science & Technology  
Thomas J. Watson Research Center  
P.O. Box 218  
Yorktown Heights, NY 10598, USA

Professor Dr. Bharat Bhushan  
Ohio State University  
Nanotribology Laboratory  
for Information Storage  
and MEMS/NEMS (NLIM)  
Suite 255, Ackerman Road 650  
Columbus, Ohio 43210, USA

Professor Dr. Dieter Bimberg  
TU Berlin, Fakultät Mathematik/  
Naturwissenschaften  
Institut für Festkörperphysik  
Hardenbergstr. 36  
10623 Berlin, Germany

Professor Dr., Dres. h.c. Klaus von Klitzing  
Max-Planck-Institut  
für Festkörperforschung  
Heisenbergstr. 1  
70569 Stuttgart, Germany

Professor Hiroyuki Sakaki  
University of Tokyo  
Institute of Industrial Science  
4-6-1 Komaba, Meguro-ku  
Tokyo 153-8505, Japan

Professor Dr. Roland Wiesendanger  
Institut für Angewandte Physik  
Universität Hamburg  
Jungiusstr. 11  
20355 Hamburg, Germany

NanoScience and Technology ISSN 1434-4904  
ISBN 978-3-642-25571-7 e-ISBN 978-3-642-25572-4  
DOI 10.1007/978-3-642-25572-4  
Springer Heidelberg Dordrecht London New York

Library of Congress Control Number: 2012934554

© Springer-Verlag Berlin Heidelberg 2012

This work is subject to copyright. All rights are reserved, whether the whole or part of the material is concerned, specifically the rights of translation, reprinting, reuse of illustrations, recitation, broadcasting, reproduction on microfilm or in any other way, and storage in data banks. Duplication of this publication or parts thereof is permitted only under the provisions of the German Copyright Law of September 9, 1965, in its current version, and permission for use must always be obtained from Springer. Violations are liable to prosecution under the German Copyright Law.

The use of general descriptive names, registered names, trademarks, etc. in this publication does not imply, even in the absence of a specific statement, that such names are exempt from the relevant protective laws and regulations and therefore free for general use.

Printed on acid-free paper

Springer is part of Springer Science+Business Media (www.springer.com)

# Preface

This is the first book on bionanoelectronics which deals with the applications of nanoelectronics in biology and medicine. Nanoelectronics is the most advanced area of nanotechnologies having huge applications in daily life. The mobile phones at which we are communicating every day as well as the desktop and laptop computers and iPhones are all results of the development of nanoelectronics, which is now able to fabricate with high reproducibility trillions of very large scale integrated circuits, integrating a huge number of transistors in a single chip. The nanoelectronics technologies are so effective that even 10 years ago the number of transistors contained in DRAM memories was greater than the number of grains of rice produced in the same year, and the price of a transistor was significantly lower than that of a grain of rice. These nanoscaled chips contain one billion transistors, which act as Boolean switches, connected in complicated paths, with a total length of 20 km, but confined and packed in an area of few  $\text{cm}^2$ . The nanoelectronics technology has developed so significantly according to the Moore law, which states that the dimensions of transistors reduce with 30% every 3 years, such that today the software of any iPhone is more powerful than that of the Apollo 11 lunar module, which landed on the Moon 30 years ago.

After publishing the second edition of the book *Nanoelectronics. Principles and Devices*, at Artech House, in 2009, which followed the first edition after only 3 years, we started to think that the last chapter of this book, called “Molecular and biological nanodevices,” must be extended into a separate book, taking into account the amazing applications of bionanoelectronics in rapid DNA sequencing, tissue engineering, controlled drug delivery, bioinspired devices, targeted cancer therapy, or even nanoelectronic artificial organs such as the nose, liver, or lung. More than 20 therapy products based on nanotechnologies are already in use, with very promising results, and other hundreds of nanomedicine-related devices are researched and are under clinical tests. However, we were a bit reluctant to start such an endeavor. We have known that nanoelectronic devices are governed by the rules of quantum mechanics, which prevail for any nanoscale device, and are accompanied by other fundamental laws of physics that cannot be easily adapted to the complex systems of biology. While physics uses a reductive approach to get relatively simple equations

with a universal character, also applicable in nanodevices, biology, and medicine are mainly observational science, since life manifestations are extremely complex. For example, in a human body, there are  $10^{14}$  cells and, due to cell divisions, 25 millions of new cells are generated every second; a cell has an average dimension of  $10\ \mu\text{m}$  and weighs 1 ng; each cell contains the human genome having  $3 \times 10^9$  base pairs, which means 750 MB of information; the human genome is 1 m long but is folded and packed in few microns and weighs 3 pg. Indeed, our nanoelectronics chips are simple toys compared to what nature has created. We have to recognize that human body is in itself a universe having at least a similar complexity to the cosmological universe from which we originate.

So we have thought how to make accessible to the engineering and physical community the amazing accomplishments of nanoelectronic devices and nanotechnologies applied in various areas of biology and medicine. The reason of such important steps forward in bionanoelectronics are due to the fact that the size of nanodevices and nanomaterials are similar to that of cells, and even of the DNA. The result of our efforts is the present book. The book is not focused on complicated biological, medical, or chemical considerations, although we inevitably use terms from these sciences, briefly explained in the text.

The main idea of the book is to provide to the reader the basic knowledge of nanosciences, i.e., the theoretical concepts and the basic technologies, as well as their applications in biosensing, imaging, bioarchitectures, molecular devices, bioinspired devices, controlled drug delivery, implants, biochips, etc. Thus, the book has achieved an internal coherence reflecting the dual interaction between nanoelectronics on one side and biology and medicine on the other, manifested by bioinquiring devices, when nanotechnologies are used to sense, control, or heal biological systems, and by bioinspired devices, when innovative nanoelectronic devices mimic the function of biological systems.

The first chapter of the book contains the basic principles and theoretical concepts of nanosciences and nanotechnologies, which are further used in the entire book. The second chapter is dedicated to the sensing of biomolecules, including single biomolecules such as DNA, using various techniques, for example, nanoelectronic devices based on nanowires, carbon nanotubes, or graphene, nanocantilevers, or plamonic devices. An artificial nose, which is able to sense various gases in very small quantities, of even few molecules, and to detect the gases associated with diseases such as lung cancer ends this chapter. Chapter 3 is dealing with the imaging tools used in nanotechnologies, such as atomic force microscopy (AFM), which are applied to determine important parameters of various biological systems. The manipulation of biomolecules using optical tweezers and dielectrophoresis is also described in this chapter. These three chapters form the basis for understating the bioinquiring nanodevices. Chapter 4 is focused on the applications in medicine of nanoelectronic devices, which perform complex tasks such as controlled drug delivery monitored by external signals, targeted cancer cell therapy, and mimicking organs such as lung.

Chapters 5, 6, and 7 are dedicated, respectively, to biomolecular architectures, molecular devices, and biocomputing. These chapters present biological

devices that perform mechanical, optical, or electrical actions usually associated to nonbiological devices. On the contrary, Chap. 8 gathers examples of bioinspired devices, which refer to mechanical, optical, or electrical devices designed based on nature's lessons. The book ends with Chap. 9, which deals with nano-bio integration, a subject that could prove invaluable in the future innovative nanodevices. The applications of nanotechnologies in biology and medicine will produce soon a revolution similar to that of communications and computers, which made possible the occurrence of the internet, mobile phones, and laptops. In the case of bionanoelectronics and nanomedicine, we hope that the final result will be a better and healthier life, in a cleaner environment, the nanotechnologies contributing to the diagnosis and therapy of serious diseases as well as to the development of environmental-friendly technological processes.

Many thanks are addressed to Dr. Claus Ascheron from Springer Verlag, who has encouraged us during the writing of this book.

Bucharest

*Mircea Dragoman  
Daniela Dragoman*



# Contents

<b>1</b>	<b>Fundamentals on Bionanotechnologies</b> .....	1
1.1	Transport Phenomena at the Nanoscale .....	1
1.2	Nanotechnologies for Bionanoelectronic Devices .....	18
1.2.1	Deposition Techniques for Bionanoelectronic Devices .....	18
1.2.2	Nanolithography .....	20
1.2.3	Nanomaterials .....	27
1.3	Conduction Properties of Biological Materials .....	35
1.4	Microfluidics and Nanofluidics .....	46
	References .....	54
<b>2</b>	<b>Sensing of Biomolecules</b> .....	57
2.1	Nanotransistors Based on Nanotubes, Nanowires, and Graphene for Biosensing .....	57
2.2	DNA Detection and Sequencing Using Nanopores .....	73
2.3	MEMS/NEMS Biodetection .....	80
2.4	Plasmonics Biodetection .....	87
2.5	Nanoelectronic Noses and Various Disease Detection .....	98
	References .....	102
<b>3</b>	<b>Imaging and Manipulation of Biomolecules</b> .....	107
3.1	Bioapplications of Atomic Force Microscopy .....	107
3.2	Bioapplications of Scanning Tunneling Microscopy .....	114
3.3	Manipulation of Biological Materials .....	117
	References .....	123
<b>4</b>	<b>Nanomedicine</b> .....	127
4.1	Drug Delivery and Healing Based on Nanomaterials .....	127
4.2	Biochips—DNA Arrays and Other Chips for Diagnosis .....	144
4.3	Artificial Tissues and Organs .....	146
	References .....	148

<b>5</b>	<b>Biomolecular Architecture for Nanotechnology</b> .....	151
5.1	DNA-Based Molecular Architectures .....	152
5.2	Self-Assembled DNA Nanowires .....	155
5.3	Two- and Three-Dimensional Bioarchitectures as Scaffolds .....	159
5.4	Nonperiodic Biological Scaffolds for Inorganic Structures .....	165
5.5	Inorganic Scaffolds for Biomolecules .....	169
	References .....	170
<b>6</b>	<b>Biomolecular Machines</b> .....	173
6.1	Biological Actuators and Switches .....	174
6.2	Biological Walkers .....	180
6.3	Biological Motors .....	183
	References .....	187
<b>7</b>	<b>Biomolecular Computing</b> .....	189
7.1	Principles of Biomolecular Computing .....	189
7.2	Boolean Biomolecular Computing .....	192
7.3	Self-Assembly Biomolecular Computing .....	198
7.4	Biomolecular Logical Deductions .....	200
7.5	Biomolecular Memory Devices .....	201
7.6	Logical Drug Delivery and In Vivo Computation .....	203
	References .....	205
<b>8</b>	<b>Bioinspired Devices</b> .....	207
8.1	Bioinspired Materials .....	208
8.2	Bioinspired Devices .....	215
8.3	Bioinspired Technological Processes .....	222
8.4	Devices Mimicking Biological Organs/Functionalities .....	224
	References .....	229
<b>9</b>	<b>Nano-Bio Integration</b> .....	233
9.1	Nano-bio Materials for Electronics and Optoelectronics .....	233
9.2	Nano-bio Mechanical Devices .....	236
9.3	Nanobioelectronics and Optoelectronics .....	239
	References .....	246
	<b>Index</b> .....	249
	<b>About the Authors</b> .....	253

# Chapter 1

## Fundamentals on Bionanotechnologies

**Abstract** This is the introductory chapter of the book. The basic theoretical and experimental facts regarding the application of electronics at the nanoscale and for biological systems are developed here. Transport phenomena at the nanoscale, the principles of nanotechnologies, the physical properties of biological materials, and micro/nanofluidics are reviewed and explained in this chapter. The knowledge gained in this chapter will then be used in the entire book.

### 1.1 Transport Phenomena at the Nanoscale

When electronic devices are scaled down from few microns up to nanoscale, they become comparable with living organisms, such as bacteria, viruses, or the dimensions of DNA bases. The nanoscale is represented in Fig. 1.1. This fact is of paramount importance for sensing, detecting, or manipulating microorganisms or biomolecules.

The reduced nanometer dimensions of electronic devices changes completely the transport properties. A nanoscale device is an electron device where one, two, or even all three spatial dimensions have few nm. If at a scale of few microns any electronic device can be described by macroscopic physical equations such as Ohm's law, at the nanoscale, microscopic equations are replaced by equations based on quantum mechanics. Quantum mechanical effects manifest at the nanoscale even at room temperature.

A homogenous semiconductor has a conduction band (the first empty band), a valence band (the last occupied band), and a bandgap that separates them. The distribution function of charge carriers in these bands is described by the Fermi-Dirac function

$$f(E) = 1/\{1 + \exp[(E - E_F)/k_B T]\}, \quad (1.1)$$

where  $E_F$  is the Fermi energy level. In semiconductors, the Fermi level is located inside the energy bandgap. In Fig. 1.2, we have displayed the Fermi function at two temperatures.

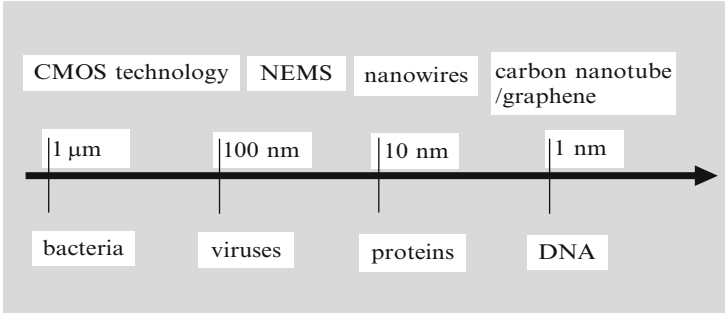
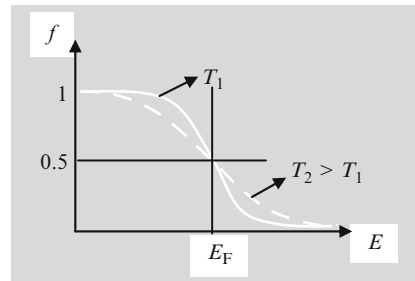


**Fig. 1.1** Dimension scale of biological systems and electron devices, where NEMS stands for nanoelectromechanical systems

**Fig. 1.2** The Fermi–Dirac distribution function



In the case of nanoscale devices, the confinement of carrier wavefunctions produces a discretization of the energy spectrum of charge carriers as well as discontinuities in the density of states. These effects cause further important changes in the transport properties of charge carriers depending on the number of dimensions along which the motion of carriers is restricted.

In bulk materials with dimensions of few millimeters, the transported carriers move randomly due to repeated scatterings with impurities and phonons. The carrier transport is thus of a diffusive type, which is modeled in general by a stochastic Boltzmann equation. The Boltzmann equation loses its validity as soon as the dimensions of the material shrink to nanoscale. The nanoscale is often termed as mesoscale since it is intermediate between the macroscopic scale and the atomic scale, where the atoms and molecules with sizes of the order of  $1 \text{ \AA} = 10^{-10} \text{ m}$  are described by quantum mechanical laws.

At the nanoscale, the electron transport is dictated by the relation between the dimensions of the sample and three parameters (Datta 1997):

1. The mean-free path  $L_{fp}$ , which is the average distance between two electron collisions with phonons or impurities that cancel the initial momentum of a charge carrier.
2. The phase relaxation length  $L_{ph}$ , which represents the propagation distance after which the electron coherence, i.e., the phase memory of electrons, vanishes as a result of time-reversal breaking. Examples of such processes are

electron–electron collisions, dynamic scatterings, or certain impurity scattering processes in which an internal degree of freedom changes; the phase relaxation length is often called the coherence length.

3. The electron Fermi wavelength, denoted as  $\lambda_F$ .

When one or more dimensions of a device are smaller than the mean-free path and the phase relaxation length, the number of scatterings reduces dramatically, and the transport in the device is termed ballistic. In this case, the electrons behave no longer as particles but as waves that follow all the reflection and refraction rules of common light or acoustic waves. As will be seen later, the ballistic transport manifests over distances of few hundreds of nanometers in carbon nanotubes (CNTs), graphene, or high-mobility transistors at room temperature.

In Fig. 1.3, we have schematically displayed a transistor with scaled down dimensions. The transport is diffusive when the transistor has gate lengths of  $1\ \mu\text{m}$  or greater and ballistic as soon as the gate channel shrinks to tens of nanometers. In the ballistic transport regime, the carriers traverse the gate channel in a much shorter time and with higher speeds.

The transport of ballistic charge carriers with electron effective mass  $m$  and constant energy  $E$  can be modeled by the time-independent Schrödinger equation

$$-\frac{\hbar^2}{2}\{m^\alpha\nabla[m^\beta\nabla(m^\alpha\Psi)]\} + V\Psi = E\Psi, \quad (1.2)$$

when the coupling phenomena between different electron bands can be neglected (Dragoman and Dragoman 1999). In (1.2),  $\Psi$  denotes the envelope electron wavefunction, which has a slow variation over the unit cell of the crystalline lattice and  $V$  is the potential energy. The material-dependent parameters  $\alpha$  and  $\beta$  are

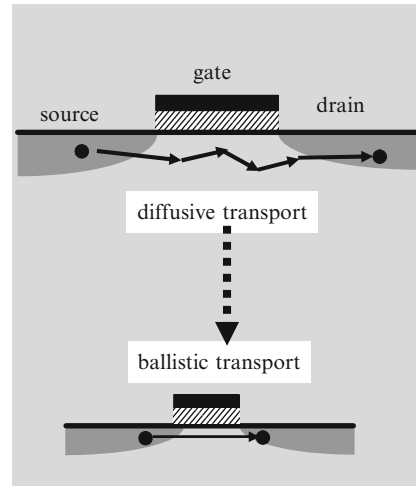


**Fig. 1.3** The scaling down of a transistor

related by  $2\alpha + \beta = -1$  and are equal to  $\alpha = 0$  and  $\beta = -1$  in AlGaAs compounds, which were the first semiconductors that displayed ballistic transport.

The spatial restrictions on electron motion are expressed in the specific form of the boundary conditions imposed on the Schrödinger equation. A structure in which electrons are confined at the nanoscale by potential barriers along the, say,  $z$  direction but are free to travel along the transverse  $x$  and  $y$  directions is referred to as quantum well (QW). In a quantum well with infinite-height potential barriers, the Schrödinger equation is accompanied by the boundary conditions  $\Psi(x, y, 0) = \Psi(x, y, L_z) = 0$ , where  $L_z$  is the width of the quantum well.

If  $V = 0$ , the solution of the Schrödinger equation can be written as  $\Psi(x, y, z) = (2/L_z L_x L_y)^{1/2} \sin(k_z z) \exp(ik_x x) \exp(ik_y y)$ , where  $L_x$  and  $L_y$  are, respectively, the dimensions of the structure along  $x$  and  $y$ . In ballistic devices,  $L_z$  is comparable to the Fermi wavelength  $\lambda_F$  and  $L_z < L_x, L_y \ll L_{fp}, L_{ph}$ . Another effect of the boundary conditions is a discrete spectrum for the  $z$  component of the electron momentum  $k_z = p\pi/L_z$ , which induces a discretization of the energy levels along the direction of spatial restriction. The energy dispersion relation in the quantum well in which the bottom of the conduction band  $E_c$  is considered as reference is given by

$$E(k_x, k_y, k_z) = E_c + \frac{\hbar^2}{2m} \left( \frac{p\pi}{L_z} \right)^2 + \frac{\hbar^2}{2m} (k_x^2 + k_y^2) = E_{s,p} + \frac{\hbar^2}{2m} (k_x^2 + k_y^2), \quad (1.3)$$

where  $E_{s,p}$  is the cutoff energy of the discrete subband labeled by the integer  $p$ ; the subbands are also referred to as transverse modes. The difference in energy between adjacent subbands is greater for more confined electrons, i.e., for smaller  $L_z$ .

For an arbitrary energy distribution in the  $\mathbf{k}$  space, which takes  $E(\mathbf{k})$  constant values on a  $\mathbf{k}$ -space surface  $\Sigma$ , a spin-degenerate density of states (DOS) can be defined as

$$\rho(E) = (2\pi)^{-3} \int_{\Sigma} \frac{dS}{|\nabla_{\mathbf{k}} E|_{E=\text{const.}}} \quad (1.4)$$

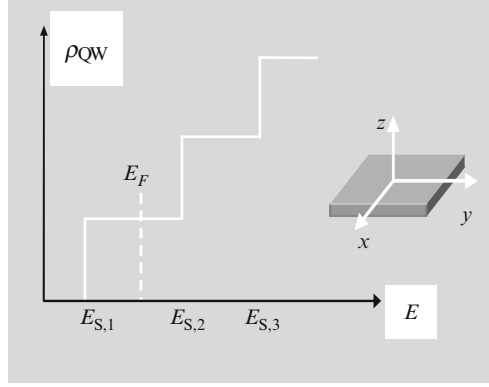
Then, in the quantum well case, the DOS particularizes to

$$\rho_{\text{QW}}(E) = \frac{m}{\pi \hbar^2 L_z} \sum_p \vartheta(E - E_{s,p}), \quad (1.5)$$

where  $\vartheta$  denotes the unit step function. As follows from (1.5), and as illustrated in Fig. 1.4, the DOS in the quantum well is discontinuous, in contrast to the case of bulk semiconductors, where the absence of spatial constraints leads to a continuous DOS.

At equilibrium conditions at temperature  $T$ , the electrons occupy the discrete energy levels of the quantum well according to the Fermi–Dirac distribution function (1.1), so that the electron density per unit area at equilibrium is given by (Ferry and Goodnick 2009)

**Fig. 1.4** Density of states in a quantum well



$$n = L_z \int_0^{\infty} \rho_{\text{QW}}(E) f(E) dE = k_B T \frac{m}{\pi \hbar^2} \sum_p \ln[1 + \exp(E_F - E_{s,p})/k_B T]. \quad (1.6)$$

In the degenerate limit or at low temperatures, when  $k_B T \ll E_F$ , the Fermi–Dirac distribution function is proportional to  $\vartheta(E_F - E)$ , so that all electron subbands below the Fermi energy are filled with electrons, and all subbands above it are empty. At low temperatures, the electrons with energy  $E$  reside in a number of subbands  $M(E)$ , which can be determined by counting the transverse modes with cutoff energies below  $E$ .

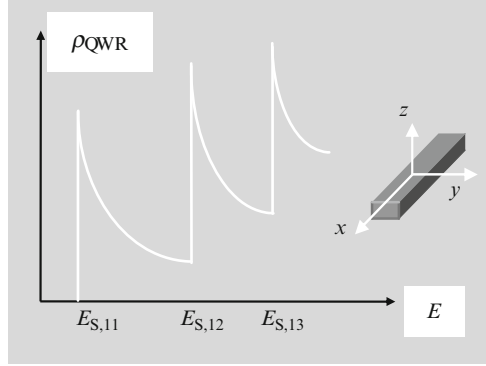
When the Fermi energy level in a quantum well is positioned between the first and the second energy subband, as displayed in Fig. 1.4, we have a two-dimensional electron gas (2DEG), which has a metallic behavior because  $E_F$  is inside the conduction band. In this case, the Fermi wavenumber  $k_F$ , determined from the electron kinetic energy as  $E_{\text{kin}} = E_F - E_{s,1} = \hbar^2 k_F^2 / 2m$ , is correlated to the electron density per unit area  $n = (m/\pi \hbar^2)(E_F - E_{s,1})$  through the formula (Ferry and Goodnick 2009)

$$k_F = (2\pi n)^{1/2}. \quad (1.7)$$

The Fermi wavelength is defined as  $\lambda_F = 2\pi/k_F$ .

A nanoscale structure is called quantum wire (QWR) if the electron motion is spatially restricted by energy potentials in regions of widths  $L_y$  and  $L_z$  along two directions:  $y$  and  $z$ , but the electron can move freely along  $x$ . If the constraining potentials have infinite heights, the electron wavefunction has the expression  $\Psi(x, y, z) = [2/(L_y L_z L_x)^{1/2}] \sin(k_y L_y) \sin(k_z L_z) \exp(i k_x x)$ , and boundary conditions similar to those in the quantum well case imply that  $k_y = p\pi/L_y$ ,  $k_z = q\pi/L_z$ , with  $p, q$  integer numbers. The energy dispersion relation in QWR is then given by

$$E(k_x, k_y, k_z) = E_c + \frac{\hbar^2}{2m} \left( \frac{p\pi}{L_y} \right)^2 + \frac{\hbar^2}{2m} \left( \frac{q\pi}{L_z} \right)^2 + \frac{\hbar^2 k_x^2}{2m} = E_{s,pq} + \frac{\hbar^2 k_x^2}{2m}, \quad (1.8)$$

**Fig. 1.5** The DOS of QWR

so that the DOS becomes

$$\rho_{\text{QWR}}(E) = \frac{(2m)^{1/2}}{\pi \hbar L_y L_z} \sum_{p,q} (E - E_{s,pq})^{-1/2}. \quad (1.9)$$

The DOS of QWR is represented in Fig. 1.5.

Similar to the optical waveguides, the QWRs with  $L_y, L_z < L_x \ll L_{\text{fp}}, L_{\text{ph}}$  and  $L_y, L_z \cong \lambda_{\text{F}}$  are called electron waveguides if the energy difference between adjacent subbands is higher than the thermal energy  $k_{\text{B}}T$  and the possible potential drop along the waveguide,  $eV$ , where  $V$  is the applied bias ([Dragoman and Dragoman 2004](#)). At temperatures around 4 K, this condition is satisfied in modulation-doped AlGaAs/GaAs heterostructures for  $L_y, L_z \cong 0.1\text{--}0.5 \mu\text{m}$  and  $V < 1 \text{ mV}$ .

In a quantum dot (QD), the motion of charge carriers is spatially constrained along all three directions in regions much smaller than the mean-free path and the phase relaxation length. In this case, the discrete energy dispersion is given by

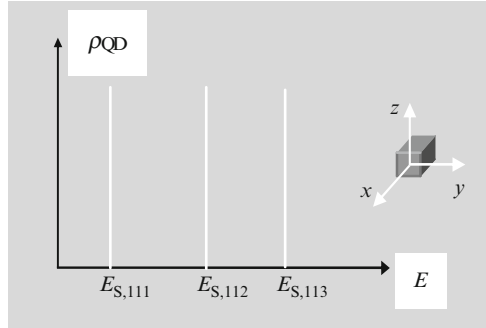
$$E(k_x, k_y, k_z) = E_c + \frac{\hbar^2}{2m} \left( \frac{p\pi}{L_x} \right)^2 + \frac{\hbar^2}{2m} \left( \frac{q\pi}{L_y} \right)^2 + \frac{\hbar^2}{2m} \left( \frac{r\pi}{L_z} \right)^2 = E_{s,pqr}, \quad (1.10)$$

and the DOS is proportional to the Dirac function

$$\rho_{\text{QD}} \propto \delta(E - E_{s,pqr}). \quad (1.11)$$

The DOS of QD is shown in Fig. 1.6. The discrete energy spectrum of quantum dots is similar to that of atoms or molecules, and therefore, sometimes, QDs are referred to as artificial atoms.

In the ballistic regime, only electrons with energies around  $E_{\text{F}}$  take part at transport, whereas in the diffusive regime, electrons with a wide energy spectrum contribute to electrical transport.

**Fig. 1.6** The DOS of QWR

When a one-dimensional (1D) ballistic conductor is situated between two contacts with the role of electron reservoirs, an external bias  $V$  induces the electron transfer and imposes a nonequilibrium regime, with no common Fermi energy level across the structure. However, it is possible to define a spatially varying local quasi-Fermi level, with values  $E_{FL}$  and  $E_{FR}$ , respectively, in the left and right contacts. Then, in a ballistic quantum wire conductor, supposing that  $E_{FL} > E_{FR}$  and that the contacts are reflectionless, we have  $eV = E_{FL} - E_{FR}$  if the bias is not very large. At zero temperature, the electrons participating at current flow have energies only in the  $E_{FR} < E < E_{FL}$  interval. Moreover, for a ballistic conductor with unchanging cross section, in which no electron scattering between different subbands occurs, each occupied subband adds a term of  $I = ev\delta n$  to the total net current, where  $\delta n = (dn/dE)eV$  denotes the additional electron density in the left contact and  $v = \hbar^{-1}(dE/dk)$  is the velocity of electrons along the direction of current flow. The total current is then  $I = (2e^2/h)MV$  if the number of subbands  $M(E)$  does not change across the energy range  $E_{FR} < E < E_{FL}$ . In this case, the conductance is given by

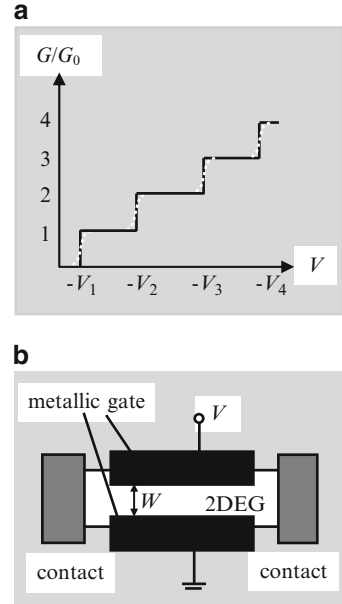
$$G = I/V = 2e^2M/h \quad (1.12)$$

and is an integer multiple of  $G_0 = 2e^2/h$ , called quantum conductance. In the ballistic regime, the resistance  $R = 1/G = 1/(MG_0) \cong 12.9 \text{ k}\Omega/M$  originates in the difference at the conductor/contact interface between the infinite number of subbands in the contacts and the finite number of transverse modes in the conductor. So  $R$  is termed contact resistance, and its value becomes increasingly smaller than the quantum value  $R_0 = 12.9 \text{ k}\Omega$  as the number of occupied energy subbands in the conductor raises.

In bulk materials, Ohm's law states that the conductance  $G$  is inversely proportional to the length of the sample. In deep contrast, in ballistic structures, the conductance does not depend on the conductor length but only on its width  $W$  since the number of subbands that are occupied by electrons with the Fermi wavenumber  $k_F$  is given by  $M \cong \text{Int}[k_F W/\pi]$ , where  $\text{Int}[x]$  symbolizes the integer value of the argument  $x$ .

The step-like conductance dependence on the number of occupied subbands in (1.12) was demonstrated experimentally by low-temperature measurements on a

**Fig. 1.7** (a) The gate voltage dependence of conductance at zero temperature (*solid line*) and finite temperatures (*dotted line*) in (b) a 1D ballistic conductor with tunable width

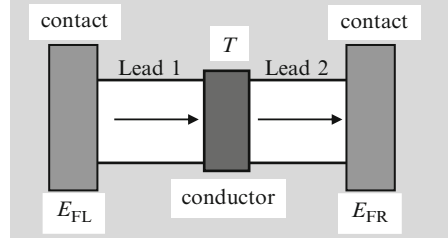


ballistic wire with a variable width, as illustrated in Fig. 1.7a (del Alamo et al. 1998). The conductance rises in steps of  $G_0$  for any increases with one unity of  $M$ , this stair-like shape being “smoothed” as the temperature increases due to thermal vibrations. A split-gate geometry as that displayed in Fig. 1.7b must be used to obtain a 1D ballistic quantum wire from a 2DEG. In this geometry, a narrow slit, which has a width  $W$  on the order of  $\lambda_F$ , is cut in a depleting gate patterned above the 2DEG. The effective width  $W$  of the conductor can be decreased by applying a gradually increasing negative gate voltage  $V$ , so that the number of transverse modes  $M$  is modified in a stepwise manner. The split-gate configuration is termed quantum point contact if the constriction length is small enough (in fact, is comparable to its width) and is referred to as electron waveguide if the constriction is much longer than  $W$ .

The hypothesis made in deriving (1.12), i.e., that all electrons originating in the left contact reach the right contact, is not always valid. For instance, if the ballistic conductor is composed of several sections with different potential energies or widths, the electrons from the left contact are only partially transmitted to the right contact. If  $T$  designates the transmission probability of the ballistic conductor attached to reflectionless contacts via ballistic leads, as illustrated in Fig. 1.8, the zero-temperature conductance between the contacts is given in this situation by the Landauer formula (Datta 1997)

$$G = \frac{2e^2}{h} MT, \quad (1.13)$$

**Fig. 1.8** The model of a ballistic conductor



where  $M$  is the number of subbands in the leads. The current that flows between contacts at low temperatures is then  $I = (2e^2/h)MTV$ .

In this case, the total resistance between contacts,  $R = h/(2e^2MT)$ , can be written as a sum between  $h/(2e^2M)$ , which has the meaning of contact resistance, and  $R_s = h(1-T)/(2e^2MT)$ , which is the resistance of a scatterer with transmission  $T$ . In the same way, the resistance of a succession of scatterers with transmissions  $T_i$  is  $R_s = \sum_i R_{s,i}$ , where  $R_{s,i} = h(1 - T_i)/(2e^2MT_i)$ . This formula suggests that a series of scatterers is equivalent to a single scatterer with total transmission probability given by  $(1 - T)/T = \sum_i (1 - T_i)/T_i$ , expression that results from adding all partially transmitted waves.

We have assumed up to now that the Fermi–Dirac distribution  $f(E)$  can be approximated with a step function, but this assumption does not hold at higher temperatures (see Fig. 1.2), case in which the electrons contributing at electrical conduction have energies in the range  $E_{FR} - \Delta E < E < E_{FL} + \Delta E$ , where  $\Delta E$  is a few  $k_B T$ . Then, the current flowing between the left and right contacts, which have respective Fermi–Dirac quasi-distribution functions  $f_L(E)$  and  $f_R(E)$ , is given by [Datta \(1997\)](#)

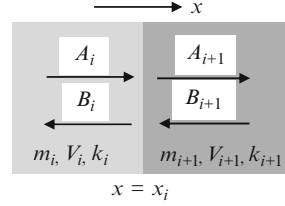
$$I = \frac{2e}{h} \int M(E)T(E)[f_L(E) - f_R(E)]dE. \quad (1.14)$$

From (1.14), it follows that the calculation of the transmission probability is essential for current estimation using the Landauer formula. The transmission probability can be computed using the transfer Hamiltonian formalism, the Green's function approach, or the Kubo formalism ([Datta 1997](#); [Ferry and Goodnick 2009](#)), but the easiest method to determine it is the matrix formalism, described below.

The transmission probability can be calculated once the electron wavefunctions are known. In the simplest case, when the 1D ballistic conductor is composed of a succession of several regions with constant but different electron effective masses and potential energies, which extend along the  $x$  direction, the solution of the Schrödinger equation (1.2) in the  $i$ th region,  $\Psi_i(x) = A_i \exp(ik_i x) + B_i \exp(-ik_i x)$ , can be regarded as a superposition of waves that propagate forward and backward with wavenumbers  $k_i = \hbar^{-1} \sqrt{2m_i(E - V_i)}$ . Continuity conditions require that at each interface between layers  $i$  and  $i + 1$ , situated at  $x = x_i$ , as shown in Fig. 1.9, the wavefunction and  $(\partial\Psi/\partial x)/m^{\alpha+1}$  are constant.

If  $\alpha = 0$  in (1.2), these requirements connect the wavefunction components on each side of the interface via a transfer matrix

**Fig. 1.9** Forward- and backward-propagating components of the electron wavefunction at an interface between adjacent layers  $i$  and  $i + 1$



$$\begin{pmatrix} A_i \exp(ik_i x_i) \\ B_i \exp(-ik_i x_i) \end{pmatrix} = \frac{1}{2} \begin{pmatrix} (1+v_{i+1}/v_i) (1-v_{i+1}/v_i) \\ (1-v_{i+1}/v_i) (1+v_{i+1}/v_i) \end{pmatrix} \begin{pmatrix} A_{i+1} \exp(ik_{i+1} x_i) \\ B_{i+1} \exp(-ik_{i+1} x_i) \end{pmatrix}, \quad (1.15)$$

where  $v_i = \hbar k_i / m_i$  is the electron velocity in layer  $i$ . Analogously, the  $2 \times 2$  transfer matrix for free propagation across the  $i$ th layer between planes situated at  $x = x_{i-1}$  and  $x = x_i$  is diagonal, with nonvanishing elements  $\exp[ik_i(x_i - x_{i-1})]$  and  $\exp[-ik_i(x_i - x_{i-1})]$ . As a result, the transmission probability for a structure composed of a succession of  $N$  layers is given by

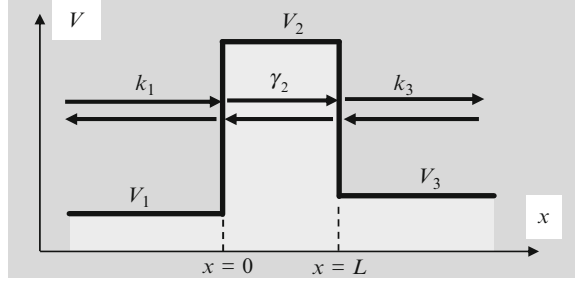
$$T = v_N |A_N|^2 / (v_1 |A_1|^2) = v_N / (v_1 |M_{11}|^2) \quad (1.16)$$

and is directly dependent on the element  $M_{11}$  of the total transfer matrix with elements  $M_{pq}$ ,  $p, q = 1, 2$ , determined by multiplying the matrices corresponding to each interface and each layer. The transmission probability is the ratio between transmitted and incident electron probability currents, defined in any layer  $j$  as  $J_j = (\hbar/2m_j i)(\Psi_j^* \partial_x \Psi_j - \Psi_j \partial_x \Psi_j^*)$ , where \* signifies complex conjugation and  $\partial_x$  is a shorthand notation for partial derivation with respect to  $x$ .

When some of the wavenumbers  $k_i$  are imaginary, we encounter the tunneling phenomenon, widely used in nanodevices, and which can be modeled using the matrix formalism described above. The wavenumber is imaginary only if the electron energy is smaller than the potential energy, situation in which electron propagation is not allowed from a classical point of view. Therefore, tunneling is a quantum phenomenon. The layer with an imaginary wavenumber is a barrier for electron propagation, and the electron wavefunction decays exponentially inside it, analogous to evanescent electromagnetic waves. Because the transmission probability across a barrier layer becomes zero unless it is narrow enough, tunneling of electrons propagating with constant energy  $E$  occurs only through thin potential barriers or a succession of such barriers surrounded by quantum wells, i.e., regions with real wavenumbers.

However, classical transport across a potential barrier is permitted if the electron acquires extra energy. When this additional energy is thermal, the process is called thermionic emission. At finite temperatures, thermionic emission accompanies the tunneling process and becomes the major electron transport mechanism at high temperatures (Appenzeller et al. 2004). The thermionic emission contributes to the net current across a rectangular barrier with a temperature-dependent term  $I \propto T^2 \exp(-\phi/k_B T)$ , where  $\phi$  is the barrier height.

**Fig. 1.10** The geometry of a tunneling structure consisting of a single barrier



In tunneling devices, the direction of electron propagation, denoted by  $x$  in the expressions above, is determined by the direction of the applied electric field, and the transfer matrix method remains applicable as long as  $\Psi$  denotes the  $x$ -dependent part of the envelope wavefunction of electrons and the electron motion along the longitudinal  $x$  direction can be separated from that along the transverse  $y$  and  $z$  directions. The transmission probability through a single barrier, which is the simplest tunneling structure displayed in Fig. 1.10, is given by

$$T = \frac{4v_1v_3}{(v_1 + v_3)^2 + [(v_1^2 + v_2^2)(v_2^2 + v_3^2)/v_2^2] \sinh^2(\gamma_2 L)}, \quad (1.17)$$

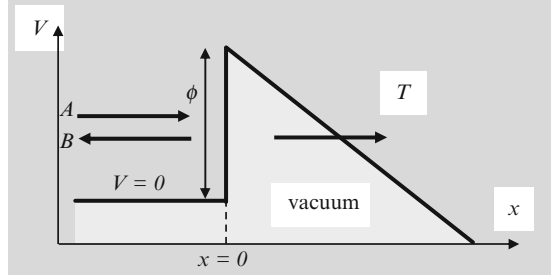
where  $v_2 = \hbar\gamma_2/m_2$  and  $k_2 = -i\gamma_2$  is imaginary in the barrier region labeled by 2 and surrounded by regions 1 and 3 with real wavenumbers.

From (1.17) it follows that, if  $\gamma_2 L \gg 1$ , the transmission probability decreases exponentially with the barrier width  $L$ :  $T \propto \exp(-2\gamma_2 L)$ . At low temperatures, when all electrons contributing to transport have energies around  $E_F$ , this expression can be rewritten as  $T \propto \exp[-2L\sqrt{2m_2(V_2 - E_F)}/\hbar]$  (Zhu 2001). In this case, the current density through the structure is proportional to  $T$  and therefore decreases also exponentially with  $L$ , while the conductance is much smaller than  $G_0$ .

The example of electron transmission through a single barrier is relevant for many applications, such as scanning tunneling microscopy or vacuum microelectronic devices, which contain flat panel field emission displays and electron sources for microscopes. In these devices, electrons tunnel from a solid surface into vacuum under the influence of a high electric field (Zhu 2001).

The potential barrier in the vacuum region, given by the electron affinity  $\phi$ , takes a triangular shape in the presence of an applied electric field  $F$ , acquiring a spatial dependence of  $\phi - eFx$  (see Fig. 1.11). The wavefunction of the electron in vacuum with mass  $m_0$  is then a solution of the Schrödinger equation with a triangular barrier, which, if  $\alpha = 0$ , is a superposition of Ai and Bi Airy functions:  $\Psi_{\text{vac}}(\xi) = A_{\text{vac}}\text{Ai}(\xi) + B_{\text{vac}}\text{Bi}(\xi)$ , with  $\xi = [2m_0/(eF\hbar)^2]^{1/3}(\phi - eFx - E)$ . The condition of current flow along the positive  $x$  direction imposes the following values for the constant coefficients:  $A_{\text{vac}} = 1$ ,  $B_{\text{vac}} = i$ , so that the transmission coefficient  $T$  across the barrier has the expression

**Fig. 1.11** Geometry of electron emission in vacuum by tunneling through a triangular potential barrier



$$T = \left( \frac{2eF}{\hbar^2 m_0^2} \right)^{1/3} \frac{m}{\pi} \frac{|A|^2}{k} \quad (1.18)$$

for incident electrons with energy  $E$ , mass  $m$ , and wavefunction  $\Psi(x) = A \exp(ikx) + B \exp(-ikx)$ . In (1.18),  $k = (2mE/\hbar^2)^{1/2}$  and the coefficients  $A$  and  $B$  are obtained from the continuity conditions imposed on the wavefunction and its derivative at  $x = 0$ .

At low temperatures and high electric fields, and for  $m = m_0$ , the current density associated to the transmission coefficient in (1.18) is

$$J = \frac{em_0 k_B T}{\pi^2 \hbar^3} \int T(E) \ln \left[ 1 + \exp \left( \frac{E_F - E}{k_B T} \right) \right] dE \propto F^2 \exp \left( -\frac{4}{3\hbar F} \sqrt{2m_0 \phi^3} \right), \quad (1.19)$$

where the logarithmic term describes the effect of the transverse degrees of freedom on the Fermi–Dirac distribution function. Formula (1.19) is the so-called Fowler–Nordheim equation, which models the current–voltage characteristic of devices based on field emission.

Let us consider now the case when electrons tunnel through a structure consisting of two (or several) barriers that alternate with quantum well regions. Because ballistic electrons propagate coherently, constructive or destructive interferences appear between quantum waves that are only partially reflected and transmitted at different interfaces. So we expect high and low transmission probability values in a typical geometry such as that displayed in Fig. 1.12, containing a quantum well surrounded by two thin barriers. This phenomenon is analogous to the occurrence of high- and low-intensity values associated with interference between coherent light beams. A large transmission probability through a structure consisting of two (or several) barriers, each of them with a low transmission probability, defines the phenomenon of resonant tunneling.

This phenomenon can be described also with the transfer matrix method developed above. For the case of a structure containing two barriers that surround a quantum well with width  $L$  in which electrons propagate with a wavevector  $k$ , the total transmission probability  $T$  is determined by the  $M_{11}$  element of the transmission matrix  $M$  through the whole structure, found by first multiplying the transmission matrix  $M_L$  of the left barrier with the diagonal matrix with elements  $\exp(-ikL)$  and  $\exp(ikL)$ , corresponding to free propagation across the quantum well,

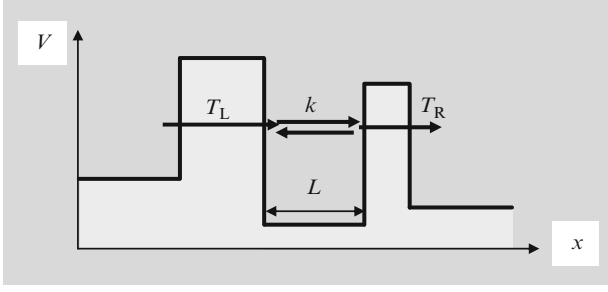


**Fig. 1.12** Geometry of the double-barrier tunneling structure

followed by multiplication with the transmission matrix  $M_R$  of the right barrier. The final result is  $M_{11} = M_{L,11}M_{R,11} \exp(-ikL) + M_{L,12}M_{R,21} \exp(ikL)$ , where  $M_{L,11}$  stands for the 11-element of the  $M_L$  matrix, which gives

$$T = \frac{T_L T_R}{(1 - \sqrt{R_L R_R})^2 + 4\sqrt{R_L R_R} \cos^2 \theta}. \quad (1.20)$$

In (1.12),  $T_L$  and  $T_R$  are, respectively, the transmission probabilities through the left and right barriers,  $R_L = 1 - T_L$  and  $R_R = 1 - T_R$  denote the related reflection probabilities, and

$$\theta = kL + (\arg M_{L,12} + \arg M_{R,21} - \arg M_{L,11} - \arg M_{R,11})/2.$$

Equation (1.20) suggests that  $T$  can be close to unity if the energy resonance requirement  $\theta = (2n + 1)\pi/2$  holds, with  $n$  integer, even if  $T_L$  and  $T_R$  have small values, for which  $1 - \sqrt{R_L R_R} \cong (T_L + T_R)/2$ . The resonance transmission probability,  $T_{\text{res}} = 4T_L T_R / (T_L + T_R)^2$ , can become unity if  $T_L = T_R$ , irrespective of the values of  $T_L$  and  $T_R$ , or can be approximated with  $4 \min(T_L, T_R) / \max(T_L, T_R)$  if  $T_L$  and  $T_R$  differ significantly. At resonance, when the energy of incident electrons  $E$  equals a resonant value  $E_{\text{res}}$ , besides being transmitted with high probability, the electron travels through the structure faster than in off-resonance conditions. In general, the devices based on resonant tunneling are ultrafast. Around resonance, we have

$$T(E) \cong \frac{\Gamma_L \Gamma_R}{(\Gamma_L + \Gamma_R)^2/4 + (E - E_{\text{res}})^2}, \quad (1.21)$$

where  $\Gamma_L = (dE/d\theta)T_L/2$  and  $\Gamma_R = (dE/d\theta)T_R/2$  (divided by  $\hbar$ ) are, respectively, the rates at which an electron situated in the well leaks out of it through the left and right barriers. Close to resonance,  $T$  is very sensitive to the values of  $E$  and  $E_{\text{res}}$ . The last parameter can be easily tuned by applying a bias across the structure.

It is quite remarkable that, although the coherent nature of the electron transport is explicitly used in deriving (1.20), which implies that electrons are transmitted in

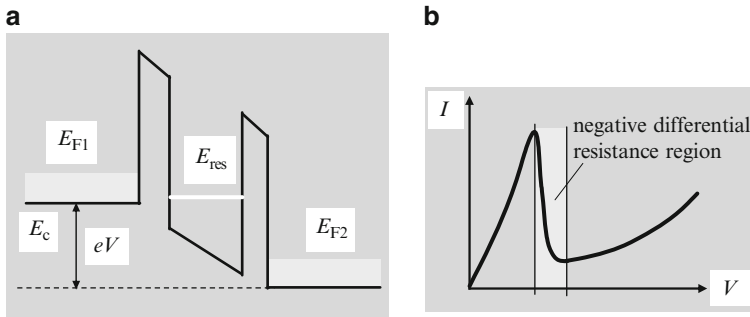


**Fig. 1.13** (a) Energy band representation of a resonant tunneling diode, and (b) a typical current-voltage characteristic

a single quantum process through the whole structure, this expression can be used also if sequential tunneling occurs.

The most notorious device based on the resonant tunneling phenomenon is the resonant tunneling diode (RTD), displayed in Fig. 1.13. The RTD is a biased double-barrier structure, which has a single resonant energy level  $E_{\text{res}}$  in the quantum well region that filters the electrons from the left contact (emitter). In consequence, only the electrons with energy  $E_{\text{res}}$  from all electrons in the emitter with energies between the Fermi energy  $E_{F1}$  and the bottom of the conduction band  $E_c$  can tunnel toward the contact on the right (collector) with Fermi energy  $E_{F2}$ . As a result, the  $I - V$  characteristic of the RTD displays a negative differential resistance (NDR) region since  $E_{\text{res}}$  drops below  $E_c$  at a sufficiently high bias and electron tunneling into the collector is no longer possible. Consequently, the current decreases drastically. The NDR of the RTD occurs even at room temperature. RTDs have numerous applications as bistable elements, oscillators, or logic circuit components (Dragoman and Dragoman 2009a).

When a constrained structure such as a quantum well, quantum wire, or quantum dot is positioned in the immediate neighborhood of another constrained structure of the same type, the interaction strength between electrons in the two structures depends on the height and width of the barrier separating the confined structures. The quantum wells (quantum wires or quantum dots) are said to be coupled when the electrons interact and the electron wavefunction expands over the whole structure, whereas when the electrons in neighboring structures do not interact, we have a series of noninteracting structures, called multiple quantum wells (quantum wires or quantum dots). In the last case, the electrons localized in one quantum well (quantum wire or quantum dot) are transferred to the other confined structure only through sequential tunneling. Nanoscale structures separated by finite barrier regions are coupled by the exponentially decaying electron wavefunction in the barriers, which allows overlapping of the envelope electron wavefunctions in neighboring wells if the potential barriers are thin enough.

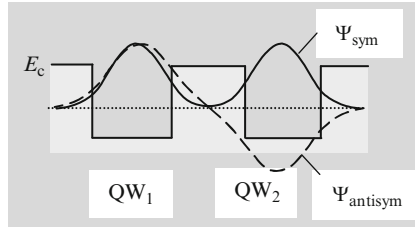


**Fig. 1.14** Electron wavefunction splitting into an antisymmetric (*dashed-dotted line*) and a symmetric (*solid line*) part when two identical quantum wells are brought in close proximity. The dashed line represents the coordinate axis

In particular, if two identical quantum wells, denoted by QW<sub>1</sub> and QW<sub>2</sub> in Fig. 1.14, are coupled, the resonant energy levels in individual quantum wells are no longer degenerated, and the electron wavefunction breaks up into a symmetric and an antisymmetric part,  $\Psi_{\text{sym}}$  and  $\Psi_{\text{antisym}}$ , respectively, which expand over the entire structure. On the contrary, in two nonidentical coupled quantum wells, the electron wavefunction is still confined in one of the two wells except when the different individual resonant energy levels in the wells align in the presence of an applied bias that produces a resonance in the structure. Only in this last situation the electron wavefunction delocalizes and breaks up into a symmetric part and an antisymmetric part.

A generalization of the previous example involves several identical quantum wells, which form a periodic structure with period  $\Lambda$  and are brought in close proximity. Then, they become coupled, and the delocalized electrons experience a periodical energy potential distribution with the same period  $\Lambda$ . In particular, in a quantum structure consisting of  $N$  periods, each  $N$ -fold degenerate energy level in the quantum wells splits, so that each well provides one state to the resulting energy bands containing discrete levels.

In the limiting case of quantum structures with a large number of periods and sufficiently narrow barriers, the allowed and forbidden electron energy bands become almost continuous, analogous to bulk materials, in which electrons feel the periodicity of the crystalline lattice; these energy bands of a periodic structure are illustrated in Fig. 1.15. Such a quantum structure that can be assimilated with an artificial lattice with a controllable unit cell is a superlattice. The widths and positions of the allowed and forbidden electron energy bands depend on the spatial distribution of the periodic potential, which can be modulated at will using advanced semiconductor techniques.

The prospect of tuning the energy dispersion of electrons in a semiconductor superlattice is especially useful in optoelectronics when the period of the superlattice is equal to the wavelength of the electromagnetic field. In this situation, allowed and forbidden frequency bands develop also for the electromagnetic radiation, analogous to the case of electrons in superlattices or bulk materials; the position and width of these bands are controllable. A comprehensive theory of electron

**Fig. 1.15** Allowed and forbidden electron energy bands in the periodic potential of a superlattice

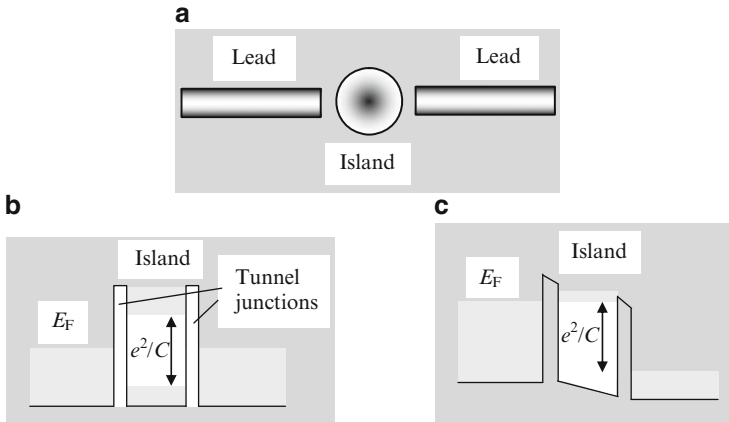
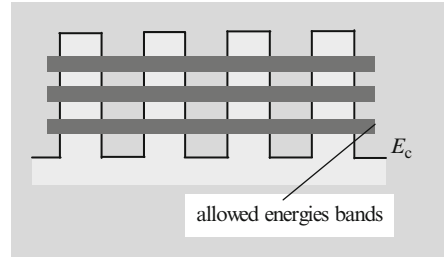


**Fig. 1.16** (a) Schematic representation of an island connected to metallic leads through tunneling junctions. (b) Energy gap opening at the Fermi level due to the Coulomb energy needed to tunnel in or out of the island, (c) which is overcome by a bias  $V = e/C$

transport in superlattices that involves nonequilibrium Green functions can be found in [Wacker and Jauho \(1998\)](#).

Another interesting quantum phenomenon is encountered in tightly confined nanostructures, in particular in quantum dots. Here, the Coulomb interaction is considerable, and the electronic states depend on the number of electric charges (electrons) in the dot, which takes discrete values. A manifestation of this dependence is illustrated by the Coulomb blockade, in which an energy gap opens at the Fermi level in the electron energy spectrum in small metallic clusters or semiconductor quantum dots coupled by tunneling barriers to metallic leads; these confined structures are generically called islands. The configuration of a Coulomb blockade device is schematically represented in Fig. 1.16a ([Ferry and Goodnick 2009](#)). This gap in the energy spectrum, analogous to the energy gap in semiconductors, is modeled as an additional energy needed by an electron to tunnel in or out of the island, which originates in the Coulomb interaction between electrons in the island.

This additional energy is equal to  $e^2/2C$  in metallic islands, where  $C$  is the capacitance between the island and the surrounding medium, and leads to a gap of  $e^2/C$  in the electron energy spectrum at the Fermi level since, in addition to electrons, holes need the same additional energy  $e^2/2C$  to tunnel in or out of the island. The Coulomb blockade phenomenon is observed when  $e^2/C \gg k_B T$ , which implies low temperatures, and when the electron number on the island is constant. The last condition is fulfilled if  $e^2/C$  is much larger than the lifetime broadening  $\hbar/\tau$ , where  $\tau$  denotes the electronic lifetime. Alternatively, in terms of an effective  $RC$  time, this requirement can be written as  $R \gg \hbar/e^2$ , which means that the island is decoupled from the reservoirs through tunneling barriers with much larger resistances in comparison to the quantum resistance.

As displayed in Fig. 1.16b, c, in the presence of Coulomb blockade, an electron can tunnel into a metallic island only if a large enough bias is applied,  $V > e/C$ , which overcomes the charging energy. As a result, in the  $I - V$  characteristic of the island, the current has very low values around zero bias. On the contrary, when  $V = e/C$  a single electron from one lead can tunnel in the island, leading to an increase of the Fermi energy in the island by  $e^2/C$ , and a subsequent tunneling event is forbidden by the opening of another energy gap, unless the applied bias raises to  $V > 3e/C$  or the additional electron in the island tunnels out of it. Summarizing, the average electron number in the island augments with one whenever the voltage increases with  $2e/C$ . As a consequence of these correlated tunneling events into and out of the island, the net current increases, and the  $I - V$  characteristic acquires a staircase shape when the two junctions differ significantly (Ferry and Goodnick 2009).

The Coulomb blockade phenomenon in ballistic semiconductor islands can be treated in an analogous manner except that the quantization of energy must be included in the model (size quantization effects are not relevant in metallic clusters because the conditions for ballistic transport are not satisfied, in general). In this case, the additional energy needed to add an electron to the island is  $e^2/C + \Delta E$ , where  $\Delta E$  is the difference between the energies of adjacent discrete quantum states.

The single-electron Coulomb blockade phenomenon is caused by the discreteness of electric charge that can be transferred to and from a conducting island connected through thin barriers to electron reservoirs. On the contrary, resonant tunneling devices are based on the discreteness of resonant energy levels in a quantum well coupled to electron reservoirs through thin barriers. The Coulomb blockade effect controls precisely the (small) number of electrons in the island and is employed in low-power switching devices that are essential for an increased level of circuit integration. In general, single-electron devices based on Coulomb blockade have an additional control of the electric charge in the island via a gate electrode, which leads to periodic current oscillations through the leads as the gate voltage is modified.

## 1.2 Nanotechnologies for Bionanoelectronic Devices

The nanotechnologies for bionanoelectronic devices rely on the technologies used in electronics to produce complex circuits based on AIII-BV semiconductors and micrometer and submicrometer-scale Si integrated circuits. Silicon is still the main material for micro- and nanoscale devices, but carbon allotropes, AIII-BV semiconductors, and biomolecular assemblies could end its dominance. There are two main approaches for nanotechnologies: top-down and bottom-up.

In the top-down approach, the major steps are (1) deposition of a single or multiple layers on a substrate, followed by (2) the transfer onto the layers grown in the first step of desired patterns, process that involves in turn several steps to remove unnecessary materials that are not included in the desired pattern. The first major step is called deposition technique, whereas the second is called lithography or nanolithography when the desired patterns have nanosized features.

The bottom-up nanotechnology techniques have no counterpart in the electronic technologies. For example, in the self-assembly technologies, which are maskless techniques, the mask manufacturing process characteristic for the top-down approach is replaced by less expensive specific chemical reactions able to form desired three-dimensional (3D) patterns consisting of metallic or semiconducting nanosized materials. However, it is not uncommon to fabricate nanoelectronic devices, especially biosensors, by a combination of bottom-up and top-down approaches.

### 1.2.1 Deposition Techniques for Bionanoelectronic Devices

In this section, we examine briefly the most important deposition techniques for micro- and nanoscale devices. An extended review with comprehensive references can be found in [Ziaie et al. \(2004\)](#).

To start with, the fabrication of  $\text{SiO}_2$  by oxidation of silicon is an essential process at both micro- and nanoscale, although other oxides, such as  $\text{HfO}_2$ , are increasingly studied.  $\text{SiO}_2$  is a dielectric material used to isolate a variety of metallic electrodes from other conductive substrates and can be deposited on silicon substrates with thicknesses ranging from few nm up to  $2\ \mu\text{m}$ . In particular,  $\text{SiO}_2$  is encountered in many transistors and micro-electro-mechanical systems (MEMS) or nano-electro-mechanical systems (NEMS), for example, switches. It is grown in the presence of oxygen or water at temperatures of about  $1,000\text{--}1,200^\circ\text{C}$  into furnaces containing a quartz tube, an electrical resistance heater, and a wafer holder. The thickness of the  $\text{SiO}_2$  depends on the temperature and the gas flow.

Another basic technological process in microelectronics, which is associated to deposition, is semiconductor chemical doping, performed with the aim of changing dramatically its electrical, optical, or mechanical characteristics. The process of changing these characteristics is generically referred to as functionalization or

material engineering. At the microscale, chemical doping is used to fabricate active electronic devices, such as diodes and transistors, at very large scale, and MEMS devices with specific mechanical characteristics (Dragoman and Dragoman 2001). Chemical doping of intrinsic silicon relies on a controllable introduction of p- or n-type impurities via ion implantation techniques or high-temperature diffusion from liquid or solid sources. At nanoscale, although chemical doping is still used in CNT transistors, for example, the diversity of functionalization techniques is greatly enhanced. For instance, nanowires or quantum dots can be functionalized also via electric fields, hydrogenation, oxygenation, adsorption of molecules or biomolecules, or other methods discussed throughout the book.

Deposition techniques for nanosized devices are based on chemical vapor deposition (CVD), in which thin films, with thicknesses up to fractions of nm, are deposited on a substrate using chemical reactions of specific gaseous components. In general, these chemical reactions need high amounts of energy generated by (1) plasma excitation, (2) optical excitation, or (3) heating the substrate at very high temperatures. The first two processes work at lower temperatures than the last one.

CVD techniques comprise two basic methods: low-pressure CVD (LPCVD) and plasma-enhanced CVD (PECVD). LPCVD requires electrical heated furnaces where a very low pressure (at 0.1–0.7 torr) is maintained by a pumping system. Thin films of a certain material are deposited on both faces of a wafer positioned on a holder inside the furnace. For instance, thin films of  $\text{SiO}_2$  (using as gaseous components  $\text{N}_2\text{O}$  and  $\text{SiCl}_2\text{H}_2$  at  $900^\circ\text{C}$ ), polysilicon (from gaseous  $\text{SiH}_4$  at  $600^\circ\text{C}$ ), or  $\text{Si}_3\text{N}_4$  (from gaseous components  $\text{NH}_3$  and  $\text{SiH}_4$  at  $800^\circ\text{C}$ ), as well as Ti, Mo, Cu, and Ta metallic thin films can be deposited using LPCVD.

PECVD is based on the plasma produced by a high-power radio frequency (RF) source. The main advantage of PECVD is the lower temperature ( $100\text{--}300^\circ\text{C}$ ) needed to heat the substrate. PECVD consists of a plasma reactor with a RF source; a pumping system, which injects gases inside the reactor and produces a high vacuum inside the reactor chamber; and two parallel plates. On one plate, the RF signal is applied, and on the other, which contains also the wafer placed above an electrical heater, the RF generator is grounded. PECVD is used to deposit  $\text{Si}_x\text{N}_y$  (the nonstoichiometric form of silicon nitride), amorphous silicon,  $\text{SiO}_2$ , and CNTs produced from a mixture of  $\text{NH}_3$  and  $\text{C}_2\text{H}_2$  gases.

The CVD-based epitaxial techniques boosted the semiconductor industry because they made possible the growth of monolayers of several AIII-BV semiconductor heterostructures, such as InP/GaInAs or GaAs/AlAs, which are widely used in the advanced nanoelectronic devices based on quantum wells, wires, and dots. In the epitaxial growth based on CVD, a crystalline material is first grown on the substrate, and an additional crystalline material can be subsequently grown on top of it if their lattices match or are slightly different, case in which a strain between the crystals is induced. This strain can be used, for instance, to tune the bandgap of the resulting heterostructure to a desired value corresponding to a specific emission wavelength in quantum well or quantum wire lasers.

Two CVD-based techniques are mainly used to grow heterostructures: metal organic chemical vapor deposition (MOCVD) and molecular beam epitaxy (MBE).

The MOCVD technique relies on vapors of organic compounds with group-V hydrides and group-III atoms, which are placed inside the CVD chamber that can switch gases very fast. The MBE needs a CVD chamber containing a certain substrate in a high-vacuum environment. The substrate is exposed to molecular beams produced by several thermally evaporated basic sources, the beam exposure/growth order depending on the desired heterostructure.

### ***1.2.2 Nanolithography***

Nanoscale lithography is a key concept in nanotechnologies, the patterning of different surfaces with current nanolithographical methods attaining a resolution (the smallest achievable feature) of few nm; for an excellent review on nanolithography, see [Harriot and Hull \(2004\)](#).

In principle, lithography refers to the transfer of a desired geometrical pattern (a mask containing the desired features to be imprinted) onto a substrate. Lithography is typically performed by covering the substrate with a resist material, having a thickness of 0.2–2  $\mu\text{m}$ , with the help of a spinner and then illuminating the deposited resist with light or energetic particles, such as electrons or ions. Because the resist is sensitive to illumination, which is made through a mask that transmits the excitation (optical, or particle beams) in wanted spatial regions and blocks it in undesired regions, the required pattern is imprinted in the resist after illumination and the following developing process. More recently, especially in the case of particle lithography, the pattern is directly written in the resist, the procedure being termed maskless lithography. In general, the fabrication of nanoelectronic devices is based on a combination of lithographical techniques at microscale, among which optical lithography is mostly used for the device contacts, for example, and nanolithographical techniques, where the nanosized features of devices are implemented.

In optical lithography, for instance, the mask is fabricated from glass or fused silica plates, which are selectively coated with an absorbing Cr layer with a thickness of 80–100 nm. Mask fabrication is a challenging step when nanoscale resolution and small number of defects are needed. In these situations, the desired pattern is written with a pattern generator into the resist deposited on Cr by a laser beam, process followed by resist developing and etching of the Cr layer.

Typically, the mask is a scaled down version of a pattern designed at a much larger scale, the reduction process having the net advantage that all cut defects and errors are reduced with the same scale as the pattern. Nevertheless, masks directly made at the 1:1 scale are used in X-ray lithography.

In the resist material, selective chemical reactions occur at illumination. Depending on the resist type, positive or negative, the illuminated areas are dissolved and removed in the developing stage of the resist or, respectively, are kept intact, as shown in [Fig. 1.17](#). In both cases, the required pattern is imprinted in the resist, which is deposited on the substrate.

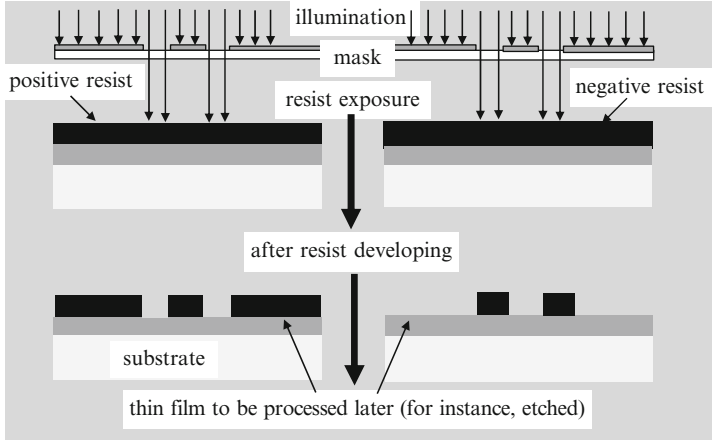


**Fig. 1.17** The optical lithography process

If necessary, the lithographical process is repeated several times using various resists and masks, which need to be aligned at each step, the procedure being accompanied by etching and deposition processes in a prescribed order to obtain the final nanodevice or integrated circuit. The principal parameters of the lithographical system are resolution and mask alignment (interlevel alignment values).

The resist materials are generally polymers, such as diazonaphthoquinone (DNQ) or (poly)methylmethacrylate (PMMA) in the optical lithography case, the resist type being a function of the illumination source (particle beams, optical, X-ray). The exposure of the resist is performed in a direct write mode, when it is illuminated point-by-point, through a mask, which is fully exposed, and the pattern is imprinted in the resist by contact or proximity alignment of the resist surface to the mask (see Fig. 1.17), or by projecting the image of the mask. The mask is in direct contact with the resist in the contact exposure method, which assures a good resolution but damages the mask in the process, while in the proximity method, the mask is situated at a distance  $d_{m-r}$  from the resist, which determines the minimum feature size:

$$w_{\min} \approx (\lambda d_{m-r})^{1/2}. \quad (1.22)$$

In (1.22),  $\lambda$  denotes the wavelength of the illumination source. In the proximity method,  $d_{m-r}$  must be very small to obtain printed feature sizes the same as that on the mask, which is a challenge in nanotechnologies. Therefore, the projection exposure method is the most widespread high-resolution procedure in nanolithography. In this method, an optical system projects the image of the mask on the resist, improving the best resolution, which is given by

$$R = \beta\lambda/NA, \quad (1.28)$$

where NA is the numerical aperture of the imaging lens and  $\beta \cong 0.8$ . The ratio  $\beta/\text{NA}$  is nearly 1 in the optical projection exposure method, the resolution being directly proportional with the excitation wavelength.

In a typical optical lithographic system, which uses mercury arc lamps with pronounced emission peaks at 365 and 435 nm, only geometrical line widths exceeding 0.25  $\mu\text{m}$  can be obtained. If thinner line widths are needed, excimer lasers such as ArF ( $\lambda = 193$  nm), F<sub>2</sub> ( $\lambda = 157$  nm), and KrF ( $\lambda = 248$  nm) must be used to lower the geometrical line widths up to 0.13  $\mu\text{m}$ .

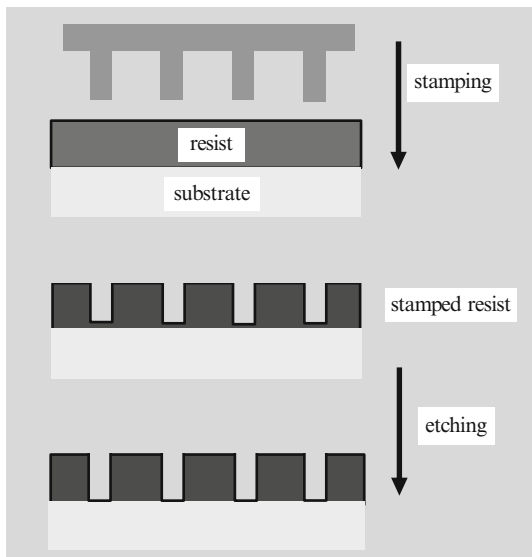
Higher resolutions, of 30 nm, and interlevel alignments as small as 10 nm can be achieved with extreme ultraviolet lithography (EUV), which uses wavelengths of 10–14 nm. However, there are many difficulties in mask fabrications at these wavelengths, the reflective elements of EUV masks being multilayered Bragg mirrors deposited on Si. A synchrotron or plasma source illuminates the mask, the tolerances of the imaging system in the projection exposure method being of only few angstroms. Despite these difficulties, the EUV displays very high yields, including a high speed of feature patterning, of about  $10^{11}$  features/s. At the extreme end of the electromagnetic spectrum, lithography with X-rays uses high-energy (few keV). X-ray sources such as Cu target systems emitting X-rays or electron synchrotrons. X-ray lithography works in the proximity-printing mode and has a resolution of 50 nm. The main drawback of this method is the 1:1 scale mask fabrication.

The particle nanolithography is based on electrons or ions, the lithographical process displaying very good performances, with resolutions of 10 nm for ions and 50 nm for electron lithography. Even smaller features, of 5 nm, can be obtained using this method.

The electron beam lithography (EBL) technique relies on two configurations. In the first, direct writing EBL, a focalized electron source, is directed to a substrate or a substrate covered with a resist such as PMMA. The electron beam is then scanned with the help of magnetic or electrical deflection systems and writes the desired pattern in the resist. The disadvantage of this method is the very slow writing process, which needs hours to write a high-resolution pattern. The second EBL method is the electron beam projection lithography, similar to the optical lithographical technique with the same name described above. In this case, the electron beam passing through the mask, which is a membrane with holes, focuses an image of the pattern on a resist with the help of an imaging system. The interested reader can consult (Tseng et al. 2003) for an excellent review on this subject.

The focused ion beam (FIB) lithography consists of scanning directly a substrate with a focused high-energy ion beam. This technique does not require masks or resists, and the point-by-point lithographical process relies on two different principles: (1) subtraction of surface atoms or (2) decomposition over the substrate of an organic vapor. In the first case, the desired pattern is imprinted directly on the substrate by scanned sputtering of atoms from the surface, while in the second case, the desired pattern is formed by the material deposited on the substrate. The FIB lithographical process can be monitored/imaged in real time by the ions and electrons emitted as a result of the interaction between the substrate and the

**Fig. 1.18** The nanoimprint process



ion beam. The throughput, which represents the number of patterned features in one second, is quite low, of  $10\text{--}10^2$  features/s for the direct writing EB and FIB techniques, but increases dramatically, up to  $10^{10}$  features/s, for the EB projection method.

The nanoimprint lithography is a high-resolution nanolithography, displaying high reproducibility in a short time. Its throughput is as large as  $10^{12}$  features/s, while the resolution is as small as 10 nm. Typically, the nanoimprint technique utilizes a master or stamp fabricated from  $\text{SiO}_2$  or Si, which contains the desired pattern fabricated via EB or FIB. This stamp is then used to imprint a resist with the desired pattern. The resist is generally a polymer, which can be UV-curable or thermoplastic (heated above its glass temperature), such as PMMA. After the polymer is stamped, the resist residues are removed by etching. The nanoimprint lithography, schematically displayed in Fig. 1.18, is excellently reviewed in Guo (2004).

The extreme top-down nanolithography technique is based on atomic beams, collimated and focused, similar to optical systems, by atomic lenses, atomic apertures, etc. In general, the atom beam interacts with laser beams and the resulted optical-atomic forces are utilized for (1) depositing atoms in order to built nanoscale structures or (2) patterning various shapes in a lithographic method (Meschede and Metcalf 2003). The atomic lithographic technique is based on an incoming atomic beam that is incident on a standing wave created by a laser and a mirror system, as shown in Fig. 1.19. The standing wave plays the role of a light mask for the incident atoms and is analogue to an array of lenses diffracting the atoms in the optical antinodes or nodes as a function of the sign of the difference between the laser frequency and the resonant frequency of atoms. In consequence, the desired pattern

**Fig. 1.19** The principle of atomic beam lithography

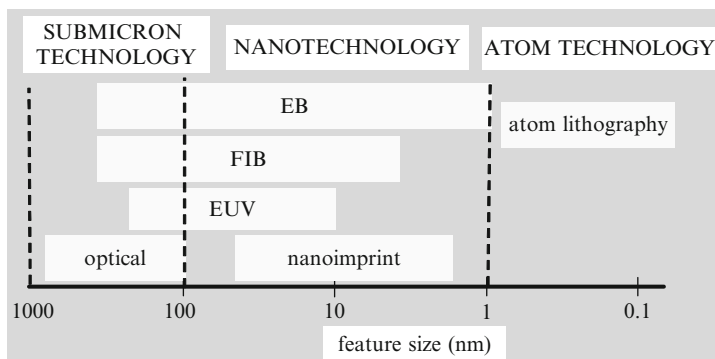
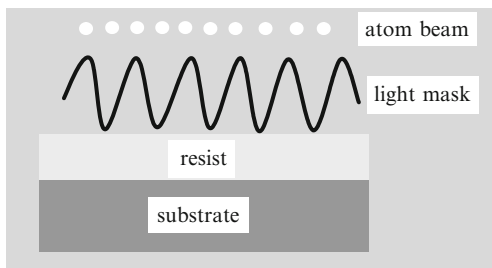


**Fig. 1.20** The performances of the main lithographical techniques

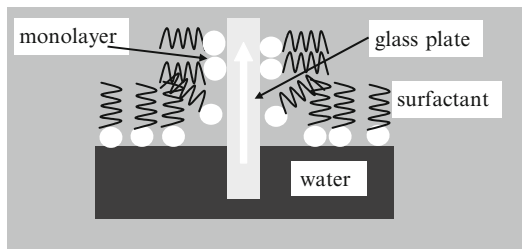
is generated via the antinodes and nodes of the light beam. The incoming atoms pass through the mask and are deposited on a resist, which is subsequently developed.

The performances of various nanolithography techniques are illustrated in Fig. 1.20. There are several recent reviews dealing with nanolithography and its ultimate limits, which indicate also the strategies to be adopted when a certain device with certain features must be fabricated (Pease and Chou 2008; Saavedra et al. 2010).

The bottom-up approach to nanotechnologies is best represented by the self-assembly techniques. The self-assembly process stands for spontaneous organization of several components, such as molecules or nanoparticles, into a desired pattern. The organization process involves chemical, physical, or biochemical interactions, such as electrostatic and surface forces, or chemical hydrophilic and hydrophobic interactions. All these processes are extremely selective and have low defect rates, the resulted structures possessing a high quality (Hue 2003). Some basic self-assembly techniques are explained below.

The Langmuir–Blodgett (LB) technique is a well-known self-assembly method for thin film fabrication in which the pattern results by growing one monolayer at a time. A monolayer of a required material, originally adsorbed at a gas–liquid interface, is placed on the substrate on which the self-assembly structure will form. For instance, a monolayer of a fatty acid or, in general, a surfactant, is first spread

**Fig. 1.21** The principle of the Langmuir–Blodgett technique



over a water surface. If a glass microscope slide acting as the self-assembly substrate is introduced in the water, a monolayer attaches to it when pulling the glass slide out of water, as shown in Fig. 1.21. The process can be repeated, and a monolayer is deposited each time the glass slide passes through the water surface. In practice, the LB technique requires specialized instruments such as a Langmuir trough, a dipping device for the lowering or raising substrate, and a movable barrier, which is controlled by a pressure sensor and maintains a constant surface pressure by sliding on the gas–liquid interface. The LB technique was used to fabricate polymeric films, 2D gold nanoparticle arrays, and semiconducting quantum dots. A good review about LB films is [Rietman \(2001\)](#).

Electrostatic self-assembly is a widespread technique based on the electrostatic interaction between nanoparticles or molecules. The origin of this self-assembly technique resides in the fabrication of multilayer films, in which each layer contains negatively and positively charged colloid particles, for example, Al and Si. The method is used in the fabrication of nanostructured films containing semiconductors, metals, polymers, magnetic materials, or organic molecules.

The thin films fabricated by electrostatic self-assembly are stable and uniform because of the strong ionic bonds between positive- and negative-charged particles, while the combination between polymers and the layers of electrically charged nanoparticles minimizes the eventual defects. In the electrostatic self-assembly process, a clean substrate is first immersed into a cationic solution, then rinsed, and dried, followed by another dip of the substrate already coated with cations into an anionic solution and subsequent rinsing and drying processes. This procedure can be repeated several times, the resulting nanostructured film growing with one layer/cycle (see Fig. 1.22). As an example, a heterostructure containing consecutive layers of gold and silver nanoparticles can be fabricated by first self-assembling positively charged Au nanoparticles on a negative glass substrate by dipping the substrate into 4-ATP (aminothiophenol)-capped Au solution having  $\text{pH} = 4$ , then depositing a monolayer of negatively charged Ag nanoparticles by dipping the previous Au-coated glass into a 4-CTP (carboxythiophenol)-capped Ag solution having  $\text{pH} = 8.5$ , and repeating the cycle as many times as necessary ([Huie 2003](#)). In a similar manner, it is possible to self-assemble a multilayer film consisting of conducting polymer chains and nanosized iron oxide, which combines the strength and flexibility of polymers with the magnetic properties of iron. In both cases, the

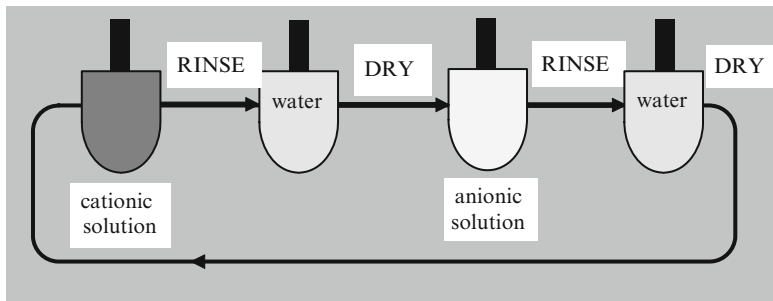


**Fig. 1.22** The principle of the electrostatic self-assembly method

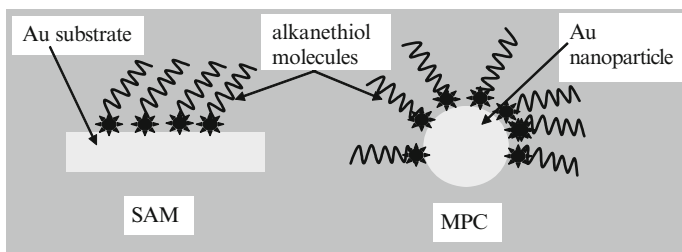


**Fig. 1.23** Schematic representations of the SAM and MPC methods

properties of the final nanostructure are a mixture of the properties of the constituent layers, which is a typical characteristic for self-assembled nanostructures.

Chemical self-assembly methods are very frequently used to fabricate nanostructures, among them the SAM (self-assembled monolayers) and MPC (monolayer-protected clusters) techniques being prevalent. In the SAM method, monolayers form spontaneously by immersion of an appropriately chosen substrate into a solution, whereas MPC uses chemisorption to obtain nanoclusters with surfaces derivatized by ligand molecules, as displayed in Fig. 1.23.

Finally, proteins and DNA are the basic constituents of biomolecular self-assembly, which is used to fabricate (1) self-assembly of semiconducting nanoparticles, for example, ensembles of CdSe quantum dots; (2) functionalized metallic nanoparticles; or (3) biomolecular–metal complexes, for instance, DNA–Au complexes.

Many other self-assembly methods for nanostructures exist, the self-assembly strategy being one of the major techniques for fabricating new devices or materials (Shenhar et al. 2004). As an example, metal nanowires with lengths in the 20–50  $\mu\text{m}$  range and widths between 2 and 50 nm can be fabricated by self-assembly techniques in a defined 3D geometry, without lithography (Saif et al. 2003). These long and ultrathin metal nanowires are obtained by PECVD coating a Si substrate with  $\text{SiO}_2$  incorporating OH impurities, which produce compressive stress in the Si/ $\text{SiO}_2$  film. This film is subsequently annealed at 600°C for a long time to

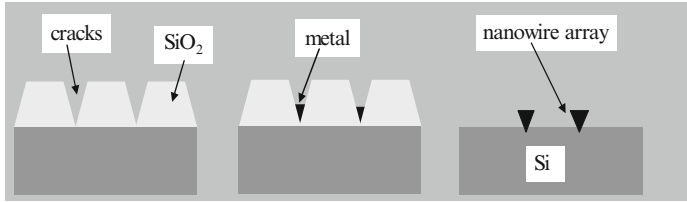


**Fig. 1.24** Fabrication of a metal nanowire array by self-assembly

eliminate the OH impurities, process in which tensile stress develops in the film. As a result, the film cracks, the nanoscale cracks being able to extend up to the Si substrate. Finally, a metal is deposited in the cracks, and wet etching is used to remove the oxide. The geometry of the cracks depends on the type of the generated stress. For instance, a parallel array of cracks, and thus a parallel array of metal nanowires, as displayed in Fig. 1.24, is obtained due to an uniaxial stress.

### 1.2.3 Nanomaterials

The strength of bionanoelectronics resides in the fact that one or more dimensions of the nanoscale materials, termed as nanomaterials, are of the same size as bacteria, viruses, or biomolecules, such as DNA, from which the entire living matter is made (Gruner 2006). In what follows, we present briefly the main nanomaterials. The interaction of these nanomaterials with living matter is the main subject of the book.

Nanoparticles are frequently used in bionanoelectronics, especially for targeted drug delivery and sensing of biomolecules. Nanoparticles having few nm in diameter can be metallic, semiconducting, or even isolators, but their physical properties depend strongly on their size and differ dramatically from those of the bulk material from which they are made. A typical example is the transformation of the conduction band of bulk metals in discrete energy levels in a metallic nanoparticle, which resembles a quantum dot described in Sect. 1.1. The discrete nature of electronic states in a metallic nanosized particle is described by the average spacing between adjacent quantum levels, called Kubo gap:

$$\delta = 4E_F/3n, \quad (1.29)$$

where  $n$  is the number of electrons in the nanoparticle and  $E_F$  denotes the Fermi energy level. The nanoparticle behaves as a metal, i.e., the Kubo gap is not apparent, if  $k_B T > \delta$ . For instance, an Ag particle with a 3-nm diameter is metallic at ambient temperature because  $k_B T \cong 25$  meV for  $T = 300$  K, while  $\delta = 10$  meV. Almost all metal nanoparticles (Au, Ag, Pd, Ni, Cu) are fabricated via evaporation of the bulk metal counterpart in vacuum.

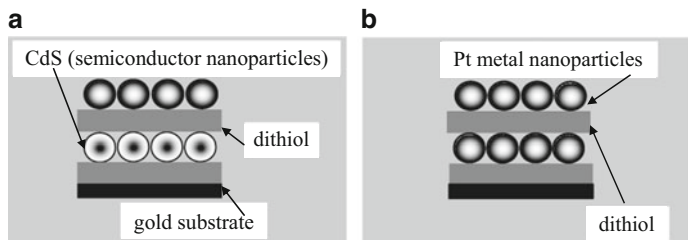


**Fig. 1.25** Tridimensional assemblies of (a) metal nanoparticles–semiconductor nanoparticles and (b) metal nanoparticles–metal nanoparticles

Metal particles covered with organic molecules such as thiols are able to self-organize in 1D, 2D, and 3D arrays (Rao et al. 2000). In particular, 2D nanoparticle arrays are fabricated by mixing a hydrosol incorporating metal nanoparticles (Pd, Au) with a toluene solution of alkali thiol. Subsequently, the mixture of 3–4-nm metal nanoparticles and thiol is deposited on a surface and form a large and regular 2D array in which the nanoparticles are equally spaced in the  $x$  and  $y$  directions by about 5–6 nm (Rao et al. 2000). This 2D array is in fact an array of quantum dots in which the Coulomb blockade phenomenon manifests in electrical measurements.

Three-dimensional assemblies are fabricated via producing solutions of dithiol molecules and metal particles and then dipping a substrate into these solutions, followed by washing with toluene solution, and drying. Metal nanoparticle–semiconductor nanoparticle or metal nanoparticle–metal nanoparticle assemblies can be fabricated using this method (see Fig. 1.25a, b, respectively).

Nanoparticles are not only metallic but also semiconducting, such as silicon nanoparticles, elemental II–VI semiconductor quantum dots, and III–V nanoclusters. A review of fabrication of various types of nanoparticles is Adair et al. (1998). Nanoparticles play a central role in many areas of bionanoelectronics, especially in the area of controlled drug delivery and cancer therapies based on nanomaterials (Biswas et al. 2010). Also, core/shell nanoparticles are extremely used in biosensing, drug delivery, or cell labeling. The core/shell nanoparticles are of several types: (1) inorganic core/shell nanoparticles such as silver/silica or CdSe/CdTe nanoparticles, (2) organic/inorganic core/shell nanoparticles, in particular polymer/metal nanoparticles, such as CuS/PVA or TiO<sub>2</sub>/celulose, and (3) polymeric nanoparticles such as PMMA/PVC (Sounderya and Zhang 2008).

Also, many applications involve nanoparticles from group IV such as carbon nanoparticles. Because carbon is the key element of any known form of life, and in the human body carbon is the most encountered element after oxygen (Fan and Chu 2010), carbon nanoparticles such as diamond and graphite nanoparticles display important applications in the area of bioimaging and drug delivery nanosystems.

Similar to nanoparticles, nanowires are metallic, semiconducting, superconducting, or magnetic and are widespread used in many bionanoelectronic applications. The physical properties of nanowires, such as the quantized conductance behavior

showing a staircase shape, are not retrieved in the bulk materials from which they are fabricated.

A nanowire confines the carriers in two dimensions. The NW has a diameter of a few nm and lengths of 100–300 nm, but longer nanowires were also fabricated. Nanowires can be obtained through many methods, for example, bottom-up approaches (Bowler 2004). Another method to fabricate nanowires is based on Si(001), which is more reactive if not hydrogenated. Therefore, hydrogen can be used as a nanoscale mask, and other materials adsorbed on the nonhydrogenated regions can generate a nanowire. For example, (low-quality) Fe, Al, Co, Ga, or Ag nanowires can be obtained in the depassivated regions. There are several methods to fabricate self-assembled nanowires, such as methods based on specific chemical reactions and surface forces. For instance, rare-earth nanowires are fabricated by depositing the rare-earths on a Si(001) substrate and subsequent annealing. Similarly, Bi nanowires with a length of 200–600 nm and a width of 1.5 nm appear spontaneously when a Si(001) substrate covered with Bi is annealed around 600°C.

Template synthesis is, however, the most common method to fabricate nanowires. The template is, in fact, a prescribed pattern, for example, hexagonal, of nanosized pores or voids in a host material. Nanowires form when these pores are filled with the constituent material, termed source material. There are few reviews on nanowire growth such as Wang and Zhang (2008) or Bandaru and Pichanusakorn (2010).

Figure 1.26 illustrates the most common template for nanowire growth, which is anodic alumina. The alumina template results from anodizing Al thin films in specific acids. If an electrical current flows between the Al film and the cathode during anodization, an alumina film (membrane) displaying a regular hexagonal array of parallel and nearly identical cylindrical pores is obtained as the result of the etching process, as illustrated in Fig. 1.26. These nanopores have diameters within the 20–200-nm range, pitches of 50–400 nm, and a density that varies between  $10^9$  and  $10^{11} \text{ cm}^{-3}$  as a function of the etching conditions. The anodization process produces regular pore geometries. Nanochannels in glasses and etched polymers are also widely used to fabricate nanowires.

Precise templates can be created also by chemical etching of particle tracks resulted from ion bombardment. Nearly all types of nanowire can be fabricated using template techniques followed by a deposition method, and a subsequent extraction procedure of the source material.

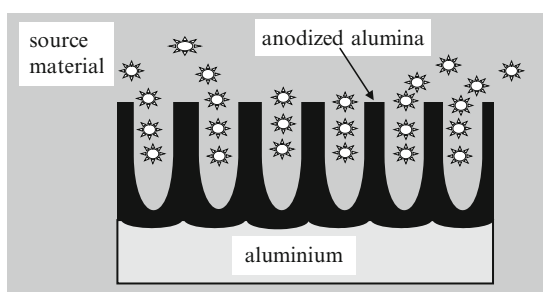


**Fig. 1.26** Nanowire growth in an alumina template

Electrochemical deposition is frequently employed for growing not only thin films but also nanowires. The deposition procedure is restricted to a template consisting of nanopores, which is coated with a metallic thin film acting as a cathode on one side. Semiconductor nanowires of CdS, metallic nanowires of Co, Fe, Cu, Ag, Au, Pb, Ni, or superlattices A/B containing two constituents A and B, for instance, Co and Cu, were fabricated using the electrochemical deposition.

Extremely thin nanowires can be grown using MOCVD or CVD. In these methods, the precursor material of the nanowire is heated to generate vapors that fill the nanopores of the template, which is subsequently cooled to obtain the solid nanowires. Almost single-crystal nanowires are fabricated with the CVD method, polycrystalline nanowires being obtained otherwise. Examples of single-crystal nanowires grown with CVD techniques include GaAs, GaN, Bi, and InAs, with diameters smaller than 10 nm, as well as CNTs. A recent review of carbon growth techniques and applications in the area of electronics is [Javey and Kong \(2009\)](#).

The vapor–liquid–solid (VLS) growth method of nanowire relies on the fact that a liquid (L) droplet of a catalyst absorbs the vapors (V) of the source material. The nanowire forms as a result of the solidification (S) of the source material due to the liquid saturation and a subsequent nucleation process, which produces a preferential site for future deposition at the boundary of the liquid. Thus, other nucleation processes are avoided, and growth is allowed only in a single direction, as displayed in [Fig. 1.27](#). The VLS method has been used to grow nanowires of Ge, Si, and ZnO. In situ electron microscopy can visualize and control the growth of Si and Ge NWs through the VLS method. Images and movies are produced in a transmission electron microscope, which is able to deposit catalysts and introduce CVD precursor gases in the sample under observation. In this way, the nucleation, the surface structure, and the growth kinetics are measured ([Ross 2010](#)).

Nanowires could be grown to form superlattices of the form XYXYXYXY... consisting of two types of nanowires, X and Y ([Chik and Xu 2004](#)). [Figure 1.28](#) represents an InP/InAs superlattice ([Björk et al. 2002](#)), while [Fig. 1.29](#) illustrates the energy band of a superlattice made of an alternation of intrinsic CNTs and

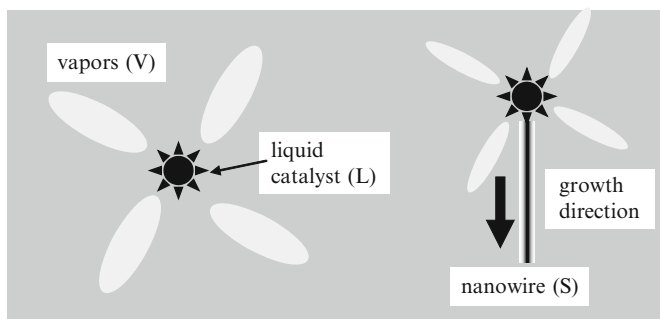


**Fig. 1.27** The VLS method of growing nanowires

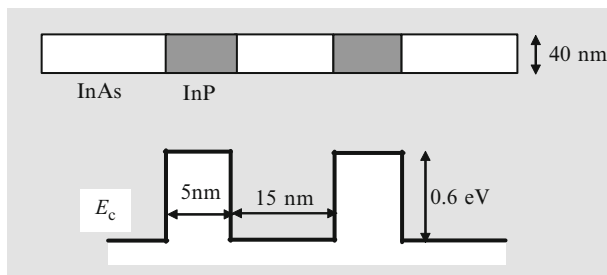
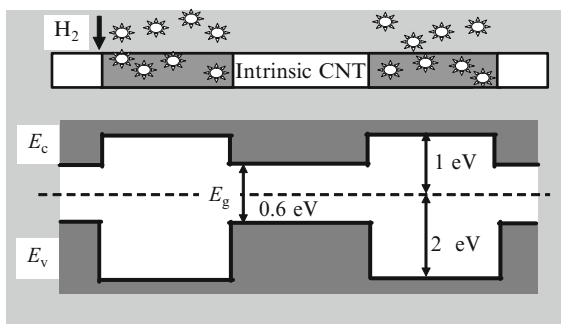


**Fig. 1.28** Circular nanowire InP/InAs superlattice (*top*) and its conduction band diagram (*bottom*)

**Fig. 1.29** Carbon nanotube superlattice (*top*) and its energy band diagram (*bottom*)



hydrogen functionalized semiconducting CNT; the energy bandgaps  $E_g$  of these material differ (Gülseren et al. 2003).

Both superlattices display a marked negative differential resistance and, as resonant tunneling diodes, can generate electromagnetic radiation with very high frequencies or can be employed as logic elements. The nanowire superlattice can be seen also as a series of three-dimensionally confined quantum dots, the transport through the structure taking place via coherent tunneling between adjacent quantum dots. If the width of the quantum barrier region increases, the tunneling process becomes sequential.

As in the case of core/shell nanoparticles, nanowire superlattices with radial periodicity can be fabricated by growing several nanowire shells with dissimilar properties. Typical examples are the coaxial Ge/Si and Si/Ge nanowires, obtained by initially growing one nanowire using the VLS method and then applying CVD deposition methods to grow the second nanowire over the first one (Lauhon et al. 2002).

Besides growing nanowires with prescribed properties, it is also important to align and position them using self-assembly techniques. Millions of CNTs, for example, can be aligned via a large-scale assembly method similar to biomolecular self-assembly processes (Rao et al. 2003). In this technique, millions of CNTs spread in solution are aligned on top of chemically functionalized patterns fabricated on a surface. The functionalization is achieved with two distinct regions, which are

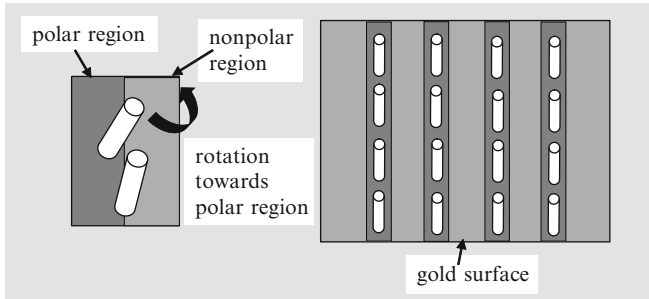


**Fig. 1.30** The principle for aligning millions of carbon nanotubes by self-assembly

coated with nonpolar or polar groups. Because the CNTs in liquid suspension are attracted by the polar regions only, millions of CNTs align in less than 10 s, as illustrated in Fig. 1.30. The CNTs are rotated by the electrostatic attraction force in the direction of the polar region and are immobilized only in this region (Fig. 1.30).

Graphene is the most recent nanomaterial and has already attracted attention due to its unusual physics and potential applications, as demonstrated by awarding the Nobel Prize for physics in 2010 to A. Geim and K. Novoselov (Geim and Novoselov 2007) for groundbreaking research in this domain. Graphene is a monolayer sheet of graphite, with a thickness as small as 0.34 nm, consisting of carbon atoms in a  $sp^2$  hybridization state, in which each atom is covalently bonded to three other atoms forming a honeycomb lattice. This lattice can be understood as consisting from two interpenetrating triangular sublattices. Graphene is at the origin of many carbon-based materials. For instance, graphite is formed by stacking millions of graphene layers, and single-walled carbon nanotube forms when graphene rolls up along a certain direction.

Graphene is a planar crystal and a natural 2D gas of charged particles. In its basic configuration, graphene is deposited on a 300-nm-thick  $\text{SiO}_2$  layer grown on top of an  $n^+$  silicon substrate. Only in this case it can be seen at an optical microscope. The wavelength at which graphene can be seen and its type, monolayer or bilayer graphene flakes, is determined by filtering a white light source and depends strongly on the  $\text{SiO}_2$  thickness (Blake et al. 2007): for a 300-nm-thick  $\text{SiO}_2$  layer graphene is optimally discriminate in green light, while blue light is most favorable for a  $\text{SiO}_2$  layer with a thickness of 200 nm.

In the basic configuration mentioned above, containing a doped Si substrate, silicon is acting as gate which, upon applying a gate voltage  $V_g$ , controls the surface charge density  $n$  according to the expression (Novoselov et al. 2004)

$$n = \varepsilon_0 \varepsilon_d V_g / t e. \quad (1.30)$$

In (1.30),  $\varepsilon_0$  and  $\varepsilon_d$  are the dielectric permittivities of air and  $\text{SiO}_2$ , respectively, and  $t$  denotes the thickness of the  $\text{SiO}_2$  layer. The carriers induced by the gate voltage exemplify the electrical doping effect, which is analogous to the chemical

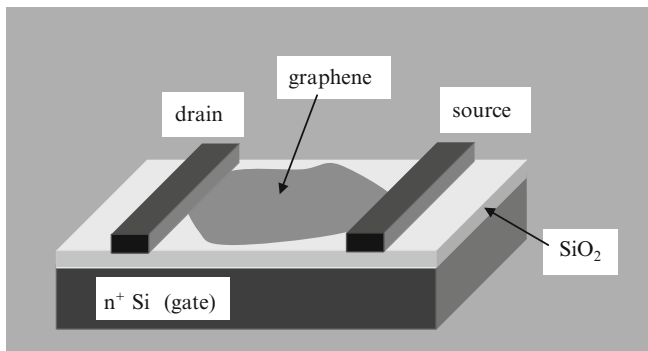


**Fig. 1.31** Schematic representation of the graphene FET

**Table 1.1** Characteristics of the main methods to produce graphene

Starting material	Brief description of method	Yield	Quality	Area
HOPG	Repetitive peeling	Low	Very high	Small
SiC	Reduction of Si at the surface of SiC at very high temperatures	Medium	Medium	Wafer size
GO	GO dispersion in hydrazine	High	Medium	Large
Gas mixture (CH <sub>4</sub> and H <sub>2</sub> )	CVD	Very high	High	Very large

doping in semiconductor devices because both effects shift the Fermi energy level. In particular, the analogues of chemical p or n doping in graphene are obtained by applying negative or positive electrostatic gate voltages, respectively.

To implement specific devices, electrodes need to be patterned on the graphene sheet after its deposition on the Si/SiO<sub>2</sub> structure. An example of such a device is the graphene-based field-effect transistor (FET), displayed in Fig. 1.31.

The customary method to deposit graphene on Si/SiO<sub>2</sub> relies on mechanical exfoliation of highly ordered pyrolytic graphite (HOPG) using an adhesive tape, and a subsequent release of the graphene flake on Si/SiO<sub>2</sub> following tape removal. HOPG is a 3D structure consisting of vertically stacked graphene sheets. The fragments of HOPG obtained by mechanical exfoliation, including graphene, stick to the Si/SiO<sub>2</sub> surface due to van der Waals forces. This quite rudimentary method allows the production of graphene flakes with dimensions up to 1 mm (Geim 2009). More complicated techniques to obtain and handle graphene include the AFM microcleavage of HOPG pillars and subsequent deposition on Si/SiO<sub>2</sub> surfaces, epitaxial growth of graphene, and the growth of graphene by CVD techniques. All these graphene growth techniques were recently reviewed in Soldano et al. (2010). Table 1.1 presents the characteristics of the main methods to produce graphene.

Graphene has amazing physical properties. In particular, it has ambipolar transport characteristics, which can be controlled by the gate voltage in configurations similar to that displayed in Fig. 1.31. Moreover, the room-temperature mean-free

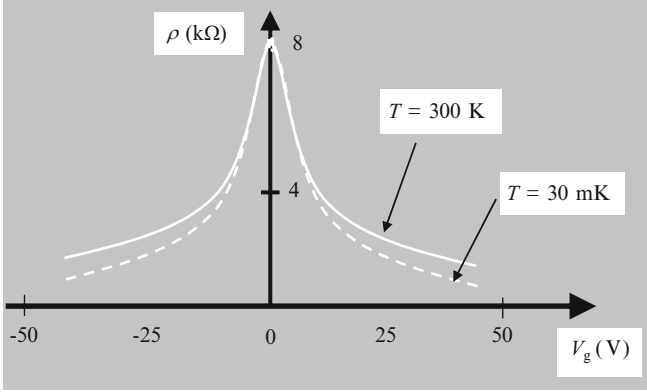


**Fig. 1.32** Typical temperature and gate voltage dependence of graphene resistivity

path for ballistic transport is around 300 nm, and the carrier mobility takes a typical value of  $15,000 \text{ cm}^2\text{V}^{-1} \text{ s}^{-1}$  at room temperature (Geim and Novoselov 2007) but can increase at  $200,000 \text{ cm}^2\text{V}^{-1} \text{ s}^{-1}$  in suspended graphene sheets with a carrier concentration of  $n = 2 \times 10^{11} \text{ cm}^{-2}$  (Bolotin et al. 2008). The graphene resistivity has only a slow variation with temperature, especially in samples with low mobility, but depends strongly on the gate voltage, as illustrated in Fig. 1.32. This behavior contrasts the strong resistivity dependence on temperature in other semiconductors or metals. The weak dependence of resistivity on temperature is determined by the dominant scattering mechanism, caused in low-mobility samples by static impurities and in high-density samples by residual electron-phonon scattering (Tan et al 2007).

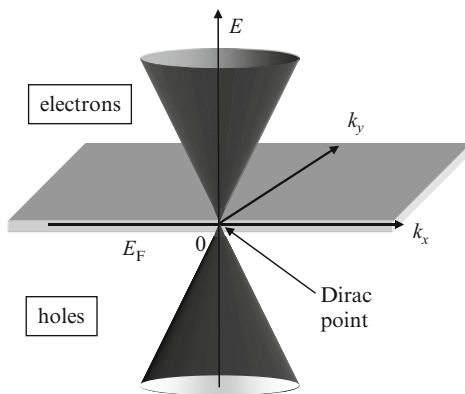
In common semiconductors, the electron and hole transport are described by two independent Schrödinger equations, whereas in graphene, the electron and hole states are correlated through the so-called charge-conjugation symmetry (or chirality), and a Dirac-like equation for massless particles is needed to model their behavior. In particular, both electrons and holes in graphene are characterized by a linear dispersion relation, given by

$$E = \pm |\hbar\mathbf{k}| v_F, \quad (1.31)$$

where  $E$  is the energy of charge carriers with wavevector  $\mathbf{k} = i k_x + j k_y$ , and  $v_F$  is the Fermi velocity. In Fig. 1.33, which illustrates this linear dispersion, the positive sign in (1.31) is assigned to electrons, while the negative sign corresponds to holes. The distinctive dispersion relation (1.31) shows that the valence and conduction bands touch each other in a point termed Dirac point, i.e., graphene is a gapless semiconductor.

A linear dispersion relation such as that in graphene is met only in photons propagating in vacuum, for which  $E = \hbar\omega = hc/\lambda$ , with  $c$  the speed of light. Note that the two situations correspond to completely different physical systems: graphene is a 2D gas of massless fermions, whereas photons are bosons.

**Fig. 1.33** The dispersion relation in graphene



In graphene, the linearity of the dispersion relation means that the effective mass of electrons and holes is zero, and the charge carriers propagate ballistically with the velocity  $v_F = 10^6 \text{ m s}^{-1} \cong c/300$ .

The gapless nature of graphene is in fact a disadvantage in many devices, so that different methods have been sought to open bandgaps in this material. A possibility is to confine the charge carriers by etching the graphene sheet contacted with electrodes. The resulting narrow strips, with typical length of 1–2  $\mu\text{m}$ , are called graphene nanoribbons (GNR). The width  $W$  of such a strip controls the width of the energy gap, which opens at the Dirac point, according to the relation (Han et al 2007)

$$E_g = \alpha / (W - W^*), \quad (1.32)$$

where  $\alpha = 0.2 \text{ eV} \times \text{nm}$  and  $W^* = 16 \text{ nm}$  are experimentally determined fitting parameters. Thus, band engineering becomes possible by tailoring the dimensions of the graphene nanoribbons. For example, the bandgap ranges from 100 to 3 meV if the width of the nanoribbon varies in the 20–90-nm interval.

The physics and applications of graphene are reviewed in many recent papers such as (Dragoman and Dragoman 2009b) and Wei and Liu (2010). Graphene has also important applications in the area of bionanoelectronics, biomolecule sensing, DNA sequencing, and drug delivery. More details are found throughout this book, especially in the chapter dedicated to sensing of biomolecules, such as DNA.

### 1.3 Conduction Properties of Biological Materials

The conduction of biological materials relevant for nanoscale electronics is related to the charged ions, which can be small molecules ( $\cong 0.2 \text{ nm}$ ), protein composites ( $\cong 10 \text{ nm}$ ), or giant polymers (DNA is often few centimeters long and contains millions of negative-charged groups in its backbone) (Waigh 2007). The charged ions are surrounded by water molecules. Examples of charged ions are the  $\text{COO}^-$

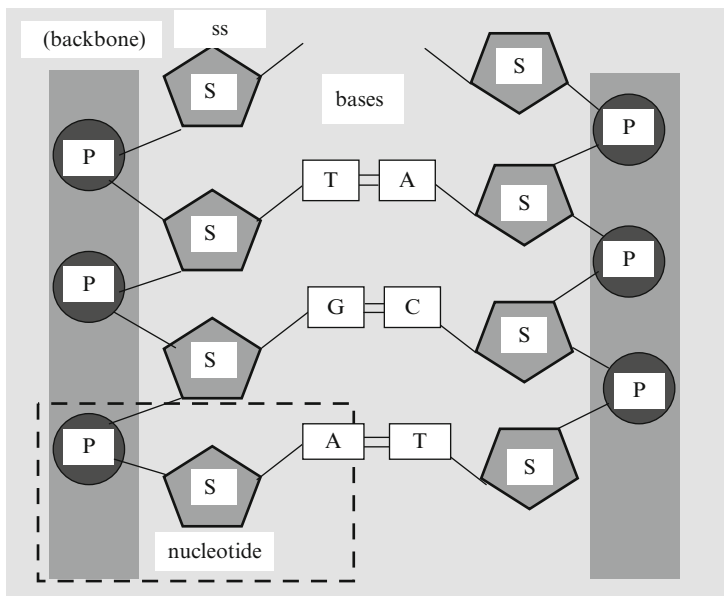


**Fig. 1.34** The schematic DNA structure

carboxylic acid encountered in aspartic and glutamic acid in proteins and fatty acids, or the phosphate group in DNA. Their role is essential in the main functions of life:  $\text{Ca}^{2+}$  ions regulate the molecular motors in muscles, while a combination of  $\text{Na}^+$ ,  $\text{K}^+$ , and  $\text{Ca}^{2+}$  ions control the propagation of electrical pulses in nerves. The role of charged ions in living organisms is excellently reviewed in [Waigh \(2007\)](#).

In what follows, we will focus on the conduction properties relevant for nanoscale electronics. DNA, the blueprint of life, is considered the most complex molecule, which not only contains the code of life but is considered as a good candidate for a series of devices associated with molecular electronics and thus is seen as a “material” due to the hybridization of its single strands, which is associated with self-assembly processes, and to its ability to be synthesized in an huge number of sequences ([Kwon et al. 2009](#); [Yang et al 2010](#)). The single-stranded DNA (ssDNA) is formed by four bases and the phosphate backbone and is schematically represented in [Fig. 1.34](#). The four bases of DNA are thymine (T), adenine (A), cytosine (C), and guanine (G). In the double-stranded DNA (dsDNA), the bases are bonded by hydrogen bonds in complementary manner: A–T and G–C. The dsDNA has a double-helix structure, with a width of 2 nm and a distance between stacked base pairs of about 3.4 Å. Billions of such base pairs in the folded dsDNA form the genome, which is found in any cell of eukaryote organisms.

On the other hand, in the last years, many nanoscale devices were tested for DNA sequencing, all based on the negative charging of the DNA backbone in solution. DNA is the best example that conduction of biological materials is quite

far from the conduction in crystals, which is quite well understood. The DNA is conducting due to the interbase hybridization of  $\pi_z$  orbitals, placed perpendicular to the planes of stacked bases (Enders et al. 2004). However, DNA is not a crystal; it is not periodic. The potential barrier between two bases is very large, reaching 0.6 eV, which indicates an Anderson localization of electronic states of base pairs. In the double-helix DNA conduction experiments, the hydrophobic bases avoid contact with water, and the immediate environment consists of counterions formed by positive charges, which neutralize the negatively charged backbone. These considerations suggest that the conduction of biomolecules is strongly dependent on environment, in contrast to many electrical experiments at room temperature on inorganic nanodevices, where the environment plays no role. Moreover, at room temperature, the root-mean-square vibration amplitudes of DNA bases is ten times smaller than the distance between stacked base pairs, and one order of magnitude greater than in any crystal, DNA being nearly in a “melted” state, essential, however, for an easy replication or repair of its sequence. So, when dealing with biomolecules in general, and with DNA in particular, the precautions that must be taken in conduction measurements and the interpretation of results are far from the common experience with usual crystals in electronic laboratories.

The studies of DNA conductance have indicated a rich variety of DNA behavior, encompassing insulator, semiconductor, or conductor characteristics. In principle, ssDNA molecules are insulating at room temperature, but dsDNA in the form of short periodic structures such as poly(G)–poly(C), or bundles of  $\lambda$ -DNA, can conduct electricity due to hybridization.

As we have mentioned, the conduction in dsDNA is due to  $\pi - \pi$  interactions between base pairs, which originate in the delocalized  $\pi$  bonding and  $\pi^*$  antibonding orbitals separated by an energy bandgap  $E_g$  of almost 4 eV, and which are produced by the  $p_z$  atomic orbitals perpendicular to the base plane. The DNA can be doped, as can common semiconductors, the doping involving chemical oxidation or reduction reactions. So a band engineering of DNA is possible, its transformation in a conducting wire occurring by further functionalization with metal particles, such as Ag.

In experiments, DNA acts as insulator, semiconductor, or conductor, depending on the different types of electrodes used to contact DNA; the various types of DNA strands, ssDNA or dsDNA; the length of the sample; and the specific base sequence. Many experiments are summarized in Table 1.1 of the key reference Enders et al. (2004). In Fig. 1.35, we have represented the work functions of DNA bases and metals, to get an insight into how DNA must be contacted to behave resistively or in a Schottky-like manner. In this figure, LUMO and HOMO stand for lowest unoccupied molecular orbital and highest occupied molecular orbital, respectively.

The conduction of DNA could be measured due to advancements in self-assembly and nanoscale lithographic technique, as well as in STM (scanning tunneling microscope), which is able to measure the tunneling current with high accuracy by approaching a sharp tip to the conductive sample (the distance between them is 1–2 nm). The STM will be extensively described in Chap. 3.

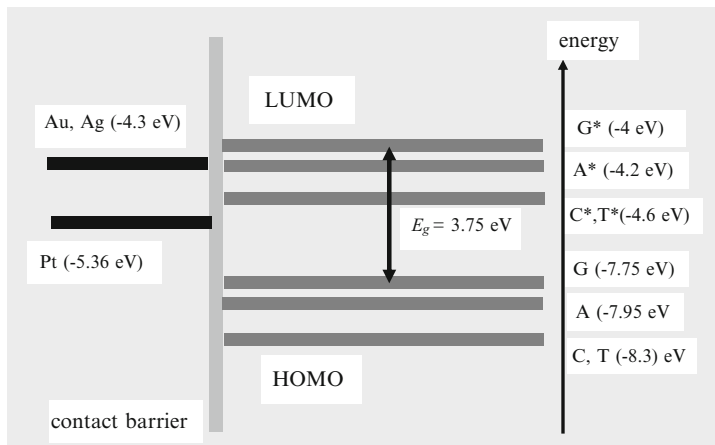


**Fig. 1.35** Work functions of metals and DNA bases

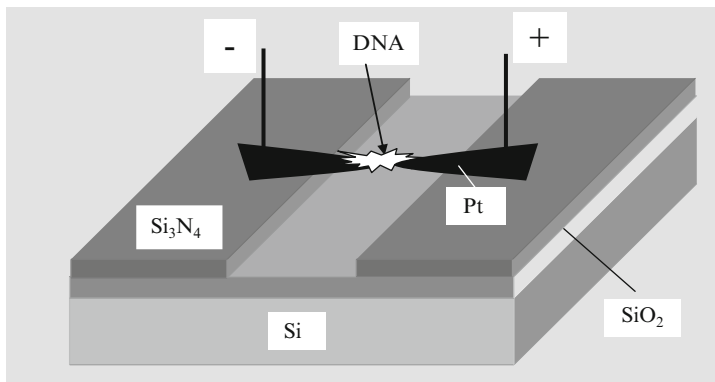


**Fig. 1.36** DNA molecule trapped between gap electrodes for conduction measurements

The wide bandgap semiconducting behavior of dsDNA was demonstrated in [Porath et al. \(2000\)](#), in which it was considered that there is an overlap of  $\pi$  orbitals of neighboring base pairs in a 10.4-nm-long dsDNA structure, which covers the gap between two Pt electrodes and contains 30 base pairs of the same type (poly(G)–poly(C)). The DNA was trapped by electrostatic trapping when a bias was applied between the two electrodes (see Fig. 1.36).

The  $1 \mu\text{l}$  of DNA from a dilute aqueous solution, which contained one DNA molecule per  $(100 \text{ nm})^3$ , was trapped between the electrodes. The gap between electrodes is 8 nm and was obtained by EBL. The  $I - V$  characteristic of the device, similar to that of a Zenner diode, is displayed in Fig. 1.37. The authors in [Porath et al. \(2000\)](#) have attributed this behavior to the offset between the Fermi level of the nanogap electrodes and the molecular energy bands of DNA (see Fig. 1.35).

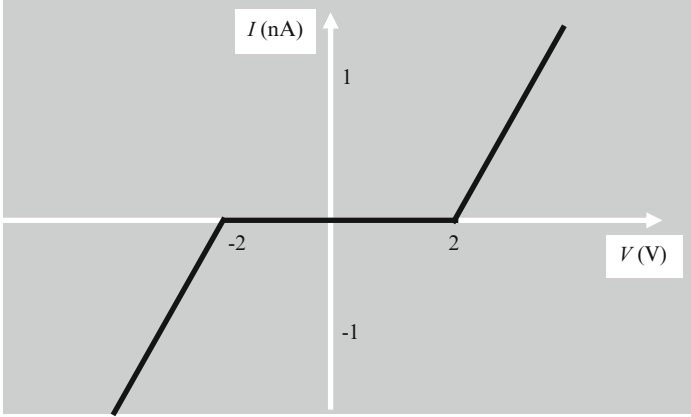


Fig. 1.37 The Zenner behavior of DNA between two electrodes

This is the typical semiconductor behavior of DNA, with a bandgap of about 1 eV at room temperature. It was shown that the overlapping of the  $\pi$  orbitals in the base-pair stack coupled to the backbone is enough to explain the opening of the bandgap in short DNA base sequences at room temperatures (Cuniberti et al. 2002). Using a Hamiltonian approach, it was evidenced that backbone coupling of overlapping  $\pi$  orbitals controls the energy gap opening in electron transmission along a DNA oligomer consisting of 30 G–C base pairs.

In this case, the transmission is written as

$$T = \frac{4\delta^2 \sin^2 \theta}{[\sin(N+1)\theta - \delta^2 \sin(N-1)\theta]^2 + 4\delta^2 \sin^2 N\theta}, \quad (1.33)$$

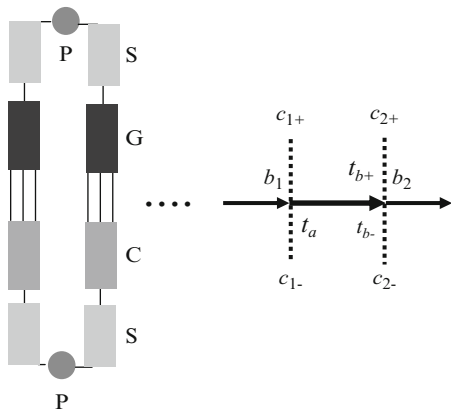
where  $\Phi = \cos \theta$  is the backbone coupling parameter and  $N$  is the number of resonances at the molecular orbitals, which are broadened by the spectral density parameter  $\delta$ . The gap opening is easily understandable by the dispersion equation of the infinite G–C lattice:  $\Phi(E) = -\cos q$ , where  $q$  is the adimensional longitudinal momentum of the lattice. The lack of electronic states between LUMO and HOMO determines the bandgap opening.

The charge propagates along the  $\pi$  orbitals by nearest-neighbor hopping with probabilities  $t_a$  and/or is hybridized at the two edges of the structure with probabilities  $t_{b\pm}$ . Based on this conduction mechanism model, a model of charge propagation in C–G periodic base pairs forming a short DNA molecule is depicted in Fig. 1.38. The localized charges at the central and edge states are denoted by  $b$  and  $c_{\pm}$ , respectively, with an additional label indicating the specific base pair.

Using the above model and assuming that  $t_{b+} = t_{b-} = t_b$ , the gap in transmission, which corresponds to a gap in the current according to the Landauer formula, is given by

$$T_g = 2(t_a^2 + t_b^2)^{1/2} - 2t_a \quad (1.34)$$

**Fig. 1.38** The charge propagation in a GC periodic structure



and fits the  $I - V$  curve at 18 K for  $t_a = 0.37$  eV and  $t_b = 0.74$  eV. Either the charge propagation or the coupling backbone model described above indicates that the bandgap is opened due to high reflections near zero energies, which correspond to a gap in electronic states between LUMO and HOMO.

DNA is not behaving only as a semiconductor. For example, DNA behaves as an electrical conductor with conductivity similar to that of conducting polymers, if several DNA molecules associate in ropes with lengths of 600 nm (Fink and Schönenberger 1999). In this case, the DNA is much longer than in the previous example where only 30 base pairs are used. The length and shape of DNA molecules and the number of bases dictate the conduction properties, as can be seen from the examples collected in Di Ventra and Zwolak (2004).

Thus, if DNA is conducting, there are three possible responsible mechanisms: thermal hopping, sequential tunneling from site to site, or coherent tunneling along the entire length of DNA. The tunneling rate, expressed as

$$R \cong \exp(-\gamma L), \quad (1.35)$$

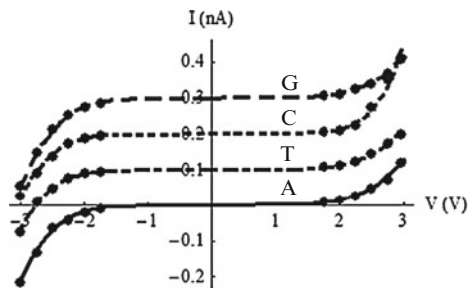
is exponentially decreasing with the length of DNA,  $L$ . The  $\gamma$  parameter in (1.35) is  $0.01 \text{ nm}^{-1}$  for sequential tunneling and  $0.1 \text{ nm}^{-1}$  for coherent tunneling.

A step forward is to identify the conduction characteristics of the bases themselves. This was done by STM measurements (Xu et al. 2007). The electrical signals, and in particular the work functions of the four DNA bases, are different and, hence, unique, as resulted from STM measurements. A simple fitting formula for the  $I - V$  signature of the four bases can be written as Dragoman and Dragoman (2009c)

$$I(V) = V/R + aV^2 \exp(-b/V), \quad (1.36)$$

where the first term in the rhs is due to a series resistance  $R$  and the last term originates from the Fowler–Nordheim behavior, which expresses the one-dimensional field emission from a triangular barrier of height  $\phi$  in the presence of an applied electric field. Thus, the DNA bases are understood as potential barriers for

**Fig. 1.39** The electric signature of the four bases of the DNA



field-emitted electrons, with heights  $\phi$ . The work functions of the four DNA bases are then determined from

$$b = \frac{4L}{3} \frac{\sqrt{2m_0}}{e\hbar} \phi^{3/2}, \quad (1.37)$$

where  $m_0$  is the free electron mass and  $L$  is the distance between the STM tip and the sample. The fitting  $I - V$  curves are illustrated in Fig. 1.39 with solid line for A, dashed-dotted line for T, dotted line for C, and dashed line for G, the points on all the curves representing experimental data taken from Fig. 1.3a of (Xu et al. 2007). The characteristics for G, C, and T have been raised with 0.3, 0.2, and 0.1 nA, respectively, to render them easily readable. As can be seen from Fig. 1.39, the  $I - V$  characteristics are not symmetric with respect to the origin. The forward polarization data were fitted with a series resistance value of 500  $\Omega$  for A, 1,000  $\Omega$  for T, 1,000  $\Omega$  for C, and 454  $\Omega$  for G, and the corresponding  $a$  parameters in (1.36) have values of 0.34, 0.27, 5.51, and 0.35 nS  $V^{-1}$ . On the contrary, the fitting series resistances for the backward polarization data are 555  $\Omega$  for A, 100  $\Omega$  for T, 500  $\Omega$  for C, and 666  $\Omega$  for G, the corresponding  $a$  parameters being 0.95, 1.35, 1.15, and 0.75 nS/V. Using (1.37), the work functions of the bases are found from the  $b$  parameters of the fit. These have, again, different values for positive and negative polarizations. For positive voltages, they are 9.7 V for A, 9.3 V for T, 16 V for C, and 10.1 V for G, while for negative voltages, the corresponding values are 11.2 V for A, 12.9 V for T, 12.2 V for C, and 10 V for G.

The different fitting parameters for the two polarizations are caused by specific base interactions with the substrate. The average work functions  $\phi$  obtained from data at positive and negative polarizations are 1.74 eV for A, 1.81 eV for T, 2.12 eV for C, and 1.7 eV for G, for an estimated  $L$  value of 0.66 nm. It is interesting to note from Fig. 1.39 that all bases behave as semiconductors, displaying a Zener diode-like behavior.

The conduction of DNA is an active research issue. For example, short dsDNA molecules formed from 13 base pairs of poly(dA)–poly(dT) were measured on a gold substrate, with gold nanoparticles with diameters of 10 nm as electrodes (Qian et al. 2009). The conduction type detected with the STM for a single dsDNA molecule was discovered to be semiconducting. Double-stranded DNA molecules were bonded with thiol to the gold film and are terminated with a single gold nanoparticle as electrode for STM tip measurements (see Fig. 1.40).

**Fig. 1.40** The dsDNA terminated with nanoparticles as electrodes

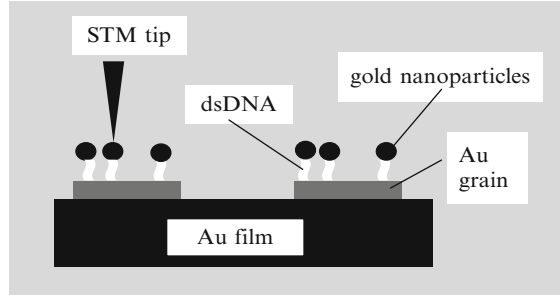
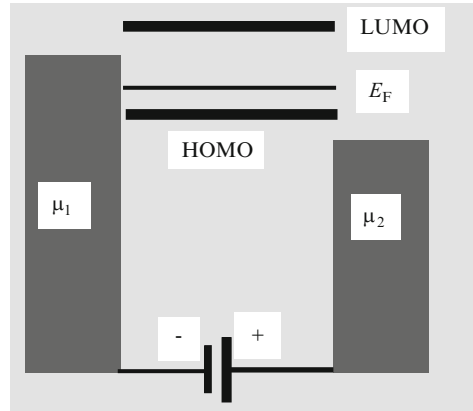


**Fig. 1.41** The energy diagram of the single DNA molecule connected to a nanoparticle STM electrodes



The Landauer model is again used to explain the conduction mechanisms encountered in the above nanostructure. Considering that the dc voltage  $V$  is applied between the STM tip and the gold substrate, the electrochemical potential of the tip,  $\mu_2$ , differs by the quantity  $eV$  from the electrochemical potential of the substrate  $\mu_1$ : it is higher or smaller than  $\mu_1$  if a negative or a positive voltage  $V$ , respectively, is applied. The energy level diagram is presented in Fig. 1.41 when a positive voltage is applied on the tip. Thus, the current is given by

$$I = \frac{2e}{\hbar} \frac{\Gamma_1 \Gamma_2}{\Gamma_1 + \Gamma_2} [f(E, \mu_1) - f(E, \mu_2)], \quad (1.38)$$

where  $\Gamma_{1,2}$  are the widths of the broadened molecular energy levels in the presence of metallic contacts,  $E$  is the energy level of the molecule, and  $f(E, \mu_{1,2})$  are the Fermi functions of the contacts. Charging effects are expressed by a built-in electric potential  $U_{\text{bi}} = U(N - 2f_0)$ , where  $U$  is the potential per electron in the nonequilibrium state,

$$N = 2 \frac{\Gamma_1 f(E, \mu_1) + \Gamma_2 f(E, \mu_2)}{\Gamma_1 + \Gamma_2} \quad (1.39)$$

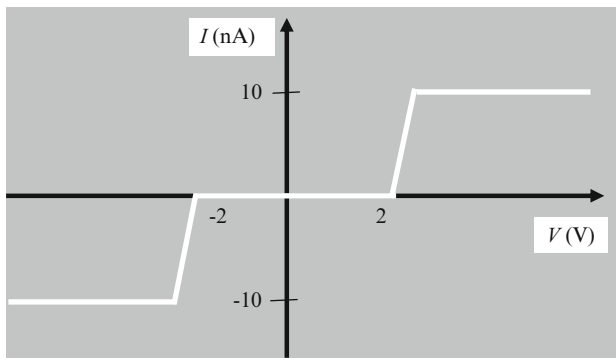


**Fig. 1.42** The  $I - V$  characteristic for a single DNA molecule having as contacts nanoparticles and a STM tip

is the number of electrons on the molecular level with energy  $E$ , and  $f_0 = f(E_0, E_F)$  is the Fermi–Dirac distribution function at equilibrium, when the molecular level has energy  $E_0$ . In the presence of an applied potential,  $E = E_0 + U_{bi}$ .

Equations (1.38) and (1.39) were solved, the theoretical  $I - V$  characteristics were found to be in good agreement with experimental data when  $\Gamma_1 = 0.1$  eV,  $\Gamma_2 = 0.4$  eV,  $U = 0.1$  V, and the LUMO and HOMO levels of the DNA are of about  $-7.99$  and  $-5.29$  eV, respectively. The electrochemical potentials were written as

$$\mu_1 = E_F - \gamma eV \quad (1.40a)$$

$$\mu_2 = E_F + (1 - \gamma)eV, \quad (1.40b)$$

where  $\gamma \cong 0.43$  describes the electrostatic potential distribution between the (DNA–nanoparticle)–substrate junction and the tip–(DNA–nanoparticle) junction. Under these conditions, a typical  $I - V$  characteristic is displayed in Fig. 1.42.

Strong nonlinear current–voltage behavior was found in circular DNA bundle samples immersed in an aqueous solution, due to charge hopping through the DNA network (Romano et al. 2007). Inside DNA molecules, the tunneling mechanism describes the transport of carriers through the bases. The water solution containing the circular DNA bundle was deposited over the 1-mm gap between vacuum-evaporated gold electrodes deposited on a nylon substrate containing pores of 450 nm diameter (see Fig. 1.43). In a hopping model for charge transport, the charges hop from one localized site to the adjacent one due to the energy provided by the applied bias and thermal vibrations. The thermally activated current is in this case

$$I \cong \sinh(erV/2k_B T) \exp(-E_a/k_B T), \quad (1.41)$$

where  $E_a$  is the thermal activation energy and  $r = a/d$ , with  $a$  the hopping distance and  $d$  the gap between electrodes. By fitting the current–voltage data with the above formula, the experimental and theoretical curves are found to be similar for  $E_a =$

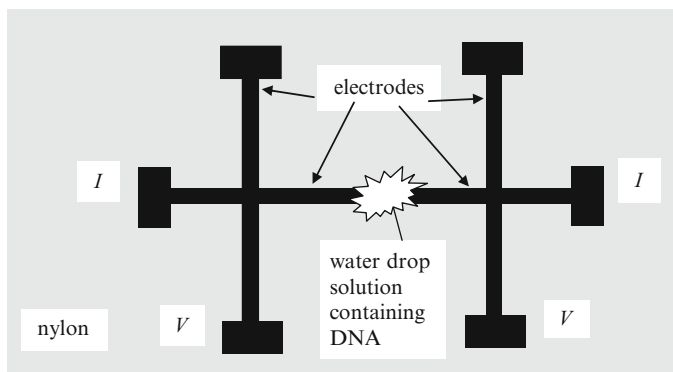


**Fig. 1.43** The gap electrode configuration for circular DNA in water

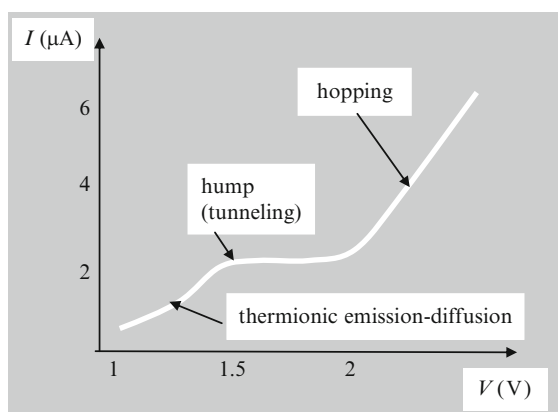


**Fig. 1.44** Conduction mechanisms in circular DNA in water

300 meV. However, a hump located at  $V_h = 1.5$  V in the curve, and present in nearly all samples, cannot be explained by the above equation (Fig. 1.44).

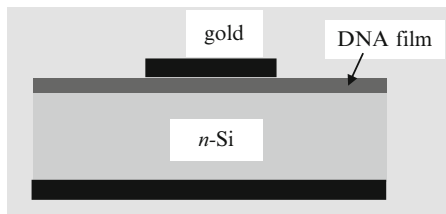
As pointed out above, the transport in DNA and in general in any organic molecule is the result of several different charging mechanisms. The hump is explained by the potential barrier that the charges must tunnel through inside the DNA molecules. For a rectangular barrier, the tunneling current is given by

$$I \cong \exp(2\phi_T - eV)^{1/2}, \quad (1.42)$$

where  $\phi_T$  is the barrier energy, which has values between 2.5 and 4.5 eV in different samples, consistent with the gap between HOMO and LUMO.

At low voltages, the effects of the contact between DNA and gold become visible in the  $I - V$  characteristic, and the dominant transport mechanism is the thermionic emission–diffusion process expressed by the formula

**Fig. 1.45** The DNA thin film Schottky contact diode



$$I \cong \exp\left(-\frac{n\phi_b - eV}{nk_B T}\right), \quad (1.43)$$

where  $\phi_b$  is the potential barrier between electrodes and sample and  $n \cong 18$  is a system-dependent constant.

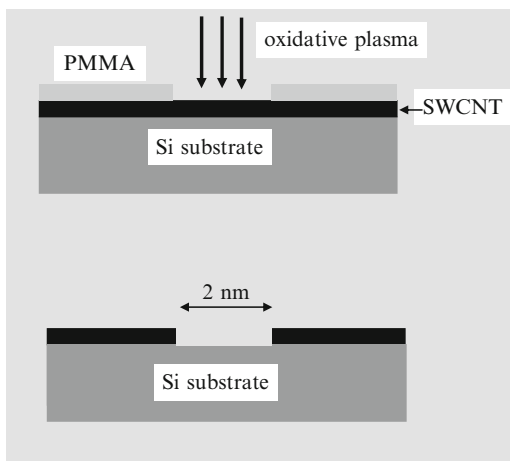
So there are three conduction mechanisms which can be retrieved in a single experiment on circular DNA dispersed in water. In Fig. 1.44, we have displayed the regions of the current–voltage dependence in which each of these conduction mechanisms dominate. From fitting data analysis, the  $\phi_b$  parameter is determined to be in the 400–500-meV range.

DNA thin films sandwiched between a  $n$ -doped Si substrate and a gold top contact display rectifying characteristics. The thickness of the thin film containing DNA extracted from wheat leaf tissues is about 19 nm, and the Au/DNA/ $n$ -Si structure behaves like a Schottky diode with an ideality factor of 1.22 and a barrier height of 0.78 eV (Sönmezolu et al. 2010). So, in the case of DNA thin films, the thermionic transport mechanism is dominant, and a Schottky-like diode with good performances can be obtained.

We can see from the above examples that there are two basic methods to connect biomolecules to metallic electrodes. One method is the top contact, as in the case of STM tip–(nanoparticle–DNA) electrodes in Fig. 1.40 or the DNA Schottky diode in Fig. 1.45. The other method consists of the nanogap electrodes, as in the case of the DNA molecule in Fig. 1.36 formed from 30 base pairs of poly(G)–poly(C), which displays a semiconducting behavior.

Nanogap electrodes are mostly used when one or few molecules must be connected to metallic contacts. Because the nanogap electrode has a planar configuration, this can be used for further integration with other electronic devices. However, it is quite difficult to fabricate gap widths of 1–8 nm, but many methods recently reviewed in Li et al. (2010) are presently able to produce a nanogap electrode or an array of nanogap electrodes. For example, FIB is a maskless method able to create nanogaps with dimensions between 10 and 20 nm in combination with EBL and optical lithography. The two electrodes of the nanogap are the drain and source of a transistor, and between them a CNT, a nanowire, or graphene can be deposited. For the subject treated in this book, nanogap electrodes are bridged by biological molecules. Conversely, nanogap electrodes can be fabricated over CNTs or nanowires, which are used as channels for ballistic field-effect transistors (FETs) where the two arms of the nanogap act as drain and source. In these cases, nanogap

**Fig. 1.46** Nanogap made in a single-walled CNTs



widths of 10–50 nm obtained by particle lithographic techniques are more than enough, but when we want to contact electrically only one molecule, the oxidative plasma is used to cut the electrodes in a precise manner, as in the example presented in Fig. 1.46. Nanogaps as small as 2 nm can be obtained in this way. Further, the CNT can be functionalized with the COOH group, and the device is ready to detect the hybridization of DNAs via conduction measurements (Guo et al. 2008).

Not only metallic contacts but also nanowires (Tian et al. 2010) and graphene (He et al. 2010) can be used as nanogap electrodes. The biosensing applications of electric nanogaps are reviewed by Chen et al. (2010).

## 1.4 Microfluidics and Nanofluidics

The last section of this chapter is addressed to micro- and nanofluidics. Micro- and nanofluidics is an area dedicated to the miniaturization of plumbing and the control of fluidic flows, which enable system integration of various biological sensors and the development of devices such as lab on a chip, which are analogous to the electrical integrated circuits. However, some microfluidics applications are encountered in the daily life: inkjet printing and liquid-crystals displays.

An interesting fact about the scale of electronic and fluidic processes is pointed out in Squires and Quake (2005). The success of integration of transistors on a chip reaching nowadays a density of 2–3 billions/chip is due to the fact that the downscaling of the geometrical dimensions of electronic devices does not affect their physical properties (up to gate lengths of 10–30 nm, where short channel effects strongly perturb the behavior of CMOS transistors). On the contrary, fluidic systems change strongly their properties depending on the length scales. Microfluidics deals with channels with dimensions of 100  $\mu\text{m}$ , the corresponding volume of a cube with 100  $\mu\text{m}$  sides being 1 nl. Some microchannel shapes are displayed in Fig. 1.47.

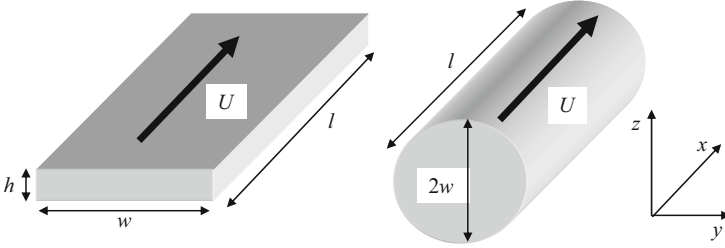


Fig. 1.47 Microchannels of various shapes

The fluid inside microchannels is considered a continuous media, and the velocity flow is described by the Navier–Stokes equation

$$\rho[(\partial \mathbf{v} / \partial t) + \mathbf{v} \nabla \mathbf{v}] = \nabla \hat{\boldsymbol{\sigma}} + \mathbf{f} = -\nabla p + \eta \Delta \mathbf{v} + \mathbf{f}, \quad (1.44)$$

where  $\mathbf{v}$  is the fluid velocity,  $\mathbf{f}$  denotes the external forces (gravitational, electric, or magnetic) per unit volume exerted on the fluid,  $\rho$  is the fluid density,  $\hat{\boldsymbol{\sigma}}$  is the fluid stress tensor (viscosity contribution),  $\eta$  is the shear viscosity, and  $p$  is the pressure.

If the inertial force, which is nonlinear, is small (situation encountered in almost all microfluidic devices), the Navier–Stokes equation becomes the Stoke equation

$$\rho(\partial \mathbf{v} / \partial t) = \nabla \hat{\boldsymbol{\sigma}} + \mathbf{f} = -\nabla p + \eta \Delta \mathbf{v} + \mathbf{f}. \quad (1.45)$$

In both equations, the mass conservation requirement imposes that

$$\partial \rho / \partial t + \nabla(\rho \mathbf{v}) = 0 \quad (1.46)$$

holds. To decide if the inertial forces are important in the steady state condition

$$\partial \mathbf{v} / \partial t = 0, \quad (1.47)$$

we must calculate the Reynolds number, defined as the ratio between the inertial force and the viscous force

$$\text{Re} = \left| \frac{\rho(\mathbf{v} \nabla \mathbf{v})}{\eta \Delta \mathbf{v}} \right| = \rho U L / \eta = U L / \nu, \quad (1.48)$$

where  $U$  is a characteristic flow velocity scale,  $L$  is a typical length scale, and  $\nu = \eta / \rho$  is the viscous coefficient.

Relation (1.48) tells us that the Reynolds number decreases as the dimensions of the systems decrease. If the fluid velocity is in the range of  $\text{cm s}^{-1}$  and  $L = 10 \mu\text{m}$ , we obtain  $\text{Re} \cong 10^{-1}$ , so that the convective (inertial) force is negligible compared to the viscous force. No convection means that there is no turbulence in microfluidic systems. In microfluidic devices, the flow is linear or laminar, is described by the

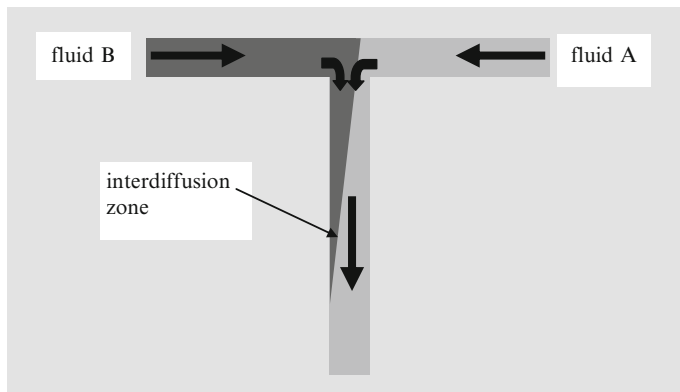


**Fig. 1.48** The T-mixer

Stokes equation, and is deterministic and predictable. However, if the microchannels are curved, convection appears if the curvature is much greater than the channel radius, and the centrifugal and the convective (inertial) forces generate a secondary flow, the Dean flow. This effect is used to create microfluidic devices such as micromixers.

Another quantity of interest is the inertial time scale

$$\tau_i = \rho L^2 / \eta, \quad (1.49)$$

which indicates the duration after which the flow reaches the steady state. This time is small, of about 10 ms in a 100 –  $\mu\text{m}$  channel.

Although almost all microfluidic devices display regular, deterministic flows, there are effects, such as capillarity or electrokinetic effects, where the nonlinearity could increase if the dimensions are shrinking. However, in the real world, the fluids are described by high Re numbers.

The ratio between the regimes of convection and diffusion is named Péclet number

$$\text{Pe} = Uw/D, \quad (1.50)$$

where  $D$  is the diffusion coefficient and  $w$  is the channel width. In the case of a biomolecule flow in a 100  $\mu\text{m}$  microchannel with velocity of 100  $\mu\text{m s}^{-1}$ , we get  $\text{Pe} = 250$  if  $D = 40 \mu\text{m}^2 \text{s}^{-1}$ . The Pe parameter is crucial for the mixing of liquids.

An example of a microfluidic device, which mixes liquids, is the T-shape mixer presented in Fig. 1.48. The two fluids are flowing alongside each other in the channel, and an interdiffusion zone is produced since the molecules of the two fluids diffuse into each other. This simple system was used to measure the analyte concentrations, or antigen–antibody binding via the injection of antibody solution along a labeled solution of antigen.

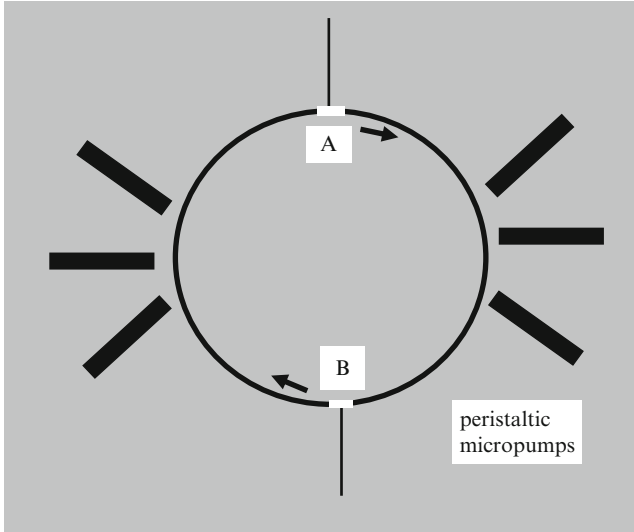


**Fig. 1.49** The schematic view of a rotary mixer

Mixing of fluids is of paramount importance in micro- and nanofluidics. A basic physical mechanism for mixing is the Taylor dispersion, which is based on the dispersion of a tracer along the stationary flow in a small-dimension microchannel or a capillary. If we consider that the concentration  $C$  is homogenous along the transverse direction, the equation for the tracer spot spreading is

$$DC/Dt = \partial C/\partial t + U \partial C/\partial x = D_{\text{eff}} \Delta C, \quad (1.51)$$

where the flow direction is denoted by  $x$ , and the effective diffusion coefficient is given by

$$D_{\text{eff}} = D[1 + \beta(Uh/D)^2], \quad (1.52)$$

where  $h$  is the channel height and  $\beta$  is a parameter dependent on the cross-sectional shape of the microchannel. Expression (1.52) tells us that when Péclet is high, the diffusion coefficient is increasing with the square of the velocity of the fluid. This effect is called Taylor diffusion and, based on it, a rotary mixer device as that in Fig. 1.49 can be designed.

The peristaltic pumps in Fig. 1.49 are driving the flow around the ring. The two fluids A and B are mixed after few rotations and, due to the Taylor diffusion, this occurs in tens of milliseconds. In this way, such a rotary mixer can extract DNA from a single cell and amplify it. Another way of rapid mixing is flow focusing, where a central fluid stream is narrowed using a constriction. The mixing in this case is performed in tens of  $\mu\text{s}$ . There are various ways of driving or manipulating fluids via electrokinetics effects, such as electroosmosis and electrophoresis. We will not detail further the theory of microfluidics since this is beyond the scope



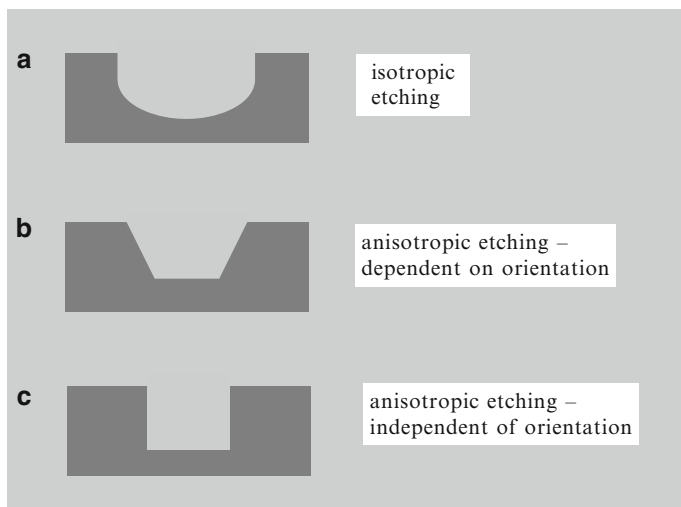


**Fig. 1.51** Si etching techniques

There are many other types of lab-on-chips, all performing the following tasks:

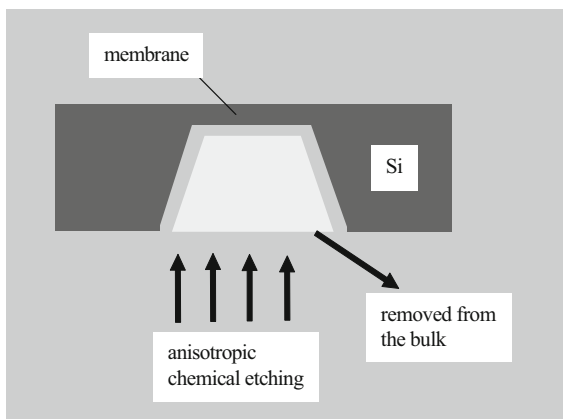
- Fluid transport
- Fluid control (valves)
- Fluid mixing
- Fluid separation
- Detection
- Readout

The development of microfluidic technology is related to the development of microelectromechanical systems (MEMS). Although there are other materials in which microfluidic devices are made, in what follows, we will briefly describe some Si MEMS techniques to fabricate them because in this way, the microfluidic devices can be integrated with electronic devices, which are able to process the information. The microfluidic devices are fabricated by etching silicon.

Various etching shapes result from different techniques, as shown in Fig. 1.51. There are two main categories of etching techniques: wet or chemical etching, illustrated in Fig. 1.51a, b, and dry or plasma etching, shown in Fig. 1.51c. The final goal is to fabricate high-precision and low-roughness microchannels with controllable shapes or other microfluidic devices using the etching process. However, ideal vertical walls can be realized only with plasma-etching techniques.

There are two basic types of micromachining techniques: bulk micromachining and surface micromachining. In bulk micromachining, a specific mechanical structure is fabricated from a wafer by etching the back side of it. A typical example, of producing a micromechanical membrane, is illustrated in Fig. 1.52. Such a membrane, with a thickness of  $1\ \mu\text{m}$  and a surface as large as  $2 \times 2\ \text{cm}^2$ , can be produced using chemical or plasma-etching methods. In the case of bulk micromachining,

**Fig. 1.52** The bulk Si micromachining technique



the desired shape and the precision of micro- or nanosized mechanical structures is controlled by etching stop techniques. On the contrary, in surface micromachining, MEMS or NEMS are fabricated by consecutive depositions of thin film layers on a common substrate, and a subsequent selective etching of one of these layers, referred to as the sacrificial layer.

Nanofluidics deals with fluid motion in narrow channels, with dimensions smaller than 100 nm. There are some important differences in the fluidic motion at such small dimensions in comparison to microfluidics. In principle, due to the very high aspect ratio between the surface and the volume of the devices, the fluid interaction with the walls becomes significant. It is important to note that according to [Sparreboom et al \(2010\)](#), the Stokes equation is still valid for channels with dimensions of at least 10 nm. If the dimensions of the channels are less than 10 nm, as in the case of single-walled CNTs, the discrete nature of molecules participating at the flow must appear explicitly in the flow equations. It is extremely interesting to note that liquids preserve their continuous character up to very small dimensions, while in a transistor channel with widths of 10 nm, the transport of electrons is fully quantized.

In nanofluidics, the motion of fluids is no longer induced by the pressure difference as in the case of microfluidic channels. The typical fluid motion in nanofluidics channels is an electroosmotic flow. The electroosmotic flow, i.e., the liquid transport driven by an axial applied electric field, is encountered also in microfluidic systems, but in nanofluidics, it becomes a basic tool for fluid transport.

Electrical charges are transported by a solid surface in contact with an aqueous solution, which is conductive due to the ionic groups at the surface, dissolved salts, etc. This excess of surface charge attracts the counterions and repels similarly charged co-ions. The thickness of this ionic double layer, which depends on the ionic concentration, is named Debye length. Beyond the Debye length, the fluid has no charge; it is neutral. The electroosmotic flow is the result of an applied electric field along the fluid. The velocity profiles for the flow due to pressure difference (microfluidics) and electroosmotic flow (nanofluidics) are depicted in [Fig. 1.53](#).

From [Fig. 1.53](#), it can be seen that in nanofluidics channels, the velocity of the fluid is constant (outside the Debye length), in contrast with the microfluidic

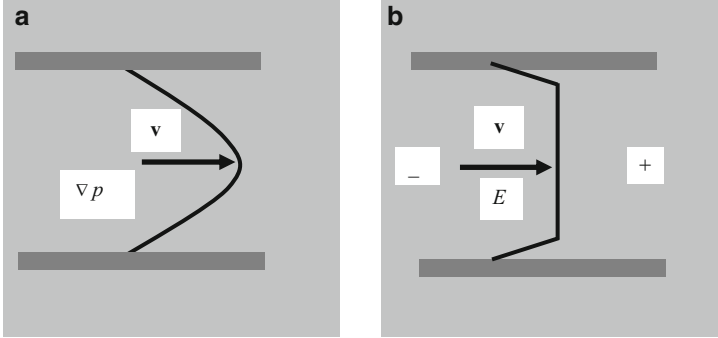


**Fig. 1.53** Typical (a) microfluidics and (b) nanofluidics flow mechanisms

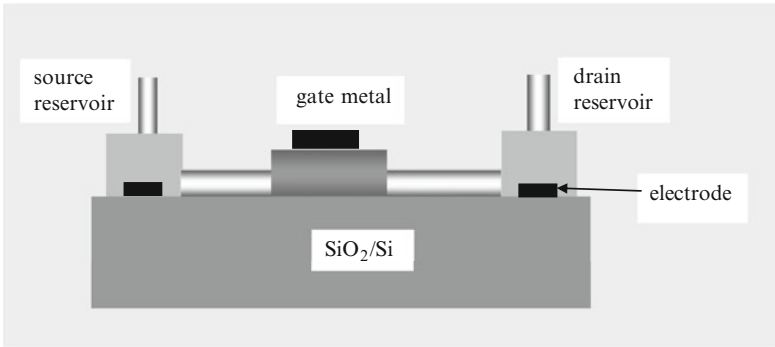


**Fig. 1.54** The nanofluidics transistor

channels where, due to pressure difference, the velocity distribution has a parabolic shape (Poiseuille flow).

The velocity of the electroosmosis flow profile beyond the Debye length is given by

$$v = -\epsilon_0\epsilon_r E \phi_s / \eta, \tag{1.53}$$

where  $\phi_s$  is the potential at the surface and  $E$  is the applied electric field in the flow direction. Formula (1.53) reveals the constant velocity profile for electroosmotic flow.

The Debye length  $l_D$  decreases when the ion concentration  $n_i$  increases,  $l_D \propto n_i^{-1/2}$ , and ranges from 1 to 100 nm for aqueous solutions. In microchannels, the Debye length is much smaller than the channel dimensions, so that the solution is isolated from the surface charge and is neutral. On the contrary, in nanochannels with a dimension smaller than the Debye length, the electrostatic field penetrates through the channel and thus controls the flow via the field effect. This effect is analogue to the effect of the gate on a FET transistor, and the devices with 1D nanochannels analogous to FET channels and working on the above principle are termed nanofluidic transistors (Karnik et al. 2005) (see Fig. 1.54). In the case of nanofluidics channels, the ion concentration is modulated by an electrostatic gate.

More advanced nanofluidics devices based on CNTs are used in various applications such as “water wires,” membranes, gas transport, filtration (Noy et al. 2007), or as biosensors (Lee et al. 2009). The biosensors, which are of paramount importance for bionanoelectronics, will be the subject of the next chapter. The technologies for the fabrication of nanochannels and nanofluidic devices are the top-down and bottom-up approaches described in this chapter (Mijatovic et al. 2005).

## References

- Adair JH, Li T, Havey KK, Moon J, Mecholsky J, Morrone A, Talham DR, Ludwig MH, Wang L (1998) Recent developments in the preparation and properties of nanometer-size spherical and platelet-shaped particles and composite particles. *Mater Sci Eng R* 23:139–242
- Appenzeller J, Radosavijevic M, Knoch J, Avouris Ph (2004) Tunneling versus thermionic emission in one-dimensional semiconductors. *Phys Rev Lett* 92:048301
- Bandaru PR, Pichanusakorn P (2010) An outline of synthesis and properties of silicon nanowires. *Semicond Sci Technol* 25:024003
- Biswas A, Wang T, Biris AS (2010) Single metal nanoparticles spectroscopy: optical characterization of individual nanosystems for biomedical applications. *Nanoscale* 2:1560–1572
- Björk MT, Ohlsson BJ, Thelander C, Persson AI, Deppert K, Wallenberg LR, Samuelson L (2002) Nanowire resonant tunneling diode. *Appl Phys Lett* 81:4458–4460
- Blake P, Novislov KS, Castro Neto AH, Jiang D, Yang R, Booth TJ, Geim AK, Hill EW (2007) Making graphene visible. *Appl Phys Lett* 91:063124
- Bowler DR (2004) Atomic-scale nanowires: physical and electronic structure. *J Phys: Condens Mater* 16:R721–R754
- Bolotin KI, Sikes KJ, Jiang Z, Klima M, Fudenberg G, Hone J, Kim P, Stormer HL (2008) Ultrahigh electron mobility in suspended graphene. *Solid State Commun* 146:351–355
- Chen X, Guo Z, Yang G-M, Li J, Li M-Q, Liu J-H, Huang X-J (2010) Electrical nanogap devices for biosensing. *Mater Today* 13:28–41
- Chik H, Xu JM (2004) Nanometric superlattices: non-lithographic fabrication, materials, and properties. *Mater Sci Eng R* 43:103–138
- Cuniberti G, Craco L, Porath D, Dekker C (2002) Backbone-induced semiconducting behaviour in short DNA wires. *Phys Rev B* 65:241314
- Datta S (1997) *Electronic transport in mesoscopic systems*. Cambridge University Press, Cambridge
- del Alamo JA, Eugster CC, Hu Q, Melloch MR, Rooks MJ (1998) Electron waveguide devices. *Superlattice Microstruct* 23:121–137
- Di Ventra M, Zwolak M (2004) DNA electronics. In: *Encyclopedia of nanoscience and nanotechnology*. Nalwa HS (ed), American Scientific Publishers, California 1–19
- Dragoman D, Dragoman M (1999) *Advanced optoelectronic devices*. Springer, Berlin
- Dragoman D, Dragoman M (2001) Micro/nano-optoelectromechanical systems. *Prog Quantum Electron* 25:229–290
- Dragoman D, Dragoman M (2004) *Quantum-classical analogies*. Springer, Berlin
- Dragoman M, Dragoman D (2009a) *Nanoelectronics. Principles and devices*. Artech House, London
- Dragoman M, Dragoman D (2009b) Graphene-based quantum electronics. *Progr Quantum Electron* 33:165–214
- Dragoman D, Dragoman M (2009c) The real-time detection of deoxyribonucleic acid bases via their negative differential conductance signature. *Phys. Rev E* 80:022901
- Enders RG, Cox DL, Singh RRP (2004) The quest for high conductance DNA. *Rev Mod Phys* 76:195–214

- Erickson D, Li D (2004) Integrated microfluidic devices. *Anal Chim Acta* 507:11–26
- Fan J, Chu PK (2010) Group IV nanoparticles: synthesis, properties and biological applications. *Small* 6:2080–2098
- Ferry DK, Goodnick SM (2009) *Transport in nanostructures*. Cambridge University Press, Cambridge
- Fink H-W, Schönenberger C (1999) Electrical conduction through DNA molecules. *Nature* 398:407–410
- Geim AK, Novoselov KS (2007) The rise of graphene. *Nat Mater* 6:183–191
- Geim AK (2009) Graphene: Status and prospects. *Science* 324:1530–1534
- Gruner G (2006) Carbon nanotube transistors for biosensing applications. *Anal Bioanal Chem* 384:322–335
- Gülseren O, Yildirim T, Ciraci S (2003) Formation of quantum structures on a single nanotube by modulating hydrogen adsorption. *Phys Rev B* 68:115419
- Guo LJ (2004) Recent progress in nanoimprint technologies and its applications. *J Phys D* 37:R123–R141
- Guo X, Gorodetsky AA, Hone J, Barton JK, Nuckolls C (2008) Conductivity of a single DNA duplex bridging a carbon nanotube gap. *Nat Nanotechnol* 3:163–167
- Han MY et al (2007) Energy band-gap engineering of graphene nanoribbons. *Appl Phys Lett* 98:206805
- Harriott LR, Hull R (2004) Nanolithography. In: Di Ventra M, Evoy S, Heflin JR Jr (eds) *Introduction to nanoscale science and technology*. Kluwer Academic Publishers, Dordrecht 7–40
- He Y, Dong H, Li T, Wang C, Shao W, Zhang Y, Jiang L, Hu W (2010) Graphene and graphene oxide nanogap electrodes fabricated by atomic force microscope nanolithography. *Appl Phys Lett* 97:133301
- Huie JC (2003) Guided molecular self-assembly: a review of recent efforts. *Smart Mater Struct* 12:264–271
- Javey A, Kong J (eds) (2009) *Carbon nanotube electronics*. Springer, Heidelberg
- Karnik R, Fan R, Yue M, Li D, Yang P, Majumdar A (2005) Electrostatic control of ions and molecules in nanofluidic transistors *Nano Lett* 5:943–948
- Kopp MU, de Mello AJ, Manz A (1998) Chemical amplification: continuous-flow PCR on a chip. *Science* 280:1046–1047
- Kwon Y-W et al (2009) Material science of DNA. *J Mater Chem* 19:1353–1380
- Lauhon LJ et al (2002) Epitaxial core-shell and core-multishell nanowire heterostructures. *Nature* 420:57–61
- Lee M, Baik KY, Noah M, Kwon Y-K, Lee J-O, Hong S (2009) Nanowire and nanotube transistors for lab-on-a-chip applications. *Lab on a Chip* 9, 2267–2280
- Li T, Hu W, Zhu D (2010) Nanogap electrodes. *Adv Mater* 22:286–300
- Meschede D, Metcalf H (2003) Atomic nanofabrication: atomic deposition and lithography by laser and magnetic forces. *J Phys D* 36:R17–R38
- Mijatovic D, Eijkel JCT, van den Berg A (2005) Technologies for nanofluidic systems: top-down vs. bottom-up—a review. *Lab on a Chip* 5:492–500
- Novoselov KS, et al (2004) Electric field effect in atomically thin carbon films. *Science* 306:666–669
- Noy A, Park HG, Farnasiero F, Holt JK, Grigoropoulos CP, Bakajin O (2007) Nanofluidics in carbon nanotubes. *Nanotoday* 2:22–29
- Pease RF, Chou SY (2008) Lithography and other patterning techniques for future electronics. *Proc IEEE* 96:248–270
- Porath D, Bezryadin A, de Vries S, Dekker C (2000) Direct measurement of electrical transport through DNA molecules. *Nature* 403:635–637
- Qian J, Liao S, Xu S, Stroschio MA, Dutta M (2009) Direct measurement of electrical transport through single DNA molecules. *J Appl Phys* 106:033702
- Rao CNR, et al (2000) Metal nanoparticles, nanowires and carbon nanotubes. *Pure Appl Chem* 72:21–33

- Rao SG, Huang L, Setyawan W, Hong S (2003) Large-scale assembly of carbon nanotubes. *Nature* 425:36–37
- Rietman EA (2001) *Molecular engineering of nanosystems*. Springer, New York 158–185
- Romano P, Polcari A, Verruso B, Colantuoni V, Saldarriaga W, Baca E (2007) Nonlinear current-voltage characteristics measured across circular deoxyribonucleic acid (DNA) molecule bundles. *J Appl Phys* 102:103720
- Ross FM (2010) Controlling nanowire structures through real time growth studies. *Rep Prog Phys* 73:114501
- Saavedra HS, Mullen JT, Zhang P, Devey DC, Claridge SA, Weiss PS (2010) Hybrid strategies in nanolithography. *Rep Prog Phys* 73:036501
- Saif T, Alaca E, Sehitoglu H, Nano wires by self assembly, 16th IEEE Annual Conference on Micro Electro Mechanical Systems MEMS 03, Kyoto, Japan, 19–23 January 2003, pp. 45–47
- Shenhar R, Norsten TB, Rotello VM (2004) Self-assembly and self-organization. In: Di Ventra M, Evoy S, Heflin JR Jr (eds) *Introduction to nanoscale science and technology*. Kluwer Academic Publishers, Dordrecht pp 41–74
- Soldano C, Mahmood A, Dujardin E (2010) Production, properties and potential of graphene. *Carbon* 48:2127–2150
- Sönmezolu S, Sönmezolu ÖA, Çankaya G, Yildirim A, Serin N (2010) Electrical characteristics of DNA-based metal-insulator-semiconductor structures. *J Appl Phys* 107:124518
- Sounderya N, Zhang Y (2008) Use core/shell structured nanoparticles for biomedical applications. *Recent Patents Biomed Eng* 1:34–42
- Sparreboom W, van den Berg A, Eijkel JCT (2010) Transport in nanofluidic system: a review of theory and applications. *New J Phys* 12:015004
- Squires TM, Quake SR (2005) Microfluidics: fluid physics at the nanoliter scale. *Rev Mod Phys* 77:977–1026
- Tabeling P (2009) A brief introduction to slippage, droplets and mixing in microfluidic systems. *Lab on a Chip* 9:2428–2439
- Tan Y-W, et al (2007) Temperature dependent electron transport in graphene. *Eur Phys J Special Topics* 148:15–17
- Teh S-Y, Lin R, Hung L-H, Lee AP (2008) Droplet microfluidics. *Lab on a Chip* 8:108–220
- Tian W-C, Finehout E (eds) (2008) *Microfluidics for biological applications*. Springer, Heidelberg
- Tian X, Li J, Xu D (2010) Nanowire-based nanogap electrodes by annealing of multisegmented Pt/Au/Pt nanowire stir. *Electrochem Commun* 12: 1081–1083
- Tseng AA, Chen K, Ma KJ (2003) Electron beam lithography in nanoscale fabrication: recent developments. *IEEE Trans Electronic Packag Manufact* 26:141–1949
- Wacker A, Jauho A-P (1998) Quantum transport: the link between standard approaches in superlattices. *Phys Rev Lett* 80:369–372
- Waigh T (2007) *Applied biophysics: a molecular approach for physical scientists*. Wiley, New York, p 206
- Wang N, Zhang RQ (2008) Growth of nanowires. *Mater Sci Eng R* 60:1–51
- Wei D, Liu Y (2010) Controllable synthesis of graphene and its applications. *Adv Mater* 22:3225–3241
- Xu M, Enders RG, Arakawa Y (2007) The electronic properties of DNA bases. *Small* 3:1539–1542
- Yang D, et al (2010) Novel DNA materials and their applications. *Wiley Interdisciplin Rev Nanomed Nanobiotechnol* 2:648–669
- Ziaie B, Baldi A, Atashbar MZ (2004) *Introduction to Micro/Nanofabrication*. In: Bhushan B (ed), *Springer handbook of nanotechnology*. Springer, Berlin 147–184
- Zhu W (ed) (2001) *Vacuum microelectronics*. Wiley, New York

## Chapter 2

# Sensing of Biomolecules

**Abstract** This chapter is dedicated to the label-free detection of various biomolecules using nanodevices such as field-effect transistors having channels with nanometric dimensions made from various nanomaterials like nanowires, nanotubes, or graphene; cantilevers, optical waveguides, nanopores, and other nanosized devices will be described for sensing of biomolecules.

### 2.1 Nanotransistors Based on Nanotubes, Nanowires, and Graphene for Biosensing

In the field-effect transistor (FET), the transport of carriers is controlled by an electrode called gate. The carriers flow along a channel bordered by two contacts termed drain and source. The gate controls the charge density in the channel by an electric field and is separated from the channel by an insulator. The FET can be driven in an on and an off state by tuning the drain and gate voltages and constitute a genuine switch.

The MOSFET (metal-oxide-semiconductor FET) is the basic configuration for the majority of nanosized transistors having a gate length smaller than 100 nm, irrespective of the channel type, which could be made entirely from nanomaterials, such as nanowires or graphene, or from a heterostructure. The name MOSFET indicates that the metallic gate is isolated from the channel region by an oxide. Typically, a MOSFET consists of doped Si channel/active region isolated by a SiO<sub>2</sub> layer from a metallic gate. Other isolator materials are Si<sub>3</sub>N<sub>4</sub> or high-permittivity dielectrics.

Initially, MOSFETs had a *p*-channel (PMOS), but the successive *n*-channel transistors (NMOS) were faster switches than PMOS. Both MOSFET types are integrated in a CMOS (complementary MOSFET) transistor, which is a low-power-consuming device with a similar high switching rate as NMOS.

The MOSFET transistor is the most effective and simplest electronic device, and therefore, CMOS is an essential element in integrated circuits, allowing an

unprecedented downscaling of its dimensions. Nowadays, commercial MOSFETs have gate lengths of less than 100 nm, more precisely, in the range 50–70 nm, depending on applications. Billions of such transistors are integrated in various very large-scale integrated circuits such as memories or microprocessors, which are present in any computer or mobile phone. The semiconductor technology is so efficient and cheap that, in 2002, a DRAM contained a larger number of CMOS transistors than the amount of rice grains produced that year, one grain of rice being as expensive as 100 transistors (Van der Spiegel 2004).

The reduction of MOSFET dimensions is described by Moore's law (Moore 1995), which states that at every 1.5 years since 1970, the number of transistors per integrated circuit chip, for instance per microprocessor, doubles. However, adverse effects termed as short-channel effects occur once the MOSFET dimensions shrink and reduce drastically the transistor performances. So, emerging transistors with other types of channels, for example, based on nanomaterials, are increasingly used and will be described within this chapter.

The MOSFET transistor can be understood with the help of a simple configuration, referred to as MOS capacitor (see Fig. 2.1), which contains a substrate and a top metal gate, separated by a dielectric layer. The substrate is a doped semiconductor, typically *p*-Si, and the dielectric/isolator layer which is usually SiO<sub>2</sub>. A negative gate voltage  $V_G$  applied between the semiconductor and the metal traps the holes at the interface between the dielectric and the semiconductor. Conversely, when  $V_G$  is positive, the holes are forced away from the interface, generating a depletion region, with width

$$x_{\text{dep}} = (2\varepsilon_s|\psi_s|eN_s)^{1/2}, \quad (2.1)$$

where  $\varepsilon_s$  is the substrate permittivity,  $|\psi_s|$  is the surface potential originating from the bending of Si energy bands caused by  $V_G$ , and  $N_s$  denotes the substrate concentration.

The bending of the Si conduction energy band has an effect on the transport of electrons in *p*-Si, which are the minority carriers, toward the top of the depleted layer. As  $V_G$  increases, it reaches a threshold gate voltage  $V_{\text{th}}$ , at which the electron concentration balances the concentration of holes in the substrate, higher gate voltage inducing the creation of an inversion layer beneath the dielectric, called

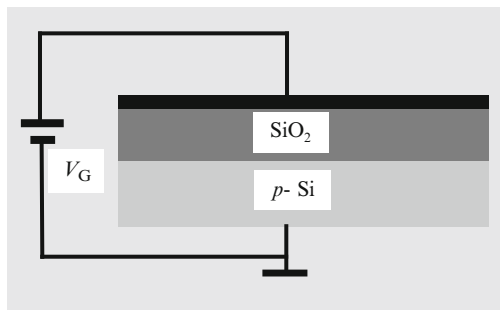


**Fig. 2.1** Schematic representation of the MOS capacitor

channel. In the channel, the density of electrons overcomes the hole density, and it reaches its maximum value for

$$\psi_s = 2\phi_F, \quad (2.2)$$

where  $\phi_F = \pm(E_i - E_F)/e = (k_B T/e) \ln(N_s/n_i)$  is the Fermi potential. In (2.2),  $E_i$  and  $n_i$  are, respectively, the intrinsic energy and concentration of charge carriers;  $E_F$  denotes the Fermi energy; and the + or - sign is associated to the  $p$ -type or  $n$ -type substrate, respectively. The maximum width of the depletion layer is then given by

$$x_{\text{dep,max}} = [4\varepsilon_s k_B T \ln(N_s/n_i)/(e^2 N_s)]^{1/2}, \quad (2.3)$$

and the corresponding charge per unit area is

$$q_{\text{dep}} = \mp e N_s x_{\text{dep}}. \quad (2.4)$$

The threshold voltage can be determined from the equality

$$V_{\text{th}} = V_{\text{fb}} + 2\phi_F - q_{\text{dep}}/C_{\text{ox}}, \quad (2.5)$$

where  $V_{\text{fb}}$  is the flat band voltage, which corresponds to a gate voltage that does not bend the substrate energy bands, and  $C_{\text{ox}}$  is the dielectric capacitance per unit area. Typical values for  $V_{\text{th}}$  are situated in the 0.2–0.4 V range.

The electric charge in the inversion layer is finally given by the expression

$$q_n = -C_{\text{ox}}(V_G - V_{\text{th}}), \quad (2.6)$$

which shows that it is directly proportional to the gate voltage, as is the current.

The MOSFET, as can be seen from Fig. 2.2, consists of two diode regions named source S and drain D, which surround a MOS capacitor. The voltage between source and drain is denoted by  $V_D$ , while  $V_G$  stands for the voltage between gate G and source. The electrons in the channel are transported toward the drain if the drain is forward biased with  $V_D$ , case in which  $V_G > V_{\text{th}}$ , the electron distribution being

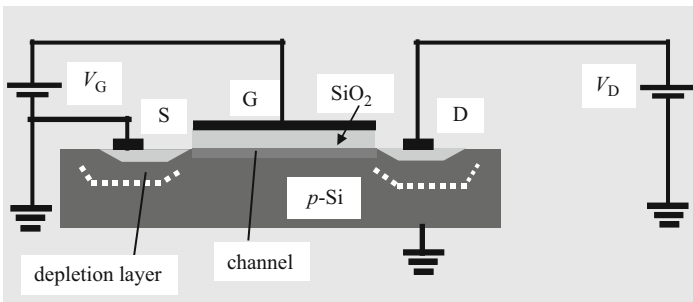


Fig. 2.2 The MOSFET transistor

uniform along the channel at small  $V_D$  values. Under such conditions, the channel with width  $W$  and length  $L_G$  is equivalent to a resistor and, according to Ohm's law, the drain current  $I_D$  is given by

$$I_D = \mu_n C_{ox} W (V_G - V_{th}) V_D / L_G, \quad (2.7)$$

where  $\mu_n$  is the mobility of electrons in the channel. From (2.7), it can be seen that  $I_D$  depends linearly on  $V_D$  and can be tuned via  $V_G$ . This situation corresponds to the linear region of the transistor, in which an input signal is amplified.

When  $V_D$  is further increased, it induces a nonuniform electron distribution in the channel. In the particular case of a linear distribution of electrons in the channel for  $V_G - V_{th} > V_D$ , such that the density of electrons is maximum at the source and minimum at the drain, we get the second region of the MOSFET, called triode region, in which

$$I_D = \mu_n C_{ox} W [(V_G - V_{th}) V_D - m V_D^2 / 2] / L_G. \quad (2.8)$$

The coefficient  $m$  is given by  $m = 1 + (1/C_{ox}) / (\epsilon_s q N_s / 4 |\phi_F|)^{1/2}$  and is termed body effect coefficient; its typical values range between 1.1 and 1.4. The triode region is a nonlinear region.

Increasing further  $V_D$ , we arrive at a regime with no charges near the drain, in which the channel is pinched off, and thus, the drain current does not depend on  $V_D$ . This is the saturation regime of the MOSFET, which starts at  $V_D = (V_G - V_{th}) / m = V_{DSat}$  and is characterized by a saturation current

$$I_D = \mu_n C_{ox} W (V_G - V_{th})^2 / 2m L_G. \quad (2.9)$$

In the saturation region, the transistor works digitally, switching between the off state, when there is no current flow and  $V_D = 0$ , and the on state corresponding to the saturation region, for which  $V_D \geq V_{DSat}$ . The three working regimes of the MOSFET are visualized in Fig. 2.3.

Other essential parameters for any FET are the gain or transconductance, defined as

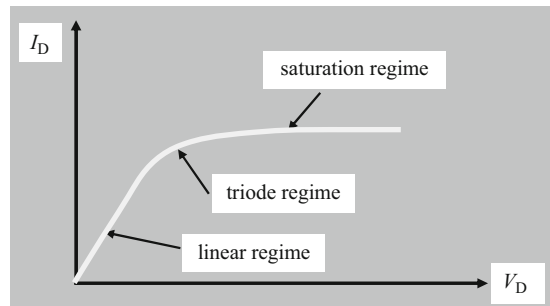


**Fig. 2.3** The working regimes of a MOSFET at a certain value of the gate voltage

$$g_m = \partial I_D / \partial V_G, \quad (2.10)$$

and the conductance of the channel

$$g_D = \partial I_D / \partial V_D. \quad (2.11)$$

The cutoff frequency of the transistor is given by

$$f_c = g_m / 2\pi C_G, \quad (2.12)$$

where  $C_G$  is the gate capacitance.

The three regions of the FET described above and the parameters (2.10)–(2.12) are encountered in any type of FET, irrespective of the channel, which can be a 2D electron gas (2DEG), a single nanowire or carbon nanotube (CNT), or a network of such structures, or graphene.

The FET transistors which will be used further as label-free sensors of biomolecules often work in the ballistic regime described in Chap. 1. The theory of ballistic FETs, known as Natori theory of FETs, is applicable also for nanowires and CNT transistors and is described in detail in (Lundstrom and Guo 2006); it will not be reproduced here. Further, we will describe each important transistor used as label-free detector for biomolecules and will focus on some examples illustrating label-free detection.

The first example is the label-free sensor for Si-based FETs described above. The DNA hybridization was achieved using a commercially available p-type FET having as gate a multilayer thin film consisting of  $\text{SiO}_2$  (100 nm)/ $\text{Si}_3\text{N}_4$  (100 nm)/ $\text{Ta}_2\text{O}_5$  (40 nm) (Ohtake et al. 2004). The DNA was immobilized on the  $\text{Ta}_2\text{O}_5$  thin film by immersing the gate electrode in 3 vol% 3-aminopropyltrimethoxylane comprising  $\text{CH}_3\text{OH} : \text{H}_2\text{O}$  (19:1) solution for 30 min in ambient conditions. In this way, the gate surface consisting of the thin film  $\text{Ta}_2\text{O}_5$  was modified by silane. Then, the silanized FET was immersed in dimethylformamide (DMF) to create a linker for DNA. Finally, the DNA immobilized on the gate was incubated overnight. The amount of immobilized molecules is about  $3.6 \times 10^5 \text{ cm}^{-2}$ . The label-free detection consists in the decrease of the drain current due to the negative-charged DNA, which is deposited on the gate. This effect is visible, for example, in the  $I_D - V_G$  dependence. The measurements are performed in a buffer solution of Tris-HCl +  $\text{MgCl}_2$ , having Ag/AgCl as reference electrode, as indicated in Fig. 2.4.

The difference in the threshold voltages  $V_{th}$  of the FET functionalized with ssDNA and dsDNA was 10 mV, for a gate length  $L_G = 30 \mu\text{m}$  and width  $W = 350 \mu\text{m}$ , and the sum of gate capacitances was about 60 fF. From this data, the extra charge due to DNA hybridization can be estimated to be  $0.2 \text{ nC/cm}^2$ .

A similar work was done by Xuan et al. (2005). However, in comparison with the label-free detection reported above, there is no gate surface treatment and no immobilization chemical processes. The dsDNAs containing between 5,000 and 35,000 bases were diluted with deionized water. For the measurements, a drop of  $0.5 \mu\text{L}$  and about 2 mm in diameter was deposited on the gate region. In the linear

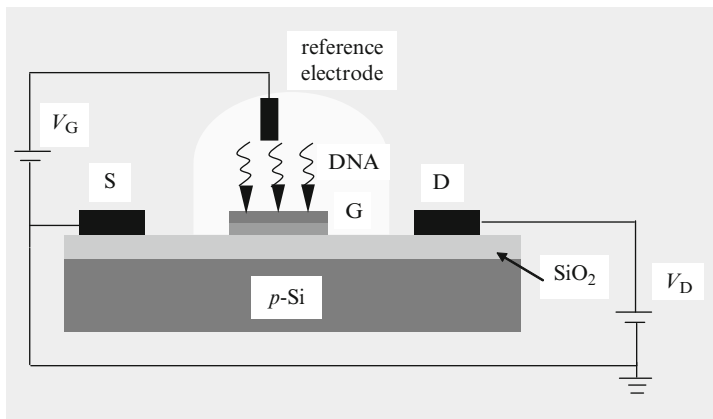


**Fig. 2.4** The label-free detection of DNA using a MOSFET-like transistor

region of the FET, the drain current has decreased as the DNA concentration has increased, producing a positive shift in  $V_{th}$  as

$$I_D = \mu_n C_{ox} W (-V_{th} V_D - V_D^2/2) / L G. \quad (2.13)$$

The threshold voltage is shifted due to changes in the work function  $\Delta\Phi_{ms}$  or dielectric changes in capacitances:

$$\Delta V_{th} = \Delta\Phi_{ms} - \Delta Q_{eff} / C_{ox}. \quad (2.14)$$

The experiments indicated that  $\Delta\Phi_{ms}$  is about 180 meV and  $\Delta Q_{eff}$  is  $-9 \text{ nC cm}^{-2}$ . Considering that the Debye length of  $0.25 \mu\text{m}$  contains about  $9 \times 10^6$  molecules above the gate, this change in the total charge corresponds to  $2.4e/\text{molecule}$ . Taking into account that the area of the FET is  $1 \times 8 \mu\text{m}^2$ , the sensitivity of the label-free detector is 0.1 mV, indicating that even a single molecule can be detected in the device presented in Fig. 2.5. The electrodes are covered with a polymer to integrate the sensor with a microfluidic channel.

Very recently, a FET having as channel a thin doped silicon wire fabricated by electron beam techniques, with the width of 80 nm and the length of  $15 \mu\text{m}$ , was used to detect a breast cancer biomarker (Chen et al. 2010). In this label-free sensor, the gate is silanized, as the FET in Fig. 2.4, and the drain–source changes in the differential conductance  $\Delta G$  are monitored. First, antibiotic in solution was detected with this transistor at very small concentrations (0.2–1.7 nM), the detection limit being of 20 pM. The conductance varies almost linearly in the range 40–100 nS as a function of antibiotic concentration. Next, the cancer antigen CA15.3 is dialyzed in solution with  $10 \mu\text{M}$  phosphate buffer and  $150 \mu\text{M}$  NaCl. Then, the FET is functionalized with antibody CA15.3. The  $\Delta G$  is varying linearly with the concentration  $m$  of CA15.3 due to the specific binding of the biomarker. This linear

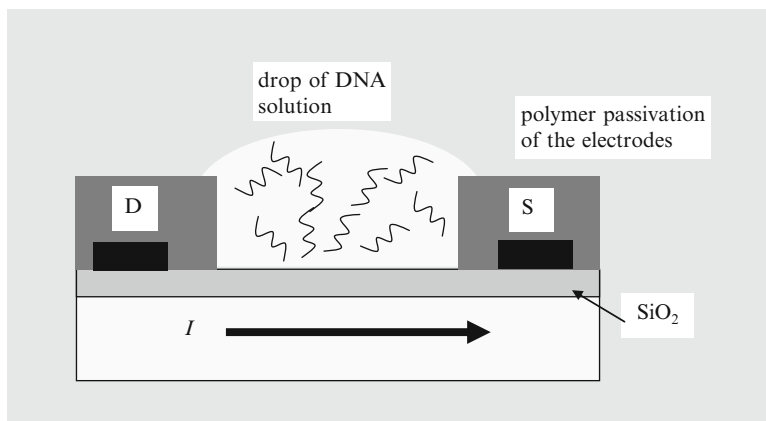


Fig. 2.5 FET label-free sensor of DNA

dependence can be described by

$$\Delta G \cong \alpha + \beta m, \quad (2.15)$$

where  $\alpha$  is 307 nS and  $\beta$  is  $-30$  pS. The detection limit of the CA15.3 biomarker is 1.7 nS, corresponding to 60 pM. So, the label-free FET nanowire biosensor is an extremely sensitive technique, able to sense cancer biomarkers in very low concentrations.

Many biomolecules, such as DNA or proteins, and biological key parameters such as pH, gas concentration, etc., were sensed using high-electron-mobility (HEMT) transistors (Kang et al. 2008; Pearton et al. 2010).

The HEMT is a FET transistor with a channel consisting of a 2DEG generated at the interface between a doped wider-bandgap semiconductor and an undoped narrower-bandgap semiconductor that form a heterostructure. Technologies developed for AIII-BV semiconductors or nitrides can create a HEMT channel at the interfaces.  $n$ -AlGaAs/GaAs and AlGaN/GaN are typical examples of such heterostructures. The HEMT working principle is based on the fact that the Fermi level in the narrower-bandgap semiconductor is lower than the Fermi energy in the wider-bandgap semiconductor, so that the electrons are transported from the doped toward the undoped semiconductor, leaving positively charged donors in the doped semiconductor. As a result, the energy bands of the heterostructure bend and trap the electrons in the quantum well that develops at the interface (see Fig. 2.6a). The spatial separation of negative and positive charges at the interface, as well as the fact that the Fermi energy in the well is higher than the first resonant level, generates an electron gas in the quantum well. More precisely, the electrons are free to move in the well, with a low rate of scattering processes due to the separation of the well from donor impurities. In this 2DEG, the electrons behave ballistically, reaching very high mobilities.

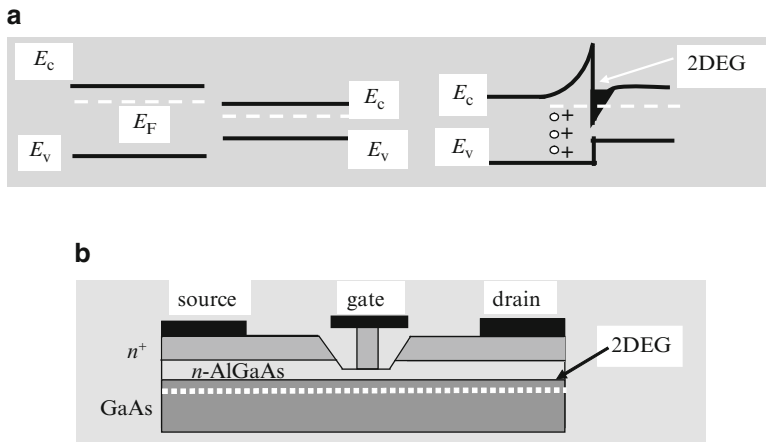


**Fig. 2.6** (a) Formation of a 2DEG and (b) the HEMT transistor

The 2DEG has a carrier density of  $2 \times 10^{11}$ – $2 \times 10^{12} \text{ cm}^{-2}$  and a mobility of  $10^7 \text{ cm}^2/\text{Vs}$ . This sheet of ballistic electrons forms a channel in a FET transistor if additional processing defines the source and drain electrodes, the  $n^+$  doping beneath their respective areas, and the gate electrode. The latter has the role of depleting the electrons in the 2DEG in the presence of a negative applied voltage. The HEMT transistor is schematically represented in Fig. 2.6b. It is similar to a MOSFET where the  $\text{SiO}_2$  layer at the  $\text{Si}/\text{SiO}_2$  interface corresponds to the wider semiconductor. Although the inversion layer in MOSFET has the properties of a 2DEG, like in the case of AlGaAs/GaAs heterostructures, the quality of the  $\text{Si}/\text{SiO}_2$  interface is inferior than in AIII-BV compounds or nitrides, and therefore, many 2DEG properties are lost in MOSFETs at room temperature.

Natori (1994) developed the first theory of the ballistic HEMT and found analytic expressions for channel charges and the saturation current. The HEMT ballistic transport was explored further (Wang and Lundstrom 2003) by generalizing the analytic model of ballistic transistors (Rahman et al. 2003). This theory relies on the fact that the channel is located at the top of the barrier between source and drain because the gate voltage reduces the barrier height to control the density of electrons in the channel. The ballistic FET is modeled classically in the channel region, a quantum mechanical analysis being necessary only if tunneling is accounted for. Tunneling always worsens the MOSFET's and HEMT's properties.

In the Datta–Lundstrom model of HEMT, which takes into consideration only the top of the source–drain barrier and models classically the transport in the channel, the carrier distribution function at the top of the barrier is composed of two halves corresponding to equilibrium injection of electrons in the source and drain (see Fig. 2.7a). The key parameters of the equivalent circuit model of the HEMT, displayed in Fig. 2.7b, are the three capacitors  $C_S$ ,  $C_D$ , and  $C_G$ , representing, respectively, the effects of source, drain, and gate electrodes on the top of the barrier.

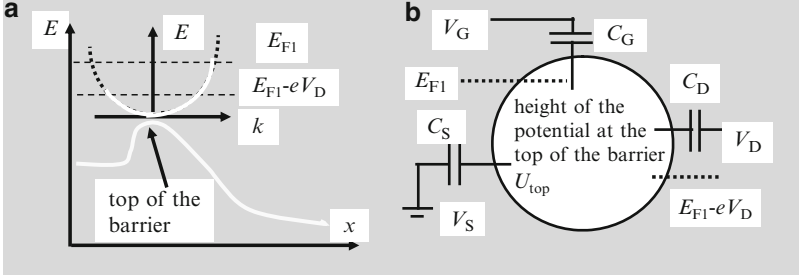


**Fig. 2.7** (a) Energy map for the ballistic HEMT in the Datta–Lundstrom model and (b) the Datta–Lundstrom equivalent circuit

In this model, the maximum potential energy value between source and drain is

$$U_{\text{top}} = -e[(C_G V_G / C_{\text{tot}}) + (C_D V_D / C_{\text{tot}}) + (C_S V_S / C_{\text{tot}})] + e^2 n_{\text{mob}} / C_{\text{tot}}, \quad (2.16)$$

where  $C_{\text{tot}} = C_G + C_S + C_D$  and  $C_G \gg C_S, C_D$ . The density of mobile charges in the channel,  $n_{\text{mob}}$ , is calculated by filling with electrons the  $+k$  and  $-k$  states in conformity with the source and drain Fermi energies, respectively, starting from the bottom of the conduction band at  $U_{\text{top}}$ , assumed known.  $U_{\text{top}}$  is computed iteratively by increasing the density of mobile charges until convergence is reached, and  $I_D$  is estimated from the known electron populations in the two halves of the energy dispersion curve above  $U_{\text{top}}$ .

Nevertheless, contrary to common expectations, the mobility of ballistic carriers in short-channel HEMTs, is much lower than in long-channel HEMTs (Shur 2002). The effective mobility can be written as

$$1/\mu_{\text{eff}} = 1/\mu_{\text{ball}} + 1/\mu_0, \quad (2.17)$$

where  $\mu_0$  denotes the mobility in the long-channel regime, in which collisions dominate, and  $\mu_{\text{ball}}$  is the mobility associated to ballistic carriers. In the nondegenerate case, the ballistic mobility has the expression  $\mu_{\text{ball}} = 2eL/\pi m v_{\text{th}}$ , whereas in the degenerate case, the thermal velocity  $v_{\text{th}} = (8E_{\text{th}}/\pi m)^{1/2}$  in this relation, with  $E_{\text{th}} = k_B T$ , must be replaced with the Fermi velocity  $v_F$ . From (2.17), it follows that the mobility decreases significantly when the gate length decreases, in agreement with experiments; for instance, in GaAs, the mobility is 10,000  $\text{cm}^2/\text{Vs}$  for a gate length of 10  $\mu\text{m}$  and only 3,000  $\text{cm}^2/\text{Vs}$  for a gate length of 150 nm.

For low drain voltage values, the expression of the drain current can be simplified as

$$I_D = W q_i(0) \mu_{\text{ball}} V_D / L, \quad (2.18)$$

where  $q_i(0)$  denotes the electron distribution at the source. On the contrary, for high drain voltages, we obtain

$$I_{\text{DSat}} = Wq_i(0)\overline{v_{\text{thd}}} = Wq_i(0)[v_{\text{thd}}F_{1/2}(\zeta)/F_0(\zeta)], \quad (2.19)$$

where  $v_{\text{thd}} = (2E_{\text{th}}/\pi m)^{1/2}$  is the unidirectional thermal velocity,  $F_{1/2}(\zeta)$  is the Fermi–Dirac integral, and  $\zeta = (E_{\text{F}} - E_{\text{S}_0})/E_{\text{th}}$ , with  $E_{\text{S}_0}$  the energy of the first electron subband at the source.

The AlGaIn/GaN HEMT was extensively used for various sensing applications (Kang et al. 2008). The 2DEG is induced and can be tuned by piezoelectric polarization of the strained AlGaIn layer and the spontaneous polarization between AlGaIn and GaN. Sensing applications are favored in this HEMT transistor since the 2DEG is located in the vicinity of the surface, and its density is tunable due to polarization, being thus very sensitive to ambient conditions around the surface. A gateless AlGaIn/GaN HEMT is used as sensor by exposing its gate area to various analytes. The HEMT biosensor is represented in Fig. 2.8.

The HEMT configuration in Fig. 2.8 is used as a pH sensor, various cover layers deposited above the gate area improving the sensitivity of the biosensor. DNA detection and its hybridization were achieved also in such HEMT transistors (Kang et al. 2006). In this case, the HEMT structure consisted of a 3- $\mu\text{m}$ -thick GaN buffer, a 3-nm-thick  $\text{Al}_{0.3}\text{Ga}_{0.7}\text{N}$  spacer layer, and a 22-nm-thick cap layer from Si-doped  $\text{Al}_{0.3}\text{Ga}_{0.7}\text{N}$ . The Ti/Al/Pt/Au drain and source contacts have a gap of 4  $\mu\text{m}$  between them, as shown in Fig. 2.9. In the gap, 5 nm of gold, which allows the immobilization of thiol-modified ssDNA, was deposited as gate metal. The drain and source electrodes were then covered with a polymer, and only the gate region was intentionally opened to allow the liquid, which contains the DNA solution, to flow through the gap. DNA hybridization is detected by measurements of the variation of the drain–source current when the transistor is exposed to matched and mismatched DNA. In the former case, the drain current decreases in time until the hybridization process is completed and remains constant afterward, the current difference compared to the mismatched DNA case reaching 115  $\mu\text{A}$ . This value is

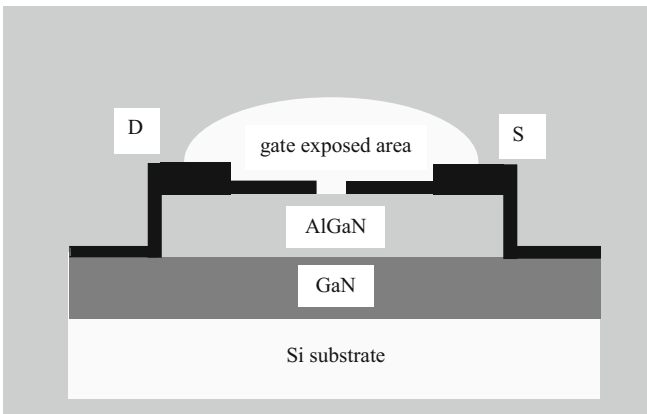
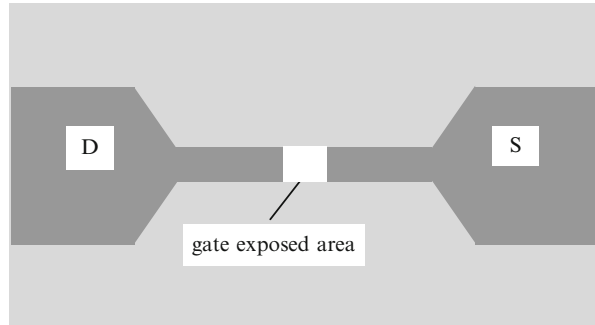


Fig. 2.8 The HEMT biosensor

**Fig. 2.9** Gate exposed is of AlGaN/GaN HEMT transistor for DNA detection



easily detected on current dependences taken on a timescale of tens to hundreds of minutes (the hybridization is completed after 20 min).

Other biomolecules detected with the help of HEMT have proven the validity of this biodetection method. In this respect, the PSA marker of prostate cancer, the KIM-1 urinary antigen for acute injury, as well as pH and glucose were all detected individually in the exhaled breath condensation with HEMT biosensors. Recently, with the same HEMT configuration as in Fig. 2.8, fast detection of protozoan pathogen *Perkinsus marinus* was performed. This protozoan causes widespread mortality of oysters in farms or in their natural environment (Wang et al. 2009). In the case of this protozoan detection, the exposed gate length was of  $5\ \mu\text{m}$  and was functionalized with an antibody linked to the metallic gate via the thioglycolic acid. The water infected with this dangerous protozoan was monitored during 400–1,000 s. The gate attachment of *Perkinsus marinus* leads to the reduction of the drain current with about  $50\ \mu\text{A}$ , allowing fast detection (less than 5 s) of the infested water. Other details can be obtained from the extensive review of (Pearson et al. 2010) regarding wide-bandgap devices and, especially HEMTs, applications for biological and gas detection.

Another important category of biosensors incorporates FETs with semiconducting nanowire (NW) channels. Presently, NWs are produced on a large scale with high yield and reproducible properties (Lu and Lieber 2006). The mobility of FETs based on NWs is low compared to that of HEMTs, but the NW technology is advancing fast and starts to compete with the well-established CMOS technology. In any case, the mobility is not the determinant parameter for biosensors. NW-based FETs have various geometries and implicate several semiconductors such as Si, SiGe, GaAs, GaN, etc. The typical configuration of a NW FET is represented in Fig. 2.10. The NW connects the source S and drain D electrodes and is isolated from the gate electrode by an oxide layer.

In principle, a NW FET can be obtained by manipulating a single NW and locating it between the drain and the source. This is, however, a demanding task, so that usually the NWs are extracted from a colloidal suspension and dispersed in the area of the S and D contacts. The procedure is illustrated in Fig. 2.11.

**Fig. 2.10** Schematic configuration of the NW FET transistor

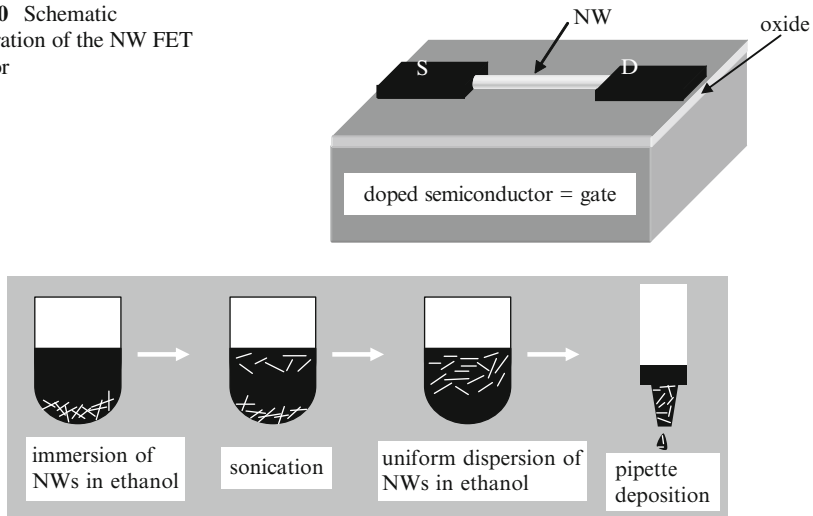
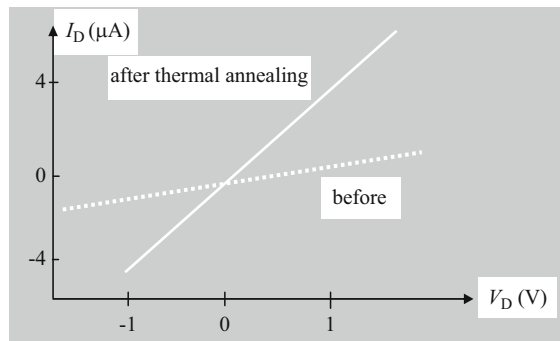


**Fig. 2.11** The deposition steps of NWs between NW FET contacts

**Fig. 2.12** The effect of thermal annealing on the source–drain  $I_D$ – $V_D$  characteristic in a Si NW FET



In general, the metal contacts of FETs based on NWs are of Schottky types, and thus, the FET characteristics depend strongly on the contact properties. In Si NW FETs, however, it was found that thermal annealing and passivation of oxide defects enhance their performances, which become similar to those of Si MOSFETs (Cui et al. 2003). Si NW FETs are produced using the steps illustrated in Fig. 2.11, followed by a 3-min thermal annealing process in hydrogen atmosphere at 600°C. As a consequence, the mobility and the transconductance of the FET increase 20 times (see Fig. 2.12).

Many other technologies described in Chap. 1 can be used for the fabrication of NW devices. For instance, electrodes for NW devices can be produced by room-temperature nanoimprint lithography, which generates metal features on plastic substrates. The NWs are deposited afterward on the plastic substrate using the deposition steps in Fig. 2.11. This method is used to fabricate many devices,

including LEDs, inverters, and transistors, but more complex electronic devices, such as NW transistor logic, crossbar memory elements, or addressable arrays, require bottom-up methods (Lu and Lieber 2007).

The NW FET biosensors are based on the changes in  $I_D - V_D$  characteristics, as in the cases of other FETs. The concentration of charge carriers can be expressed as

$$n = V_{th}C/e\pi(d/2)^2L, \quad (2.20)$$

where  $V_{th}$  is the threshold voltage,  $d$  denotes the NW diameter,  $L$  is the active length of the NW channel, and the capacitance is given by

$$C = 2\pi\epsilon_0\epsilon_dL/\ln[(2h+d)/d], \quad (2.21)$$

where  $\epsilon_d$  and  $h$  are, respectively, the permittivity and thickness of the gate dielectric.

The dc characteristics of ballistic Si NW FETs with coaxial gates are found using the Natori theory which, for a nondegenerate carrier statistics, predicts that

$$I_D = C v_T (V_G - V_{th}) [1 - \exp(eV_D/k_B T)] / [1 + \exp(eV_D/k_B T)], \quad (2.22)$$

where  $v_T = (2k_B T / \pi m_{eff})$ , whereas in the case of a degenerate carrier statistics, for very small charges in the channel, we have

$$I_D = (2e^2/h)V_D. \quad (2.23)$$

Unlike in a standard MOSFET, in which the channel conductance is controlled by  $V_G$ , in NW FETs, this conductance is independent of  $V_G$  if the gate voltage has sufficiently large values to induce carrier degeneracy.

NW FETs can be fabricated also from different nanowires, in particular the core/shell Ge/Si nanowire depicted in Fig. 2.13a (Xiang et al. 2006). Figure 2.13b shows that a 1D hole gas develops in the inner Ge NW, which becomes a quantum well with high mobility and low carrier scattering rates. The transport of charge carriers is ballistic for devices shorter than the mean-free path of 500 nm. Because the Fermi level is located below the Ge valence band and in the bandgap of Si, the contacts are not Schottky-like, but ohmic. These better contacts and the efficient carrier confinement in these radial NWs with a length of 1  $\mu\text{m}$  and an outer diameter of 20 nm encouraged the production of FETs with high- $k$  dielectrics gate isolator layers and high performances. Typical high- $k$  dielectric materials are  $\text{HfO}_2$  and  $\text{ZrO}_2$ . The transconductance of the radial NW FETs is of  $3.3 \text{ mS}(\Omega\text{m})^{-1}$  and its on-current takes a value of 2.1 mA, both parameters exceeding several times the corresponding values in state-of-the-art MOSFETs.

Another common way to produce high-quality NW FETs focuses on decreasing the contact resistance of the transistor. To achieve this, multiple NWs are arranged in parallel by dielectrophoresis, performed by a low-frequency alternative current flowing between drain and source. The multi-NW transistor is presented in Fig. 2.14.

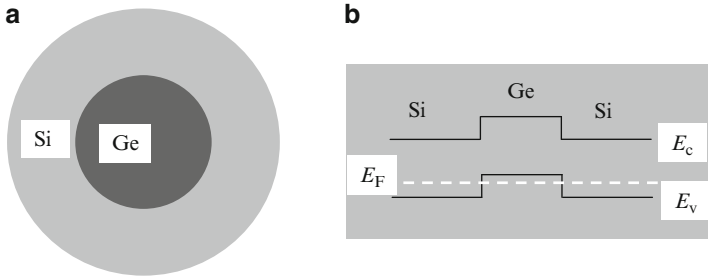


**Fig. 2.13** (a) Cross section of the radial Ge/Si heterostructure and (b) the corresponding energy band diagram

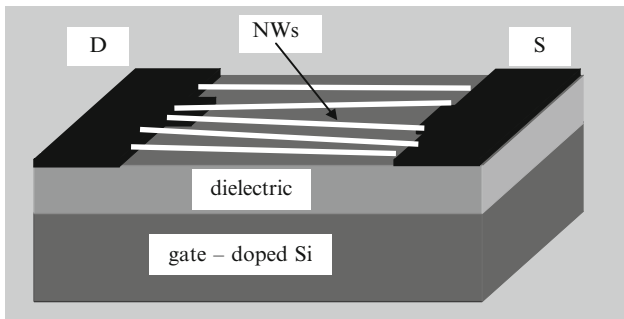


**Fig. 2.14** The NW FET with millions of NWs in parallel as channel

For biomolecule sensing applications, the NW FET must be functionalized. In general, only the NW is functionalized, while the source and drain contacts are protected against unwanted adsorption of biomolecules or chemical reactions by polymer or oxide layer coatings. In the noncovalent functionalization case, when the detection method is based only on electrostatic interactions with electrically charged biomolecules, which attach to the NW and alter the channel conductivity of NW FET biosensors, the sensitivity of the sensor is defined as

$$S = |G - G_0| / G_0 = \Delta G / G_0, \quad (2.24)$$

where  $G$  and  $G_0$  are the NW conductance values in the presence and absence of immobilized biomolecules, respectively. In NW FET sensors with longer channels than the mean-free path, a semiclassical model is adequate to describe the conductance of the biosensor (Nair and Alam 2007) which in the absence of biomolecules is

$$G_0 = eN_D\mu\pi d^2/4L. \quad (2.25)$$

In (2.25),  $\mu$  is the mobility of charge carriers,  $d$  is the diameter and  $L$  the length of the NW, and  $N_D$  denotes the doping density. The semiclassical approach is valid

in Si NW FETs with channel lengths in the range of 2–20  $\mu\text{m}$ , for example, which are much longer than the mean-free path, of 10–20 nm. The presence of charged immobilized biomolecules can be modeled as a uniform electrical surface density  $\sigma$  due to which the NW charge increases or decreases with  $\Delta q = \pi\sigma d$ . Thus, the conductance change originating in molecular conjugation processes at the NW surface is given by

$$\Delta G = \pi d \mu \sigma / L, \quad (2.26)$$

and the sensitivity is

$$S = 4\sigma / edN_D. \quad (2.27)$$

From (2.27), it follows that good sensitivity is achieved for weakly doped and thin NWs. The NW FET biosensor is displayed in Fig. 2.15.

The NW FET biosensors have many applications (Patolsky et al. 2007). For example, the presence of a virus can be detected by monitoring the change in conductance due to variations in the electrical charge when a single virus becomes immobilized on the functionalized substrate. If the virus unbinds, we detect the  $G_0$  value of the conductance, while in the presence of the virus, the conductance reaches the  $G$  value; a temporal measurement of the conductance reveals the dynamic of the virus interaction with the functionalized NW.

Finally, we present briefly the biosensing with the help of CNTs and graphene. In principle, the CNT transistors (CNT FETs) are well described in (Dragoman and Dragoman 2009), and we do not repeat here the theory of these transistors. The sensing mechanism is similar to NW FETs, i.e., the conductance of CNT FET is modulated in time when a biomolecule is sensed by the functionalized CNT channel. There are two basic configurations of CNT FETs for biosensing applications (Gruner 2006): a FET with a channel consisting of a single CNT, or a FET with a channel formed by a network of CNTs, which are randomly oriented. There are very simple methods to functionalize CNTs in order to immobilize biomolecules (Yang et al. 2007), and various biomolecules such as DNA, RNA, or proteins are detected with CNT FETs. An example is presented in what follows.

A simple CNT-based biosensor to detect streptavidin (a protein) and the IgG (immunoglobulin G) mouse antibody (Atashbar et al. 2006) is represented in

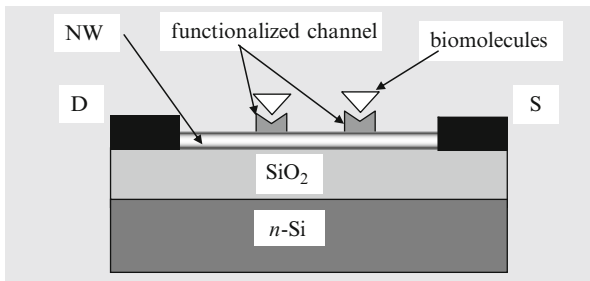


Fig. 2.15 FET NW biosensor configuration

**Fig. 2.16** CNT biosensor based on a CNT network

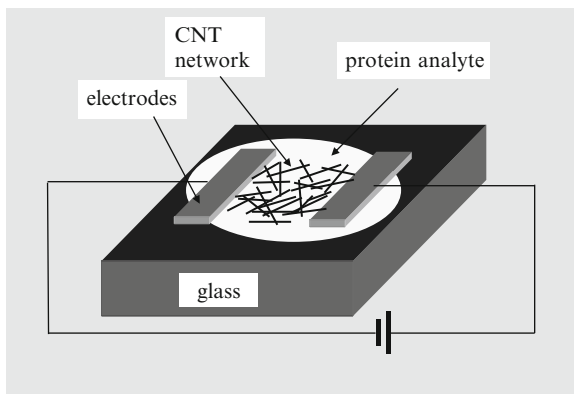


Fig. 2.16. The CNT biosensor in this figure is a nanosized gap between two Ag electrodes. The gap is covered with a CNT network consisting of a suspension of functionalized single-walled CNTs. If we apply a voltage of 1 V across the electrodes, the conductance is decreased with 40% (36%) when  $1\ \mu\text{M}$  of protein (antibody) solution was added over the CNT network. In this way, DNA, RNA, proteins, or viruses can be electrically detected.

The CNT biosensor in Fig. 2.16 can be easily transformed into a CNT FET with a liquid gate sensor by inserting a Pt electrode into a conducting liquid placed over the CNT network and the source and drain electrodes. In this case (Gruner 2006), the detection is based on a shift of the drain–source current dependence as a function of gate voltage (Gruner 2006). The CNT FET with liquid gate is displayed in Fig. 2.17. The attachment of biomolecules such as a protein on the CNT network forming the FET channel is detected in real time.

Moreover, the CNT FET in Fig. 2.17 is able to detect viruses or other bioentities, and even a single biomolecule. CNT FETs working in solution, as above, are able to detect the hybridization of a single molecule of DNA. A single ssDNA probe molecule is covalently attached to a point defect engineered in CNT, and the drain–source conductance is measured in the presence of the complementary DNA target. By measuring the fluctuations in time of the conductance, the temperature-dependent kinetics of DNA matching can be studied, and in this way, the rate constants, activation energies, and melting curves can be determined (Sorgenfrei et al. 2011).

Graphene has impressive physical properties, as discussed in Chap. 1. FETs based on graphene are developing very fast (Schwierz 2010) and their cutoff exceed 300 GHz (Liao et al. 2010). A top gate graphene FET is depicted in Fig. 2.18. The  $\text{SiO}_2$  layer is deposited on a doped silicon (not shown) which acts as back gate.

Recently, such graphene FETs were used for an electronic nose (Lu et al. 2010). The graphene FET was functionalized with two ssDNA sequences, and the drain–source current variation in time was used to detect vapors of analytes such as nitrogen, propionic acid, or methanol. Large variations of the drain current were

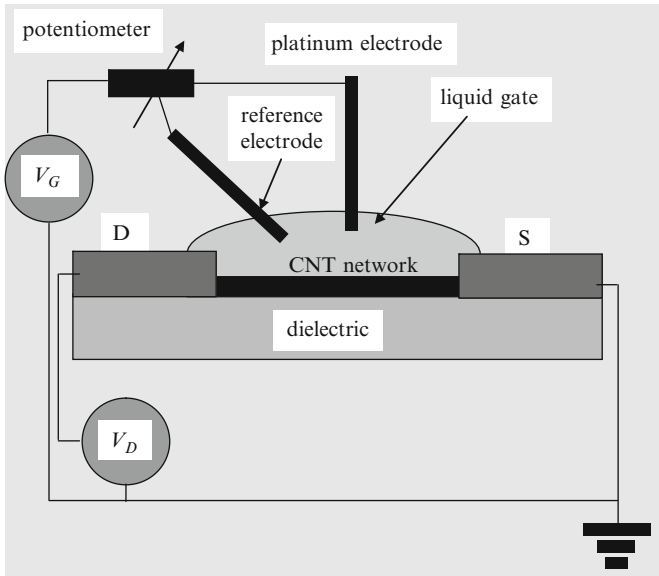
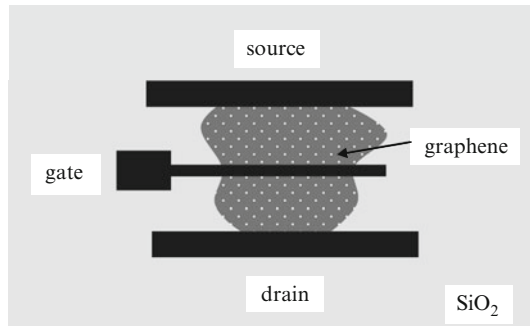


**Fig. 2.17** The CNT FET with a liquid gate

**Fig. 2.18** The graphene top transistor (top view)



detected, ranging from 9% to 35% for different vapors. An array of such graphene FETs is a fine electronic nose. A simple and effective protein detection using thermally reduced graphene oxide sheet decorated with gold antibody conjugates was also reported (Mao et al. 2010).

## 2.2 DNA Detection and Sequencing Using Nanopores

This section is dedicated to DNA sequencing, i.e., to detecting the sequence of bases A, G, C, T, using techniques based on nanotechnologies. DNA sequencing is of paramount importance for the decoding of the human genome, and based

on the revealed information, the ultimate understanding of various diseases such as cancer, the personalized treatment of various illnesses, and the early warning detection of various diseases are expected. There are various techniques to detect DNA and its associate sequence of bases, which are reviewed in (Shendure and Ji 2008). Sequencing techniques, such as the Sanger sequencing method, are utilized for more than 30 years, but are very slow. In addition, it is very expensive: the price for sequencing a microbial genome is 20,000–50,000 dollars, while a single human genome costs 10–25 millions dollars. However, these methods attain an impressive degree of accuracy, of 99.99% (Xu et al. 2009), taking into account the complexity of the problem, i.e., that a human genome contains three billion DNA base pairs.

So, a low-cost and rapid DNA sequencing technique is of high demand. Further, we focus only on electronic detection of the DNA sequence which traverses a nanopore. This is the most promising DNA sequencing method in terms of costs and efficiency and, as will be seen, can be extended to protein detection or RNA detection.

One of the most important properties used in DNA sequencing is that the DNA backbone is negatively charged in solution, such that a single negative charge is associated to each nucleotide, or two charges are associated to a pair of nucleotides for dsDNA. The negative electrically charged DNA can be pull through a nanopore with a diameter of 1–2 nm with the help of an electric field, and the bases are readout with the help of two electrodes, followed by low-noise amplification and electronic processing (Zwolak and Di Ventra 2008). In general, electronic DNA sequencing refers to ssDNA sequencing. This imposes a requirement on the nanopore diameter to be no wider than 1–2 nm, which impedes the translocation of dsDNA, with a diameter of 2 nm; the length of a nucleosite is 0.7 nm. These are amazingly low dimensions, at the limit of common equipments in nanotechnology. However, as we will see below, there are a large number of methods and materials to fabricate nanosized nanopores. A nanopore device for DNA sequencing is displayed in Fig. 2.19. This figure shows that there are two main parts in the nanopore device dedicated for DNA sequencing: a part consisting of two ionic chambers, with the role of capturing and translocating the DNA sequence, and the part dedicated to electronic detection.

The DNA capture and translocation occurs between the two ionic chambers labeled with *cis* and *trans*. When a dc bias is applied across the membrane containing the nanopore, the following effects occur: (1) an ionic current flows through the pore, and (2) the negatively charged DNA is captured and dragged through the nanopore. So, there are two related effects that take place in the nanopore surroundings, i.e., capture of the DNA and its translocation through the nanopore. DNA capture depends on the concentration of DNA in the solution and the strength of the applied dc electric field, while the translocation is dependent of the applied field (bias) and many other factors (viscosity, ionic concentrations, etc.), which can be gathered together under the term DNA–pore interaction effects. During the translocation, which occurs in a certain time duration  $t_d$ , the DNA strand is blocking the flow of ions located in the neighborhood of the pore. Since the DNA nucleotide located in the pore has a much slower velocity than the ions, the presence of DNA

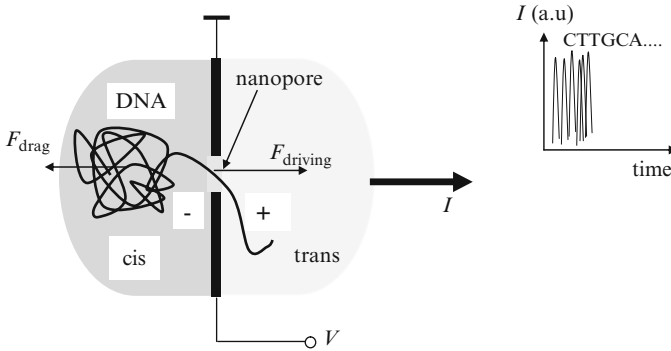
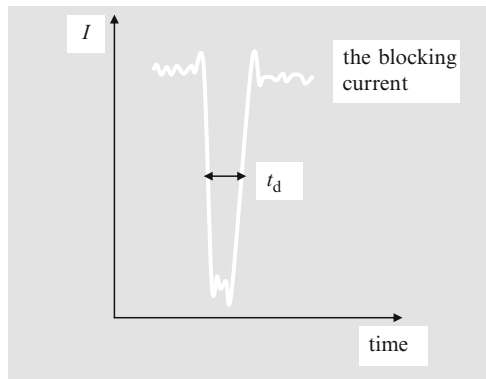


**Fig. 2.19** DNA sequencing using a nanopore

**Fig. 2.20** A schematic behavior of the DNA blocking current



nucleotides inside the pore manifests as a blocking current (see Fig. 2.20). As a result, the ionic current displays a sharp decrease with durations ranging from 300 to 1,300  $\mu\text{s}$  (Zwolak and Di Ventra 2008). The blockade current offers information about the length of the DNA sequence and about its base content, since each base has its own geometrical dimensions, affecting  $t_d$  in a quite different manner.

The voltage drop is located around the nanopore, which has a much higher resistance than the ionic solution surrounding it, and the presence of DNA significantly changes the voltage distribution, so that the applied bias drops mainly on the nucleotides. Considering that the bias is applied only on the nanopore, there are two forces acting in the two ionic chambers. The first is the driving force acting on DNA in the pore region, given by

$$F_{\text{driving}} \cong -0.5eNE, \tag{2.28}$$

where  $N$  is the number of folds in the pore region, and  $E$  is the applied electric field. The DNA–pore interaction is modeled as a drag force expressed as

$$F_{\text{drag}} \cong N\gamma v, \tag{2.29}$$

where  $\gamma$  is a coefficient determined by the contact surface area of the DNA and the pore surface, and  $v$  is the DNA velocity. If we assume that the DNA velocity is constant, we get

$$F_{\text{drag}} = F_{\text{driving}}. \quad (2.30)$$

The above equality assures us that the DNA velocity is the same irrespective of the folded or unfolded DNA conformation. Some other important effects related to the blocking current are summarized below (Zwolak and Di Ventra 2008).

Denoting by  $I_0$  the open pore current and by  $I_b^N$  the blocking current for an  $N$  folded DNA, we have

$$(I_0 - I_b^N)t_d = \text{const.} \quad (2.31)$$

which implies that the charge is conserved at translocation of the folded DNA, which has an equivalent linear region of length  $NL_N$ , where  $L_N$  is the length of the folded DNA sequence. The open pore current is given by

$$I_0 = e\mu nE_z, \quad (2.32)$$

where  $n$  is the charge carrier density,  $\mu$  is the ion mobility, and  $E_z \cong V/L_p$ , with  $V$  the voltage drop on the nanopore and  $L_p$  the nanopore length. Considering the volume exclusion as the unique cause of the blocking current, the carrier density during the blockade event is

$$n_b = Fn, \quad (2.33)$$

where  $F = 1 - V_n/V_p$  with  $V_n$  ( $V_p$ ) the volume of a nucleotide (pore volume for one repeat unit of the polynucleotide) or

$$(I_0 - I_b^N)/I_0 = 1 - F. \quad (2.34)$$

The generic nanopore for DNA sequencing based on blockade ionic current is  $\alpha$ -hemolysin, which has a diameter of 1.4 nm. Various experiments have demonstrated that the ionic blockade current is able to provide information about base signatures and other characteristics of DNA, RNA, etc. For example, in experiments with RNA formed from poly(A), poly(U), and poly(C) sequences (Akeson et al. 1999), it was found that the translocation time of poly(U) is 1.4  $\mu\text{s}$ /nucleotide (nt), while the translocation time for poly(A) is 22  $\mu\text{s}$ /nt, for a pore bias of 0.12 V. In turn, poly(C) gives 95% blockade of ionic current and translocates in about 5  $\mu\text{s}$ /nt, while poly(U) and poly(A) give 85% blockade of ionic current. Poly(A) contains a secondary helical structure, so its translocation time is larger than that of poly(U), where such a secondary structure is absent.

The problem with the DNA sequence technique based on blockade ionic currents is that, when a resolution of a single base is required, the ionic blockade current varies with only few percents, considering that the change in blockade ionic current is due only to the excluded volume. However, the noise of the ionic current, composed of intrinsic noise of the ionic carriers and that produced by the structural fluctuations of the nucleotides, exceeds by far the few percent value, being around

30% of the average current for a homogenous sequence. So, single-base resolution is not reached, and various methods are studied to obtain this resolution. The temperature, the pH, the introduction of a molecule in the pore, and the use of a special pore with a molecular affinity that confers it the property of interacting distinctively with each of the bases are ways to alleviate the lack of sensitivity of the blockade ionic current, such that the sensitivity of this DNA sequence method can increase up to 95%.

The transverse electronic current method is used to improve the sensitivity of DNA sequence detection by adding two dc biased electrodes on the two sides of the nanopore and by monitoring the transverse current, as shown in Fig. 2.21. The parallel electric field,  $E_{\parallel}$ , pulls the DNA through the nanopore, while the transverse field,  $E_{\perp}$ , is applied for DNA sequencing purpose, since each base has a very distinct current signature, as displayed in Table 2.1 (Zwolak and Di Ventra 2005).

From Table 2.1, it can be observed that, when nucleotides translocate through the nanopore, the transverse current provides a direct and distinct electronic signature of DNA bases. The current for different nucleotides varies with almost three orders of magnitude between T and A, while between G and C, the difference is of a factor of 2. The origin of the distinct currents associated to different DNA bases is the Fermi level position with respect to HOMO and LUMO, and the DOS values (Zwolak and Di Ventra 2005). The bases, more precisely their corresponding molecular orbitals, have different spatial extensions. The largest base is adenine, which is easily detected by this method. Considering that the transverse bias is nearly zero, the tunneling current through the nanopore at a single energy level  $E_N$

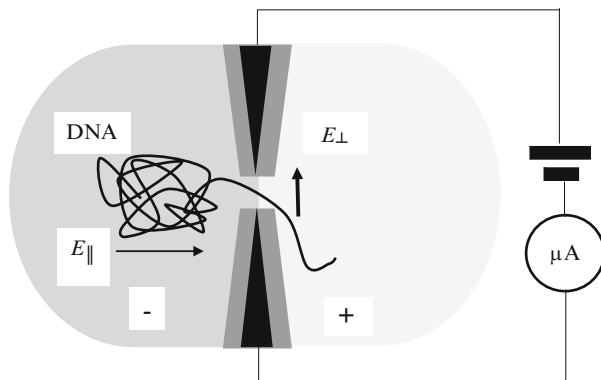


**Fig. 2.21** The DNA sequencing using transverse current method

**Table 2.1** DNA sequencing based on base tunneling current signature

Base	Ratio $I_{\text{base}}/I_{\text{adenine}}$
A	1
G	20
C	40
T	660

is given by [Zwolak and Di Ventra \(2008\)](#)

$$I \cong 2 \frac{e^2}{h} \frac{\Gamma_L(E_F) \Gamma_R(E_F)}{(E_F - E_N)^2} V, \quad (2.35)$$

where  $\Gamma_L$  and  $\Gamma_R$  are coupling coefficients, which have very different values for each base, due to their different extensions and corresponding wavefunctions. On the contrary, the energy levels of different bases have almost the same distance to the Fermi energy  $E_F$ .

An important condition for DNA sequencing is that DNA must have a slow translocation velocity, necessary for nucleotide orientation by the transverse field in hundreds of ps when the nucleotide reaches the electrodes. This is expressed as

$$E_{\parallel} \ll E_{\perp}. \quad (2.36)$$

Using the above method, it is estimated that the three billion bases of a human ssDNA can be sequenced in approximately 7 h ([Zwolak and Di Ventra 2008](#)). Again, the main disadvantage of the transverse current sequence technique is the noise, especially the ionic noise, caused by ionic fluctuations.

There are methods dedicated to sequencing DNA based on similar principles. For instance, the method based on the capacitance change of a MOS capacitor with an integrated nanopore [see ([Zwolak and Di Ventra 2008](#)) and the references therein]. In this case, voltage fluctuations are monitored instead of currents, as in the examples above. The sensitivity required from this method is high, since DNA sequencing means in this situation the detection of differences between the dipole moments of different bases, which could be retrieved from voltage oscillations at translocation through the nanopore ([Gracheva et al. 2006](#)). The molecular capacitances of nucleotides are displayed in [Table 2.2](#) ([Lu and Zhang 2008](#)).

[Table 2.2](#) suggests that the DNA bases A and G have a distinct capacitance signature compared to C and T. If we compare the above capacitances with that of a plate capacitor with an area of  $0.1 \text{ nm}^2$  and a distance between plates of  $1.5 \text{ nm}$ , the difference in the base capacitances could be equivalent with a difference in effective permittivity between 2 and 5.

There are also various optical methods based on nanopores, but the label-free character of these methods is partially lost due to the use of DNA magnification sequence and florescent tagged ssDNA.

There are two types of nanopores used for DNA sequencing: biological nanopores and solid-state nanopores, more exactly dielectric nanopores

**Table 2.2** Base capacitances

Base	Molecular capacitance (aF)
A	0.29
G	0.22
C	0.94
T	0.94

(Dekker 2007). The biological nanopore already mentioned in this section, for example,  $\alpha$ -hemolysin, is a protein generated as toxin by *Staphylococcus aureus*, which is inserted in a lipid membrane and has a minimum width of 1.4 nm. This nanopore was first used for DNA sequencing in the years 90, when nanotechnologies were in infancy. Today, biological nanopores are not only used to study DNA sequencing at the single molecule level but are also used to study peptides, nucleic acids, and polymers (Ma and Cockroft 2010).

Solid-state nanopores are the result of silicon micromachining technology and the usage of EBL and/or FIB technology to process such small nanopores. There are two basic methods to obtain nanopores. The first is the ion beam sculpting method, where a focused ion beam directed to mill a large nanopore in a thin membrane is combined with exposure to an  $\text{Ar}^+$  beam which, subsequently, activates pore closure due to a diffusion process; an  $\text{Ar}^+$  ion detection technique placed under the membrane determines when to stop this diffusion-induced pore shrinking process (Li et al. 2001). The second method is based on micromachining of Si, SiN, or  $\text{SiO}_2$  membranes, followed by EBL and etching (Storm et al. 2003). Basically, an electron beam drills the hole in the Si membrane, and at the same time, the hole is monitored by TEM, the electron beam reducing the hole dimension in a systematic manner, at a rate of  $0.3 \text{ nm min}^{-1}$ .

Tunneling junctions are fabricated and embedded in the nanopore for detecting simultaneously both ionic and tunneling currents, which contain the DNA base signatures (Ivanov et al. 2011). Short-lived translocation events of type I are recorded in sub-ms time ranges, and only the ionic current is recorded in this case, while for type II events, which are assigned for translocation times longer than 1 ms, both ionic and tunneling currents are recorded.

Solid-state nanopores are used to translocate RNA molecules and to compare the electronic signature of dsRNA with those of homopolymers poly(A), poly(U), and poly(C). The blockade ionic current is used for such studies, and the molecular identification is due to the high applied voltages, of 0.6 V, which stretch these flexible acids (Skinner et al. 2009). It was observed that while the blockade conductances of dsRNA and dsDNA are slightly increasing from 1.5 to 2 nS for an applied voltage range 0.1–0.6 V, the poly(A), poly(C), and poly(U) conductances decrease in the same voltage interval from 1.5 to 0.5 nS. So, these distinct signatures could be used for detection of hybridization events and for base identification (see Fig. 2.22).

Solid-state nanopores map also the DNA repair protein RecA attached along the DNA length, using the distinct electrical signatures of the bare DNA and the RecA-coated DNA, with a larger diameter of 7 nm. A high speed is achieved to locate and map the RecA distribution with a spatial resolution of 8 nm, which corresponds to five RecA proteins binding to 15 DNA base pairs, and single protein resolution is soon expected (Kowalczyk et al. 2010).

MicroRNAs (miRNAs) are biomolecules with a paramount role in gene regulation and RNA silencing therapies. MiRNAs play a key role in a variety of cancers and are associated with RNA-induced silencing complexes, which bind the messenger RNA and thus stop protein production. Rapid electronic detection

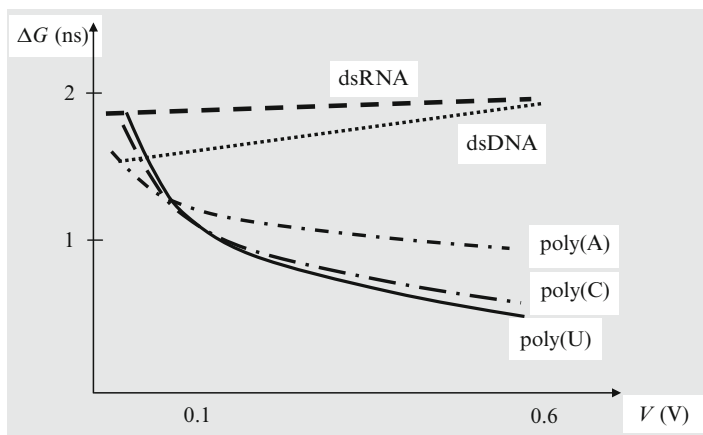


**Fig. 2.22** Schematized electronic signatures for dsRNA and the homopolymers A, C, and U

of probe-hybridized miRNA from cellular RNA was recently reported (Wanunu et al. 2010). Practically, a target miRNA is hybridized to a probe and then enriched with the p19 protein. The miRNA is further detected using a nanopore, the method having the ability to detect miRNA at picogram levels.

Graphene is the last discovery in the area of nanopore sensing. The hole in graphene is fabricated using the FIB technique (Schneider et al. 2010). Despite the fact that graphene is a one-atom-thick material, it is a remarkable ionic isolator (Garaj et al. 2010), and its small thickness makes it the ideal nanopore for the electronic DNA base sequence detection.

### 2.3 MEMS/NEMS Biodetection

MEMS (microelectromechanical systems) and NEMS (nanoelectromechanical systems) are devices in which the mechanical and electrical properties are simultaneously exploited in a series of applications such as sensing, imaging, or even computing. MEMS have at least one dimension at the micrometer scale (1–100  $\mu\text{m}$ ), while in the case of NEMS, one dimension is in the nanometer ( $10^{-9}$  m) range.

The most widespread MEMS or NEMS device is the cantilever, which is schematically represented in Fig. 2.23. The cantilever can be integrated with electronic and/or optoelectronic devices able to process the information or to control its mechanical movement. The cantilever is, in principle, a mechanical resonator that bends due to a thermal, electric, magnetic, or optical force. The typical actuation of a cantilever involves electrical forces, case in which the cantilever is often ended with a nanoscale metallic tip. The cantilever bends toward the substrate due to the attractive electrical force exerted by the voltage  $V$  applied between the substrate electrode and the cantilever.

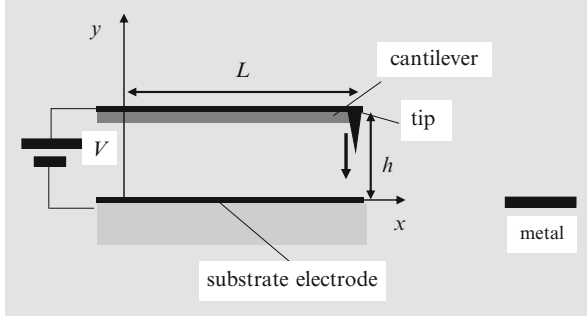


**Fig. 2.23** The electrically actuated cantilever

For a cantilever with length  $L$ , width  $W$ , and thickness  $t$ , the electrostatic force  $F_{e-s}(y)$  is given by

$$F_{e-s}(y) = dU/dy = (V^2/2)dC/dy, \quad (2.37)$$

where  $C$  is the capacitance between the cantilever and the substrate and  $U = CV^2/2$  is the electrostatic energy.

In terms of the cantilever dimensions, the electrostatic force can be expressed as

$$F_{e-s}(y) = (V^2/2)\epsilon_0 WL/[y + (t/\epsilon)]^2, \quad (2.38)$$

where  $\epsilon_0$  and  $\epsilon$  are the electrical permittivities of the free space and the cantilever material, respectively.

Cantilevers are fabricated from a variety of materials: semiconductors such as Si (Stowe et al. 1997) and GaAs (Harris et al. 1996), metals (Chand et al. 2000), nanotubes, nanowires, and even graphene (Zhu et al. 2011). The cantilevers can be functionalized with various materials for sensing applications. MEMS cantilevers are tens-of- $\mu\text{m}$  long and have thicknesses and widths of a few microns, while nanocantilevers are few-microns long and have nanoscale thicknesses and widths.

The cantilever bending is described by the equation

$$d^2y/dx^2 = M(x)/EI, \quad (2.39)$$

where  $E$  is the Young modulus of elasticity,  $I$  is the moment of inertia given by

$$I = \int_{-t/2}^{t/2} y^2 dy \int_{-W/2}^{W/2} dz = Wt^3/12, \quad (2.40)$$

and  $M(x)$  is the total moment at position  $x$ :

$$\begin{aligned}
M(x) &= (1/L) \int_{x'=x}^L F_{e-s}(y(x'))(x-x')dx' \\
&= -\varepsilon_0 W \int_{x'=x}^L (x-x')/[y(x') + (t/\varepsilon)]^2 dx'. \quad (2.41)
\end{aligned}$$

Introducing (2.40) into (2.39), the cantilever bending equation becomes

$$d^2y/dx^2 = -V^2(6\varepsilon_0/Et^3) \int_{x'=x}^L (x-x')/[y(x') + (t/\varepsilon)]^2 dx'. \quad (2.42)$$

Considering further that  $y(x') \approx h$ , the solution of (2.42) can be approximated by

$$y(x) = h - V^2(6\varepsilon_0/Et^3)[L^2x^2/4 - Lx^3/6 + x^4/24]/[h + (t/\varepsilon)]^2, \quad (2.43)$$

and the maximum deflection, which corresponds to  $x = L$ , is given by

$$y_{\max} = y(L) = h - V^2(3\varepsilon_0/4Et^3)L^4/[h + (t/\varepsilon)]^2. \quad (2.44)$$

The deflection due to a force concentrated in a single point  $x$  (Petersen 1978) has the expression

$$y_{\text{conc}} = x^2(3L-x)Wf(x)dx/6EI, \quad (2.45)$$

whereas if the electrostatic force is distributed uniformly along the cantilever, the corresponding deflection is

$$y_{\text{unif}} = W \int_0^L (3L-x)x^2 f_{e-s}(x)(6EI)^{-1} dx, \quad (2.46)$$

where  $f_{e-s}(x) = -(\varepsilon_0/2)V^2/[t - y(x)]^2$  is the electrostatic force per unit area.

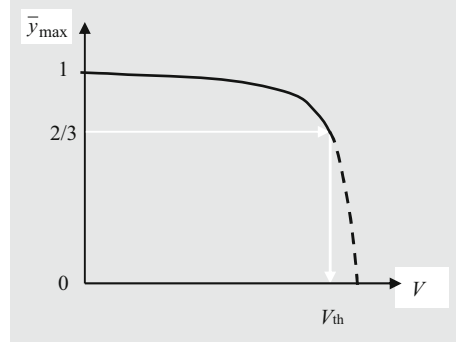
For a square-law cantilever bending  $y(x) = (x/L)^2 y_{\max}$ , the deflection in 2.46 is found by solving numerically the equation

$$\begin{aligned}
\varepsilon_0 WL^4 V^2 / 2EIh^3 &= (4\bar{y}_{\max})[(2/3)(1 - \bar{y}_{\max}) - \tanh^{-1}(\bar{y}_{\max})^{1/2}/(\bar{y}_{\max})^{1/2} \\
&\quad - \ln(1 - \bar{y}_{\max})/3(\bar{y}_{\max})]^{-1}, \quad (2.47)
\end{aligned}$$

where  $\bar{y}_{\max} = y_{\max}/h$  is the normalized deflection. Figure 2.24 represents the voltage dependence of normalized deflection calculated from (2.47).

The cantilever is in dynamical equilibrium when the elastic  $F_{el}$  and electrostatic forces are balanced, i.e., when

**Fig. 2.24** Voltage dependence of the normalized deflection of a cantilever



$$F_{e-s}(y) - Ky = 0, \quad (2.48)$$

where  $K = 3EI/L^3 = Et^3W/4L^3$  is the spring constant. From Fig. 2.24, it follows that the equilibrium is preserved up to a normalized deflection of  $h/3$ , the balance between the elastic and electrostatic forces being destroyed above this deflection value, so that the cantilever falls down on the substrate electrode. This process occurs at the threshold voltage

$$V_{th} = \sqrt{8Kh^3/27WL\epsilon_0}, \quad (2.49)$$

or

$$V_{th} = \sqrt{8EIh^3/9\epsilon_0L^4W}. \quad (2.50)$$

More about MEMS cantilevers, in particular their fabrication methods, the deflection readout principles, functionalization, and applications, can be found in the recent review (Boisen et al. 2011).

At the nanoscale, cantilevers behave often very different in comparison to their counterpart with microscale geometries. In Fig. 2.25, we have displayed a CNT cantilever indicating the forces acting on it.

The theory developed above is still valid if the van der Waals force  $F_{vdW}$ , which is an attractive force significant only at the nanoscale, is included in the treatment. Then, the equation obeyed by a CNT cantilever becomes (Dequesnes et al. 2002)

$$EId^4y/dx^4 = d[F_{e-s} + F_{vdW}]/dy = f_{e-s} + f_{vdW}, \quad (2.51)$$

where the electrostatic force per unit length is given by

$$f_{e-s} = \pi\epsilon_0V^2/R[y(y+D)/R^2]\log^2\{1+y/R+[y(y+D)/R^2]^{1/2}\}, \quad (2.52)$$

with  $R$  the CNT radius,  $D = 2R$  its diameter, and the van der Waals force per unit length

$$f_{vdW} \propto (1/h^7)[1/(y+2R)^2 - 1/y^2]. \quad (2.53)$$

**Fig. 2.25** Nanoscale metallic CNT cantilever and the forces acting on it

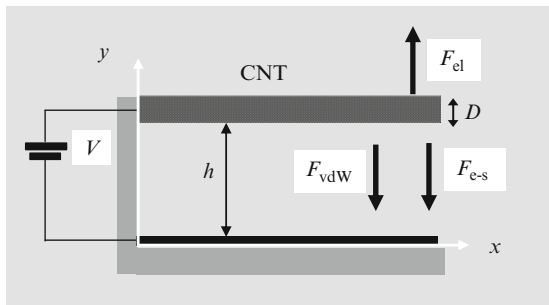
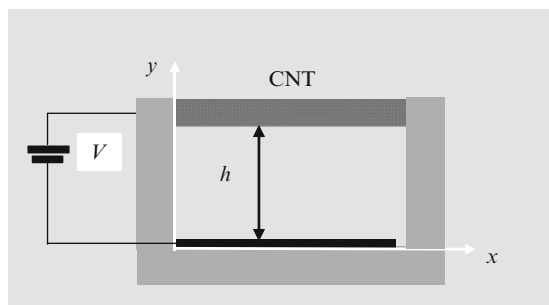


**Fig. 2.26** Double-clamped CNT working as a switch



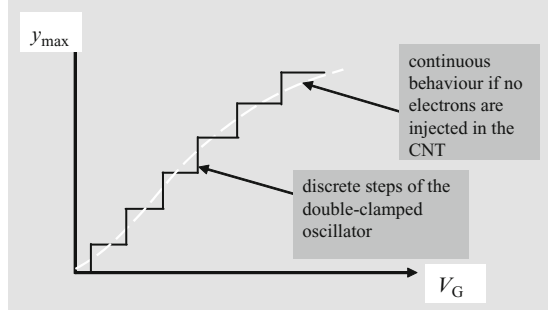
The van der Waals force influences dramatically the deflection of nanocantilevers. It can attract the cantilever toward the substrate electrode even in the absence of an applied voltage; because it is an attractive force, this phenomenon occurring especially when the distance between the cantilever and the substrate is of only few nanometers. Moreover, the van der Waals force reduces the threshold voltage of the cantilever illustrated in Fig. 2.25, but has no significant effect for double-clamped CNT. A double-clamped CNT cantilever, as that represented in Fig. 2.26, whether of microscale or of nanoscale dimensions, can act as a switch in the presence of a substrate electrode or as a mechanical resonator in the absence of this electrode. In the last case, the double-clamped CNT resonator has a mechanical oscillation frequency given by  $f_{\text{osc}} \cong 1.03(E/\rho)^{1/2}(2R/L^2)$ , where  $\rho$  is the density of the cantilever material.

When a bias  $V$  is applied between the contacts of the double-clamped CNT cantilever, its deflection is not a continuous function of the actuation voltage but a discrete function if the carriers are injecting from the contacts in the cantilever via tunneling (Sapmaz et al. 2003). Each step of the cantilever deflection corresponds to an electron injected inside the CNT. In addition to the deflection induced by the gate voltage  $V_G$ , the CNT bends due to an electrostatic contribution of the bias  $V$ , which generates a maximum discrete deflection of the double-clamped CNT resonator given by

$$y_{\text{max}} = 0.013(ne)^2 L^2 / ER^4 h, \quad (2.54)$$

when the total stress  $T$  is much larger than  $EI/L^2$ , and

**Fig. 2.27** The quantized displacement of a double-clamped CNT



$$y_{\max} = 0.24(ne)^{2/3}L^{2/3}/(E^{1/3}R^2h^{1/3}), \quad (2.55)$$

otherwise. Thus, the CNT acquires a quantized displacement as a function of the actuation voltage, illustrated in Fig. 2.27, when  $y$  is measured with respect to the position of the clamps.

If the distance between an actuation electrode and a mechanical oscillator represented by a cantilever, a double-clamped oscillator, or other types of nanomechanical oscillators, is of few nanometers, the weird Casimir force appears. A recent review about the Casimir force and its implication in NEMS is found in (Lamoureux 2005). So, a wealth of quantum effects manifest in NEMS, despite their simple geometrical structure.

Taking into consideration all the above-mentioned properties, it results that MEMS are very sensitive sensors, which change their deflection due to any external excitation. It is necessary to introduce some additional parameters to fully understand the cantilever-based devices. One such parameter is the fundamental frequency of oscillation of a rectangular cantilever,

$$\omega_0 = 2\pi f_0 = 1.015(t/L^2)(E/\rho)^{1/2}, \quad (2.56)$$

and the superior oscillation frequencies labeled by a positive integer  $n$ ,

$$\omega_n = (c_n/L)^2(EI/m_B)^{1/2}, \quad (2.57)$$

where  $\rho$  is the density of the cantilever material,  $m_B = \rho A$  is the cantilever mass per unit length with  $A$  the cantilever area, and  $c_n$  is constant, for instance,  $c_1 = 1.9$ . On the other hand, for a cylindrical cantilever consisting of a multiwalled CNT, the resonance frequencies are

$$\omega_n = 2\pi\beta_n[(E/\rho)(d_{\text{out}}^2 + d_{\text{in}}^2)]^{1/2}/8\pi L^2, \quad (2.58)$$

where  $n \geq 0$ ,  $d_{\text{in}}$  and  $d_{\text{out}}$  are the inner and outer diameters of the CNT, and  $\beta_n$  is constant, for example,  $\beta_0 = 1.875$  and  $\beta_1 = 4.694$ . For single-walled CNTs, the term  $(d_{\text{out}}^2 + d_{\text{in}}^2)$  in (2.58) must be replaced by  $d^2$ , where  $d$  is the diameter of

the CNT. The resonant frequency of CNTs varies from a few MHz to a few GHz depending on the length and diameter of the nanotube. Many other details about cantilevers, such as noise, quality factors, etc., can be found in (Dragoman and Dragoman 2009).

The oscillation frequencies of cantilevers and double-clamped NEMS are very sensitive to an additional mass; in fact, NEMS are the most sensitive mass detectors. The cantilevers working as mass sensors can be modeled, irrespective of their geometry, as a damped harmonic oscillator with a spring constant  $K$ , case in which its oscillation frequency is  $2\pi f = \sqrt{K/M}$ , where  $M$  is the cantilever mass. Denoting by  $\Delta f = f_0 - f$ , the shift of the resonant frequency  $f_0$  for the unloaded cantilever with mass  $M_0$ , given by  $2\pi f_0 = \sqrt{K/M_0}$ , the additional mass  $m = M - M_0$  is given by

$$m = (K/4\pi^2)[1/(f_0 - \Delta f)^2 - (1/f_0)^2], \quad (2.59)$$

relation that can be simplified as

$$m/\Delta f = 2M_0/f_0, \quad (2.60)$$

when  $\Delta f \ll f_0$ .

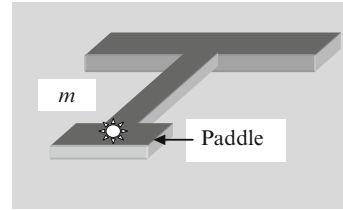
There are astounding examples in literature for unprecedented small mass detection with the help of cantilevers or other NEMS devices. For example, a rectangular cantilever made of polycrystalline silicon with a thickness of 160 nm, a width of 500 nm, and length of 4  $\mu\text{m}$ , ended with a square paddle with an area of 1  $\mu\text{m} \times 1 \mu\text{m}$ , is able to detect 0.39 attograms (1 attogram = 1 ag =  $10^{-18}$  g) via a resonance frequency shift of about 3 kHz (Ilic et al. 2004a). Moreover, zeptogram (1 zeptogram = 1 zg =  $10^{-21}$  g) or even yoctogram ( $10^{-24}$  g) masses can be sensed with CNT cantilevers in high vacuum and at low temperatures. The frequency of a CNT sensor that can detect ultra low masses is given by (Nishio et al. 2005)

$$f = 0.32 \times [K/(m_{\text{CNT}} + 4m)]^{1/2}, \quad (2.61)$$

where the cantilever mass is  $m_{\text{CNT}} = 1.4 \text{ fg}$  (1 femtogram = 1 fg =  $10^{-15}$  g). This cantilever has a length  $L = 3.6 \mu\text{m}$  and a frequency resolution of 10 Hz, so that masses  $m$  less than 100 zg can be measured at room temperature.

The MEMS or NEMS mass sensor is easily transformed in a very sensitive biological sensor by functionalization into a coupling substrate. For example, it was found (Ilic et al. 2004b) that a single virus can be detected with a polycrystalline silicon cantilever coated with an antibody solution that immobilizes an insect baculovirus. This cantilever has the following dimensions:  $L = 6 \mu\text{m}$ ,  $t = 150 \text{ nm}$ , and  $W = 0.5 \mu\text{m}$ , and its free end is ended with a paddle with an area of 1  $\mu\text{m} \times 1 \mu\text{m}$ . Because the mass sensitivity of this sensor is  $10^{-19}$  g Hz, it is large enough to detect a single virus bound to the cantilever, which has a mass of 1.5 fg, the corresponding resonance frequency shift being 3.8 kHz. Other viruses, for example, the vaccinia virus, were sensed with cantilevers (Gupta et al. 2004). The

**Fig. 2.28** Cantilever mass sensor



vaccinia virus has a weight of 5 fg, and the associated frequency shift, of 60 kHz, was measured with a Si cantilever with  $L = 3.6 \mu\text{m}$ ,  $t = 30 \text{ nm}$ , and  $W = 1.7 \mu\text{m}$ . A mass-sensitive cantilever acting as a biosensor is depicted in Fig. 2.28. Very recently, the white spot syndrome virus was detected using a piezoelectric cantilever made of lead–magnesium niobate–lead titanate material (Capobianco et al. 2010).

The cantilever and NEMS can be considered also as label-free sensors. For example, a single nucleotide mismatch was detected by monitoring the optical deflection assay (Hansen et al. 2001), while a suspended microfluidic channel with a cantilever shape was used to weigh biomolecules, single cells, and single nanoparticles (Burg et al. 2007). This microfluidic cantilever was so sensitive that the mass resolution is six orders of magnitude better than in quartz crystal microbalances. The microfluidic cantilever made on SOI weighs only 200 ng and has a mechanical quality factor of 15,000.

Label-free detection of the carcinoembryonic antigen (CEA) biomarker using a piezoelectric PZT cantilever was recently reported (Lee et al. 2008). The critical value of CEA, which is 30 pM or  $5 \text{ ng ml}^{-1}$ , is known as the threshold biomarker for various cancers (breast, cervix, rectum, prostate, stomach, intestine, pancreas, lung) and was detected by the binding of the antigen to antibody contained in a silica sol–gel glass that coated the cantilever. A recent review of NEMS and their applications in biological/chemical recognition is found in Eom et al. (2011).

## 2.4 Plasmonics Biodetection

There are many optical methods suitable for label-free detection of biomolecules. One of the most sensitive is based on plasmonic sensors. Plasmonics is a new area in nanophotonics, which covers the generation, propagation, and detection of plasmonic waves. Plasmonic waves are collective electronic excitations produced by an electromagnetic field, which propagates along a metal–dielectric interface, around metallic nanoparticles or nanowires placed on a dielectric substrate, or through an array of nanoholes in a metallic surface.

The simplest plasmonic configuration is the metal–dielectric interface. The interaction between matter and the electromagnetic field is confined to and plasmons propagate along this interface. These confined surface electromagnetic waves are termed surface plasmon polaritons (SPP) (Barnes 2006) and play an important role

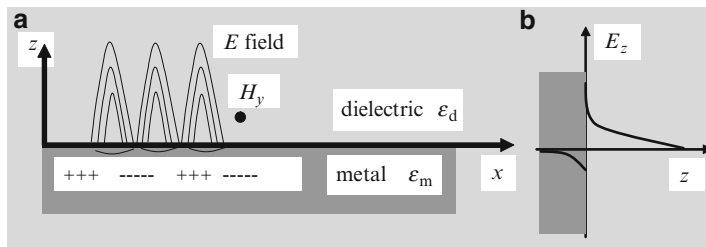


**Fig. 2.29** (a) SPP waves at the dielectric/metal interface and (b) field penetration depth in the dielectric and the metal

in label-free biosensors, since they enhance electromagnetic waves at the metal–dielectric interface and are very sensitive when the propagating media changes.

There are several methods to generate SPPs, which involve metal–dielectric interfaces, nanoparticles, or nanowires. A recent review on this subject is found in (Dragoman and Dragoman 2008). The dispersion relation of SPPs can be derived considering as example an interface between a metal and a dielectric (see Fig. 2.29), with SPPs propagating along it. Around the interface, as shown in Fig. 2.29, there are periodical spatial oscillations of regions with positive and negative charges, which decay rapidly away from the dielectric–metal interface and impose the periodicity of the electric field in the dielectric and metal.

The dispersion relation is found assuming that SPPs are coherent charge oscillations that propagate on both sides of the interface situated in the  $(x, y)$  plane and are confined along the  $z$ -direction, which is perpendicular to the interface. SPPs are a combination of longitudinal and transverse components of the electromagnetic field assumed propagating along the  $x$ -direction. The solutions of Maxwell's equations for the two media (metal and dielectric) can be separated into two categories:  $s$  (TE) and  $p$  (TM) polarized waves. The TE solution corresponds to the case when the electric field is parallel to the interface, whereas in TM waves, the magnetic field is parallel to the interface. SPP are TM waves because they propagate along the interface, i.e., along the  $x$  axis, and have a nonvanishing  $E_z$  component of the electric field perpendicular to the interface.

From Maxwell's equations written for the two media (metal and dielectric) with permittivities  $\epsilon_m$  and  $\epsilon_d$  and wavevector components along  $z$  denoted by  $k_{zm}$  and  $k_{zd}$ , we get the SPP dispersion relation in the form

$$k_{zm}/\epsilon_m + k_{zd}/\epsilon_d = 0, \quad (2.62)$$

which implies that SPP waves exist only if the two media have dielectric permittivities of opposite signs:

$$\text{sgn}(\epsilon_m) = -\text{sgn}(\epsilon_d). \quad (2.63)$$

So, one of them must have a negative dielectric permittivity, condition that is satisfied by all metals in the visible optical spectrum. The wave number of SPPs is determined from

$$k_i^2 = k_{\text{SPP}}^2 + k_{zi}^2 = \varepsilon_i k_0^2, \quad (2.64)$$

where  $k_i$ ,  $i = m, d$ , denotes the wavenumber in media  $i$ , or

$$k_{\text{SPP}} = k_0[\varepsilon_m \varepsilon_d / (\varepsilon_m + \varepsilon_d)]^{1/2} = n_{\text{SPP}} k_0, \quad (2.65)$$

where  $n_{\text{SPP}}$  is the effective index of the SPP, and  $k_0 = \omega/c$  is the wavenumber in vacuum. If the dielectric has positive permittivity,  $\varepsilon_d > 0$ , and the metal has a complex dielectric permittivity  $\varepsilon_m = \varepsilon'_m + i\varepsilon''_m$  where  $\varepsilon''_m < |\varepsilon'_m|$ , the SPP wavenumber is imaginary:

$$k_{\text{SPP}} = k'_{\text{SPP}} + ik''_{\text{SPP}}. \quad (2.66)$$

The real and imaginary parts of the SPP wavenumber are then

$$k'_{\text{SPP}} = k_0[\varepsilon_d \varepsilon'_m / (\varepsilon_d + \varepsilon'_m)]^{1/2}, \quad (2.67)$$

$$k''_{\text{SPP}} = k_0[\varepsilon_d \varepsilon'_m / (\varepsilon_d + \varepsilon'_m)]^{3/2} (\varepsilon''_m / 2\varepsilon_m^2). \quad (2.68)$$

The SPP wavelength, defined as  $\lambda_{\text{SPP}} = 2\pi/k'_{\text{SPP}}$ , is thus found to be

$$\lambda_{\text{SPP}} = \lambda_0 \sqrt{\frac{\varepsilon_d + \varepsilon'_m}{\varepsilon_d \varepsilon'_m}}, \quad (2.69)$$

where  $\lambda_0 = 2\pi c/\omega$ , value that satisfies the essential relation

$$\lambda_{\text{SPP}} < \lambda_d, \quad (2.70)$$

where  $\lambda_d = \lambda_0 \varepsilon_d^{-1/2}$  is the wavelength of the electromagnetic wave incident from the dielectric side of the interface. The ratio  $\lambda_{\text{SPP}}/\lambda_d$  varies typically between 0.5 and 0.9 as a function of the dielectric permittivity of metal, excitation wavelength, etc. Inequality (2.70) is the basic relation for subwavelength optics.

It is important also to estimate the capabilities of SPP to propagate along certain distances. Thus, if the intensity of the electromagnetic radiation depends on  $x$  as

$$I(x) \cong I_0 \exp(-x/\delta_x) \cong I_0 \exp(-2|k''_{\text{SPP}}|x), \quad (2.71)$$

the parameter  $\delta_x \cong 1/2k''_{\text{SPP}}$  can be regarded as the propagation length of the SPP. Considering that the metal has low losses, we obtain

$$\delta_x = (1/k_0)(\varepsilon_m^2/\varepsilon''_m). \quad (2.72)$$

Equation (2.72) suggests that a long propagation length can be obtained in a metal with a large real part of the electrical permittivity, which is negative at the working wavelength, and a very low value of its imaginary part. In such case, the SPP

propagation length is much longer than the optical wavelength. If the metal is silver, the propagation length ranges between 50 and 300  $\mu\text{m}$  in the wavelength interval 500–1,500 nm.

It is also necessary to determine the penetration depths of the electromagnetic field in both dielectric and metal. These parameters are given by

$$k_{zd} = k_0 \varepsilon_d / (\varepsilon_d + \varepsilon'_m)^{1/2}, \quad (2.73)$$

$$k_{zm} = k_0 \varepsilon'_m / (\varepsilon_d + \varepsilon'_m)^{1/2} \quad (2.74)$$

and are purely imaginary since  $(\varepsilon_d + \varepsilon'_m)$  is always negative in plasmonic devices. Under these conditions, the field component perpendicular to the interface is evanescent, its value decreasing with  $1/e$  in the dielectric and metal after a distance

$$\delta_{zi} = 1/|k_{zi}|, \quad (2.75)$$

with  $i = m, d$ . More precisely, the penetration depth of the SPP wave in the dielectric is

$$\delta_{zd} = (1/k_0)|(\varepsilon'_m + \varepsilon_d)/\varepsilon_d^2|^{1/2}. \quad (2.76)$$

For example, the penetration depth in air at the air/silver interface in the wavelength range 500–1,500 nm varies between 450 and 2,500 nm and increases as a function of the excitation wavelength. This parameter is important for excitation and manipulation of SPP modes, especially in sensing applications.

Analogously, in metal, the penetration depth,

$$\delta_{zm} = (1/k_0)|(\varepsilon'_m + \varepsilon_d)/\varepsilon_m^2|^{1/2}, \quad (2.77)$$

is about 26 nm for the air/silver interface in the wavelength range 500–1,600 nm and is nearly independent of the wavelength. This penetration depth dictates the thickness of metal deposition needed for SPP launching and propagation. Generally, the penetration depth in metal is much smaller than in dielectric.

Further, by comparing the SPP dispersion relation,

$$k_{\text{SPP}}/k_0 = [\varepsilon_d \varepsilon_m / (\varepsilon_d + \varepsilon_m)]^{1/2} = n_{\text{SPP}}, \quad (2.78)$$

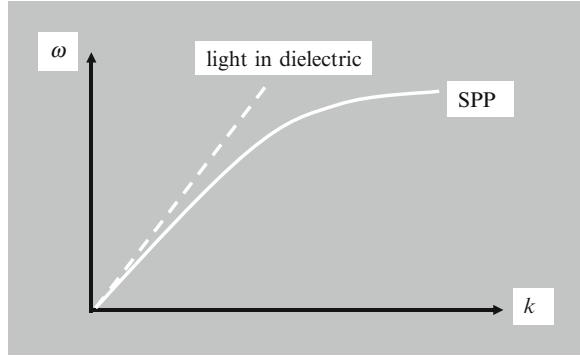
with that of a photon propagating in the dielectric (often free space),

$$k_d/k_0 = (\varepsilon_d)^{1/2}, \quad (2.79)$$

we obtain

$$k_d < k_{\text{SPP}}. \quad (2.80)$$

**Fig. 2.30** The SPP wavenumber mismatch in the dispersion relation



From this relation, it follows that there is a wavenumber mismatch between SPP and the incoming electromagnetic wave excitation (see Fig. 2.30), so that SPP is a nonradiative wave that propagates on a smooth interface.

The matching between the incoming electromagnetic wave moment and that of the SPP is achieved by several methods. One of these methods relies on a prism, which increases the moment of incoming photons, while others change the surface of the metallic medium from a smooth one into a nonsmooth surface, with gratings, perforations, or holes.

If the incoming optical field illuminates a half-cylindrical prism with permittivity  $\varepsilon_p$ , its wavenumber is modified from  $k_d$  to  $k_0(\varepsilon_p)^{1/2}$ , being thus enhanced with a factor of  $(\varepsilon_p/\varepsilon_d)^{1/2}$ . It then becomes possible for the incoming field with an excitation frequency  $\omega_{exc}$  to match the SPP wavevector component along the interface for a specific incident angle  $\varphi_0$  for which

$$\varepsilon_p^{1/2} \omega_{exc} \sin \varphi_0 = ck_{SPP}. \quad (2.81)$$

SPPs can only be excited if the matching condition (2.81) is satisfied. The incident angle for which this requirement is met and SPP propagation is enabled is called resonant angle. At resonance, the reflectivity of the entire structure is zero, since the SPP is entirely localized along the interface.

Based on this principle, there are two main matching configurations named Otto and Kretschmann configurations, respectively, which make use of prisms that can have a variety of shapes besides the half cylinder. These two configurations for prism-SPP matching are illustrated in Fig. 2.31.

If we use a metallic grating with period  $\Lambda$  embedded in a dielectric with permittivity  $\varepsilon_d$  to excite SPPs by exciting the grating with an electromagnetic field incident under an angle  $\varphi_0$ , as shown in Fig. 2.32, the matching condition becomes

$$k_{SPP} = k_d \sin \varphi_0 + k_{grat} = k_0 \varepsilon_d^{1/2} \sin \varphi_0 \pm m2\pi/\Lambda, \quad (2.82)$$

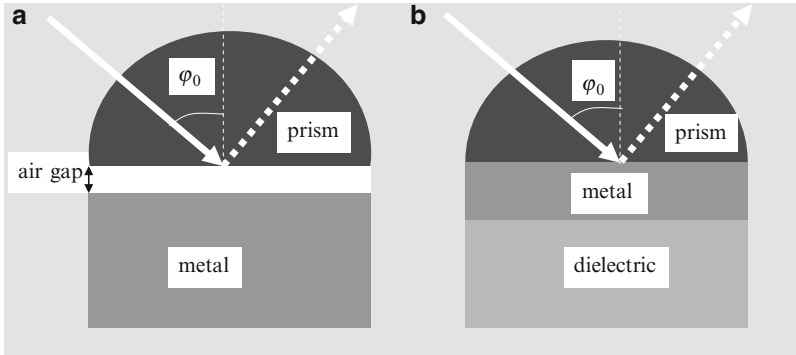
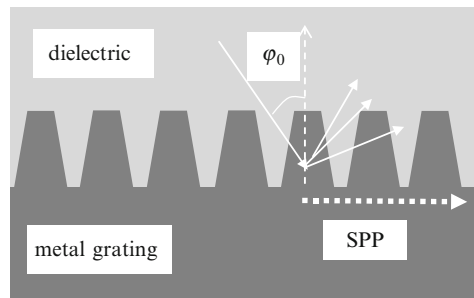


**Fig. 2.31** The matching of SPP and light wavevector components using half-cylindrical prisms: (a) Otto configuration, (b) Kretschmann configuration

**Fig. 2.32** SPP launching using a metallic grating



with  $m$  an integer. As in the previous example with a prism, it is possible to excite an SPP wave at the interface between the metallic grating and the dielectric at a particular incidence angle.

Irrespective of the method of SPP excitation, the dependence of reflectivity on the incidence angle of the optical excitation, i.e.,  $R = f(\varphi)$ , has a sharp minimum at the resonance angle  $\varphi_0$ , which indicates that SPP launching along the interface is successful. This behavior, represented in Fig. 2.33, is named SPP resonance.

The sharp reflectivity decrease at SPP launching is the basic concept for label-free sensing in biomedical sciences (Englebienne et al. 2003). The decrease in reflectivity at the SPP resonance occurs when an additional molecular layer is deposited on a metal surface, for example. Because the reflectivity change is extremely sensitive to any variation of the thickness/conditions at the interface, SPP resonance measuring is one of the most advanced techniques to measure DNA hybridization, enzyme–substrate interactions, and other biomolecular processes, such as the real-time kinetics of biomolecules.

A typical configuration of an SPP label-free biosensor is illustrated in Fig. 2.34 (Iwasaki et al. 2006). Here, the incident angle of the optical excitation through the prism,  $\varphi_0$ , is not varied, but the thickness and/or the refractive index of the sensing layer varies as more and more biomolecules are captured on it. As a result, the

**Fig. 2.33** The plasmonic resonance behavior

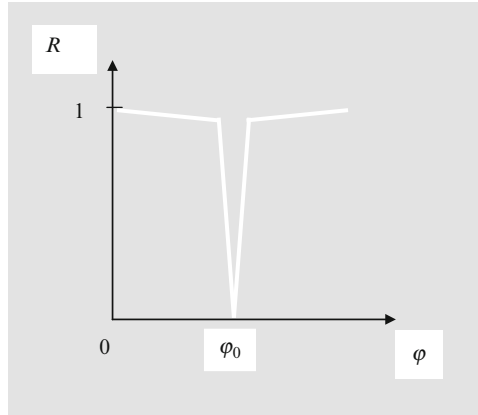
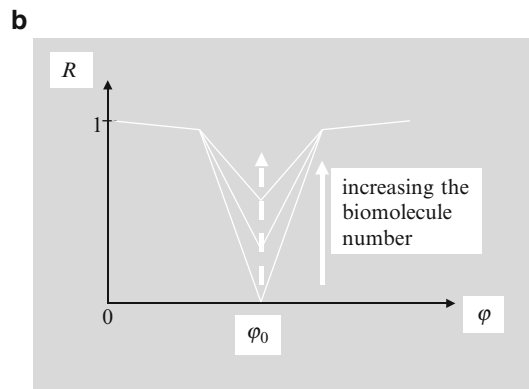
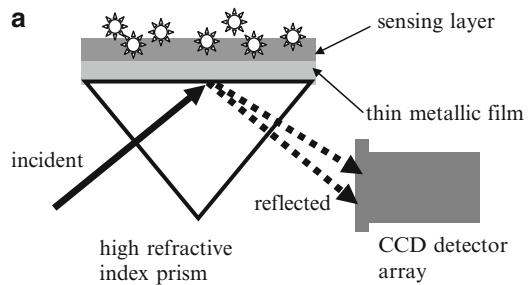


**Fig. 2.34 (a)** Typical configuration of an SPP label-free biosensor and **(b)** the SPP resonance variation with the number of immobilized biomolecules



resonant reflectivity modifies significantly, even when few molecules are attached to the sensing layer.

The model of a three-layer system (prism, metal, sensing layer) is used to understand the SPP label-free sensor. In this model, the variations in the SPP resonance angle can be written as

$$\Delta\phi = \alpha_1\Delta n + \alpha_2\Delta t, \tag{2.83}$$

where  $\alpha_1$  and  $\alpha_2$  are constant parameters. For example, when proteins bind to the sensing layer, the effective refractive index changes as

$$\Delta n = (n^2 + 2)^2 [(n_w^2 - 1)/(n_w^2 + 2)(V/V_{\text{tot}}) - (n^2 - 1)/(n^2 + 2)] (\Delta t/t)/6n, \quad (2.84)$$

where  $n$  and  $V$  are the refractive index and volume, respectively, of the protein;  $n_w$  and  $V_w$  are the corresponding parameters for water; and  $V_{\text{tot}} = V + V_w$ . The modification of the SPP resonance angle is expressed in resonance units (RU):  $10^3$  RU corresponds to a change of this angle with 0.1 degrees caused by biomolecules with a mass concentration of  $1 \text{ ng/cm}^{-2}$  immobilized on the sensing layer.

The sensitivity of SPP sensors is defined as the first derivative of the monitored parameter (angle, wavelength) with respect to the measured parameter (refractive index, thickness, concentration, etc.). When the sensitivity is expressed as a change in the angle of incidence as a function of the refractive index, it is measured in RIU (refractive index unit). Typically, the sensitivity of SPP sensors excited in a prism configuration is higher than of those based on gratings. The maximum resolution obtained with these configurations is about  $3 \times 10^{-7}$  RIU, higher resolutions, of the order of  $10^{-8} - 10^{-9}$ , being achievable in an SPP sensor integrated with an interferometer, for example, a Michelson interferometer (Yuan et al. 2006). New trends in instrumental design for SPP-based biosensors are reviewed in (Abbas et al. 2011).

SPP sensing of biomolecules, food quality, and environmental change is an area with huge applications (Shankaran et al. 2007). For instance, the SPP immunosensor is based on antigen–antibody recognition of various analytes, which is taking place at the metal–dielectric interface and so changes the reflectivity curve of the SPP sensor. An SPP immunosensor is displayed in Fig. 2.35. This SPP sensor works in a simple way, i.e., the antibodies are immobilized on the gold surface. Then, when an

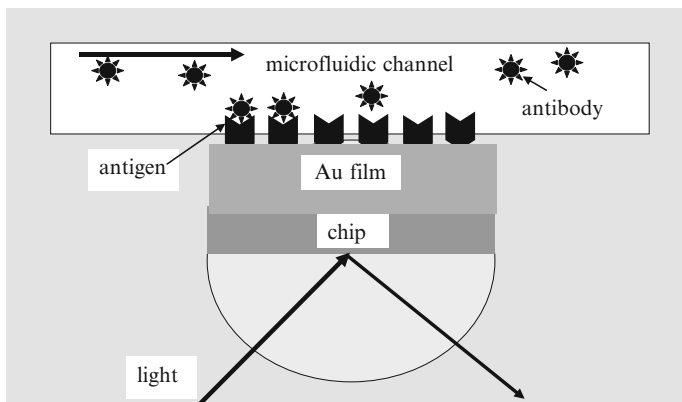


Fig. 2.35 The SPP immunosensor

analyte/antigen binds to the antibody, a change of the refractive index of the surface is taking place, and thus, the SPP resonance is shifted. As shown in Fig. 2.35, the SPP is integrated with a microfluidic channel because the majority of antigens are in solution. The net advantage of this sensor is a label-free sensing mechanism. Using such SPP sensors, very low quantities of hemoglobin (50 ppb), BSA (100 pM), and Tropotin I (2.5 ppb), which is a cardiac marker protein, were detected and reported in Shankaran et al. (2007) and the references therein. Very recently, the change in cell volumes directly grown on a gold layer was detected with SPP technique via the SPP resonance shift (Robelek and Wegener 2010), demonstrating again that SPP is a very powerful technique for label-free sensing.

There are two categories of SPP immunoassays. In the heterogeneous immunoassay, an antibody or antigen is first immobilized on the interface, and a further binding with the analyte occurs at the interface. This category of SPP immunosensor, which is by far the most widespread, is depicted in Fig. 2.35. In the other, homogenous assay, the biochemical reaction takes place in solution. There are also other SPP assays, such as direct assays, sandwich assay, displacement assays, all able to detect biomolecules or biochemical reaction in real time.

There is another type of SPP resonance, termed as localized surface plasmon (LSP), which refers to coherent charge density oscillations on metallic nanoparticles and other metallic nanostructures. LSP manifests at a certain wavelength as the result of light excitation of nanoparticles, and the resonance produces increased light scattering, intense absorption bands, and local field enhancement (Hutter and Fendler 2004).

The LSP resonance and the associated effects (scattering, absorption, and field enhancement) are influenced by the shape and size of the metallic nanostructures. The interaction with light of spherical particles is described by the Mie theory, which is based on the assumption that the nanoparticles and the surrounding medium are homogeneous and have associated permittivity function  $\epsilon_m = \epsilon'_m + i\epsilon''_m$  and  $\epsilon_d$ , respectively. Assuming that the excitation wavelength  $\lambda_{\text{exc}} \gg D = 2R$ , where  $R$  is the radius of the spherical nanoparticles and  $D$  their diameter, and that the induced polarizability is  $P = \alpha E$  where

$$\alpha = 4\pi\epsilon_0 R^3 (\epsilon_m - \epsilon_d) / (\epsilon_m + 2\epsilon_d), \quad (2.85)$$

is the polarizability factor, the LSP resonance occurs when

$$\epsilon'_m = -2\epsilon_d. \quad (2.86)$$

This resonance condition, termed Frohlich condition, is analogous to that of SPP and implies that the real parts of the permittivities of nanoparticles and the dielectric medium must have opposite signs. The LSP resonance is illustrated in Fig. 2.36.

The extinction coefficient (encompassing both absorption and scattering) of a thin dielectric film containing spherical metallic particles with a radius  $R$  much smaller than the excitation wavelength  $\lambda_{\text{exc}}$  and density per unit area  $N$  is

$$\sigma_{\text{ext}} = 24\pi NR^3 \epsilon_d^{3/2} [\epsilon''_m / (\epsilon'_m + 2\epsilon_d)^2 + \epsilon''_m{}^2] / \lambda_{\text{exc}} \ln(10). \quad (2.87)$$

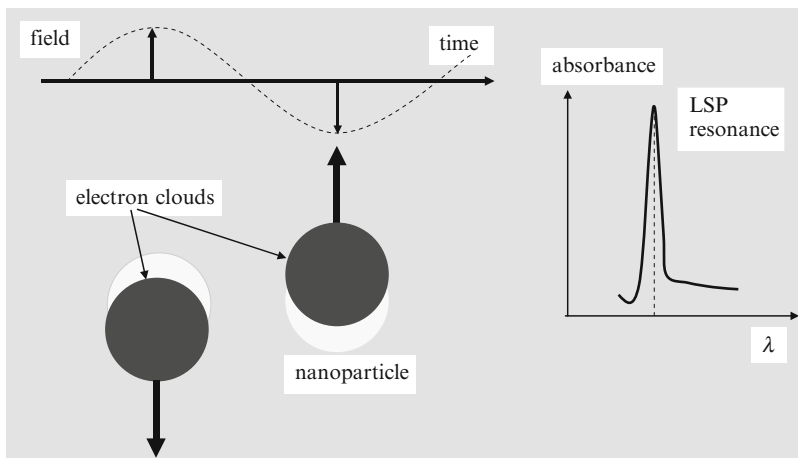


**Fig. 2.36** The generation mechanism of LSP resonance and a typical absorption spectrum

The LSP resonances of an isolated metallic sphere occur at the frequencies

$$\omega_l = \omega_p [l / (2l + 1)]^{1/2}, \quad (2.88)$$

where  $l = 1, 2, 3, \dots$  and  $\omega_p = (N_{el}e^2/m\varepsilon_0)^{1/2}$  is the plasma frequency corresponding to a concentration  $N_{el}$  of free electrons per unit volume with mass  $m$ . Because no particle size enters the above equation, a dielectric permittivity dependence on the size of various nanomaterials such as spheres, cylinders, etc., is imposed. Although, strictly speaking, the Mie theory holds for noninteracting spherical nanoparticles only, it can be generalized to nanomaterials with other shapes (needle-like, elliptical, cylindrical, etc.), which display a strong dependence of the LSP resonance on size and show multiple resonances.

As in the case of SPP, an LSP sensor could be a simple glass plate, in which multiple light reflections occur, covered with gold nanoparticles [Hamamoto et al. 2006](#). A photodetector which measures the LSP resonance and a CDD camera to monitor the reflection are other two components necessary for this LSP sensor, as illustrated in [Fig. 2.37](#).

Besides single nanoparticles or arrays of nanoparticles organized in various shapes, metallic nanowires support also LSP. The electromagnetic response of the nanowire is caused mainly by dipole moments. Assuming that the metallic nanowire has a length  $L \cong \lambda_{exc}$ , diameter  $D$ , and radius  $R \ll \lambda_{exc}$ , such that  $R$  is comparable to the skin depth in the metal, the polarization around the first LSP resonance  $L = \lambda_{LSP}/2$  induced by the electric field  $E$  parallel to the nanowire is

$$d_E = (1/3)[LR^2 f(\Delta)E\varepsilon_m] \times [1 + f(\Delta)\varepsilon_m L^2 \ln(1 + L/D) \cos \Omega/D^2], \quad (2.89)$$

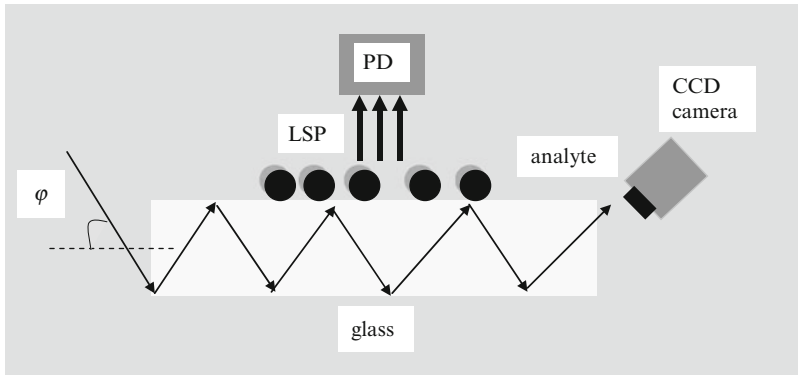


Fig. 2.37 The LSP sensor

where  $\Delta = R(2\pi\sigma_m\omega)^{1/2}/c$ ,

$$\Omega^2 = (Lk_0/2)^2[\ln(L/D) + iLk_0/2]/\ln(1 + L/D),$$

$f(\Delta) = [(1-i)/\Delta] \times J_1[(1+i)\Delta]/J_0[(1+i)\Delta]$ , and  $\sigma_m$  is the metal conductivity.

The applications of label-free sensors based on SPP in nanoparticles are reviewed in (Stewart et al. 2008). For example, changes which appear in the extinction of a nanoparticle film can be used to detect a target DNA or a protein. Simple methods, such as separate immobilization of two nucleotide fragments, A' and B', on 13-nm gold nanoparticles to form two probes, which are able to hybridize and aggregate in the presence of a target complementary nucleotide, denoted by AB, are used. The sensor is similar to those discussed above and is able to detect DNA targets at picomolar concentrations, up to femtomolar concentrations [see (Stewart et al. 2008) and the references therein]. The SPP is used also to improve the sensitivity of microarrays, which consist of immobilized biomolecules such as DNA or proteins deposited as drops of 10–500  $\mu\text{m}$  in size on a substrate, and further used to bind targets such as DNA, through hybridization, or proteins via ligand–receptor bindings for multiple detection processes. Using gold nanoparticles to label the captured DNA targets, a target signal is enhanced by silver amplification via electroless reduction of Ag ions on the surface of the Au nanoparticles. Femtomolar concentrations of target sequence in human genomic DNA can thus be detected without previous PCR amplification. Similar arrangements are used to detect the multiplexed genotyping in human genome without target amplification or real-time intracellular imaging of biomarkers in living cells. The reader must recognize how sensitive is a label-free sensor based on SPP in nanoparticles. There are many other label-free biosensors based on optical principles, such as optical resonators based on whispery gallery modes or miniaturized optical interferometers; for recent reviews, see (Fan et al. 2008; Hunt and Armani 2010).

## 2.5 Nanoelectronic Noses and Various Disease Detection

Nanoelectronic noses are gas sensors arranged into an array and able to detect an odor fingerprint, which is further identified by a signal processing unit. The nanoelectronic noses have important applications in a very large area of applications encompassing food quality control, landmine detection, or health screening (Strike et al. 1999; Arshak et al. 2004). The electronic noses were used before many nanotechnologies have appeared and are based on metal oxides, conducting polymers, surface acoustic devices, quartz microbalances, FETs, and many other principles. Odorant molecules are small, hydrophobic, have a molecular mass of about 350 Da and are a mixture of hundreds of chemical species. The detection limit for an odorant molecule is few parts per trillion, and thousands of odors can be detected. The nanomaterials have extended the nanoelectronic nose sensitivity, due to their large surface-to-volume ratio and miniaturization possibility. A simple schematic representation of a nanoelectronic nose is presented in Fig. 2.38.

A typical structure of a gas sensor is presented in Fig. 2.39. The gas molecules are sensed by changes in time in the electrical resistance (or conductance) or by the conductance dependence on variations of an electrical gate. Presently, CNTs are the most used nanostructures for gas sensing applications (Zhang et al. 2008). When molecules able to extract electrons, such as  $\text{NO}_2$  or  $\text{O}_2$ , and molecules

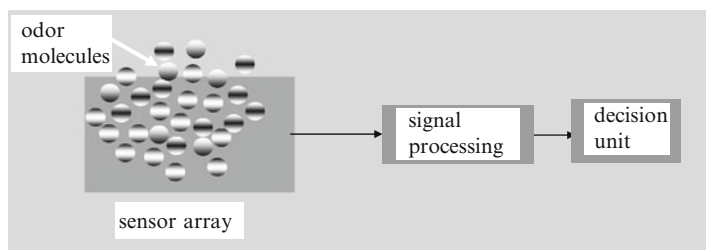


Fig. 2.38 A nanoelectronic nose

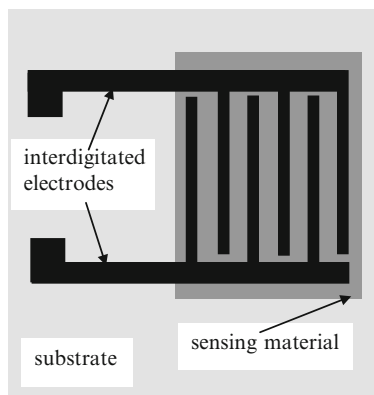
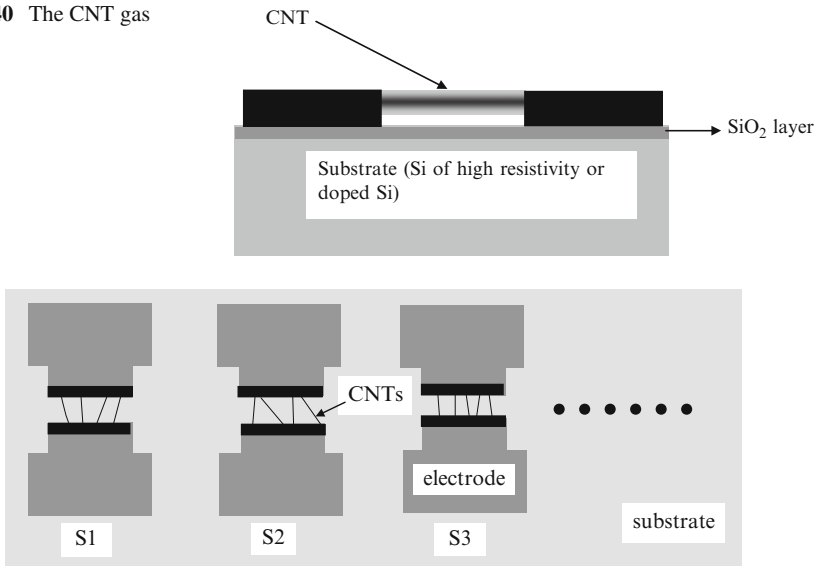


Fig. 2.39 The typical configuration of the gas sensor

**Fig. 2.40** The CNT gas sensor



**Fig. 2.41** CNT gas sensing array

that donate electrons, such as  $\text{NH}_3$ , interact with native *p*-type CNT, they change the charge carrier density in the CNT and, accordingly, the conductance of the CNT. This mechanism is applicable whether we are dealing with pristine CNTs or functionalized CNTs. A typical CNT gas sensor is displayed in Fig. 2.40.

If the substrate is high-resistivity Si, the above devices are termed as chemiresistors. On the contrary, if the substrate is doped Si, it acts as a gate, and the entire device works as a FET transistor; therefore, it is called chemFET.

The sensitive material could be a single CNT between contacts, a bundle, but in the majority of cases, it is a CNT thin film, termed also as CNT network. In 2000, the first gas sensor containing a single semiconducting CNT was demonstrated (Kong et al. 2000) at room temperature. The chemFET was of *p*-type and the conductance changed several orders of magnitude in time intervals of few seconds after exposure to  $\text{NH}_3$  and  $\text{NO}_2$ . Similar works have started using various gases and using either single CNTs, CNT networks, single sensors, or arrays of sensors, as in Fig. 2.41 (Qi et al. 2003). In this figure, S1, S2, S3 denote three sensors. Alcohol vapors, dimethyl methylphosphonate, and other gases were detected in sub-ppm concentration using these CNT gas sensors.

A much simple solution was adopted by drop-casting single-walled CNTs diluted in dimethylformamide (DMF) onto interdigitated gold electrodes. This type of sensor had a linear response from ppb up to ppm levels, with detection limits of 262 ppb for nitrotoluene and 44 ppb for  $\text{NO}_2$  (Li et al. 2003). The modern versions of such CNT gas sensors use CNT inks and print directly the sensor on a flexible substrate. Other types of CNT gas sensors are possible, such as chemicapacitors,

or even microwave resonators covered with CNTs and which experience a resonant frequency shift when gas is detected. CNT-coated surface acoustic wave (SAW) devices and other types of devices are used to sense gases when covered with CNT.

The functionalization of CNT, which was explained in Chap. 1, confers to CNT gas sensors the necessary selectivity to detect a certain gas from a mixture of gases. A simple example is the noncovalent drop cast of Nafion or polyethylenimine (PEI) on single-walled CNT chemFETs, which improves the gas sensing and selectivity of these sensors to  $\text{NO}_2$  and  $\text{NH}_3$  (Qi et al. 2003). ChemFETs based on single-walled CNT and functionalized with PEI were able to detect 1 ppb of  $\text{NO}_2$  and were insensitive to  $\text{NH}_3$ . The same device functionalized with Nafion was very sensitive to  $\text{NH}_3$  and insensitive to  $\text{NO}_2$ . PEI is used frequently to functionalize CNT gas sensors because it changes CNT conduction from native *p*-type to *n*-type. Nanoparticles deposited on the CNT surface confer to CNT the possibility to work at higher temperatures and harsh environments. In principle, Pd nanoparticles are used for  $\text{H}_2$  detection and gold nanoparticles for  $\text{NO}_2$  detection. The recovery of such sensors is done either by UV exposure or by heating, using a resistor film placed beneath the device.

The exhaled breath components contain tens of gases, which indicate certain diseases. For example, nitric oxide (NO) fluctuation is a relaxant of the blood vessel, and its concentration indicates heart problems before any clinical symptom. NO is also a neurotransmitter and is the mediator of immune system to pathogens. Also, changes in the concentration of NO signal neuron death and the Alzheimer disease. The high level of NO is a fingerprint of asthma. So, NO is an indicator of many diseases. A normal person exhales about 6–16 ppb of NO, while an asthmatic person exhales 34–50 ppb of NO. NO detection was recently performed (Kuzmych et al. 2007) using a functionalized CNT FET, with the impressive detection limit of 5 ppb at 30% relative humidity. The CNT FET used a network of CNTs covered by PEI, as indicated in Fig. 2.42. The detection limit of NO was studied under similar conditions as in breath, i.e., in the presence of  $\text{O}_2$ ,  $\text{H}_2\text{O}$  (humidity), and  $\text{CO}_2$ . It was found that  $\text{O}_2$  does not influence the detection limit, the relative humidity should be in the 15–30% range for optimal detection, and  $\text{CO}_2$  deteriorates the detection limit up to 10–15 ppb. A similar configuration can be used to detect the nonpolar volatile

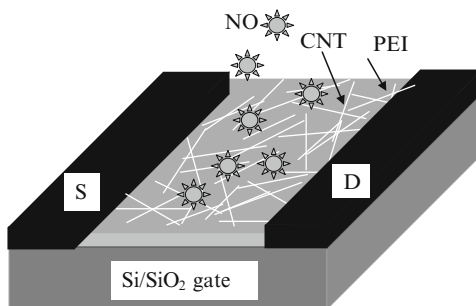
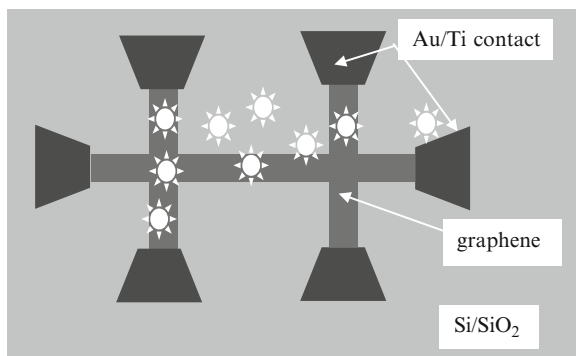


**Fig. 2.42** The detection of exhaled NO

**Fig. 2.43** Graphene Hall constriction (done by oxygen plasma etching) acting as a gas sensor



organic compounds of lung cancer using a random network of functionalized CNTs drop cast on interdigitated electrodes (Zilberman et al. 2010).

The ultimate detection limit could be obtained using graphene gas sensors. Graphene gas sensors are able to detect even a single molecule of gas attached or detached from the graphene surface (Schedin et al. 2007). The changes in graphene resistivity are about +4% for  $\text{NH}_3$ , -4% for  $\text{NO}_2$ , or -1% for  $\text{H}_2\text{O}$  after 200 s, all gases having a concentration of 1 ppm.

The graphene sensor has the shape of a Hall bar (see Fig. 2.43), and thus, Hall measurements have shown that  $\text{NH}_3$ , CO, and ethanol are donors, and  $\text{NO}_2$ ,  $\text{H}_2\text{O}$ , and iodine are acceptors. Although chemical doping induces impurities in graphene, these are kept at a relative low level, since no significant changes of mobilities were observed even beyond carrier densities greater than  $10^{12} \text{ cm}^{-2}$ . The detection limit of this sensor is 1 ppb, meaning a variation of graphene resistivity of  $\Delta\rho/\rho \propto 10^{-4}$ . Using few graphene layers to decrease the contact resistance around  $100 \Omega$ , the changes in adsorption and desorption of a single  $\text{NO}_2$  molecule were monitored using Hall resistivity; a difference in the resistance of about  $2.5 \Omega$  was recorded each time when an electron was adsorbed or detached from graphene. In this way, the detection sensitivity is of only a single molecule, but this implies complicated measurement procedures. In reality, for normal electronic noses, sensitivities of few parts per billion are easily obtained with a sensor made from a graphene monolayer with two metallic contacts, in which current flow is monitored. The functionalization of graphene with various sequences of ssDNA enables sequence-dependent detection and chemical recognition capability; hundreds of distinct sensor responses can thus be engineered, and electronic nose behavior becomes possible (Lu et al. 2010).

Lung cancer can be detected in exhaled breath using volatile organic compounds (VOCs), which in healthy breath are in concentrations of 1–20 ppb, while in the case of cancer, their concentrations increase up to 100 ppb. In fact, there are 42 VOCs used as markers (Peng et al. 2009). An array of nine cross-reactive chemiresistors is used to detect a variety of odorants, which are relevant for lung cancer. The chemiresistor is based on assemblies of 5-nm gold nanoparticles functionalized with

different organic substances and drop cast onto circular interdigitated electrodes. The variation of electrical resistance is monitored during the breath and linked with the concentrations of VOCs beyond which an early warning is triggered. Other diseases, such as diabetes, lung, breast, colorectal, and prostate cancers, are also detected via exhaled breath (Peng et al. 2010). Detection of VOCs is performed in this case by a nanoarray of functionalized nanoparticles, which are able to discriminate between VOC levels in the breath of healthy and ill patients. The sensors were implemented by successive drop-casting solutions of nanoparticles modified with different molecules on ten pairs of Ti/Au interdigitated electrodes

## References

- Abbas A., Linman MJ, Cheng Q (2011) New trends in instrumentation design for surface plasmon resonance-based sensors. *Biosensors Bioelectronics* 26:1815–1824
- Akeson M, Branton D, Kasianowicz JJ, Brandin E, Deamer DW (1999) Microsecond time scale discrimination among polycytidylic acid, polyadenylic acid and polyuridylic acid as homopolymers or as segments with single RNA molecules. *Biophys J* 77:3227
- Arshak K, Moore E, Lyons GM, Harris J, Clifford S (2004) A review of gas sensors employed in electronic nose applications. *Sensor Rev* 24:181–198
- Atashbar MZ, Bejcek BE, Singamaneni S (2006) Carbon nanotube network-based biomolecule detection. *IEEE Sensors J* 6:524–528
- Barnes WL (2006) Surface plasmon-polariton length scales: a route to sub-wavelength optics. *J Phys A* 39:S87–S93
- Boisen A, Dohn S, Keller SS, Schmid S, Tenje M (2011) Cantilever-like micromechanical sensors. *Rep Prog Phys* 74:036101
- Burg TP, Godin M, Knudsen SM, Schen W, Carlson G, Foster JS, Babcock K, Manalis SC (2007) Weighing of single cell and single nanoparticles in fluid. *Nature* 446:1066–1069
- Capobianco JA, Shih W-H, Leu J-H, Lo GC-F, Shih WY (2010) Label free detection of the white spot syndrome virus using lead magnesium niobate-lead titanate piezoelectric microcantilever sensors. *Biosensors Bioelectronics* 26:964–969
- Chand A, Viani MB, Scaffer TE, Hansma PK (2000) Microfabricated small metal cantilever with silicon tip for atomic force microscopy. *J Microelectromech Syst* 9:112–116
- Chen Y, Wang X, Hong MK, Rosenberg CL, Reinhard BM, Erramilli S, Mohanty P (2010) Nanoelectronic detection of breast cancer biomarker. *Appl Phys Lett* 97:233702
- Cui Y, Zhong Z, Wang D, Wang WU, Lieber CM (2003) High performance silicon nanowire field effect transistor. *Nano Lett* 3:149–152
- Dekker C (2007) Solid-state nanopores. *Nat Nanotechnol* 2:209–215
- Dequesnes M, Rotkin SV, Aluru NR (2002) Calculation of pull-in voltages for carbon-nanotube-based nanoelectromechanical switches. *Nanotechnology* 13:120–131
- Dragoman M, Dragoman D (2008) Plasmonics: applications to nanoscale terahertz and optical devices. *Progr Quantum Electronics* 32:1–48
- Dragoman M, Dragoman D (2009) *Nanoelectronics. Principles and devices*, Artech House, Boston
- Englebienne P, van Hoonacker A, Verhas M (2003) Surface plasmon resonances: principles, methods and applications in biomedical sciences. *Spectroscopy* 17:255–273
- Eom K, Park HS, Yoon DS, Kwon T (2011) *Phys Rep* 503:115–163
- Fan X, White IM, Shopova SI, Zhu H, Sutter JD, Sun Y (2008) Sensitive optical biosensors for unlabeled targets: a review. *Anal Chim* 620:8–26
- Garaj S, Hubbard W, Reina A, Kong J, Branton D, Golovchenko JA (2010) Graphene as a subnanometre trans-electrode membrane. *Nature* 467:190–194

- Gracheva ME, Aksimentiev A, Leburton J-P (2006) Electrical signatures of single-stranded DNA with single base mutations in a nanopore capacitor. *Nanotechnology* 17:3160–3165
- Gruner G (2006) Carbon nanotube transistors for biosensing applications. *Anal Bioanal Chem* 384:322–335
- Gupta A, Akin D, Bashir R (2004) Single virus particles mass detection using microresonators with nanoscale thickness. *Appl Phys Lett* 84:1976–1978
- Hansen KH, Ji H-F, Wu G, Datr R, Cote R, Mujumdar A, Thundat T (2001) *Anal Chem* 73:1576–1571
- Harris JGE, et al. (1996) Fabrication and characterization of 100 nm-thick GaAs cantilevers. *Rev Sci Instrum* 67:13591–3593
- Hamamoto K, Micheletto R, Oyama M, Umar AA, Kawai S, Y. Hutter E., Fendler JH (2004) Exploitation of localized surface plasmon resonance. *Adv Mater* 16:1685–1706
- Hunt HK, Armani AM (2010) Label-free biological and chemical sensors. *Nanoscale* 2:1544–1559
- Hutter E, Fendler JH (2004) Exploitation of localized surface plasmon resonance. *Adv Matter* 16:1685–1706
- Ilic B, Craighead HG, Krylov S, Senaratne W, Ober C, Neuzil P (2004a) Attogram detection using nanoelectromechanical oscillators. *J Appl Phys* 95:3694–3703
- Ilic B, Yang Y, Craighead HG (2004b) Virus detection using nanoelectromechanical devices. *Appl Phys Lett* 85:2604–2606
- Ivanov AP, Instuli E, McGilvery C, Baldwin G, McComb DW, Albrecht T, Edel JB (2011) DNA tunneling detector embedded in a nanopore. *Nano Lett* 11:279–285
- Iwasaki Y, Tobita T, Horiuchi, Seyama M (2006) Chemical sensors and surface plasmon resonance biosensors. *NTT Tech Rev* 4:21–29
- Kang BS, Pearton SJ, Chen JJ, Ren F, Johnson JW, Therrien RJ, Rajagopal P, Roberts JC, Piner EL, Linthicum KJ (2006) Electrical detection of deoxyribonucleic acid hybridization with AlGa<sub>N</sub>/Ga<sub>N</sub> high electron mobility transistors. *Appl Phys Lett* 89:122102
- Kang DS, Wang HT, Ren F, Pearton SJ (2008) Electrical detection of biomaterials using AlGa<sub>N</sub>/Ga<sub>N</sub> high electron mobility transistors. *J Appl Phys* 104:031101
- Kong J, Franklin NR, Zhou C, Chapline MG, Peng S, Cho K, Dai H (2000) Nanotube molecular wires as chemical resistor. *Science* 287:622–625
- Kowalczyk SW, Hall AR, Dekker C (2010) Detection of local protein structures along DNA using solid-state nanopores. *Nano Lett* 10:324–328
- Kuzmich O, Allen BL, Star A (2007) Carbon nanotube sensors for exhaled breath components. *Nanotechnology* 18:37502
- Lamoureux SK (2005) Casimir force: background, experiments, and applications. *Rep Prog Phys* 68:201–236
- Lee Y, Lee S, Seo H, Jeon S, Moon W (2008) Label-free detection of a biomarker with piezoelectric micro cantilever based on mass micro balancing. *J Assoc Lab Automation (JALA)* 13:259–264
- Li J, Lu Y, Ye Q, Cinke M, Han J, Meyyappan M (2003) Carbon nanotube sensors for gas and organic vapour detection. *Nano Lett* 3:929–933
- Li J, Stein D, McMullan C, Branton D, Azis MJ, Golovchenko JA (2001) Ion-beam sculpturing at nanometre length scale. *Nature* 412:166–169
- Liao Y-C, Lin M, Bao R, Cheng J, Bai Y, Liu Y, Qu, Wang KL, Huang Y, Duan X, High-speed graphene transistors with a self-aligned gate. *Nature* 467:305–308 (2010)
- Lu J.-Q, Zhang X-G (2008) Nucleotide capacitance calculation for DNA sequencing. *Biophys J* 95:L60–L62
- Lu Y, Goldsmith BR, Kybert NJ, Johnson ATC (2010) DNA-decorated graphene chemical sensors. *Appl Phys Lett* 97:083107
- Lu W, Lieber CM (2006) Semiconductor nanowires. *J Phys D* 39:R387–R406
- Lu W, Lieber CM (2007) Nanoelectronics from the bottom up. *Nat Mater* 6:841–850
- Lundstrom M, Guo J (2006) *Nanoscale transistors: device physics, modeling and simulation*, Springer, Heidelberg
- Moore GE (1995) Lithography and the future of the Moore Law. *Proc SPIE* 2437:2–17

- Ma L, Cockroft SL (2010) Biological nanopores for single-molecule biophysics. *ChemBioChem* 11:25–34
- Natori K (1994) Ballistic metal-oxide-semiconductor field effect transistor. *J Appl Phys* 76:4879–4890
- Mao S, Lu G, Yu K, Bo Z, Chen J (2010) Specific protein detection using thermally reduced graphene oxide sheet decorated with gold antibody conjugates. *Adv Mater* 22:3521–3526
- Nair PR, Alam MA (2007) Design considerations of silicon nanowire biosensors. *IEEE Trans Electron Dev* 54:3400–3408
- Nishio M, et al. (2005) Carbon nanotube oscillator toward zeptogram detection. *Appl Phys Lett* 86:133111
- Ohtake T, Hamai C, Uono T, Tabata H, Kawai T (2004) Immobilization of probe DNA on Ta<sub>2</sub>O<sub>5</sub> thin film and detection of hybridized helix DNA using IS-FET, Japanese. *J Appl Phys* 43:L1137–L1139
- Pearton SJ, Ren F, Wang Y-L, Chu BH, Chen KH, Chang CY, W. Lim, J. Lin, Norton DP (2010) Recent advances in wide bandgap semiconductor biological and gas sensors. *Progr Mater Sci* 55:1–59
- Patolsky F, Timko BP, Zhang GF, Lieber CM (2007) Nanowire-based nanoelectronic devices in life sciences. *MRS Bull* 32:142–149
- Peng G, Tisch U, Adams O, Hakim M, Shehada N, Broza YY, Billan S, Abdah-Bortnyak R, Kuten A, Haick H (2009) Diagnosing lung cancer in exhaled breath using gold nanoparticles. *Nat Nanotechnol* 4:649–673
- Peng G, Hakim H, Broza YY, Billan S, Abdah-Bortnyak R, Kuten A, Tisch U, Haick H (2010) Detection of lung, breast, colorectal and prostate cancers from exhaled breath using a single array of nanosensors. *Br J Cancer* 103:542–551
- Petersen KE (1978) Dynamic micromechanics on silicon; techniques and devices. *IEEE Trans Electron Devices* 25:1241–1249
- Qi P, Vermesh O, Grecu M, Javey A, Wang Q, Dai H, Peng S, Cho KJ (2003) Towards large arrays of multiplex functionalized carbon nanotube sensors for highly sensitive and selective molecular detection. *Nano Lett* 3:347–351
- Rahman A, Guo J, Datta S, Lundstrom MS (2003) Theory of ballistic nanotransistors. *IEEE Trans Electron Devices* 50:1853–1864
- Robelek R, Wegener J (2010) Label-free and time-resolved measurements of cell volume changes by surface plasmon resonance (SPR) spectroscopy. *Biosensors* 25:1221–1224
- Shankaran DR, Gobi KV, Miura N (2007) Recent advancements in surface plasmon resonance immunosensors for detection of small molecules of biomedical, food and environmental interest. *Sensors Actuators B* 121:158–177
- Schedin F, Geim AK, Morozov SV, Hill EW, Blake P, Katsnelson MI, Novoselov KS (2007) Detection of individual gas molecules adsorbed on graphene. *Nat Mater* 6:652–655
- Schneider GF, Kowalczyk SW, Calado VE, Pandraud G, Zandbergen HW, Vandersypen LMK, Dekker C (2010) DNA translocation through graphene nanopores. *Nano Lett* 10:3163–3167
- Schwierz F (2010) Graphene transistors. *Nat Nanotechnol* 5:487–496
- Skinner GM, van den Hout M, Broekmans O, Dekker C, Dekker NH (2009) Distinguishing single and double stranded nucleic molecules using solid state nanopores. *Nano Lett* 9:2593–2960
- Sorgenfrei S, Chiu C-Y, Gonzalez Jr RL, Yu YJ, Kim P, Nuckolls C, Shepard KL (2011) Label-free single-molecule detection of DNA-hybridization kinetics with carbon nanotube field-effect transistor. *Nat Nanotechnol* 6:126–132
- Shendure J, Ji H (2008) Next-generation DNA sequencing. *Nat Biotechnol* 26:1135–1145
- Shur MS (2002) Low ballistic mobility in submicron HEMTs. *IEEE Electron Device Lett* 23:511–513
- Sapmaz S, Blatner YaM, Gurevich L, van der Zant HSJ (2003) Carbon nanotubes as nanoelectromechanical systems. *Phys Rev B* 67:235414
- Stewart ME, Anderton CR, Thompson LB, Maria J, Gray SK, Rogers JA, Nuzzo RG (2008) Nanostructured plasmonic sensors. *Chem Rev* 108:494–521

- Storm AJ, Chen JH, Ling XS, Zandbergen HW, Dekker C (2003) Fabrication of solid state nanopores with single-nanometre precision. *Nat Mater* 2:537–540
- Stowe TD, Yasamura K, Kenny TW, Botkin D, Wago K, Rugar D (1997) Attonewton force detection using ultrathin silicon cantilevers. *Appl Phys Lett* 71:288–290
- Strike DJ, Meijerink MGH, Koudelka-Hep M (1999) Electronic noses – a mini-review. *Fresenius. J Anal Chem* 364:499–505
- Van der Spiegel J (2004) Advances in microelectronics – from microscale to nanoscale devices. In: Di Ventra M, Evoy S, Hefflin JR Jr (eds) *Introduction to nanoscale science and technology*, Kluwer Academic Publishers, Dordrecht 217–259
- Wang J, Lundstrom M (2003) Ballistic transport in high electron mobility transistors. *IEEE Trans Electron Dev* 50:1604–1609
- Wang Y-L, Chu BH, Chen KH, Chang CY, Lele TP, Papadi G, Coleman JK, Sheppard BJ, Dungen CF, Pearton SJ, Johnson JW, Rajagopal P, Roberts JC, Piner EL, Linthicum KJ, Ren F (2009) Fast detection of protozoan pathogen, *Perkinsus marinus*, using AlGaIn/GaN high electron mobility transistors. *Appl Phys Lett* 94:243901
- Wanunu M, Dadosh T, Ray T, Jin J, McReynolds L, Drndi M (2010) Rapid electronic detection of microRNAs using thin nanopore sensors. *Nat Nanotechnol* 5:807–814
- Xiang J, Wei L, Hu Y, Wu Y, Yan H, Lieber CM (2006) Ge/Si nanowire heterostructures as high performance field effect transistors. *Nature* 441:489–493
- Xu M, Fujita D, Hanagata N (2009) Perspectives and challenges of emerging single-molecule DNA sequencing technologies. *Small* 5:2638–2649
- Xuan G, Kolodzey J, Kapoor V, Gonye G (2005) Characteristics of the field-effect devices with gate oxide modification by DNA. *Appl Phys Lett* 87:103903
- Yang W, Thordarson P, Gooding JJ, Ringer SP, Braet F (2007) Carbon nanotubes for biological and biomedical applications. *Nanotechnology* 18:412001
- Yuan W, Ho HP, Wong CL, Kong SK, Lin C (2006) Surface plasmon resonance biosensor incorporated in a Michelson interferometry with enhanced sensitivity. *IEEE Sensor J* 7:70–73
- Zilberman Y, Tisch U, Shuster G, Pisula W, Feng X, Müllen K, Haick H (2010) Carbon nanotube/hexa-peri-hexabenzocoronene bilayers for discrimination between nonpolar volatile organic compounds of cancer and humid atmospheres. *Adv Mater* 22:4317–4320
- Zhang T, Mubeen S, Myung NV, Deshusses MA (2008) Recent progress in carbon nanotube-based gas sensors. *Nanotechnology* 19:332001
- Zhu S-E, R. Shabani, J. Rho, Y. Kim, B.H. Hong, J.-H. Ahn, H.J. Cho (2011) Graphene-based bimorph microactuators. *Nano Lett* 11:977–981
- Zwolak M, Di Ventra M (2005) Electronic signature of DNA nucleotides via transverse transport. *Nano Lett* 5:421–424
- Zwolak M, Di Ventra M (2008) Physical approaches to DNA sequencing and detection. *Rev Mod Phys* 80:141–165

## Chapter 3

# Imaging and Manipulation of Biomolecules

**Abstract** In this chapter, we present the main methods able to image and manipulate biomolecules, with the purpose of getting more information about their behavior. The main characterization tools related to nanotechnologies, such as the atomic force microscope and the scanning tunneling microscopy, will be presented in relation to biomolecule imaging and manipulation. Other applications will be presented as well.

The imaging of biomolecules and other biological entities is dominated by optical microscopy, fluorescence microscopy, confocal microscopy, and labeling with organic fluorophores, which are nanoparticles that emit light for in vivo analysis or in vitro detection. However, this subject is beyond the aims of this book. The reader interested in these subjects is advised to read the excellent review of [Roncali et al. \(2010\)](#). This chapter deals mainly with imaging methods directly linked to nanotechnologies

### 3.1 Bioapplications of Atomic Force Microscopy

The atomic force microscope (AFM) can detect very small forces, up to attonewtons ( $1 \text{ aN} = 10^{-18} \text{ N}$ ). These forces are applied between a cantilever ended with a tip and a surface that undergoes testing and are sensed via the cantilever deflection. Several principles can be used to measure the deflection of the cantilever, which has a very small mass, but by far, the most widespread is optical interferometry, which enables the sensing of displacements as small as  $10^{-4} \text{ \AA}$ .

The type of force detected by the AFM depends on the tip-sample distance, which dictates the interaction type between the tip and the sample. For example, interatomic forces prevail at very small tip-sample separations. These forces have two components: a short-range Born repulsive force, dominant at distances smaller than  $\leq 0.1 \text{ nm}$ , and a longer-range van der Waals force, which manifests up to  $10\text{--}15 \text{ nm}$ . As the tip-sample distance increases further, the exponentially decaying van der Waals force becomes negligible, and long-range electromagnetic,

electrostatic, magnetic, or capillarity forces determine the interaction between the tip and the sample.

The, generally attractive, Van der Waals force is strong enough to deflect the AFM cantilever at tip–sample distances of few nanometers. The van der Waals potential of two interacting molecules separated by a distance  $z$  has the following form:

$$U_{\text{vdW}} \approx -C_1/z^6, \quad (3.1)$$

where  $C_1$  is the London coefficient. For shorter tip–sample distances, the wave function of electrons situated at the cantilever tip overlaps the wave function of electrons on the sample surface, generating a significant repulsive Born force, with a potential

$$U_{\text{Born}} = C_2/z^{12}, \quad (3.2)$$

where  $C_2$  is a constant. The total intermolecular potential, called also Lennard-Jones potential, is then

$$U = C_2/z^{12} - C_1/z^6. \quad (3.3)$$

The AFM detects the sum of all repulsive and attractive forces acting between the tip and the sample.

At the macroscopic scale, the attractive van der Waals potential between two spheres with radius  $R$  and densities  $\rho_1$  and  $\rho_2$  is given by

$$U_{\text{vdW}} = -(AR/6z), \quad (3.4)$$

and the corresponding van der Waals force is then

$$F_{\text{vdW}} = -dU_{\text{vdW}}/dz = -AR/6z^2, \quad (3.5)$$

where  $A \propto \pi^2 C_1 \rho_1 \rho_2$  is the so-called Hamaker constant.

The repulsive force between macroscopic objects, called Hertz force or indentation force, can be approximated as the force on a sphere of radius  $R$  that is pushed against a flat surface and has the expression

$$F_{\text{Hertz}} = (K^2 R h_{\text{ind}}^3)^{1/2}, \quad (3.6)$$

where  $h_{\text{ind}}$  is the indentation depth.

The forces exerted between the tip and the sample has a key role in determining the various types of AFM operations. The three basic AFM operation modes, dynamical, static, and tapping modes, are displayed in Fig. 3.1.

In the *dynamical mode*, termed also as noncontact imaging mode or attractive force imaging, the tip of the cantilever makes no contact with the tested surface but is situated above it at all times during the scanning of the surface. The cantilever is driven by a piezoelectric actuator situated over it and vibrates mechanically at a frequency  $f$ . The vibrations of the AFM cantilever can be subjected either to frequency modulation (FM) or amplitude modulation (AM).

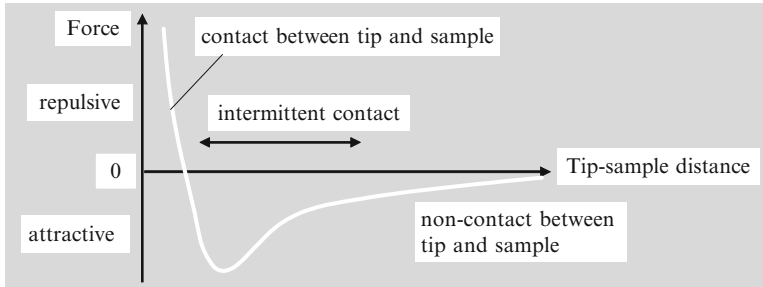


**Fig. 3.1** AFM modes of operation as a function of the tip–sample separation

In the FM mode, the interaction force between the tip and the sample modifies slightly the resonant cantilever frequency  $f_0$ , such that its shift  $\Delta f$  is proportional to the gradient of this force. The shift in frequency is then measured and the interacting force is calculated by integration. A two-dimensional distribution of this force is obtained by scanning the whole surface of the sample.

In the AM mode, the gradient of the force between the tip and the sample is proportional to the phase of the deflected signal and the cantilever amplitude, both parameters being controlled by a lock-in amplifier. Irrespective of the AFM dynamical modulation mode, a feedback signal preserves constant the frequency, amplitude, or phase of the oscillating cantilever.

In the *static mode*, termed as contact mode or repulsive mode, the cantilever makes direct contact with the sample, and the deflection of cantilever  $z(x, y)$  is induced by the weak repulsive force acting between the surface atoms and the atoms on the tip. In the contact operation mode, a feedback system maintains constant the force on the surface, and thus the deflection of the cantilever is preserved at a constant value of, generally, less than 0.1 nm. The surface topography  $z(x, y)$  is determined, with vertical and horizontal resolutions as small as 0.1 nm, by measuring the cantilever deflection. In this operating mode, the AFM responds to forces in the 10 nN–10 pN range, which is located between the hydrogen bonding force, of 10 pN, and chemical ionic bonding forces, of around 100 nN (Bhushan 2004).

In the contact mode, the surface topography is exposed at the atomic scale, such that individual atoms or clusters of few atoms can be discerned. Distinctive V-shaped cantilevers, as that displayed in Fig. 3.2, which reduce the lateral forces that could destroy the cantilever, must be used to achieve atomic resolution. These V-shaped cantilevers have a lower spring constant than an equivalent atomic spring constant of only  $0.04\text{--}1\text{ Nm}^{-1}$ . The equivalent atomic spring constant is determined from  $\omega^2 m \approx 10\text{ N m}^{-1}$ , corresponding to atoms bound to molecules or solid crystals that oscillate at 10 THz and have a mass of  $10^{-25}\text{ kg}$ . The AFM contact mode has some drawbacks, for example, some surfaces (e.g., biological surfaces) are destroyed as a result of direct contact with the cantilever tip, and strong lateral forces are produced by the capillarity of the thin water layer that is adsorbed at ambient temperature on any surface.

**Fig. 3.2** The static AFM mode

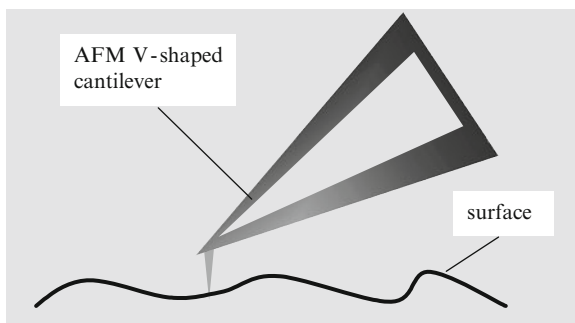
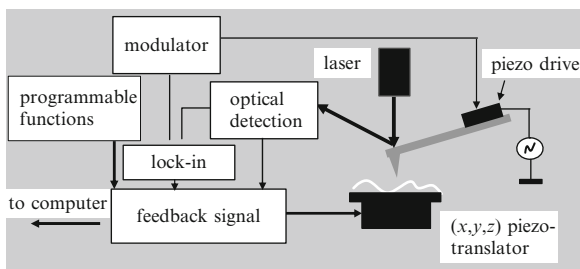


**Fig. 3.3** The block diagram of the AFM system



In the *tapping mode*, the cantilever touches periodically the sample. The cantilever is driven in resonant mechanical oscillation by a piezoelectric crystal, and any variation in amplitude or phase originating from the periodic tip–surface interaction is observed. More rigid cantilevers are used in this operation mode, with spring constants of  $20\text{--}70\text{ Nm}^{-1}$ , and higher oscillating amplitudes, of  $50\text{--}120\text{ nm}$ , are obtained. The amplitude of the tapping cantilever is usually monitored during the scanning of the surface under study, and a feedback system preserves a constant deflection at selected points on the surface by controlling the cantilever–surface distance. The feedback signal adjusts the movement of the cantilever along the vertical  $z$  direction for the duration of scanning in the  $(x,y)$  plane, so that a topographical image of the surface is finally obtained. An AFM block diagram, valid for all three modes of operation, is represented in Fig. 3.3.

There are several websites that host AFM images, which demonstrate the unprecedented capabilities of AFM “to see” atoms and surface structures of many materials, including biological materials. Two such websites are:

- (1) <http://www.jpik.com/afm.85.en.html>
- (2) [http://www.parkafm.com/AFM\\_gallery/gallery\\_main.php](http://www.parkafm.com/AFM_gallery/gallery_main.php)

The main component of an AFM system is the sensor, which detects the weak cantilever deflections reaching values below  $0.1\text{ nm}$  in the static mode, as discussed above. Because of their simplicity and effectiveness, the optical detection systems are the most widespread.

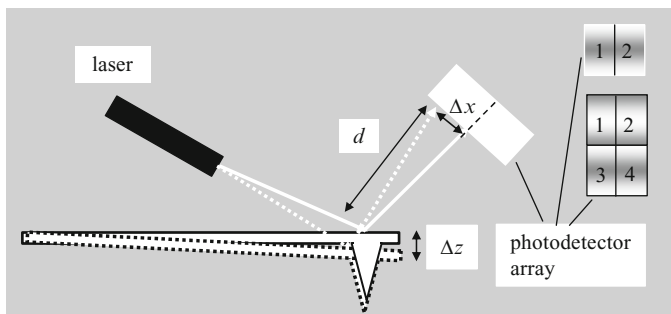


Fig. 3.4 The optical lever detection of AFMs

Optical interferometry techniques are among the most sensitive techniques ever known (Sarid 1994). The most common sensing part of an AFM is an optical lever, illustrated in Fig. 3.4, which measures the light deflected off the back of a vibrating cantilever with the help of a photodetector (PD) array consisting of two or four PDs. The signal difference between the PDs in the array is processed, amplified, and sent to the AFM feedback system.

If the sensing array consists of two PDs, the current difference between them is

$$\Delta I = I_2 - I_1 \propto L \Delta x \times N_0 \propto d \Delta z \times N_0 \quad (3.7)$$

where  $L$  is the length of the cantilever and  $N_0$  denotes the number of photons in the laser beam.

In the case of a sensing system with four PDs, which prevents the effects generated by the lateral forces that could damage the cantilever, the AFM computer is considering the following signals:

$$\Delta_{\text{normal force}} \propto [(I_1 + I_2) - (I_3 + I_4)], \quad (3.8a)$$

$$\Delta_{\text{lateral force}} \propto [(I_2 + I_4) - (I_1 + I_3)]. \quad (3.8b)$$

The sensitivity of the optical lever system is given by  $2WI_{\text{laser}}/\lambda$  ( $mW \text{ rad}^{-1}$ ), where  $I_{\text{laser}}$  and  $\lambda$  are the intensity and wavelength, respectively, of the laser, and  $W$  is the cantilever width.

The AFM resolution depends on the mechanical properties of the cantilever and on the tip geometry. The tip is generally fabricated by silicon or silicon nitride micromachining and has a pyramidal shape with high aspect ratio. Recently, CNTs with a diameter of a few nanometers, grown directly on a Si cantilever or attached on its pyramidal tip, are used as sharp AFM tips (Wilson and Macpherson 2009).

The AFM resolution is determined also by its mode of operation. For example, in the contact mode, two peaks are resolved at a minimum separation of  $2(D\Delta z)$  where  $D$  is the tip diameter and  $\Delta z$  is the minimum measurable depression of the AFM. Typically,  $D$  is 10–20 nm for Si tips and 5–6 nm for CNTs, whereas  $\Delta z$  is a

fraction of a nanometer so that the resulting resolution is of 2–5 nm. On the contrary, the resolution is  $0.8h$  in the noncontact mode, where  $h$  is the distance between the tip and the surface. Atomic resolution can be obtained when the AFM works at low temperatures and in high vacuum. The resolution worsens at ambient temperature because the tip must be well separated from the surface to avoid the attraction force of the superficial water layer.

Micromachining techniques can fabricate one million single-crystal cantilevers per square centimeter, all ended with a tip (Kawakatsu et al. 2002). The thickness and the length of these cantilevers are in the 30–100 nm and 0.5–200  $\mu\text{m}$  ranges, respectively. AFMs equipped with a huge number of cantilevers that work in parallel can save time when topographies of large surfaces are required.

By far, the most common AFM operation mode is the noncontact mode because:

- It has atomic resolution.
- It is nondestructive.

As already mentioned, the AFM in the noncontact mode can work in the frequency modulation, FM, or amplitude modulation, AM, modes. In the FM mode, the cantilever signal is shifted in phase with  $\Delta\varphi$  and is injected further into the piezoelectric actuator of the cantilever. The mechanical vibration of the cantilever is modulated in frequency, and the whole AFM loop system vibrates when the frequency  $f$  equals the resonant mechanical frequency of the cantilever  $f_0$ , if  $\Delta\varphi = \pi/2$ . A constant cantilever amplitude  $A$  is maintained by an automatic gain unit, which also memorizes frequency shifts. Denoting the tip–sample force gradient as  $F_{t-s}$ , the shift in frequency is

$$\Delta f = f_0(-\partial F_{t-s}/\partial z)/2K. \quad (3.9)$$

Atomic resolution surface imaging was obtained in the FM mode for a large number of materials of different kinds and even for single molecules.

In the AM mode, the cantilever is excited at a frequency  $f$ , equal or close to its mechanical resonance frequency  $f_0$ , and the feedback loop maintains the excitation amplitude constant. The signal determined by the cantilever deflection is measured and injected into a lock-in amplifier, which uses it as reference signal for the piezoelectric actuator. The output of the lock-in amplifier acts as the feedback signal for controlling the tip–sample distance, whereas the output phase of the amplifier is the detected parameter. The gradient of the tip–sample force is now given by

$$\partial F_{t-s}/\partial z = K(1 - A_0/A \cos \varphi), \quad (3.10)$$

where  $A_0$  is the free oscillation amplitude and  $A$  denotes the cantilever amplitude at frequency  $f$ .

The mechanical movement of the cantilever in the noncontact mode is treated as that of a damped harmonic oscillator, the deflection satisfying the equation

$$m_B d^2 z/d\tau^2 + \gamma dz/d\tau + Kz = F_{\text{appl}}, \quad (3.11)$$

where  $m_B$  is the mass of the cantilever and  $\gamma$  is the damping coefficient. Considering that  $F_{\text{appl}} = F \exp(i\omega\tau)$ , the displacement is  $z = A \exp(i\omega\tau)$ , and thus the frequency response of the cantilever is

$$A(\omega) = |F| / [\omega^4 + \omega^2(\gamma^2/m_B^2 - 2K/m_B) + K^2/m_B^2]^{1/2}. \quad (3.12)$$

Considering that  $\gamma = m_B\omega_0/Q$ , the modulus and the phase of the amplitude are, respectively,

$$|A(\omega)| = FQ\omega_0^2 / [\omega^2\omega_0^2 + Q(\omega_0^2 - \omega^2)]^{1/2}, \quad (3.13)$$

$$\varphi(\omega) = \arctan[\omega\omega_0/Q(\omega_0^2 - \omega^2)]. \quad (3.14)$$

The first natural resonance frequency is then

$$\omega_0 = 2\pi f_0 = (K/m_B)^{1/2}, \quad (3.15)$$

while the cantilever response is minimum at

$$\omega_{\min} = (\omega_0^2 - \gamma^2/2m_B^2)^{1/2}. \quad (3.16)$$

Equation (3.16) tells us that in the damped oscillator model, the frequency response of the cantilever differs from the natural frequency, the shift between these frequencies vanishing in the undamped case. Small cantilevers, with dimensions up to the order of microns, have much higher resonant frequencies ( $>500$  kHz in air) than larger cantilevers but comparable spring constants ( $<100$  mN m $^{-1}$ ).

The applications of AFM in biology are huge and are reviewed in [Le Grimmelc et al. \(2010\)](#). This reference provides also very nice images of various biomolecules. The AFM was first used for the imaging of soluble molecules such as DNA, with the aim of investigating their molecular structure ([Lyubchenko et al. 2011](#)). DNA–protein interactions and bindings between DNA polymerase with its DNA target, as well as the RNA polymerase with its DNA target are studied on bacteria such as *Escherichia coli* and on more complex structures. Images of proteins such as GroEL and GroES of *E. coli* were seen for the first time. The resolution was enhanced to 1 nm using a cryo-AFM ([Mou et al. 1996](#)). Peptides and small proteins, which are generating fibrils and/or amyloid deposits associated with the Alzheimer disease, are also studied with AFM ([Adamcik et al. 2010](#)). Biological membranes are the subject of intensive AFM studies ([Frederix et al. 2009](#)), as well as cell interactions with membranes ([Hilal et al. 2006](#)). Other applications of AFM in biology are cell imaging and the study of their mechanical properties and adhesion. In this way, it was determined that the Young modulus of cells is in the range 0.2–200 kPa depending on the cell type. These mechanical properties vary if various drugs are present or if the physiological conditions change. Ligand–receptor pair separation forces are measured as well with AFM. For example, this force is around 170 pN for avidin–biotin, 260 pN for streptavidin–biotin, etc. Not only biomolecules, cells and

other biological constituents are detected by AFM, but early detection of diseases such as the aging cartilage and osteoarthritis can be achieved with the help of the AFM (Stoltz et al. 2009).

## 3.2 Bioapplications of Scanning Tunneling Microscopy

Scanning tunneling microscopy (STM) is also able to offer images of surfaces  $z(x, y)$  with atomic resolution, including images of individual surface atoms. The STM technique relies on measuring the tunneling current between a sharp metallic tip separated from a conductive sample by nanometric distances. By applying a bias  $V$  between the tip and the sample, the electrons in the tip with energy  $E$  and mass  $m$  tunnel through a vacuum barrier of height  $\phi > E$  and arrive at the sample (see Fig. 3.5). At low voltages, the tunneling current density (Hansma and Tersoff 1987) is approximated as

$$i = V\rho_{\text{surf}}(E_F) \exp\{-2m(\phi - E)z/\hbar\} \propto V\rho_{\text{surf}}(E_F) \exp(-1.025\phi^{1/2}z) \quad (3.17)$$

where  $\rho_{\text{surf}}(E_F)$  is the density of states (DOS) of the sample at the Fermi edge and  $z$  is the tip-sample distance, i.e., the barrier width. The current drops with one order of magnitude if the width  $z$  of the barrier, with a height of 5 eV, changes with only 0.1 nm. In STM mode, the current variation is generally 2–3%, which implies that the gap changes with about 0.001 nm. Under these circumstances, the tunneling current maps the surface DOS. These considerations are accurate only in one dimension. In three dimensions, surface mapping by means of the tip-sample tunneling current is much more complex, and the full Tersoff–Hamann model must be applied to describe the STM (Hansma and Tersoff 1987). The main findings of this theory is that the tunneling current,

$$I(V) \propto \int_{E_F}^{E_F+eV} \rho(r, E)dE, \quad (3.18)$$

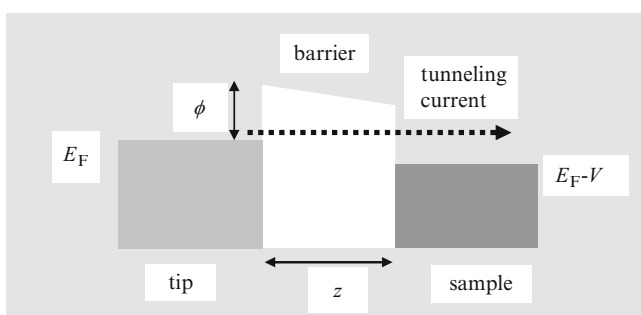
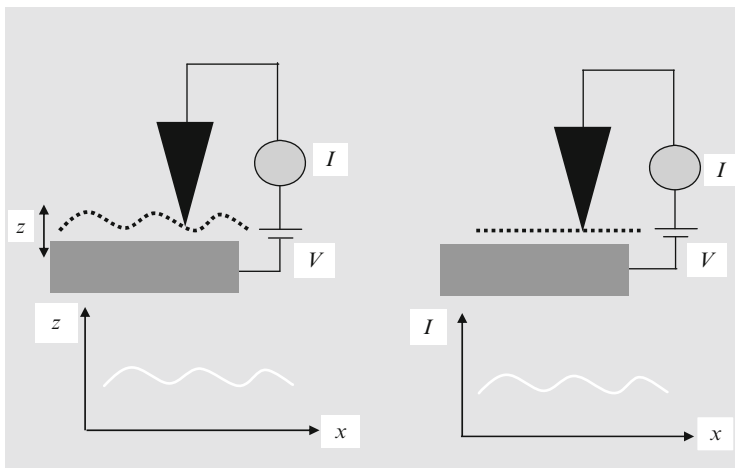


Fig. 3.5 The STM energy diagram



**Fig. 3.6** Schematic representation of the STM operation modes: (a) constant current mode and (b) constant height mode

depends on the local DOS (LDOS) in the sample,

$$\rho(r, E) = \sum_i |\Psi_i(\mathbf{r})|^2 \delta(E - E_i), \quad (3.19)$$

at the Fermi edge. In (3.18),  $\Psi_i(\mathbf{r})$  is the 3D wave function of the sample at energy  $E_i$ . From this equation, it follows that the normalized conductance obtained from the  $I - V$  curve, and defined as  $(dI/dV)/(I/V)$ , is proportional to the LDOS in the sample.

STM has two principal modes of operation, displayed in Fig. 3.6. In the constant current mode, the tunneling current is detected when the biased tip is located near the surface. The tip scans the surface of the sample, and any variation in the tunneling current is assessed by a feedback loop, which modifies the height  $z$  in order to keep the current constant. On the contrary, in the constant height mode, information on the surface is obtained by directly measuring the current as the tip scans the surface at a fixed height.

STM systems are working at room temperature and in normal atmospheric pressure, and are integrated with complicated signal processing units needed for calibrating the instrument and for removing the thermal noise. Other STM systems work at low temperatures (350 mK), in ultrahigh vacuum (UHV), and in high magnetic fields (11 T) because these extreme conditions grant an extremely high resolution and a clean environment necessary to investigate nanostructures and quantum processes. Examples of systems currently studied with STM in UHV and at low temperatures include liquid crystals, single molecules, DNA sequencing, LDOS of metals, superconductors, and semiconductors. STM can analyze the magnetic properties of some materials if equipped with magnetic tips, for instance, Fe tips.

In this situation, the spin-polarized tunneling current, which depends on the orientation of the magnetic moment of the tip, is measured in UHV conditions. There are also many STM image galleries, one of the richest being that provided by the company who invented the STM:

<http://almaden.ibm.com/vis/stm/catalogue.htm>

STM is intensively used in the sequencing of DNA using tunneling currents. The electronic properties of the four DNA bases were obtained using a UHV STM at room temperature (Xu et al. 2007). As mentioned also in Chap. 1, the experimental STM  $I$ - $V$  characteristics of the bases can be fitted with the expression (Dragoman and Dragoman 2009)

$$I(V) = V/R + aV^2 \exp(-b/V), \quad (3.20)$$

in which the first term in the right-hand side is the contribution of a series resistance  $R$ , which takes values between 500 and 1,000  $\Omega\text{m}$  for the four bases, and the last term is a typical Fowler–Nordheim contribution. The Fowler–Nordheim term describes field emission from a triangular barrier of height  $\phi_B$  in the presence of an applied electric field. Thus, DNA bases can be regarded as potential barriers for field-emitted electrons, their work function being determined from the relation

$$b = \frac{4L}{3e\hbar} (2m_0)^{1/2} \phi_B^{3/2}, \quad (3.21)$$

where  $L$  is the tip–sample distance in the STM measurements and  $m_0$  denotes the free electron mass. The average values of the work functions for  $L = 0.66$  nm obtained from data at positive and negative polarizations are  $\phi_A = 1.74$  eV,  $\phi_T = 1.81$  eV,  $\phi_C = 2.12$  eV, and  $\phi_G = 1.7$  eV for adenine, thymine, cytosine, and guanine, respectively. The electronic signatures of the DNA bases look like that of a Zenner diode.

Starting from this unique electronic signature of the four DNA bases, obtained with the STM, some developments were made toward STM sequencing of DNA bases. In this respect, (He et al. 2007) proposed to combine the nanopore tunneling with hydrogen-mediated molecular recognition. Each base in an ssDNA, which translocates by chemically functionalized electrons in a nanopore integrated with four reading heads for the identification of the four bases, is identified by a characteristic current–distance response. The electrical reading of the base pairing was demonstrated with a guanine functionalized STM probe by measurements of the tunneling current decay with distance, which is able to sense and discriminate the G–C from the G–T base pairs. Partial sequencing, i.e., the identification of the electronic signature of the G base only, was performed for a single DNA molecule using STM and an oblique pulse-injection method to deposit DNA on copper (Tanaka and Kawai 2009). In another work, the LDOS of ssDNA molecules formed by a poly(G)–poly(C) sequence of about 1  $\mu\text{m}$  in length and deposited on gold was resolved as a function of energy using the STM at cryogenic temperatures (Shapir et al. 2008).

### 3.3 Manipulation of Biological Materials

The imaging and manipulation of biomolecules, cells, and other biological materials are complementary and strongly related issues. In some cases, the AFM or STM can manipulate or arrange biomolecules or even cells (Rajagopalan and Saif 2011). But, as we will see below, there are special physical principles and experimental setups, circuits, and even equipments dedicated to this task. The main methods to manipulate, trap, and study the properties of various biological materials are dielectrophoresis or the use of optical tweezers.

Dielectrophoresis (DEP) refers to the generation of a lateral force exerted on any dielectric object, which could be a particle, a cell, DNA, etc., due to an applied inhomogeneous electric field. The time-average DEP force is given by

$$F_{\text{DEP}} = 2\pi\epsilon_m R^3 \text{CM}(\nabla E^2), \quad (3.22)$$

where  $\epsilon_m = \epsilon_0\epsilon_r$  is the permittivity of the surrounding medium,  $R$  is the radius of the dielectric object, CM is the Clausius–Mossotti factor that describes the polarizability of the particle,  $\nabla$  is the gradient operator, and  $E$  is the scalar amplitude of the electric field  $E$  expressed in rms. In a nonuniform electric field, a dielectric sphere becomes polarized, which is equivalent to generating an effective dipole moment  $p = kE$ , proportional to the applied field (see Fig. 3.7).

The DEP force can be expressed also as follows:

$$F_{\text{DEP}} = 4\pi\epsilon_m R^3 \left( \frac{\epsilon_p - \epsilon_m}{\epsilon_p + 2\epsilon_m} \right) (E \cdot \nabla) E, \quad (3.23)$$

since CM is given by

$$\text{CM} = \left( \frac{\epsilon_p - \epsilon_m}{\epsilon_p + 2\epsilon_m} \right), \quad (3.24)$$

in which  $\epsilon_p$  is the permittivity of the particle. A positive CM means that work is needed to pull out a dielectric particle from a high field region, while a negative CM means that work is required to drive the particle from a low field region to a region with high value of the electric field.

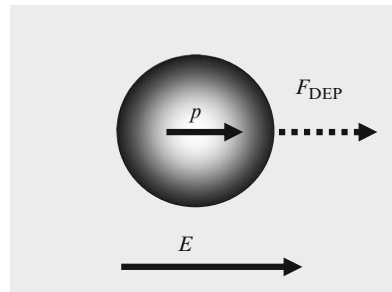


**Fig. 3.7** The dielectric sphere and its associated DEP force

The dielectric particle model applies in certain limits to bacteria, cells, and viruses because all of them contain mobile ions in their biological structures and are living in a conducting electrolyte (Pethig 2010). However, the dielectric permittivity of biological entities in an ac field is complex and given by

$$\varepsilon_p^* = \varepsilon_0 \varepsilon_p - i \sigma_p / \omega, \quad (3.25a)$$

the corresponding expression for conductivity being

$$\sigma_p^* = \sigma_p + i \omega \varepsilon_0 \varepsilon_p. \quad (3.25b)$$

The CM factor becomes also complex:

$$CM^* = \left( \frac{\varepsilon_p^* - \varepsilon_m^*}{\varepsilon_p^* + 2\varepsilon_m^*} \right), \quad (3.26a)$$

or equivalently,

$$CM^* = \left( \frac{\sigma_p^* - \sigma_m^*}{\sigma_p^* + 2\sigma_m^*} \right). \quad (3.26b)$$

At low frequencies, the current is due to the conduction of free carriers, while at high frequencies, the dielectric displacement current becomes predominant, and there is a  $\pi/2$  phase difference between the current and the applied electric field. Considering that the field is given by

$$E(r, t) = \text{Re}[E(r) \exp(i \omega t)], \quad (3.27)$$

the effective dipole moment can be written as

$$p(r, t) = \text{Re}[4\pi \varepsilon_m R^3 CM^* E(r) \exp(i \omega t)], \quad (3.28)$$

so that the DEP force is

$$F_{\text{DEP}}(t) = \text{Re}[p \exp(i \omega t)] \cdot \nabla \text{Re}[E \exp(i \omega t)]. \quad (3.29)$$

As a result, the time-average DEP force becomes

$$\langle F_{\text{DEP}} \rangle = 2\pi \varepsilon_0 \varepsilon_m R^3 \text{Re}[CM^*] \nabla |E|^2. \quad (3.30)$$

Below 50 kHz, we can use the approximation

$$\text{Re}[CM^*] \cong \varepsilon_m \left( \frac{\sigma_p - \sigma_m}{\sigma_p + 2\sigma_m} \right), \quad (3.31)$$

while beyond 50 MHz,

$$\text{Re}[\text{CM}^*] \cong \varepsilon_m \left( \frac{\varepsilon_p - \varepsilon_m}{\varepsilon_p + 2\varepsilon_m} \right). \quad (3.32)$$

Relation (3.31) is justified by the fact that at low frequencies, the DEP force is determined mainly by the conductive properties of the surrounding medium and the dielectric particles, and thus the conductivity is the prevailing mechanism of DEP. On the contrary, at high frequencies, the dielectric properties dominate, which is suggested also by (3.32), whereas at intermediate frequency values, between 50 kHz and 50 MHz, both conductive and dielectric properties are important.

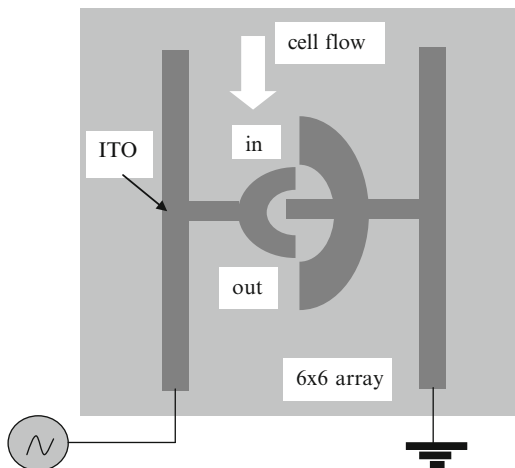
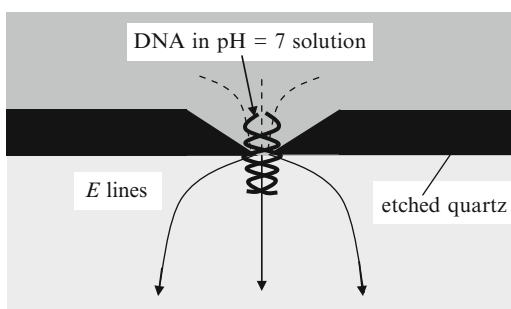
Most biological entities such as bacteria, viruses, or cells are not homogeneous dielectrics, as considered in the model presented above. This unfavorable situation is alleviated by using a multishell model. The multishell model can be simplified by assuming that the concepts of effective permittivity and conductivity still apply and by modeling cells as particles with a spherical shape. In particular, some cells, for example, the discoidal-shaped human erythrocyte, can be treated as single-shell spherical dielectric particles since they take a spherical form in cytoplasm. In this single-shell model, the permittivity of the dielectric particle becomes (Pethig 2010)

$$\varepsilon_p^* = \varepsilon_m^* \left[ \frac{\left( \frac{R}{R-d} \right)^3 + 2 \left( \frac{\varepsilon_{\text{cyt}}^* - \varepsilon_{\text{mem}}^*}{\varepsilon_{\text{cyt}}^* + 2\varepsilon_{\text{mem}}^*} \right)}{\left( \frac{R}{R-d} \right)^3 - \left( \frac{\varepsilon_{\text{cyt}}^* - \varepsilon_{\text{mem}}^*}{\varepsilon_{\text{cyt}}^* + 2\varepsilon_{\text{mem}}^*} \right)} \right], \quad (3.33)$$

where  $\varepsilon_{\text{cyt}}^*$  and  $\varepsilon_{\text{mem}}^*$  are the complex permittivities of the cell interior and plasma membrane, respectively,  $R$  denotes the outer radius of the cell and  $d$  is the thickness of the membrane.

The main application of DEP is to manipulate cells and to characterize biological entities, referred to also as soft matter, in suspensions. The implementation of DEP is made by micro-nanofabrication techniques, which consist mainly in the fabrication of various electrode shapes able to trap and manipulate cells. There is a multitude of substrates and electrode shapes for an efficient strong nonuniform electric field generation, such as interdigitated, interdigitated and castellated, spiral, sawtooth, etc. (Hölzel 2009). We present some examples of electrodes below. A planar interdigitated ring electrode (PIRE), which constitutes a cell in a  $6 \times 6$  array, is displayed in Fig. 3.8 (Hsiung et al. 2008).

The PIRE array is microfabricated on a glass substrate using standard micro-nanotechnologies and is integrated in a microfluidic device. The input gap has a width of  $10 \mu\text{m}$ , the output gap is  $15\text{--}\mu\text{m}$  wide, and the outer diameter is of  $125 \mu\text{m}$ . The  $6 \times 6$  array is able to trap a number of  $48 \pm 6$  cells when an ac signal of 5 V and a frequency of 5 MHz is applied. The electric field is nonuniform and spatially localized, being stronger in the central region of the PIRE. Adhesion of cells on the PIRE is promoted by collagen coating.

**Fig. 3.8** The PIRE electrode**Fig. 3.9** Electrodeless DEP of DNA

Nanogaps studied in the previous chapters can be used also for DEP. For example, 20-nm gold nanoparticles were manipulated using positive DEP in a nanogap with a width not exceeding 100 nm (Kumar et al. 2009). The applied signal in this case had a frequency of 1 MHz and an amplitude of 3 V. In this way, assemblies of nanoparticles can be generated. Moreover, a lab-on-chip can be created using DEP to separate cells with the help of a pair of embedded electrodes and an insulator hurdle. In this situation, the amplitude was 10 V and the frequency had a value of 200 kHz (Kang et al. 2009).

But not only planar metallic electrodes can be used for DEP but also dielectric constrictions (Chou et al. 2002). For instance, a 1- $\mu\text{m}$  gap between two etched quartz substrates, as shown in Fig. 3.9, can be used to DEP ssDNA and dsDNA molecules and to analyze their physical properties at low frequencies, of 200–1,000 Hz, when the peak-to-peak amplitude is 1 kV. In the geometry in Fig. 3.9, the force takes a maximum value not at the center of the gap but where the product between the electric field and its gradient is maximum.

Carbon nanotubes were used also as DEP electrodes with the aim of trapping short DNA molecules (Tuukkanen et al. 2006). The DEP was used as well to trap and determine the dielectric permittivity of isomated DNA. Experimental data show

that at low frequencies, DNA has a relative electrical permittivity of 80 and a conductivity of 54 mS/m, while the tobacco mosaic virus, for example, has a relative electrical permittivity of 55 at 20 MHz. The DNA DEP is reviewed in [Hölzel \(2009\)](#).

A variant of electrophoresis, namely, gel electrophoresis, can be used also in DNA sequencing if combined with molecule cutting. However, gel electrophoresis is a technique used mainly to separate and visualize DNA molecules depending on their size and charge; the gel is a matrix containing holes of various sizes, in general, a porous cross-linked polymer, so that under an applied electric field, the distance traveled through the gel by a DNA molecule (or any other molecule) is inversely proportional to its size (the smaller molecules move further). Generally, the biological molecules are stained to make their positions visible in the gel after electrophoresis is complete. Then, various molecules with different sizes and/or electric charges, spatially separated in the gel, can be easily visualized. For a review on gel electrophoresis, see ([Chéry et al. 2006](#)).

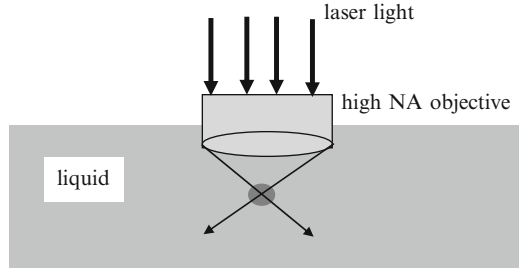
Another method to manipulate biological molecules is to use optical tweezers, which trap them with optical beams. In principle, an optical trap consists of a laser beam, which is very tightly focused by a lens with a high numerical aperture. The dielectric particle, which is placed within this beam, is under the influence of two main forces: (1) the scattering force, oriented toward the beam propagation direction, and (2) the gradient force, oriented toward the spatial gradient of light ([Neuman and Block 2004](#)). The scattering force prevails over the gradient force in most situations. The gradient force has here a similar meaning as in the case of dielectrophoresis, i.e., the force is created in the direction of the inhomogeneous field gradient, which is exerted on a dipole. So the existence of an inhomogeneous electromagnetic field is crucial as in the case of dielectrophoresis. However, the techniques to implement these inhomogeneous fields are different. In the case of an optical trapping laser, fluctuating dipoles, which interact with the inhomogeneous field, are generated in the dielectric particles, and the particles are trapped in the laser focus. Thus, to trap dielectric particles, it is necessary that the axial gradient of the force, which is dragging the particles toward the focal point, is greater than the scattering force, which drives away the particle from the focal region.

The large gradient necessary for trapping is implemented by focusing a laser beam to a diffracted-limited spot with a high numerical aperture objective. The equilibrium between the scattering force and the gradient force maintains the dielectric particle at a trap position situated a little beyond the focal point, i.e., there is an offset displacement. If this distance is small (around 150 nm), the restoring force is proportional to the offset, i.e., the trap is acting analogously to a mechanical oscillator with  $F = -K \Delta x$ . An optical trap is displayed in [Fig. 3.10](#).

If we consider that a sphere with radius  $R$  that satisfies the relation  $R \ll \lambda$ , where  $\lambda$  is the laser wavelength, is treated as a point dipole, the Rayleigh scattering theory give us the scattering force as

$$F_{\text{scat}} = I_0 \sigma n_m / c, \quad (3.34)$$

**Fig. 3.10** The optical tweezer and trapping principle



where  $I_0$  is the light intensity,  $n_m$  is the index of refraction of the medium, and  $\sigma$  is the scattering cross section of the sphere, given by

$$\sigma = \frac{128\pi^5 R^6}{3\lambda^4} \left( \frac{m^2 - 1}{m^2 + 2} \right)^2. \quad (3.35)$$

In (3.35),  $m = n_p/n_m$ , where  $n_p$  is the index of refraction of the particle. For the same spherical particle, the gradient force is

$$F_{\text{grad}} = \frac{2\pi\alpha}{cn_m^2} \nabla I_0, \quad (3.36)$$

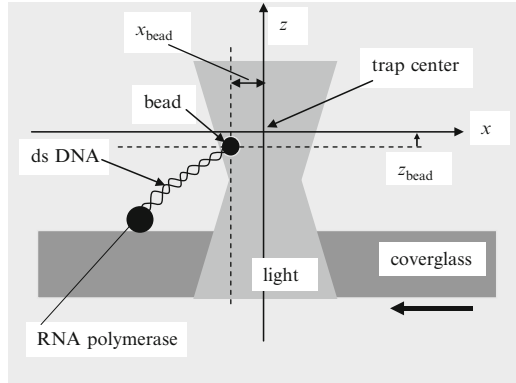
where  $\alpha$  is the sphere polarizability, expressed as

$$\alpha = n_m^2 R^3 \left( \frac{m^2 - 1}{m^2 + 2} \right). \quad (3.37)$$

In the case when  $R$  is comparable to  $\lambda$ , the above approach based on ray optics and a point-like dipole is no longer valid, and more complicated electromagnetic theories are needed to explain the trapping mechanism. The majority of objects to be trapped are in the range of  $0.1-10\lambda$ , and the minimum dimensions of trapped objects are around 30 nm. The reviews in [Neuman and Block \(2004\)](#) and [Le Grimallec et al. \(2010\)](#) explain in detail the optical systems necessary to implement the optical tweezers/traps and provide also a good description of the commercial systems for optical trapping.

In the optical trapping setups, the particles can be trapped, manipulated from a place to another, or rotated. There are numerous applications in biology where optical tweezers are used. For example, a single rod-shaped *E. coli* bacterial cell was trapped and rotated to allow its study from different perspectives ([Carmon and Feingold 2011](#)). In addition, using optical tweezers, the shear modulus of the human erythrocyte membrane was determined to be  $\mu = 2.5 \pm 0.4 \mu\text{N m}^{-1}$ . Micromanipulation of plant cytoplasm and organelles using optical tweezers were recently reported in the review in [Hawes et al. \(2010\)](#). Moreover, DNA nanomechanical properties are currently investigated with optical tweezers. The stretching of the DNA molecule with a length less than  $1 \mu\text{m}$  was achieved by fixing one

**Fig. 3.11** DNA stretch with optical tweezers



end of the DNA on a cover glass with the help of stalled RNA polymerase, while the other end was linked to a bead trapped in the optical tweezer. By moving the cover glass and recording the bead with nanometer resolution with the help of an interferometric detector (see Fig. 3.11), the double-clamped dsDNA is stretched and the force dependence on the distance  $x$  can be determined (Wang et al. 1997).

If the stiffness  $k_x$  at the trap center is given by

$$k_x \langle x_{\text{bead}}^2 \rangle = k_B T, \quad (3.38)$$

where  $\langle x_{\text{bead}}^2 \rangle$  is the mean-square thermal displacement of the bead, the force dependence on distance is given by

$$F = \frac{k_x x_{\text{bead}}}{\cos \left[ \tan^{-1} \left( \frac{z_{\text{trap}} - z_{\text{bead}}}{x_{\text{DNA}} - x_{\text{bead}}} \right) \right]}, \quad (3.39)$$

where  $z_{\text{trap}}$  is the height at the center of the trap, and  $x_{\text{DNA}}$  is determined during the experiment. Using these data, it was found that the persistence length of DNA, which quantifies its stiffness, depends on the buffer solution, but is higher than 40 nm, whereas its elastic modulus is of about 1,100 pN.

In addition, the unzipping force of dsDNA was measured with optical tweezers and found to decrease from about 16 pN to around 10 pN as the number of opened base pairs increases (Bockelmann et al. 2002). Other biomolecules like proteins and RNA are characterized using this method.

## References

- Adamcik J, Jung J-M, Flakowski J, de los Rios P, Dietler G, Mezzenga R (2010) Understanding amyloid aggregation by statistical analysis of atomic force microscope. *Nat Nanotechnol* 5:423–427
- Bhushan B (ed) (2004) Springer handbook of nanotechnology. Springer, Berlin, pp 330–331

- Bockelmann U, Thomen Ph, Essevez-Roulet B, Viasnoff V, Heslot F (2002) Unzipping DNA with optical tweezers: high sequence sensitivity and force flips. *Biophys J* 82:1537–1553
- Carmon G, Feingold M (2011) Rotation of single bacterial cells relative to the optical axis using optical tweezers. *Opt Lett* 36:40–42
- Chéry CC, Moens L, Cornelis R, Vanhaecke F (2006) Capabilities and limitations of gel electrophoresis for elemental speciation: a laboratory's experience. *Pure Appl Chem* 78:91–103
- Chou C-F, Tegenfeldt JO, Bakajin O, Chan SS, Cox EC, Darnton N, Duke T, Austin RH (2002) Electrodeless dielectrophoresis of single- and double-stranded DNA. *Biophys J* 83:2170–2179
- Dragoman D, Dragoman M (2009) Real-time detection of deoxyribonucleic acid bases via their negative differential conductance signatures. *Phys Rev E* 80:022901
- Frederix PLTM, Bosshart PD, Engel A (2009) Atomic force microscopy of biological membranes. *Biophys J* 96:329–338
- Hansma PK, Tersoff J (1987) Scanning tunneling microscope. *J Appl Phys* 61:R1–R23
- Hawes C, Osterrieder A, Sparkes IA, Ketelaar T (2010) Optical tweezers for the micromanipulation of plant cytoplasm and organelles. *Curr Opin Plant Biol* 13:731–735
- He J, Lin L, Zhang P, Lindsay S (2007) Identification of DNA basepairing via tunneling-current decay. *Nano Lett* 7:3854–3858
- Hilal N, Bowen WR, Alkhatib L, Ogunbiyi O (2006) A review of atomic force microscopy applied to cell interactions with membranes. *Chem Eng Res Des* 84(A4):282–292
- Hölzel R (2009) Dielectric and dielectrophoretic properties of DNA. *IET Nanobiotechnol* 3:28–45.
- Hsiung L-C, Yang C-H, Chiu C-L, Chen C-L, Wang Y, Lee H, Cheng J-Y, Ho M-C, Wo AM (2008) A planar interdigitated ring electrode array via dielectrophoresis for uniform patterning of cells. *Biosens Bioelectron* 24:869–875.
- Kang Y, Cetin B, Wu Z, Li D (2009) Continuous particle separation with localized AC-dielectrophoresis using embedded electrodes and an insulating hurdle. *Electrochim Acta* 54:1715–1720
- Kawakatsu H, Saya D, Kato A, Fukushima K, Tosiyoshi H, Fujita H (2002) Millions of cantilevers for atomic force microscopy. *Rev Sci Instrum* 73:1188–1192
- Kumar S, Yoon S-H, Kim G-H (2009) Bridging the nanogap electrodes with gold nanoparticles using dielectrophoresis techniques. *Curr Appl Phys* 9:101–103
- Le Grimellec C, Milhiet PE, Perez E, Pincet F, Aimé J-P, Emiliani V, Thoumine O, Lionnet T, Croquette V, Allemand J-F, Bensimon D (2010) Nanoforce and imaging. In: Boisseau P, Houdy P, Lahmani M (eds) *Nanoscience. Nanobiotechnology and nanobiology*. Springer, Berlin
- Lyubchenko Y, Shyakhtenko LS, Ando T (2011) Imaging of nucleic acids with atomic force microscopy. *Methods* 54:274283
- Mou JX et al (1996) High resolution surface structure of *E-coli* GroES oligomer by atomic force microscopy. *FEBS Lett* 381:161–164
- Neuman KC, Block SM (2004) Optical trapping. *Rev Sci Instrum* 75:2785–2809
- Pethig R (2010) Dielectrophoresis: status of the theory, technology, and applications. *Biomicrofluidics* 4:022811
- Rajagopalan J, Saif MTA (2011) MEMS sensors and microsystems for cell mechanobiology. *J Micromech Microeng* 21:054002.
- Roncali E, Tavitian B, Texier Ie, Peltié P, Perraut F, Boutet J, Cognet L, Lounis B, Marguet D, Thoumine O, Tramier M (2010) Optical tools. In: Boisseau P, Houdy P, Lahmani M (eds) *Nanoscience. Nanobiotechnology and nanobiology*. Springer, Berlin
- Sarid D (1994) *Scanning force microscopy with applications to electronic, magnetic and atomic forces*. Oxford University Press, New York.
- Shapir E, Chen H, Calzoni A, Cavazzoni C, Ryndyk DA, Cuniberti G, Kotlyar A, di Felice R (2008) Electronic structure of single DNA molecules resolved by transverse scanning tunneling spectroscopy. *Nat Mater* 7:68–74

- Stoltz M, Gottard R, Raiter R, Miot S, Martin I, Imer R, Stauffer U, Raducanu A, Düggelin M, Bascong W, Daniels AU, Friederich MF, Aszodi A, Aebi U (2009) Early detection of aging cartilage and osteoarthritis in mice and patient samples using atomic force microscope. *Nat Nanotechnol* 4:186–192
- Tanaka H, Kawai T (2009) Partial sequencing of single DNA molecule with a scanning tunneling microscope. *Nat Nanotechnol* 4:518–522
- Tuukkanen S, Toppari JJ, Kuzyk A, Hirviniemi L, Hytönen VP, Ihalainen T, Törmä P (2006) Carbon nanotubes as electrodes for dielectrophoresis of DNA. *Nano Lett* 6:1339–1343
- Wang MD, Yin H, Landick R, Gelles J, Block SM, Stretching DNA (1997) with optical tweezers. *Biophys J* 72:1335–1346
- Wilson NR, Macpherson J (2009) Carbon nanotube tips for atomic force microscopy. *Nat Nanotechnol* 4:483–491
- Xu M, Enders RG, Arakawa Y (2007) Electronic signature of DNA bases. *Small* 3:1539–1543

## Chapter 4

# Nanomedicine

**Abstract** This chapter is dedicated to the applications of nanoelectronics in medicine. In fact, almost the entire book was written with this aim. However, here we will focus only on some issues specific to nanomedicine and directly related to nanoelectronics, i.e., controlled drug delivery and biochips.

### 4.1 Drug Delivery and Healing Based on Nanomaterials

Nanomedicine is revolutionizing the entire area of medicine, irrespective of its domains, by merging the biological and medical knowledge with nanotechnologies. The subject is so vast that it is covered in many books, among which we recommend for the interested reader (Jain 2008; Boisseau et al. 2010). Also, there are journals dedicated to nanomedicine, and many comprehensive review papers have been written on this subject, such as Riehemann et al. (2009).

In principle, almost the entire book can be seen as a nanomedicine book since the applications of nanomedicine are in Shi et al. (2010):

1. *Diagnostics* (in vitro), which has the fast detection of diseases or of disease biomarkers with high sensitivity using biosensors as goal (see Chap. 2).
2. *Imaging* (in vivo), where scanning probe microscopy, targeted nanoprobe such as nanoparticles, nanotubes, quantum dots, and functionalized flakes of graphene, could provide an early warning of a disease and could monitor its progress [see Chap. 3 and the monumental work (Chen 2011)].
3. *Therapy* using certain nanomaterials, such as nanoparticles, to enhance X-ray therapy or hyperthermia used to destroy the cancer cells.
4. *Tissue engineering* and development of artificial organs created by nanotechnologies; some aspects regarding biocompatible scaffolds used for tissue engineering are treated in this chapter, while some references to this issue can be found in Chap. 5.
5. *Controlled drug delivery*, which is also the subject of this chapter.

The controlled delivery of drugs based on nanotechnologies is developed to increase the efficiency of drug treatments and, at the same time, to reduce the adverse effects that often accompany these treatments, as well as to enable new therapeutic methods based on nanotechnologies. Over 20 therapeutic products based on nanotechnologies were approved for clinical use and much more are in clinical trial.

There are several generations of controlled drug delivery systems based on nanotechnologies (Riehemann et al. 2009). The first generation is a passive delivery system, which localizes at the target, for example, a tumor. It is based on liposome, termed as a nanovector, which is confined in the tumor by the enhanced permeation and retention (EPR) effect or through the increased permeability of the tumor neovasculature. Other nanovectors of the first generation are metallic nanoparticles and albumin-paclitaxel nanoparticles, which are approved to be used in breast cancer. All these nanovectors are functionalized on their surface with a stealth layer such as polyethylene glycol (PEG) to avoid their early capture by the phagocytic blood cells and hence to extend their circulation time.

The second nanovector generation has added functionalities, enabling controlled release of various loads at the specific site of the disease or molecular recognition of the target. The nanovectors are now able to target the tumors using antibodies and other biomolecules used for tumor detection. The most known nanovectors of this generation are liposomes and nanoparticles functionalized with antibodies. Other functionalizations are studied and are based on aptamers, ligands, etc. This second generation has the ability to remotely control the activation of nanovectors, for example, to control iron oxide nanoparticles by switching a magnetic field, or to use RF signals and ultrasounds as triggers.

The third generation of nanovectors is able to perform a multitude of tasks such as the generation of multiple series of nanoparticles able to overcome various biological barriers. This third generation will enable the connection of nanoparticles and small interfering RNA (siRNA), which can suppress the action of genes that cause cancer. Codelivery and coencapsulation are the key words for the nanovectors of this last generation. Coencapsulation means the encapsulation of hydrophilic and hydrophobic drugs, which are used to control the time of codelivery of drugs and specific DNA sequences at the intracellular level (Wang et al. 2006). Another example is the incorporation in a single nanoparticle of multiple functions, such as simultaneous imaging and delivery of therapeutic biomolecules (Bagalkot et al. 2007).

The MEMS/NEMS devices for drug delivery systems are also rapidly developing (Hilt and Peppas 2005; Staples et al. 2006; Shi et al. 2010). At the end of Chap. 1, we have explained some basic facts regarding the fabrication of MEMS devices for micro/nanofluidics systems, while NEMS were explained in Chap. 2 in the context of biosensing. In the case of drug delivery systems, the MEMS are used for implantable microchips (Ainslie and Desai 2008) that are able to codeliver drugs in a prescribed manner using miniaturized pumps and reservoirs (Tsai and Sue 2007), micro- and nanoneedles for painless transdermal drug delivery, and patch vaccination (Prausnitz 2004). So, the MEMS/NEMS devices used for drug delivery are of the third generation and are part of the large category of bioMEMS/NEMS.

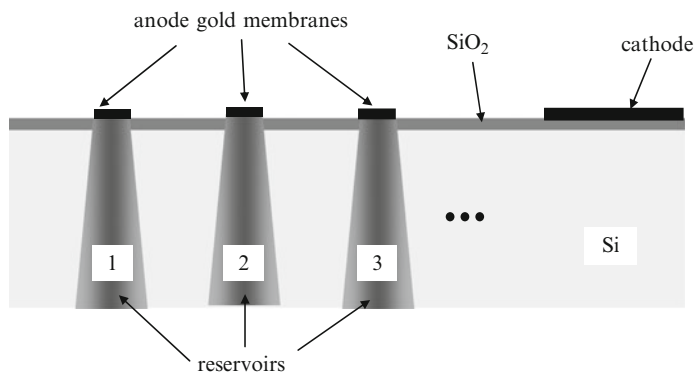


**Fig. 4.1** Controlled release of drugs via MEMS

In what follows, we will describe such bioMEMS starting with a controlled releasing microchip (Santini et al. 1999), which is a silicon chip that offers controlled release of a single or of multiple agents on demand. The device is depicted in Fig. 4.1. The release of agents contained in one or several reservoirs, denoted by 1, 2, and 3 in Fig. 4.1, is done by applying a dc voltage between the anode, which consists of a  $0.3 - \mu\text{m}$  thick gold membrane, and the cathode. The microchip has a dimension of  $17 \text{ mm} \times 17 \text{ mm} \times 310 \mu\text{m}$  and incorporates 34 reservoirs, but there is enough space to contain 1,000 reservoirs, thus demonstrating the immense power of micro/nanotechnologies. This chip was fabricated by a series of technological processes encompassing optical lithography, CVD, electron beam evaporation, and RIE.

The reservoir (see Fig. 4.2) has the shape of a square pyramid with a volume of 25 nl and releases the agent through the small square opening covered by the anode membrane. This membrane has dimensions of  $50 \mu\text{m} \times 50 \mu\text{m} \times 300 \text{ nm}$  and is made from gold because gold has low reactivity with many agents in the reservoirs and is easily processed by micro/nanofabrication techniques. The reservoirs were filled through the large openings by an ink jet printing method able to deposit 0.2 nl of gel or liquid solution of desired concentration in each reservoir. Microsyringe pumps are an alternative solution to fill the reservoirs. The prototype device was able to release various substances at an applied voltage of 1.04 V. The two situations are displayed schematically in Fig. 4.3.

The release of masses of about 250 ng was studied during those days. Each reservoir can be controlled individually by a dc voltage, and the released agents can be solid substances, liquids, or gels. This is a lab-on-chip device if the reservoirs are connected to microfluidic systems, which fill them periodically.

The drug-releasing microchip could be eventually mounted in a biocompatible case, and it can contain the power source and antenna needed for wireless communications (Prescott et al. 2006), as shown schematically in Fig. 4.4.

Such a MEMS-controllable drug delivery was used in vivo to release doses of several substances using two tracer molecules, fluorescein dye and radiolabel

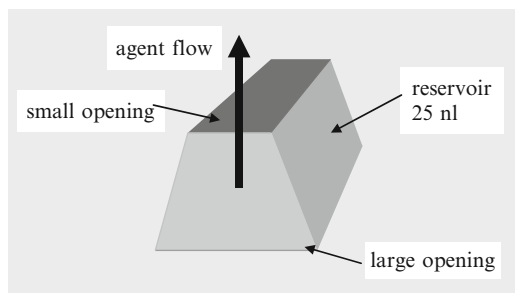


**Fig. 4.2** The reservoir (the top is the gold anode)

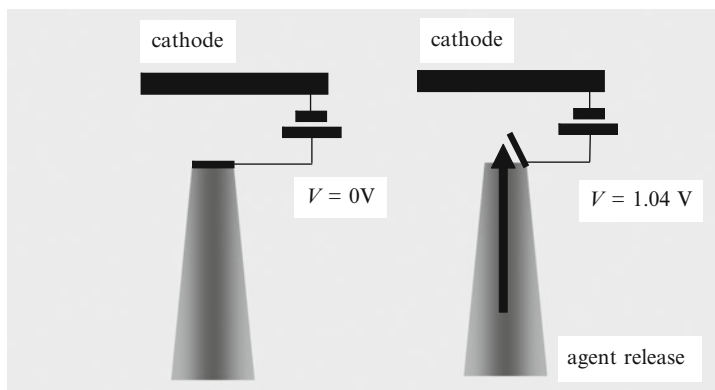


**Fig. 4.3** The reservoir in the two states

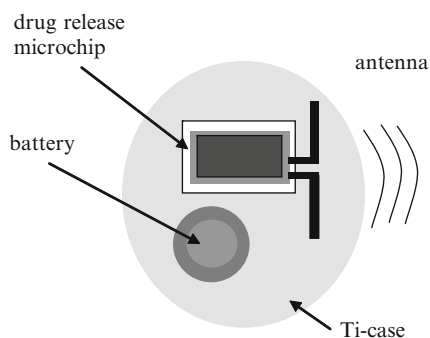


**Fig. 4.4** RF-implantable controlled drug release system

mannitol, and one chemotherapeutic agent, carmustine (BCNU). Subcutaneous release was performed in rats, and the spatial profile of fluorescein dye release was monitored by fluorometry, while the temporal profile of mannitol release functionalized with  $^{14}\text{C}$  was observed by liquid scintillation counting (Li et al., 2004). The release profile of the BCNU functionalized with  $^{14}\text{C}$  was measured with an

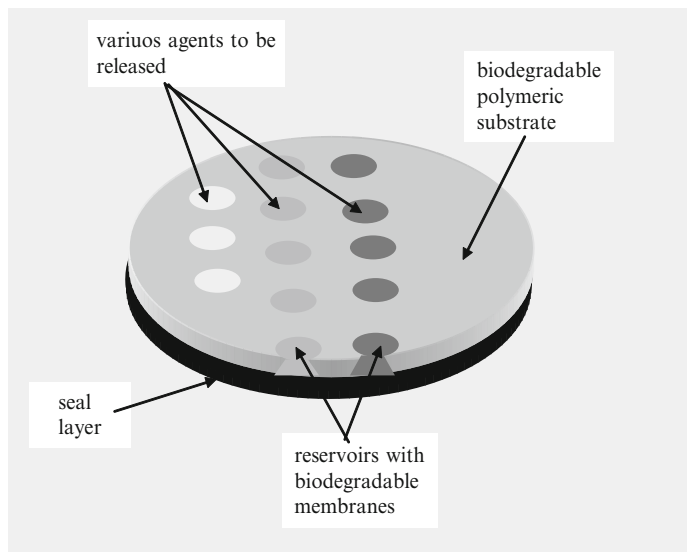


**Fig. 4.5** The controlled polymer drug delivery system

accelerator mass spectrometer. In *in vivo* experiments, drug delivery follows the electrochemical dissolution of the gold membranes placed on top of the reservoirs. These experiments have indicated that the device displayed in Fig. 4.1 is able to deliver various drugs with precise profiles in localized places. The role of the RF emitter is played by  $^{14}\text{C}$ . The need to eliminate such a MEMS drug delivery device from the body is fulfilled by a biodegradable polymer chip, which contains an array of microreservoirs terminated with different resorbable membranes. The drugs to be released are placed in microreservoirs, as illustrated in Fig. 4.5 (Grayson et al. 2003).

A similar drug release device is based on a MEMS-like polymer that seals the drug reservoir and contracts or expands, similar to a muscle, in the presence of an electric signal emitted by an electronic circuit (Staples et al. 2006). In this way, in a single-reservoir device, the contained drug is released with targeted kinetics when the biosensor is triggered by a certain electric signal. This device is displayed in Fig. 4.6.

The next generation of stents, which are made from metals, will be integrated with microprobes to allow the delivery of antirestenosis or other types of drugs. A micromachined stent is acting as an antenna for wireless control of microprobes. An inductive stent antenna, as that in Fig. 4.7, with a total length of 20 mm and a diameter of 3.5 mm is loaded with a capacitor. The stent can be thus interrogated via wireless signals. The antenna is integrated with sensors to measure the changes in pressure and flow of blood (Takahata et al. 2006).

Wireless techniques are widespread in modern biochips and implants. For example, wireless capsule endoscopy is among the most advanced techniques to assess the mucosa of the gastrointestinal tract (Moglia et al. 2007). The basic

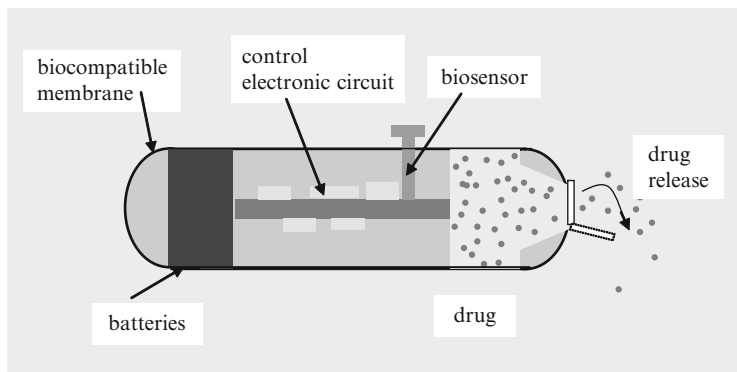


**Fig. 4.6** The electric-controlled release of the drug

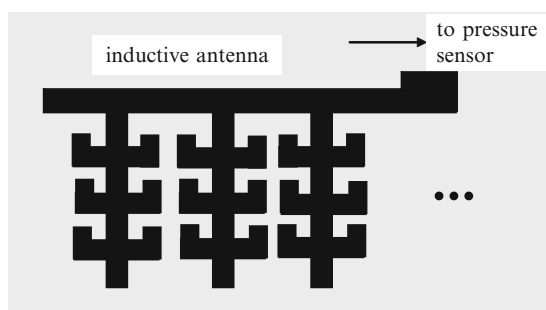


**Fig. 4.7** An inductive stent micromachined antenna

structure of such a capsule is displayed in Fig. 4.8. The future prospect of this capsule is to pass over the entire gastrointestinal tract, to send views of the organs positioned along this tract with the help of the imaging system displayed at the left end of the endoscope in Fig. 4.8, to perform drug delivery, and to collect tissue samples. The interaction with the control unit occurs via the antenna and the RF transmitter.

There are two recent reviews about microchips and capsules used in drug delivery systems: (Ainslie and Desai 2008) and (Staples 2010), both indicating the role of wireless microchips in drug delivery systems. The battery contained in these systems can be replaced by inductive coupling at radiofrequencies (RFs), solution that provides a much larger autonomy and allows the reduction of the dimensions to these intelligent drug delivery devices. In this case, the transfer of RF energy through the skin is achieved by an emitter coil and a receiving coil. In this way, the microchips could be powered by RF energy. The control of wireless drug release is performed by tens of micromachined cavities, as displayed in Fig. 4.1. In the device depicted in Fig. 4.9, it is possible to control which cavity will deliver the drug at a prescribed moment in time to power the implant or even to slow down its movement

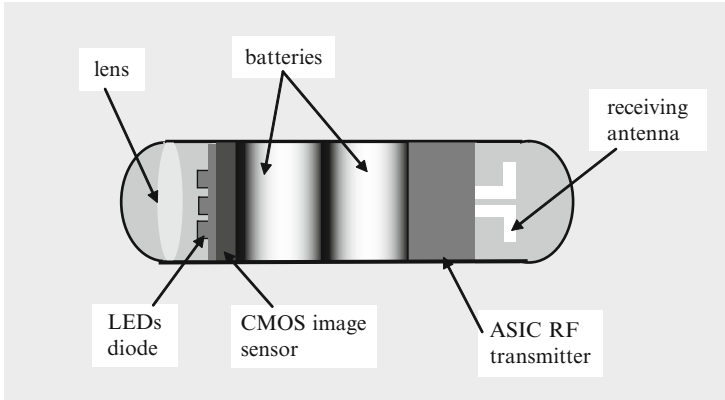


**Fig. 4.8** The wireless endoscope

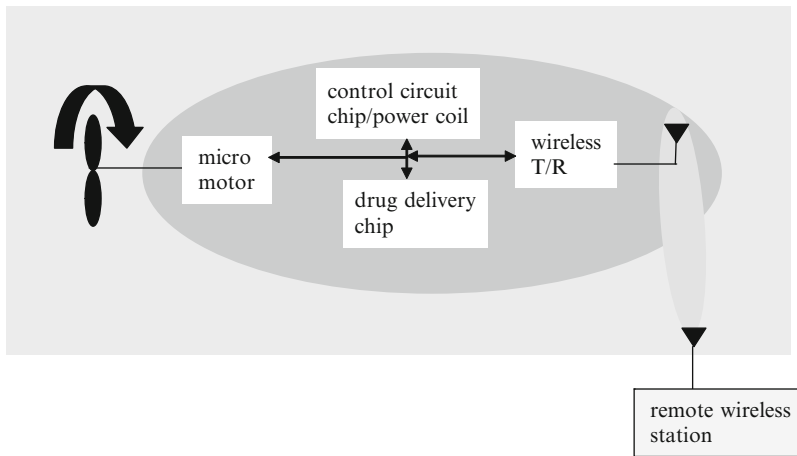


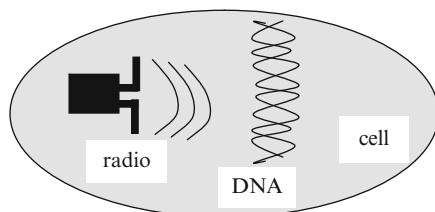
**Fig. 4.9** Wireless powering and monitoring drug release

inside the body. All these actions are accomplished via integration of a miniaturized transmitter/receiver (*T/R*) module in the implant.

Such RF implants were already used in miniaturized drug delivery systems with wireless power transfer and communications (Smith et al. 2007) and in implantable ocular drug delivery systems (Tang et al. 2008), where a miniaturized pressure sensor measures the intraocular pressure and delivers the drug when this pressure is not normal.

Moreover, the single-chip implantable RFID (radio frequency identification) system in a single-cell radio is presently under investigation (Burke and Rutherglen 2010). In this case, a radio inside the cell interrogates, monitors, and, possibly, changes the cell functions. This almost science-fictional idea depicted in Fig. 4.10 is based on the recent development of nanoradio and chip antennas.

**Fig. 4.10** The single-cell radio



The nanoradio is based on nanotubes or nanoparticles. For example, a nanoradio can consist of a single CNT cantilever that emits electrons via the field-emission effect, its emission being modulated by a remote radio transmitter signal and detected by a cathode located in vacuum near the vibrating CNT resonator (Jensen et al. 2008). Thus, a single vibrating CNT resonator is acting as a rudimentary radio able to sense the signal of a remote radio transmitter that is emitting at a frequency equal to the mechanical resonance frequency of the CNT. The minimum detectable field is  $60 \text{ dBmV m}^{-1} \text{ Hz}^{-1/2}$ , and the resonance frequency can be tuned in the 50–400 MHz range by controlling the length of the cantilever. The detection of the radio signal is performed by collecting the field-emission current of the CNT in the presence of applied dc field  $E$ . This current is expressed by the Fowler–Nordheim equation

$$I = b_1 A (\alpha E)^2 \exp(-b_2 / \alpha E), \quad (4.1)$$

where  $b_1$  and  $b_2$  are constants, and  $\alpha$  is the local field enhancement factor. The CNT is vibrating in response to a wireless signal, superimposed on the dc field, so that the enhancement factor becomes

$$\alpha(t) = \alpha_0 + \Delta\alpha(t). \quad (4.2)$$

As a result, the current has a nonstationary part

$$\Delta I(t) = I_0 (1 + a + a^2/2) (\Delta\alpha(t)/\alpha_0)^2, \quad (4.3)$$

where  $a = b_2/\alpha_0 E$ . The first two terms in (4.3) describe the amplification of the emitted current, and the last term expresses the demodulation effect in the same device. The CNT radio is displayed in Fig. 4.11. It is important to note that this CNT radio is 4–5 orders of magnitude smaller than contemporary radio devices implemented with the most advanced semiconducting technologies. In its present form, the CNT radio has some severe drawbacks. It must be biased around 200 V, which is a value that is too large for an autonomous capsule. In addition, the tunability achieved by changes in the bias is small, of only 4 MHz, which is five times lower than the FM bandwidth.

Therefore, an improved type of nanoradio—the tunneling nanoradio—was proposed in Dragoman and Dragoman (2008) to alleviate the abovementioned drawbacks. In the tunneling nanoradio, the detection method based on field emission from a vibrating CNT was replaced by a tunneling detection mechanism. The tunneling nanoradio is displayed in Fig. 4.12.

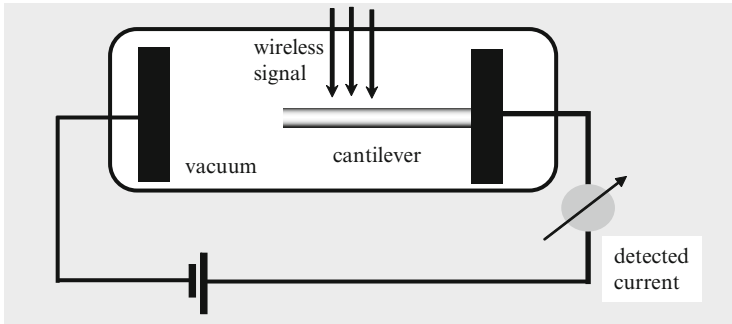


Fig. 4.11 The nanotube radio

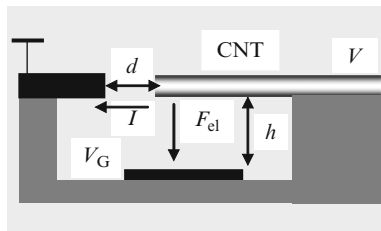


Fig. 4.12 The tunneling nanoradio

The resonant mechanical oscillations of the CNT, which are produced by radio waves with the same frequency, are detected by collecting the electron tunneling current  $I$  across the air gap of width  $d$  formed between the CNT and another electrode. The CNT resonant frequency can be tuned in a broadband range by the electrostatic force  $F_{el}$  acting between the CNT cantilever and a bottom electrode on which a gate voltage  $V_G$  is applied. For a gap of 5 nm, the current is of few  $\mu A$  at voltages not exceeding 10 V. If the CNT cantilever resonates at a high frequency, around 300 MHz, we can detect only the average value of the current,  $I_m = T^{-1} \int_0^T I(t) dt$ , where  $T$  is the period of oscillations. The fraction  $I_m/I_0$ , where  $I_0$  is the off-resonance current, for which the CNT does not vibrate is 0.91 for oscillation amplitudes, as small as  $d/10$ . Thus, the tunneling nanoradio is very sensitive to the radio signal to be detected.

Moreover, the tuning mechanism is reversible and broadband. It is based on the equivalence of the electrostatic actuation of CNT by the bottom gate electrode to an increase of its effective mass. Considering that the mechanical resonance frequency of a CNT with mass  $m$ , length  $L$ , moment of inertia  $I$ , and elastic modulus  $E$  is

$$f_0 = \frac{\beta^2}{2\pi L^2} \sqrt{\frac{EI}{m}}, \tag{4.4}$$

where  $\beta$  is a constant parameter, a shift  $\Delta f = f - f_0$  in the resonance frequency required to tune the radio can be caused by a change in the CNT effective mass.

This change originates in the electrostatic force  $F_{el}$ , which superimposes on the gravitation force  $mg$  acting upon the cantilever, the net effect being an increase in the effective mass. We have then

$$\frac{\Delta f}{f_0} = \sqrt{\frac{m}{m + F_{el}/g}} - 1, \quad (4.5)$$

with  $g = 9.8 \text{ ms}^{-2}$ . The mass per unit length of a CNT is equal to  $\rho\pi(r_{ext}^2 - r_{int}^2)$ , where  $\rho$  is the density of the CNT, and  $r_{int}$  and  $r_{ext}$  are, respectively, its inner and outer radii, while the electrostatic force per unit length is given by  $-2\pi\epsilon_0 V_{act}^2 / \sqrt{h(h + 2r_{ext})}$ . In the last expression,  $\epsilon_0$  is the vacuum permittivity,  $V_{act} = V - V_G$  is the actuation voltage, with  $V$  the voltage applied on the cantilever, and  $h$  is the distance between the undeflected CNT and the bottom electrode. To get an insight into the wideband tunability of the tunneling nanoradio, it can be easily estimated that for  $h = 300 \text{ nm}$ , and inner and outer CNT radii of 1 and 15 nm, respectively, the frequency of the CNT nanoradio can be tuned reversibly in a broad range of values, i.e.,  $\Delta f/f_0 \cong 0.6$ , by a very small actuation voltage, of less than 1 mV, as indicated in Fig. 4.13. However, this performance can only be obtained if the difference between the voltage on the cantilever and that applied on the gate is controlled with high precision.

So, in principle, there is a possibility to obtain a CNT radio able to penetrate a single cell. Moreover, as in the case of microchips, it is possible to remotely control cellular processes by electrical means via wireless inductive coupling. This amazing fact was demonstrated for the hybridization control of DNA through the inductive coupling to an attached nanoparticle antenna, the crystalline nanoparticle having a diameter of 1.4 nm (Hamad-Schifferli et al. 2002). The nanoparticles are attached to the DNA and increase locally the temperature via wireless coupling to values high enough to denaturate the DNA, while other molecules in the neighborhood are unaffected. The wireless inductive heating was performed with a microwave field having a frequency of 1 GHz. The demonstration of the working principle of this device consisted in the fabrication of 38-nucleotide hairpin loops, which are

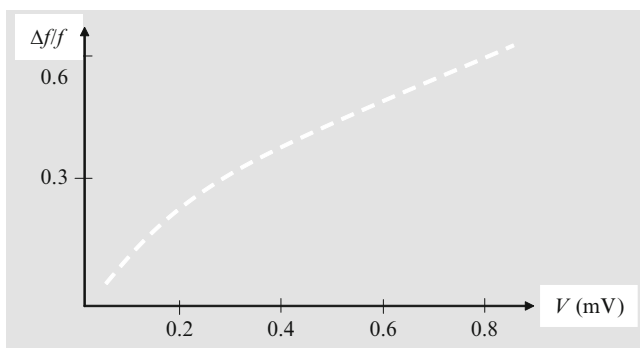
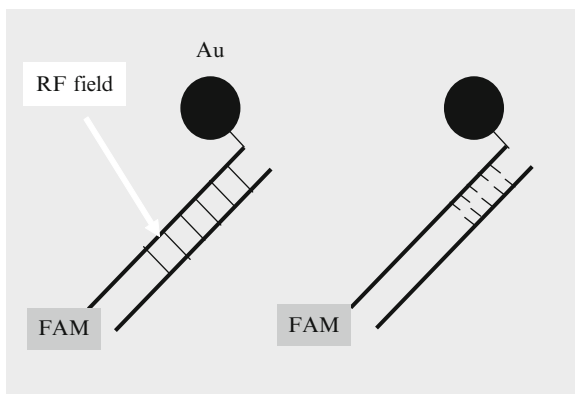


Fig. 4.13 Frequency tuning of the tunneling nanoradio

**Fig. 4.14** The remote dehybridization of DNA via a wireless microwave field

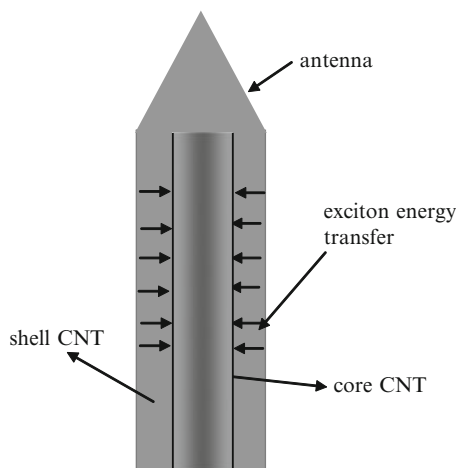


covalently linked at one end to a gold nanoparticle antenna. The dehybridization was monitored by the hyperchromicity of DNA at 260 nm, measured by optical absorbance. Alternatively, the controlled dehybridization process induced by the effective temperature rise due to the RF electromagnetic field can be observed by measuring the fluorescence signal emitted by a fluorophore FAM linked to the other end of the DNA molecule. When the latter dehybridizes, FAM diffuses into the supernatant and the fluorescence signal of the supernatant increases accordingly. A simplified antenna-induced dehybridization process is displayed in Fig. 4.14. This controlled dehybridization process could be used to manipulate the reversible production of specific RNA molecules. This could be possible because the dehybridization is selective, i.e., the biological molecules or parts of them which are not labeled with gold nanoparticles remain unchanged.

Optical antennas (Bharadwaj et al. 2009) are equally important for the wireless control of drug delivery biochips. For example, dielectrophoretically assembled core-shell CNT structures in the form of aligned filaments exchange excitation energy between the shell and the core. These core-shell structures consist of annular shells of (6,5) single-walled CNTs with a bandgap of  $E_g = 1.21$  eV and (7,5) and (8,7) single-walled CNT cores, with smaller bandgaps than the shells. The excitation energy is spatially concentrated in the center of the core-shell structures, which have a radial gradient of the bandgap (Han et al. 2010). A strong photoemission in the near infrared spectral region is observed in the (8,7) nanotubes as a result of this excitation energy exchange. The photoemission of the CNTs with the smallest bandgap is generated by illumination in a broad spectral range, which extends from near infrared to ultraviolet. Such a miniature antenna is displayed in Fig. 4.15. The tip of the antenna contains only shell CNTs.

The drug delivery method based on chips is also applicable in the brain, via electronic device interfaced with neurons. A drug delivery chip able to release locally a neurotransmitter molecule (L-glutamate) and to stimulate individual neurons is described below (Mernier et al. 2007). The neurotransmitter is filled in by a minireservoir fabricated, or release region, via Si MEMS technologies and delivered

**Fig. 4.15** A CNT optical antenna



through the opening on the front side. The surface and the cross section of the chip are displayed in Fig. 4.16a, b, respectively. The negatively charged L-glutamate molecules in a buffer solution are introduced in the reservoir. The front surface of the chip consists of a pair of Pt electrodes separated by typical distances of  $10\ \mu\text{m}$  and patterned over a  $\text{SiO}_2/\text{Si}$  substrate, in which a releasing opening is etched. This structure is placed over a plexiglas flow cell, which contains the reservoir, and the resulting device is sealed with polydimethylsiloxane (PDMS) such that another Pt wire is trapped at the interface between the flow cell and the top structure. To release the L-glutamate, a voltage is applied between the Pt electrodes, charged positively, and the Pt wire, which is charged negatively. As a result, the L-glutamate molecules tend to move away from the Pt wire and toward the Pt electrodes, being released through the opening on the top surface. The device was tested using a solution of 10 mM L-glutamate diluted in a phosphate buffer solution (PBS), which was introduced in the minireservoir, and the neurotransmitter fluorescence was monitored during actuation experiments. The electrokinetic actuation voltage on the Pt wire is able to release the drug starting at a value of  $-200\ \text{mV}$ . At a higher actuation voltage of  $-500\ \text{mV}$ , applied for during 1 s, the device is able to spread glutamate molecules in a region with a diameter of  $100\ \mu\text{m}$ ; the glutamate molecules stimulate neuron cells in the environment. Also, the diffusion of the glutamate is suppressed by applying and inverse voltage.

Neuronal drug delivery is related also to the implantable neuronal probes which initially, in the 1980s, contained a recording array consisting of ten channel microelectrodes integrated with the signal processing chip (Najafi and Wise 1986; Wang and Soper 2007). In Fig. 4.17, we have represented such a microneural probe. The probe has a length of 4.7 mm, a width of  $15\ \mu\text{m}$  at the tip and  $160\ \mu\text{m}$  near the base, and has a thickness of  $15\ \mu\text{m}$ . More sophisticated neural probes were developed.

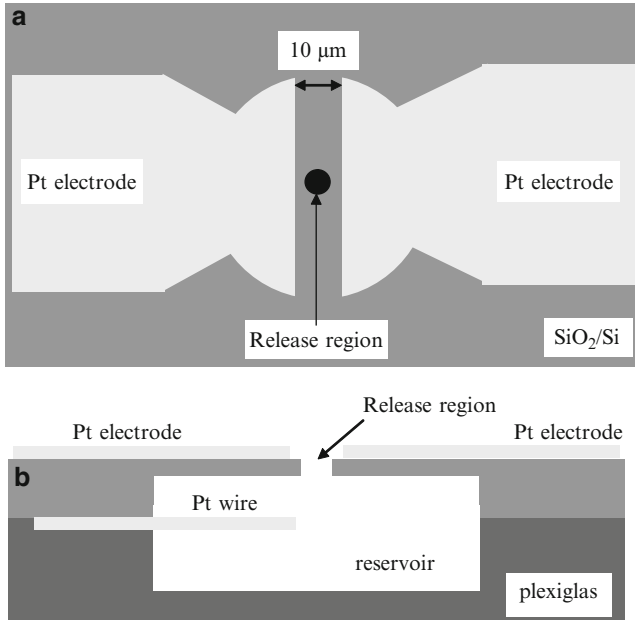


**Fig. 4.16** Top view (a) and side view (b) of the neurotransmitter chip

The MEMS technology was applied to neural probes, which can be fabricated on flexible substrates (Hollenberg et al. 2006). The array of flexible electrodes is fabricated on a Kapton substrate, which was engineered to reduce trauma when inserted in the region between the dura and the skull to get surface EEG recordings. This array has 64 gold electrodes, which form an  $8 \times 8$  grid, each electrode having a diameter of  $150 \mu\text{m}$ . This array was used to create maps of the cortical surface field potentials lasting more than 8 h with the aim of understanding the cortical activity.

Microfabrication techniques are involved also in the development of very complex arrays such as BioMEA<sup>TM</sup> (Charvet et al. 2010), which is a three-dimensional microelectrode array having several hundreds of microelectrodes, more precisely, 256 electrodes. The electrodes were fabricated by deep reactive ion etching (DRIE) and a combination of isotropic and anisotropic etching of Si on a glass substrate (see Fig. 4.18), allowing high aspect ratio of the electrodes and various shapes. The probe contains also an analog 64-channel application-specific integrated circuit (ASIC), which contains an amplifier and a current generator per channel. The microelectrode arrays can be connected in various geometries (64, 128, and 256 electrodes) to various numbers of ASICs for instantaneous stimulations or recording on all channels. This system was tested *in vivo* on mice.

Up to now, we have presented drug delivery chips in which the drug reservoirs were micromachined using MEMS technology and which were interfaced with

**Fig. 4.17** The schematic configuration of a neural probe

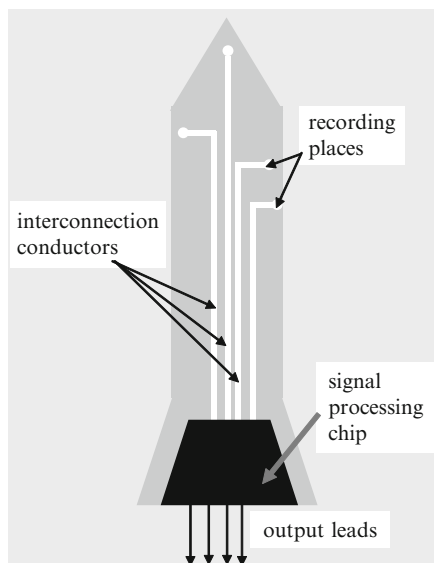
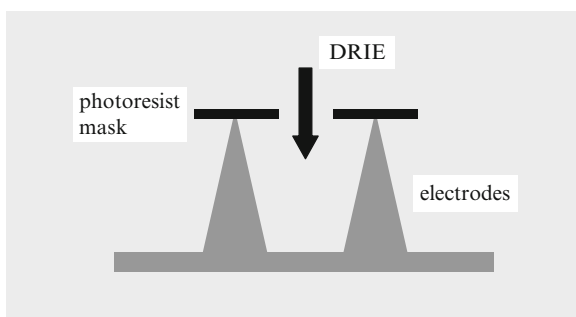


**Fig. 4.18** The DRIE electrodes for neural stimulus and recording

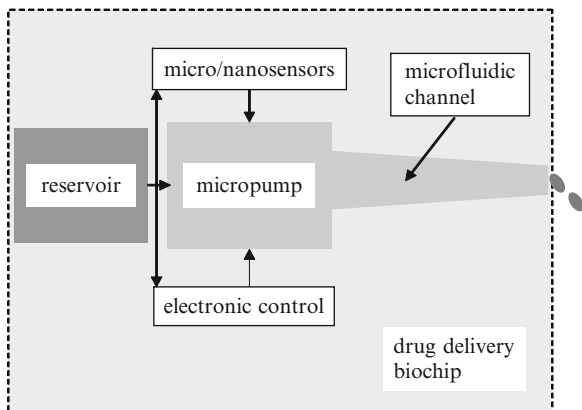


electronic circuits that allow the control of drug release or, as in the example above, the stimulation and recording of neural responses.

A very important role in controlled drug delivery is played by microfluidic/nanofluidic devices (see Chap. 1). A comprehensive review about the hard and soft micromachining applied in microfluidics and drug delivery could be found in Ziaie et al. (2004). In general, a biochip for controlled release of drugs contains the elements described schematically in Fig. 4.19. In the microfluidic biochips in Fig. 4.19, the micropumps are the core of the entire device because they disperse the drug in a prescribed order, i.e., with a certain flow rate and dose. There are a multitude of pumps, which are mechanical (peristaltic, reciprocating, or rotary pumps based on MEMS technology) and nonmechanical (electrical, magnetic, chemical, surface-tension-driven, etc.) (Tsai and Sue 2007).

An electrostatic micropump is formed from a Si membrane with two passive check valves, and it is able to attain the following performances: a maximum back

**Fig. 4.19** Drug delivery biochip based on microfluidic devices



pressure of 310 hPa in the forward direction and 70 hPa in the reverse direction, with corresponding flow rates of 850 and 200  $\mu\text{l min}^{-1}$ , respectively (Zengerle et al. 1995). The pump diaphragm, with dimensions of  $7 \times 7 \times 2 \text{ mm}^3$ , is actuated by square waves with amplitudes of 150–200 V and frequencies starting from 0.1 Hz up to a few 100 Hz. These square waves are applied between the diaphragm and the counter electrode. The total power consumption is less than 1 mW. The valve flow is quasistatic when the actuation frequency is lower than the flap, and in this case, the valve opening and the fluid flow are given by

$$x(t) = DS p_{\text{fluid}}(t), \quad (4.6)$$

$$F(t) = 4\mu l D [(2p_{\text{fluid}})^3 / \rho]^{1/2}, \quad (4.7)$$

where  $D$  is the damping constant of the valve,  $\rho$  is the fluidic density,  $p_{\text{fluid}}$  is the pressure in the fluid,  $\mu \cong 0.5 - 1$ ,  $l$  is the length of the valve, and  $S$  is the area of the valve orifice. The pump is depicted schematically in Fig. 4.20.

The example above is one among many micropumps based on piezoelectric, thermopneumatic, or shape memory alloy effects, magnetohydrodynamic, chemical, or osmotic effects. Another interesting example due to the low actuation voltages applied is the electrowetting pump (Tsai and Sue 2007). The electrowetting effect deals with the control of the surface tension  $T_{\text{ls}}$  between two different materials (solid/liquid or liquid/liquid) by an applied electrostatic force. The Lippmann–Young equation describes the relation between the contact angle  $\theta$ , the liquid–solid interface tension  $T_{\text{ls}}$ , and the capacitance  $C$  of the dielectric layer:

$$\cos \theta = \cos \theta_0 + (1/T_{\text{ls}})CV^2/2 \quad (4.8)$$

where  $\theta_0$  is the equilibrium contact angle.

The continuous electrowetting effect is used to tune the surface tension between two immiscible liquids. For example, a mercury droplet surrounded by an electrolyte

**Fig. 4.20** Schematic view of an electrostatic micropump

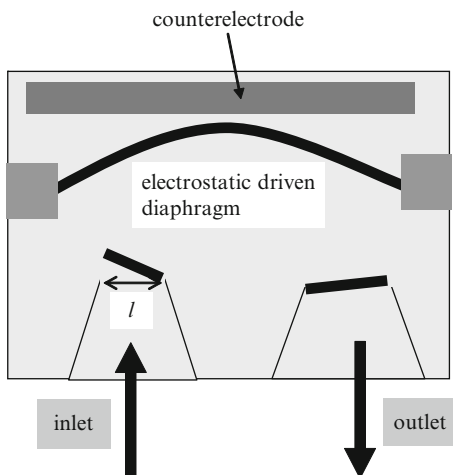
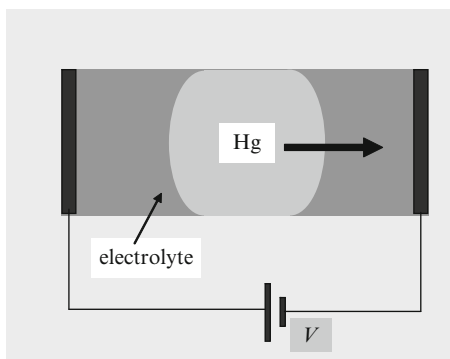


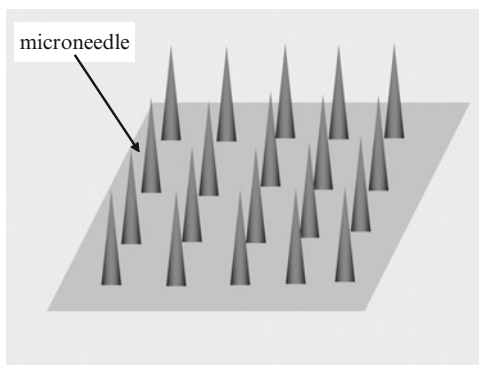
**Fig. 4.21** The continuous electrowetting effect



is moved due to the protonation effect on the mercury surface. At the application of a voltage  $V$  between the two ends of the electrolyte/mercury system, a potential difference between the two sides of the mercury droplet is produced, modifying the surface tension which pushes the mercury drop in the direction of the negative electrode, as shown in Fig. 4.21. Using the continuous electrowetting effect, a micropump could have a flow rate of  $40\text{--}100\ \mu\text{l min}^{-1}$ , a very low driving voltage of 2.3 V at 25 Hz, and a power consumption of 0.15 mW while attaining a pressure of 800 Pa (Yun et al. 2002).

Micro/nanotechnologies do not only influence the concept of drug delivery but also the way in which they are administrated. For example, micro/nanoneedles are dedicated to an enhanced transdermal delivery during which the pain felt by the patient is significantly reduced. A comprehensive review on microneedles is found in Prausnitz (2004). In principle, microneedles are made by etching Si or other materials, such as stainless steel. A typical microneedle array, as that shown in Fig. 4.22, contains 400–500 microneedles with a length of 300–500  $\mu\text{m}$ , the entire array having an area of 2  $\text{cm}^2$ . There are various ways in which these microneedle

**Fig. 4.22** A microneedle array



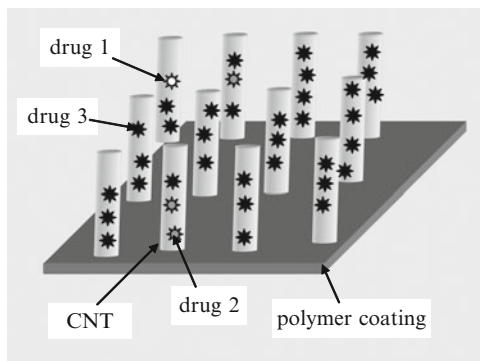
arrays are able to deliver the drug *in vivo*, the simplest being to dip the array in the drug followed by drug delivery by transdermal means.

Nanopatch arrays made from Si microneedles, which are two orders of magnitude smaller and thinner than standard needles and can be loaded with multiple agents, being thus suitable for many vaccine types, were recently fabricated (Raphael et al. 2010). The tiny Si needles are coated with multilayered dissolving nanopatches. This nanopatch, when applied to the skin, is able to penetrate it rapidly and much faster than normal needles, and the drug or vaccine in dry form is delivered by diffusion in a short time. Influenza vaccine was delivered by this method in mice and generated a strong immune response. In this way, the nanopatch, termed also as “needle-free syringe,” is able to increase significantly the effectiveness of vaccines. This type of vaccine delivery occurs at neutral pH and does not employ heating, encapsulation, or other processes that can damage the cells under the skin.

Other types of efficient microneedles are the hollow microneedles, fabricated from glass and even CNTs. The CNT needles introduced in the skin are used to sense neurotransmitters or glucose (Jia et al. 2008). Vertical CNT arrays were used as a platform of nanosyringes for intracellular delivery of plasmids and quantum dots into the cytoplasm of cancer cells and human stem cells (Park et al. 2009). This procedure opens the possibility of gene delivery for therapeutical purposes. Since CNTs are hollow, their empty inner space can be used for cargo loading of drugs (see Fig. 4.23). Several drugs can be delivered simultaneously.

CNTs have many applications in cancer therapy (Ji et al. 2010). The gene therapy and drug delivery methods mentioned above are only two important applications of CNTs in nanomedicine. For example, cancer cells can be destroyed by penetrating them with CNTs, which are able to pass through the cell barriers, and a subsequent CNT heating with radio waves at 13.56 MHz. In this way, the cancer cells in rabbits were destroyed, and no side effects were reported except the destruction of some 2–5 mm of healthy tissue by heat. The CNTs were injected directly in the tumor and then exposed for 2 min at radio waves, which penetrate in the tissues but produce no damage except when the CNTs are encountered (Gannon et al. 2007).

**Fig. 4.23** CNT array nanosyringe



## 4.2 Biochips—DNA Arrays and Other Chips for Diagnosis

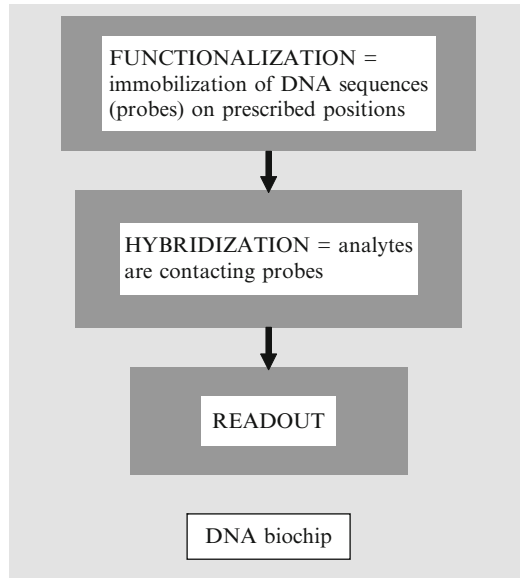
Biochips are miniaturized versions of an entire biochemical assay, which confer many advantages over the conventional methods, such as (Pasquarelli 2008):

- A relative large number of analytes can be simultaneously studied on the same biological sample.
- The needed quantity of a biological sample is quite small.
- Very high efficiency.

There are several types of biochips, but the best known are DNA chips and protein chips. The DNA chip (microarray) is a glass or quartz slide on which several probes are deposited. A single probe is formed by the same molecule, and very often, a probe is repeated several times on the slide to get a very high certitude of the results. The DNA biochip is performing the tasks depicted in Fig. 4.24.

The functionalization is the key issue of a DNA biochip. There are several techniques to perform functionalization. The DNA solution is applied on the glass slide with the help of a plotter-like robot with a spotting head. The plotter has an array of needles, which are first dipped in a plate having several DNA sequences in solution, and then the solutions are applied via a software program in the desired places on the glass slide by direct contact printing, which releases the DNA solution in the prescribed place. The spotting heads are similar to computer inkjet printers. Subsequently, the DNA chip is immersed in a solution of analytes for hybridization. The analytes contain also fluorophore molecules, which are necessary for the readout step. The readout is implemented with a scanner, which detects the fluorescence signal. The fluorophores are analyzed after being irradiated by a laser. For example, if the DNA chip tagged with a green fluorophore is immersed in known cancer cells tagged with a red fluorophore, and the scanner detects yellow spots, this means that the two sequences present in the probe and the analyte have the same gene sequence.

The additional functionalization of DNA sequences with quantum dots or nanoparticles is increasing the intensity of the fluorescent signal. An alternative

**Fig. 4.24** DNA biochip

readout is based on chemiluminescence, in which the background signal and photo bleaching are absent, in contrast to the fluorescence method. Tens of thousands of DNA probes can be analyzed simultaneously in this way.

Another chip, the protein chip (microarray), is targeting the most advanced topics of genomics, i.e., the analysis of genome at protein level. The main procedures of this biochip are similar to the DNA chip, but the protein chip is by far more complicated than the DNA chip. The reason is that there is a large variety of proteins, such as antigen–antibody, antibody–antigen–antibody, protein–protein, receptor–protein, etc., and so the functionalization methods and the hybridization processes are more complicated and more elaborate. Moreover, in the case of proteins, the polymerase chain reaction (PCR) amplification mechanism for DNA multiplication is missing. There are specific linkers for protein immobilization. The readout is more difficult than in the case of DNA chips. The readout techniques are enzyme-linked immunosorbent assays (ELISA), which are not specific at various protein interactions, and thus, many false results can be obtained. Fluorophore labeling has poor reproducibility, and therefore, the readout techniques for protein chips are oriented to label-free detection methods, such as those based on plasmonics and described in Chap. 2 of this book.

There are also lab-on-chips associated to microfluidics, which were explained briefly in Chap. 1. A good review about lab-on-chip applications is (Haeberle and Zengerle 2007). The concept of lab-on-chip can be extended to other types of biochips. For example, a plant-in-chip is a microfluidic platform for the hydroponic growth of the *Arabidopsis* plant (Parashar and Pandey 2011). The microfluidic platform consists of several microchannels, in which 1-day-old germinated seedlings are

located. The roots are growing in each microchannel and, depending on the media in a specific microchannel, the roots display different characteristics of growth. The roots are further treated with plant pathogens, and their interaction with living roots is observed.

### 4.3 Artificial Tissues and Organs

The growth of artificial tissues and organs built using nanotechnologies and nanomaterials is one of the most important tasks of nanomedicine. The transplant of organs has always two main drawbacks: (1) the very limited availability of organs to be transplanted, which generate very long waiting lists and (2) the high cost of transplants. Therefore, there are very serious researches and tests aimed at recreating human organs based on the principles of micro- and nanotechnologies. The most striking example is the nanomedicine domain termed as tissue engineering.

The aim of tissue engineering is the implementation of an artificial media able to allow the development and organization of cells into tissues with the same properties as the *in vivo* tissue to be replaced (Dvir et al. 2011). In this way, the engineering of liver (Uygun et al. 2010), arteries (Gui et al. 2009), bones (Grayson et al. 2010), and lungs were achieved (Petersen et al. 2009).

So, the main task of tissue engineering is to create artificial scaffolds, which imitate the extracellular matrix (ECM), which represents the extracellular part of a tissue that provides structural support to the cells and allows intercellular communication. A direct way to engineer delicate tissues and organs is to decellularize an organ or a tissue to get the ECM, and then reseed the ECM scaffold with new cells. The new cells recognize their natural environment and start to self-organize so that, after few days, they are able to perform the pump function of a decellularized rat heart after applying electrical and physiological stimuli, for example (Ott et al. 2008). In this way, a bioartificial heart is born again.

The ECM is a biomolecular fibrous mesh in which the cells grow, differentiate, and travel. Therefore, there are strong interactions between cells and ECM. The ECM is synthesized by the cell; cells self-assemble and decompose various ECM components, and at the same time, ECM dictates various cell functions. Cells are attached to ECM through specific molecules termed as integrins, which recognize amino acid sequences using surface receptors (see Fig. 4.25).

The ECM is composed from various molecular components (Biondi et al. 2008):

- Collagen, which is a fibrillar protein that forms the backbone of the ECM and has multiples roles in cell–cell interaction and cell–ECM interaction while providing mechanical resistance to ECM at tensile mechanical stresses
- Proteoglycans, which are carbohydrate polymers, with the role of filler substance between cells, resistance to compressive stress transport of molecules in ECM, cell adhesion, migration, and signaling

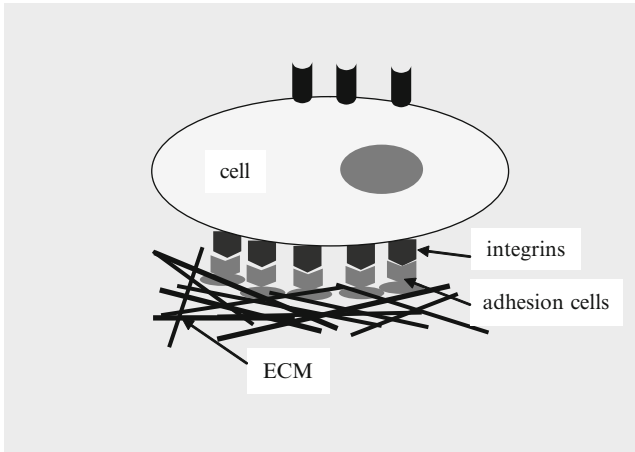


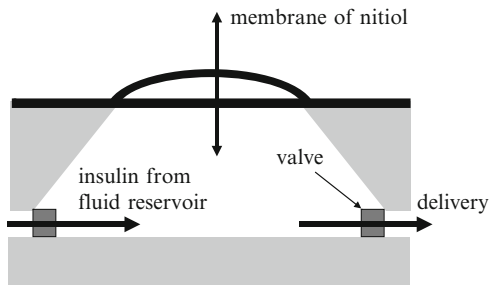
**Fig. 4.25** The cell and ECM

- Hyaluronan, which is a negatively charged polymer used for cell proliferation, differentiation, and migration
- Laminins, which are proteins that assist in the development and maintenance of membranes and adhesion
- Fibronectin, which is a protein involved in adhesion of cells at ECM and migration
- Elastin, which is a hydrophobic protein that provide ECM with elasticity and pliability

The ECM of various tissues differ in the composition of collagen, elastins, and others components. The backbone of ECM consists of micro- and nano-sized interconnected patterns of collagen and elastin bundles, which form a dense network together with the molecular components described above.

The implementation of the artificial ECM scaffold can be done in two basic ways: mimicking of ECM components to generate the cell microenvironment, or direct use of nanomaterials.

In the case of ECM analog materials, the ECM fibers such as collagen and elastins are replaced by carbon, PLA, PGA, or chitosan, which form a three-dimensional cell scaffold with adhesion properties via electrospinning. These materials perform the same function as ECM fibers when peptide amphiphile self-assembles on them (Dvir et al. 2011). A more radical way is to use CNT as a scaffold replacing entirely the ECM components. CNT confers to the artificial ECM an enhanced tensile strength and conductivity, while Ti nanowires confer better cell adhesion to the matrix and localization of biomolecules. The artificial tissue engineering plays an important role in controlled drug delivery, with the final aim of creating complex nanomaterials able to control and guide specific processes in tissues and organs.

**Fig. 4.26** The insulin pump

Artificial organs can be mimicked, or their functions can be reconstructed using very advanced integrated circuits, including micro/nanofluidics. For example, an artificial pancreas consists of two main parts. A glucose sensor implanted under the skin will detect the extracellular level and will transmit it to a computer. A drug delivery capsule having a microfluidic pump, as those described above, will then deliver the necessary amount of insulin from its reservoir (Nastruzzi et al. 2005). Such an artificial pancreas is already created but still with a limited-in-time function (Nastruzzi et al. 2005). A simple example of an insulin pump is described in Fig. 4.26. The film forming the pump takes a dome-like shape when electrically heated. In this case, insulin from a reservoir is drawn inside the pump and is released in the delivery tube when the film cools down. The film is termed nitinol and is an alloy of Ni and Ti (Schetky et al. 2003).

A biomimetic microsystem was recently fabricated to reconstitute the critical functional alveolar capillarity of the human lung (Huh et al. 2010). This is a first step toward organ-on-chip.

## References

- Ainslie KM, Desai TA (2008) Microfabricated implants for applications in therapeutic delivery, tissue engineering, and biosensors. *Lab on a Chip* 8:1864–1878
- Bagalkot V, Zhang L, Nissenbaum EL, Jon S, Kantoff PW, Langer R, Farokhzad OC (2007) Quantum dot aptamer conjugates for synchronous cancer imaging, therapy and sensing of drug delivery based on bi-fluorescence resonance energy transfer. *Nano Lett* 7:3065–3070
- Bharadwaj P, Deutsch B, Novotny L (2009) Optical antennas. *Adv Optics Photonics* 1:438–483
- Biondi M, Ungaro F, Quaglia F, Netti PA (2008) Controlled drug delivery in tissue engineering. *Adv Drug Deliv Rev* 60:229–242
- Boisseau P, Houdy P, Lahmani M (eds) (2010) *Nanoscience. nanobiotechnology and nanobiology*. Springer, Berlin
- Burke P, Rutherglen C (2010) Towards a single-chip, implantable RFID system: is a single-cell radio possible? *Biomed Microdevices* 12:589–596
- Charvet G, Rousseau L, Billoint O, Gharbi S, Rostaing J-P, Joucla S, Trevisiol M, Bourgerette A, Chauvet P, Moulin C, Goy F, Mercier B, Colin M, Spirkovitch S, Fanet H, Meyrand P, Guillemaud R, Yvert B (2010) BioMEA™: a versatile high-density 3D microelectrode array system using integrated electronics. *Biosensors Bioelectronics* 25:1889–1896
- Chen X (ed) (2011) *Nanoplatfrom-based molecular imaging*, Wiley, New York

- Dragoman D, Dragoman M (2008) Tunneling nanotube radio. *J Appl Phys* 104:074314
- Dvir T, Timko BP, Kohane DS, Langer R (2011) Nanotechnological strategies for engineering complex tissues. *Nat Nanotechnol* 6:13–22
- Gannon CJ, Cherukuri P, Yacobson BI, Cognet L, Kanzius JS, Kittrell C, Weisman RB, Pasquali M, Schmidt HK, Smalley RE, Curley SA (2007) Carbon-nanotube-enhanced thermal destruction of cancer cells in a noninvasive radiofrequency field. *Cancer* 110:2654–2665
- Grayson ACR, Choi LS, Tyler BM, Wang PP, Brem H, Cima MJ, Langer R (2003) Multi-phase drug delivery from resorbable polymeric microchip device. *Nat Mater* 2:767–772
- Grayson WL, Fröhlich M, Yeager K, Bhumiratana S, Ete Chan M, Cannizzaro C, Wan LQ, Liu XS, Guo XE, Vunjak-Novakovic G (2010) Engineering anatomically shaped human bone grafts. *Proc Natl Acad Sci* 107:3299–3304
- Gui L, Muto A, Chen SA, Breuer CK, Niklason LE (2009) Development of decellularized human umbilical as small diameter vascular grafts. *Tissue Eng A* 15:2665–2676
- Haeblerle S, Zengerle R (2007) Microfluidic platforms for lab-on-a-chip applications. *Lab Chip* 7:1094–1110
- Hamad-Schifferli K, Schwartz JJ, Santos AT, Zhang S, Jacobson JM (2002) Remote electronic control of DNA hybridization through inductive coupling to an attached metal nanocrystal antenna. *Nature* 415:152–155
- Han J-H, Paulus GLC, Maruyama R, Heller DA, Kim W-J, Barone PW, Lee CY, Choi JH, Ham M-H, Song C, Fantini C, Strano MS (2010) Exciton antennas and concentrators from core-shell and corrugated carbon nanotube filaments of homogeneous compositions. *Nat Mater* 9:833–839
- Hilt JZ, Peppas NA (2005) Microfabricated drug delivery devices. *Int J Pharm* 306:15–23
- Hollenberg BA, Richards CD, Richards R, Bahr DF, Rector DM (2007) A MEMS fabricated flexible electrode array for recording surface field potentials. *J Neurosci Methods* 153:147–153
- Huh D, Mathews BD, Mammoto A, Montoya-Zavala M, Hsin HY, Ingber DE (2010) Reconstitution organ-level lung functions on chip. *Science* 328:1662–1668
- Jain KK (2008) *The handbook of nanomedicine*, Springer, Heidelberg
- Jensen K, Weldon J, Garcia H, Zettl A (2007) Nanotube radio. *Nano Lett* 7:3508–3511
- Ji S-R, Liu C, Zhang B, Yang F, Xu J, Long J, Jin C, Fu D-L, Ni Q-X, Yu X-J (2010) Carbon nanotubes in cancer diagnosis and therapy. *Biochim Biophys Acta* 1806:29–35
- Jia J, Guan W, Sim M, Li Y, Li H (2008) Carbon nanotubes based glucose needle-type biosensor. *Sensors* 8:1712–1718
- Li Y, Swango RS, Tyler B, Henderson PT, Vogel JS, Rosenberg A, Storm PB, Langer R, Brem H, Cima MJ (2004) In vivo release from a drug delivery MEMS device. *J Controlled Release* 100:211–219
- Mernier G, De Keersmaecker K, Bartic C, Borghs G (2007) On-chip controlled release of neurotransmitter molecules. *Microelectronic Eng* 84:1714–1718
- Moglia, Menciassi A, Schurr MO, Dario P (2007) Wireless capsule endoscopy: from diagnostic devices to multipurpose robotic systems. *Biomed Microdevices* 9:235–243
- Najafi K, Wise K (1986) An implantable multi-electrode array with on-chip signal processing. *IEEE Solid-State Circuits* 21:1035–1044
- Nastruzzi C, Luca G, Basta G, Calafiore R (2005) Bio-artificial organs. *Focus Biotechnol* 88:17–37
- Ott HC, Matthisen TS, Goh S-K, Black LD, Kren SM, Netoff TI, Taylor DA (2008) Perfusion-decellularized matrix: using nature's platform to engineer a bioartificial heart. *Nat Med* 14:213–221
- Parashar A, Pandey S (2011) Plant-in-chip: microfluidic system for studying root growth and pathogenic interactions in *Arabidopsis*. *Appl Phys Lett* 98:263703
- Park S, Kim Y-S, Kim WB, Jon S (2009) Carbon nanosyringe array as a platform for intracellular delivery. *Nano Lett* 9:1325–1329
- Pasquarelli A (2008) Biochips: technologies and applications. *Mater Sci Eng C* 28:495–508
- Petersen TH, Calle EA, Zhao L, Lee EJ, Gui L, Raredon MB, Gavrilov K, Yi T, Zhuang ZW, Breuer C, E. Herzog, L. Niklasson (2009) Tissue-engineered lungs for in vivo replantation. *Science* 329:538–541
- Prausnitz MR (2004) Microneedles for transdermal drug delivery. *Adv Drug Deliv Rev* 56:581–587

- Prescott JH, Lipka S, Baldwin S, Sheppard Jr. NF, Maloney JM, Coppeta J, Yomtov B, Staples MA, Santini Jr. JT (2006) Chronic, programmed polypeptide delivery from an implant multireservoir microchip device. *Nat Biotechnol* 24:437–438
- Raphael AP, Prow TW, Crichton ML, Chen X, Fernando GJP, Kendall MAF (2010) Targeted, needle-free vaccinations in skin using multilayered, densely-packed dissolving microprojection arrays. *Small* 6:1785–1793
- Riehemann K, Schneider SW, Luger TA, Godin B, Ferrari M, Fuchs H (2009) Nanomedicine—challenge and perspectives. *Angew Chem Int Ed* 48:872–897
- Santini Jr. JT, Cima MJ, Langer R (1999) A controlled-release microchip. *Nature* 397:335–338
- Schetky LMcd, Jadine P, Moussy F (2003) A closed loop implantable artificial pancreas using thin film nitinol MEMS pumps, Proc. Int. Conf. on Shape Memory and Superelastic Technologies, 1–8, Pacific Groove, California
- Shi J, Votruba AR, Farokhzad OC, Langer R (2010) Nanotechnology in drug delivery and tissue engineering: from discovery to applications. *Nano Lett* 10:3223–3230
- Smith S, Tang TB, Terry JG, Stevenson JTM, Flynn BW, et al. (2007) Development of a miniaturized drug delivery system with wireless power transfer and communications. *IET Nanobiotechnol* 1:80–86
- Staples M, Daniel K, Cima MJ, Langer R (2006) Applications of micro- and nano- electromechanical devices to drug delivery. *Pharmaceut Res* 23:847–863
- Staples M (2010) Microchips and controlled-release drug reservoirs, *Wiley Interdisciplinary Reviews (WIRE)*. *Nanomed Nanobiotechnol* 2:400–417
- Takahata K, Gianchandani Y, Wise KD (2006) Micromachined antenna stents and cuffs for intraluminal pressure and flow. *IEEE Micromach Syst* 15:1289–1298
- Tang TB, Smith S, Flynn BW, Stevenson JTM, Gundlach AM, et al (2008) Implementation of wireless power transfer and communications for an implantable ocular drug delivery. *IET Nanobiotechnol* 2:72–79
- Tsai N-C, Sue C-Y (2007) Review of MEMS-based drug delivery and dosing systems. *Sensor Actuator A* 134:555–564
- Uygun BE et al (2010) Organ reengineering through the development of a transplanted recellularized liver graft using decellularized liver matrix. *Nat Med* 16:814–820
- Ziaie B, Baldi A, Lei M, Gu Y, Siegel RA (2004) Hard and soft micromachining for bioMEMS: review of techniques and examples of applications in microfluidics and drug delivery. *Adv Drug Deliv Rev* 56:145–172
- Zengerle R, Ulrich J, Kluge S, Richter M, Richter A (1995) A bidirectional Si pump. *Sensor Actuator* 50:81–86
- Yun KS, Cho IJ, Bu JU, Kim CJ, Yoon E (2002) A surface-tension driven micropump for low voltage and low power operation. *J MEMS* 11:454–461
- Wang Y, Gao S, Ye W-H, Yoon HS, Yang Y-Y (2006) Co-delivery of drugs and DNA from cationic core-shell nanoparticles self-assembled from a biodegradable copolymer. *Nat Mater* 5:791–796
- Wang W, Soper SA (2007) *Bio-MEMS. Technologies and applications*. CRC Press, London

## Chapter 5

# Biomolecular Architecture for Nanotechnology

**Abstract** This chapter reviews the design principles of biomolecular architecture with applications in nanotechnology and presents examples of zero-, one-, two-, and three-dimensional patterns of inorganic materials assembled on biological scaffolds. The use of nanoscale inorganic scaffolds for biomolecules is briefly discussed.

Electronic nanoscale components separated by nanosized distances, which eventually lead to faster computation, require new technologies. One possible solution to the new generation of nanotechnologies involves the use of biological molecules, and in particular DNA, as scaffolds for electronic circuits. The advantages of DNA scaffolds are the self-assembly process and the specificity of A–T and G–C hydrogen-bonding interactions, as well as our present ability to synthesize and amplify any desired DNA sequence. In addition, the nanostructures constructed from DNA scaffolds are physicochemically stable, which means that they can be stored and processed under environmental conditions that do not need to be especially restrictive to avoid decomposition. The processing of DNA material can be performed with atomic precision by highly specific enzymes.

Because of the relevance of DNA architecture to nanotechnology, many reviews exist on this subject (see, e.g., Seeman 1998; Feldkamp and Niemeyer 2006; Jaeger and Chworos 2006; Lin et al. 2009). We only focus here on specific examples of DNA-based fabrication of inorganic nanoparticle arrays or devices with applications in nanotechnology [see also (Li et al. 2009) for a recent review]. In most cases, nanotechnology-related scaffolding relies on the possibility of attaching chemical groups at certain positions, on which properly functionalized inorganic molecules bind in a subsequent process. DNA-based nanotechnology is a bottom-up self-assembly approach that follows a different strategy compared to inorganic self-assembly: nonequilibrium processes direct the assembly in biological structures, whereas equilibrium-regulated processes are commonly employed in artificial inorganic structures.

## 5.1 DNA-Based Molecular Architectures

Usually, molecular architectures are modular, i.e., composed of basic building blocks called tiles. The design of tiles depends on the application. For instance, the DNA scaffold could be flexible or rigid, dynamic or static, symmetric or asymmetric, potentially infinite or of a certain dimension. Therefore, one must take into account the properties of biological components, for example, single-strand DNA (ssDNA) and double-strand DNA (dsDNA), as well as the interconnections between them that allow their assembly into tiles and more complicated structures.

A DNA strand has two ends, denoted by 5' and 3', which confer a natural orientation to the DNA molecule, such that two complementary ssDNA strands bind in an antiparallel way with respect to these ends. The DNA double helix has a diameter of 2 nm and a helical repeat of 3.4 nm, corresponding to 10.5 bases. As a rule, ssDNA molecules are very flexible and can form tight loop structures, while dsDNA is quite rigid in short strands, up to 150 bp, and flexible if longer (Feldkamp and Niemeyer 2006). ssDNA is used as a template or, especially when immobilized, as capture probe for specific self-assembly of other molecules tagged with complementary base sequences.

The linear dsDNA molecule is still not rigid enough to form two- or three-dimensional structures. More complex DNA-based molecules are needed for this purpose, such as branched junction motifs with three and four arms, which consist of dsDNA helices. These structures, in which the helical arms are connected at the central branching point, are illustrated in Fig. 5.1, different helices being represented with different colors. Branch migration around the branching point is avoided by appropriately choosing the base sequences of all arms.

Branched DNA molecules can form more complex structures by the inclusion of internal loops, which consist of unpaired bases, in the strands (see Fig. 5.1c) or the addition of a bulge to only one strand at the branching point. In the last case, the angle between the helical arms changes to about  $180^\circ$ , as illustrated in Fig. 5.1d. Cyclic structures in which at least one of the helical arm axes does not point towards the center of the junction form knots (Seeman 1998; Feldkamp and Niemeyer 2006).

Branched molecules are still conformational flexible so that several such molecules must be linked together in even more rigid structures, called lattices. A branched DNA molecule links to another one through sticky ends. These unpaired

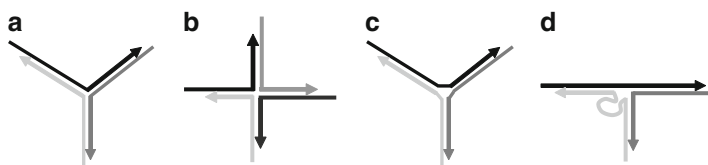


**Fig. 5.1** Branched DNA junction motifs: (a) three-arm junction, (b) four-arm junction, (c) three-arm junction with internal loop, (d) bulged three-arm junction

**Fig. 5.2** Examples of DNA lattices form by periodic assembly of (a) four-arm junctions and (b) bulged three-arm junctions

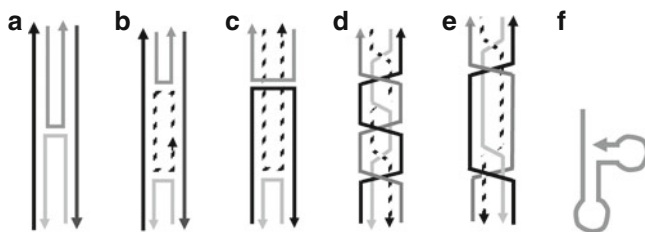
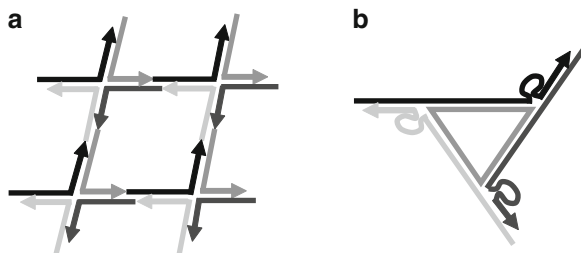


**Fig. 5.3** Crossover tiles: (a) with one crossing point, (b) DAE, (c) DAO, (d) PX, and (e) JX<sub>2</sub>. (f) TectoRNA

base sequences at the end of the helical arms allow self-assembly to other structures by chemical or enzymatic coupling.

For example, when four four-armed junctions assemble the resulting rhomboidal structure looks like in Fig. 5.2a, the acute angle is about 60°. The junctions cross orthogonally only in the presence of the RuvA protein. Similarly, bulged three-armed junctions create a triangular motif as that in Fig. 5.2b, the angles between helical arms being determined by the lengths of the edges.

Rigid regular superstructures that act as building blocks for complex architectures are called crossover tiles. A DNA crossover molecule consists of two dsDNA molecules, which interchange a single strand at a single crossover point, as shown in Fig. 5.3a; more than one crossing points can exist. For example, a double crossover tile, DX, forms by single-strand interchange between two dsDNA at two crossover points. From the five possible DX structural motifs, only two are stable enough: DAE and DAO, characterized, respectively, by an even and odd number of helical half-turns between the crossover points. In these structures, illustrated in Fig. 5.3b, c, the Coulomb repulsion between antiparallel strands is minimized since the minor groove of one helix sits in the major groove of the other. In fact, DX tiles are four-armed junctions linked by neighboring arms, in which branch migration is inhibited by a proper design of base sequences. Analogously, triple crossover tiles, TX, contain three helices that interchange single strands at three crossover points, and so on.

Other DNA motifs encountered in nanodevices based on strand replacement are the paranemic crossover molecules, PX, which form crossovers between two parallel helices at every possible point, and its topoisomerase structure, JX<sub>2</sub>

(see Fig. 5.3d, e). PX are more stable than DX molecules. Crossover tiles can act as building blocks for more complex motifs and can self-assemble in planar periodic patterns or nonplanar architectures through sticky ends, which hybridize with complementary base sequences placed as sticky ends on other tiles.

Other motifs used in bionanotechnology and that can be assembled in larger bidimensional structures are DNA quadruplexes, which consist of four guanine-rich strands that form a bundle with a square cross section in the presence of monovalent cations, and tecto-RNA structures, which contain two connected hairpin loops positioned at a right angle, as shown in Fig. 5.3f (Feldkamp and Niemeyer 2006). A more detailed discussion on RNA architectonics can be found in Jaeger and Chworos (2006). RNA molecules are less stable than DNA, and the Watson–Crick base-pairing principle is less selective. Therefore, they are seldom used in conjunction with inorganic nanotechnology.

Tubular DNA or protein structures can be considered as building blocks for three-dimensional architectures. These nanotubes are in turn assembled from smaller planar tiles, for example, DX tiles, designed such that a curved structure is favored by the orientation and spacing of crossover points. Three-dimensional structures can be obtained by joining together different types of component tiles/molecules. For example, DNA polyhedra have duplexed DNA edges and rigid multiarm junction molecules as vertices (Lin et al. 2009). In other experiments, cubes are constructed with edges consisting of two turns of DNA double helices and faces containing a cyclic strand linked twice to each neighbor (Seeman 1998). Tetrahedra can be opened or closed to act as cage for smaller molecules if hairpin loops, which can be opened by specific fuel strands and closed by corresponding antifuel strands, are incorporated on the edges of tetrahedra. A wide variety of architectures that can be build from DNA strands are described in detail in the review works (Seeman 1998; Feldkamp and Niemeyer 2006; Jaeger and Chworos 2006; Lin et al. 2009).

Nondesirable hybridization between tiles can be avoided by limiting the similarity of base sequences of strands that must not hybridize; powerful computer programs are used to design such sequences, which usually consist of short overlapping subsequences. It is important to know whether the final biomolecular pattern is symmetric or asymmetric since the number of different tiles required to form a specific structure depends on the symmetry of the structure. For example, a bidimensional array of  $N$  tiles with  $m$ -fold symmetry can be self-assembled using  $N/m$  different tiles instead of  $N$ , if this ratio has an integral value, or  $\text{Int}[N/m] + 1$  unique tiles otherwise (Lin et al. 2009). The dimension of a certain structure is controlled by replacing the sticky ends at the tiles that do not bind, i.e., on the boundaries of the structure, by hairpin loops, or blunt ends.

Biological self-assembly of DNA junctions, lattices, or tiles, occur under certain environmental conditions according to the structural information encoded in their base sequence. The self-assembly process is hierarchical, in the sense that the individual tiles form first and their association follows. Spontaneous self-assembly is possible only when the final structure has a lower free energy than the starting components. To synthesize DNA for example, purified oligonucleotides with a properly designed base sequence are mixed at the stoichiometric molar ratio in

an almost neutral buffer solution that contains divalent cations such as  $Mg^{2+}$ , are heated in order to denaturate, and then are gradually cooled such that ssDNA self-assembly by adopting the most energetically favorable conformation reached when the oligonucleotides find the (partially) complementary strands and hybridize. Hybridization takes place under mild environmental conditions and can be reversed. It is important that all hybridized components of a tile have the same hybridization efficiencies. The final motif depends on both tile geometry, which determines the unit cell of the pattern, and sticky ends, which impose the connectivity between tiles and, in particular, the dimensionality of the final structure (Lin et al. 2009). Self-assembly is not, however, a perfect process: it occurs always with a less-than-unity efficiency.

It should be mentioned that, apart from symmetric and repetitive architectures based on interconnected tiles, two-dimensional structures with areas as large as 8,500 nm<sup>2</sup> consisting entirely of distinguishable nucleotides can be obtained by the DNA origami process (Kuzuya and Komiyama 2010). In this case, the scaffold runs back and forth through the whole area and multiple parts in the scaffold are bound by staple strands. Alternatively, DNA origami can be considered as a folded long ssDNA with a resulting shape determined by multiple helper strands.

To use DNA structures as scaffolds for inorganic molecules in nanoelectronic applications, it is necessary to immobilize these molecules on DNA strands, which is achieved either by hybridization between target molecules labeled with DNA strands complementary to that of extensions in the DNA scaffold or by chemically/covalently linking functionalized target molecules with corresponding functional groups on the scaffold (Lin et al. 2009).

## 5.2 Self-Assembled DNA Nanowires

In general, bare DNA has semiconducting properties, its intrinsic conductivity being too low to render it useful as molecular wire. Therefore, metallization of DNA strands is required to increase DNA conductivity. DNA metallization is one of the most common examples of nanotechnologies involving biomolecular templates and among the first to be implemented. In most cases, the metallization process consists of producing first metallic clusters on DNA, which act as nucleation sites for the following selective deposition of a metal layer. The deposition process, which implies the growth of preformed nucleation sites, continues until the gaps between metallic clusters are bridged and a continuous metallic wire is obtained. The metallic nucleation sites are either small metallic particles bound to DNA or bounded metal complexes or ions, which are transformed to metallic clusters by a reduction process. Uniform metal-coated DNA molecules can then bind to macroscopic electrodes by specific molecular recognition. In general, DNA metallization is accompanied by a loss of DNA structural details, and the nanowires are typically several times thicker than the DNA template. Various methods used to metallize and manipulate (stretch and position) DNA nanowires are reviewed in Gu et al. (2006).

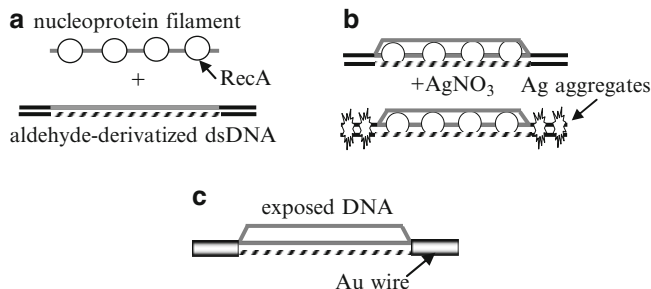


**Fig. 5.4** Main processes in sequence-specific molecular lithography: (a) binding of a nucleoprotein filament on aldehyde-derivatized dsDNA, (b) formation of Ag aggregates by an incubation of the resulting structure in (a) a  $\text{AgNO}_3$  solution, (c) formation of a metallization gap in regions protected by RecA

It should be mentioned that DNA metallization can be achieved not only by using DNA as a template but also by replacing each imino proton of each base pair with a metal ion. The resulting conducting DNA is called M-DNA. A 15 –  $\mu\text{m}$ -long M-DNA molecule that uses phage  $\lambda$ -DNA has been reported in [Rakitin et al. \(2001\)](#), the substituting  $\text{Zn}^{2+}$  metal ion being spaced at about 4 Å irrespective of the base sequence. This conductive wire has sticky ends to attach to electrodes. Imino proton substitution occurs at a pH of 9.0, and, as a consequence, the DNA molecule acquired metallic-like conduction, characterized by a finite zero bias conductance. Metal ions can also be introduced into proteins, more precisely into natural or synthetic polypeptide sequences that fold into three-dimensional structures and able to bind a metal ion ([Lu et al. 2009](#)). We do not refer further to this metallization procedure.

It is often desirable that not all, but only a part of a molecular wire is metallized, task accomplished by the sequence-specific molecular lithography ([Keren et al. 2002](#)). In this process, schematically represented in [Fig. 5.4](#), a nucleoprotein filament is first formed by polymerizing RecA proteins from the *Escherichia coli* bacteria on an ssDNA probe molecule, the filament binding in a subsequent process at a 2,027-base-pair (bp)-long homologous sequence on an aldehyde-derivatized dsDNA substrate that contains 48,502 bp. In the homologous recombination, two DNA molecules (a long dsDNA that acts as scaffold and a short ssDNA) with sequence homology cross over at equivalent sites. In the following step, after incubation in a solution of  $\text{AgNO}_3$ , Ag aggregates form on the substrate except at regions protected by RecA. These aggregates act then as catalysts for electroless Au deposition, such that the unprotected regions are transformed into conductive metal wires. The high-resolution lithography, which has as a result continuous gold wires interrupted by gaps at specific locations, is guided by DNA substrate and probe molecules, while RecA proteins act as a resist, protecting the covered DNA segment against metallization, and incentive for the homologous recombination. The size and location of the insulating gap is controlled by the length and base sequence

of the probe molecule. The length of the gap can vary between few nanometers to few micrometers and is defined with single-base accuracy, i.e., an accuracy of about 0.3 nm.

This sequence-specific lithography can also locate molecular objects and metallic clusters on specific locations along the DNA substrate or can construct DNA junctions, in which a RecA polymerized short molecule undergoes homologous recombination with one end of a long molecule followed by branch migration (Keren et al. 2002). The fabrication of a room-temperature carbon nanotube (CNT) field-effect transistor using DNA templating and homologous genetic recombination was presented in Keren et al. (2003). After the homologous recombination and before incubation in the  $\text{AgNO}_3$  solution in the technological sequence in Fig. 5.4, a streptavidin-coated single-walled CNT (SWCNT) is bound to the RecA-containing strand by first exposing this strand to a primary antibody to RecA and then to a biotin-conjugated secondary antibody with a high affinity to the primary antibodies. In this way, SWCNTs were selectively positioned on RecA via biotin–streptavidin binding. Then, the DNA–CNT complex was stretched on a passivated and oxidized Si wafer so that the DNA and the stiff CNT become aligned. The CNT–FET fabrication ends with the electroless metallization process on the silver clusters nucleation centers, in which RecA acts as resist. The SWCNT, which is longer than the gap determined by RecA, makes good contact with the metallic Au wires because metal is deposited also on the ends of the SWCNT. The technological processes following those in Fig. 5.4a are represented schematically in Fig. 5.5. CNT FETs fabricated by this method, with a p-type conduction channel and lengths of 130–200 nm, work at room temperature and use as gate electrode a  $\text{p}^+$  Si substrate.

Another method of sequence-selective metallization has been described in Burley et al. (2006). In this case, an enzymatic approach was used for selective aldehyde labeling, in which acetylene reporter groups, introduced by polymerase into selected genes, reacted with aldehyde azides to directly incorporate aldehyde functions into the genes. In the following step, Ag deposition was directed to aldehyde-modified DNA only.

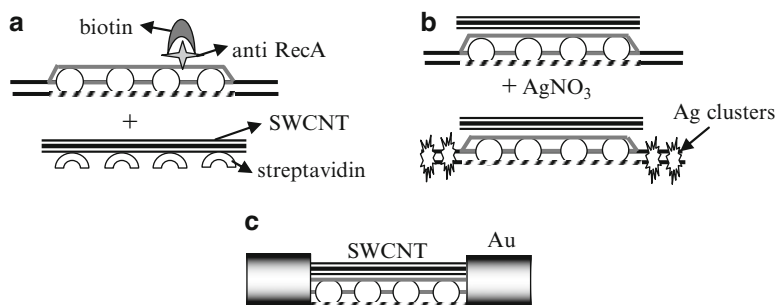


**Fig. 5.5** Fabrication steps of a CNT FET: (a) binding a SWCNT on the homologous sequence in Fig. 5.4a, (b) formation of Ag clusters by incubation of the resulting structure in  $\text{AgNO}_3$ , (c) the final CNT FET

DNA metallization or device fabrication by sequence-specific molecular lithography destroys the specific recognition properties of the DNA scaffold. This can be avoided by embedding the metallization pattern into DNA via a sequence-specific aldehyde derivatization, in which DNA molecules react with glutaraldehyde (Keren et al. 2004). In this way, the DNA scaffold is marked for metallization before the metallization process and can be used for successive biological manipulation. The silver clusters, which act as nucleation sites for the following electroless gold deposition, form by reduction of silver ions by aldehyde groups bound to DNA in the aldehyde-derivatized regions. Electroless deposition is suited for metallization of templates in solution. If immobilized on a substrate, the metallized biological templates are no longer curved or agglomerated.

Nanowire and nanowire arrays on silicon substrates can be fabricated using microtubules as templates (Zhou et al. 2008). Microtubules are rigid and hollow protein tubes with a diameter of about 25 nm and a length of few micrometers, which self-assemble from units called  $\alpha\beta$ -tubulins. Because the microtubule end exposing  $\beta$ -tubulins grows much faster than the end exposing  $\alpha$ -tubulins, growth of a microtubule on substrate is controlled and directed. Therefore, nanowires can easily form by first growing a microtubule that connects two desired locations on a substrate using a tau protein as mediator, followed by covalently binding functionalized 1.4-nm colloidal gold nanoparticles on the microtubule, and, finally, enhancing the diameter of the bound Au nanoparticles by a photochemical method. Microtubule-templated nanowires with lengths between 1 and 20  $\mu\text{m}$  can be obtained in this way, consisting of (possibly agglomerated) gold nanoparticles with diameters of 12–15 nm that enhance the initial microtubule diameter up to 80–100 nm. The resistivity of a typical nanowire with a length of 2.5  $\mu\text{m}$  is  $7.3 \times 10^{-5} \Omega\text{m}$ . In a similar way, arrays of parallel microtubules can first self-assemble and then suffer a metallization process, the average distance between microtubules in the array being of 18 nm; the gold coverage in this case is not as good as for single nanowires.

The fabrication of coaxial metal nanocables has been detailed in Carny et al. (2006). The trilayered metal–insulator–metal structure used self-assembled peptide nanotubes as scaffolds, on which small gold nanoparticles with a diameter of 1.4 nm were attached at specific sites via a recognition molecule incorporated in linker peptides. The linker peptides bind weakly to the surface of the peptide nanotube and covalently to chemical inserts used to bind other molecules, in particular gold nanoparticles. These bound Au nanoparticles act as nucleation sites for selective reduction of gold ions on the exterior surface of peptide nanotubes, the final cable having an external metal coating of 20 nm. An internal metallic layer is obtained by reducing silver on the inner surface of the hollow peptide nanotube; the coaxial nanocable has thus a silver–peptide–gold layered structure. The sequence of processes for the fabrication of the nanocable is illustrated in Fig. 5.6.

Peptide templating was also used to increase the efficiency of dye-sensitized solar cells that incorporate a hollow  $\text{TiO}_2$  nanoribbon network electrode (Han et al. 2010). The highly entangled framework of  $\text{TiO}_2$  nanoribbons, which acts as photoanode, is expected to reduce surface traps and the undesirable recombination rate of

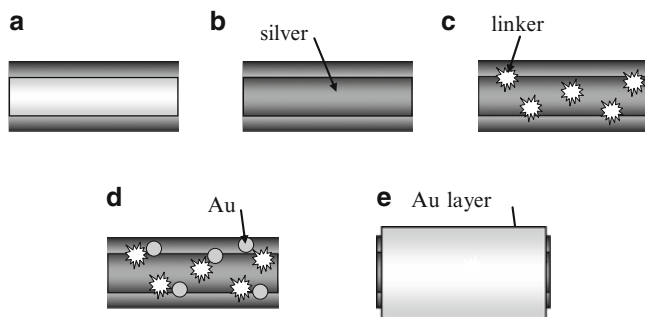


**Fig. 5.6** Fabrication of a trilayered nanocable: (a) hollow peptide nanotubes, (b) silver reduction on the inner surface of the nanotube, (c) addition of linker peptides, (d) binding of Au nanoparticles, and (e) the final nanocable

photogenerated charge carriers in comparison to  $\text{TiO}_2$  nanoparticles, used in common dye-sensitized solar cells. Thus, the 10-nm-thick hollow  $\text{TiO}_2$  nanoribbons fabricated by uniformly coating the diphenylalanine aromatic peptide template allowed an increase of the power conversion efficiency to 3.8%, compared to the 3.5% value of conventional dye-sensitized solar cells that use  $\text{TiO}_2$  nanoparticles. This peptide has a high thermal stability and supports atomic layer deposition processes. The peptide is then removed by calcination at temperatures as high as  $500^\circ\text{C}$ . The thickness of the polycrystalline nanoribbon can be controlled by the calcinating temperature.

### 5.3 Two- and Three-Dimensional Bioarchitectures as Scaffolds

More complex patterns of nanoparticles than lines are required for writing DNA-assisted electronic circuits. Functionalized inorganic nanoparticles can link to DNA strands, which can be either painstakingly assembled one by one on a surface with the help of an AFM tip (Puchner et al. 2008) or can self-assemble in sophisticated architectures. For nanotechnological applications, the latter situation is desirable, although in the first case, a larger freedom of pattern shapes and sizes and available locations can be achieved.

An example of a two-dimensional array, consisting of alternating rows of nanocomponents with different size, self-assembled on a DNA scaffold is presented in Pinto et al (2005). In this case, Au particles with diameters of 5–10 nm were coated with 3'-thiol-modified ssDNA strands complementary to the strands on specific sites on different rows, the interrow spacing being of 32 nm. The self-assembly of Au nanoparticles was caused by DNA hybridization. The pattern of the DNA scaffold consists of rows of different tiles, denoted by A, B, C, and D

**Fig. 5.7** Two-dimensional pattern consisting of alternating rows of Au nanoparticles with different diameters

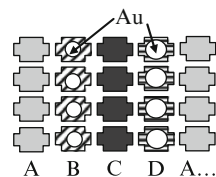
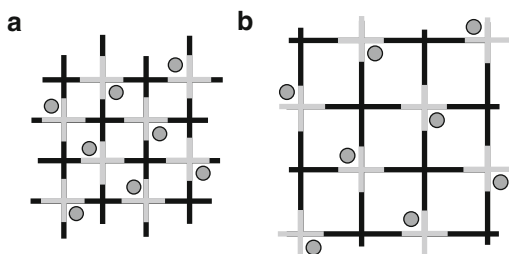


**Fig. 5.8** Two-dimensional pattern obtained from intertwined  $4 \times 4$  tiles with equal (a) or different (b) sizes, with a gold nanoparticle bound to one tile



in Fig. 5.7, the 5 and 10-nm particles hybridizing on binding sites on the D and B tile types, respectively. The tiles form by self-assembly of DX subunits in a buffer solution from a stoichiometric mixture of component oligonucleotides, the B and D tiles having protruding ssDNA sequences. The assembled scaffold is adsorbed on mica surface and then successively exposed to buffer solutions containing the functionalized gold nanoparticles with 5–10 nm diameters. A simpler structure, consisting of rows of functionalized gold nanoparticles with the same diameter, of 6 nm, separated by an interrow spacing of 63 nm, is discussed in [Le et al. \(2004\)](#).

Examples of two-dimensional DNA templates for attachment of particles can be found in [Sharma et al. \(2006\)](#) and are illustrated in Fig. 5.8. The nanoparticles are covalently functionalized with DNA linkers (109-bp ssDNA strands) and then assemble onto DNA scaffolds, which determine the interparticle spacings with nanometer accuracy. In the structures shown in Fig. 5.8, which consist of intertwined cross-shaped  $4 \times 4$  tiles (black and gray) composed of four four-arm DNA branch junctions, 5-nm gold nanoparticles bind to one of the tiles (the gray one). The Au nanoparticles can then be arranged in periodic patterns with different interparticle spacings since the tiles represented by black lines in Fig. 5.8a, b have different sizes: 19.3 and 33 nm, respectively. The patterns are fabricated, self-assembling first the tile decorated with gold nanoparticle and then mixing it with tiles of the other type in solution. The patterns are not perfect squares, but rhombus when the gold nanoparticle is present, the later being located at the obtuse angle of the stressed structure. Additionally, nanotracks can be constructed from the two tile types if assembled only along one direction. Such ribbons obtained from  $4 \times 4$  tiles can be metallized, the resistivity of such a silver nanowire being  $2.4 \times 10^{-6} \Omega\text{m}$  ([Yan et al. 2003](#)).

Another two-dimensional nanoparticle array is shown in Fig. 5.9 ([Zheng et al. 2006](#)). This time, the pattern is formed from two tiles with a triangular shape, two of the DX arms forming a two-dimensional lattice through cohesive

**Fig. 5.9** Two-dimensional pattern consisting of alternating rows of Au nanoparticles with different diameters attached to different tiles

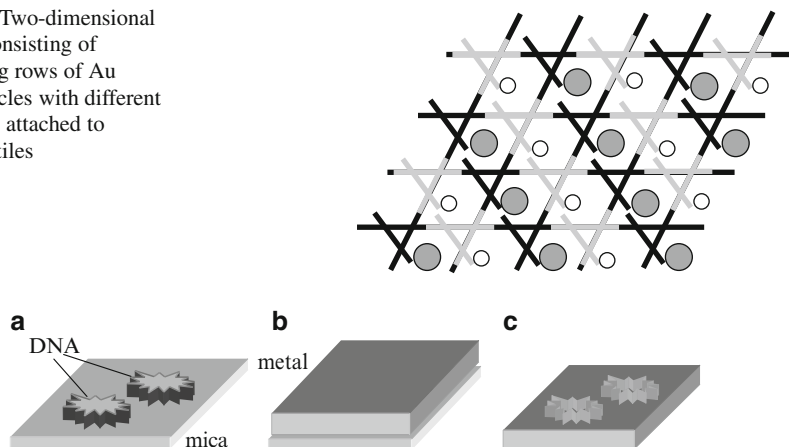


**Fig. 5.10** Negative replication of DNA structures: (a) DNA mask on mica substrate, (b) metal deposition on top of the mask, (c) negative replica of the mask in metal, after lift-off

end binding, while the third direction terminates with a blunt end and so becomes available for attachment of gold nanoparticles. The two-dimensional pattern has a lattice constant of 27.4 nm for triangles with edges consisting of 84 nucleotide pairs. The specificity of gold attachment is enhanced when it is linked with an ssDNA that is part of the motif such that its 5' end is on a blunt end. Different gold nanoparticles can be attached on the two tiles that form the lattice: nanoparticles with diameters of 5 nm are attached on the gray tiles in Fig. 5.9, and those with 10 nm diameter bind to the black tiles.

DNA molecules can affect lithography also as masks. More precisely, negative replica of self-assembled DNA structures can be directly reproduced in metal. The sequence of processes, illustrated in Fig. 5.10, involves evaporation of a 20-nm-thick gold layer on a mica substrate on which DNA masks are first deposited followed by lift-off, process in which the gold film is separated from the mica substrate (Deng and Mao 2004). The negative replica of the DNA mask is thus imprinted in the side of the gold layer that was in contact with the substrate. After peeling off the metal film, the DNA molecules are left intact on the mica substrate. The DNA mask can have any form since it can self-assemble in designed patterns by simply cooling equimolar mixtures of component strands, and its advantage is that the mask dimension is of the nanometer scale, thinner than the currently used lithographic masks. One-dimensional arrays of DX molecules with a width of 4 nm and two-dimensional tetragonal arrays with a grid pitch of 18 nm, as well as more complex structures, were successfully replicated.

Three-dimensional inorganic crystals with precise and controllable lattice constant can be fabricated using synthetic biological scaffolds consisting of cationic membranes and anionic DNA. These scaffolds self-assemble into a lamellar structure composed of one-dimensional lattices of parallel DNA chains sandwiched

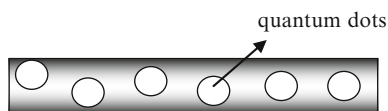
between stacked two-dimensional lipid layers. Then, arrays of CdS nanorods with tunable crystallographic orientation and widths, for example, can be obtained by placing  $\text{Cd}^{2+}$  ions into the interhelical pores situated between strands followed by a reaction with  $\text{H}_2\text{S}$  (Liang et al. 2003). The CdS (002) polar planes are aligned with the negatively charged DNA backbone due to strong electrostatic interactions, the  $60^\circ$  tilt angle between (002) planes and the rod axis having no counterpart in nanorods fabricated from II to VI semiconductors. As the charge density of lipid membranes changes, the inter-DNA spacing can be tuned between 2.5 and 5.7 nm, the type of DNA having no significant influence on the semiconducting nanorod array. However, the inter-DNA spacing decreases drastically for a large  $\text{Cd}^{2+}$  concentration, for which the DNA strands condense.

Three-dimensional crystals with applications in X-ray optics have also been fabricated using the Cowpea mosaic virus extracted from the leaves of California blackeye as template (Prasad et al. 2006). This virus can crystallize in two structures: a body-centered-cubic structure with a lattice constant  $a = 31.7$  nm and a hexagonal structure with lattice constants  $a = 45.1$  nm and  $c = 103.8$  nm. By introducing palladium and platinum inside the body-centered-cubic viral crystal using the electroless deposition method, the interconnected void spaces are filled with metal. A  $1 - \mu\text{m}$ -thick film of these metal-infiltrated three-dimensional viral crystals with unit cell dimension in the X-ray optic range has a maximum reflectivity of 7% for X-rays with a wavelength of 35 nm incident on the  $\{111\}$  crystal face.

Quantum dot arrays with controlled periodicity have been fabricated on functionalized three-dimensional DNA origami nanotubes, constructed by folding a single-stranded M13 mp18 scaffold into a six-helix nanotube bundle by 170 different staple strands; the resulting nanotubes have a diameter of 6 nm and a length of 412 nm and were dispersed on mica substrates for AFM monitoring of the resulting structures (Bui et al. 2010). A programmable quantum dot pattern can be achieved by incorporating biotin-labeled staple strands at specific evenly spaced binding sites along the nanotube axis, on which streptavidin-coated CdSe/ZnS core-shell quantum dots can then bind. Successful fabrication of DNA nanotubes with 5, 9, 15, and 29 binding sites has been reported, corresponding to periodicities of 71, 43, 29, and 14 nm, respectively, but quantum dot attachment on the last two structures was not entirely successful due to quantum dot bridging of multiple sites or steric hindrance. Figure 5.11 illustrates an array of quantum dots bound on a DNA nanotube.

Because DNA origami is synthesized in solution, random arrangements can result from uncontrolled deposition on surfaces. A technique to create selective binding sites for DNA origami on  $\text{SiO}_2$  and diamond-like carbon surfaces, which are of interest in nanotechnology, is described in Kershner et al. (2009). It involves

**Fig. 5.11** Array of quantum dots bound to a DNA nanotube



fabrication of sticky patches similar in size and shape with the DNA origami by using electron-beam lithography followed by dry oxidative etching, sites on which DNA origami bind with 70–95% probability of having an angular dispersion of  $\pm 20^\circ$  on  $\text{SiO}_2$  and of  $\pm 10^\circ$  on diamond-like carbon.

DNA origami has also been used to arrange two types of single-walled CNTs in a two-dimensional pattern (Maune et al. 2010). In this case, the different types of CNTs functionalized with DNA linker molecules bind to specific hooks in ssDNA that can be placed along DNA origami with a resolution of 6 nm. About half of the templates had a single CNT attached and remained intact, as intended. CNTs arranged in cross junctions using this method show stable field-effect transistor behavior. The functionalized CNTs showed a preference in aligning parallel to the complementary hook array.

Not only synthetic but natural biological architectures can be used as scaffolds. For example, the chilo iridescent virus can act as template for the growth of a gold shell (Radloff et al. 2005). In fact, viruses are optimal templates since they can be grown as biotemplates in sizeable quantities and have a specified composition, consisting of a capsid (proteinaceous shell) that encloses the genomic material, and adaptable site-selective surface chemistry. Viruses come also in a large variety of absolutely monodisperse morphologies, with both internal and external surfaces amenable to functionalization with organic or inorganic molecules. The resulting metallodielectric nanostructures support plasmonic resonances, which can be tuned by varying the ratio between the radii of the dielectric core and metallic shell. Nanoparticle plasmon resonances are quantized electron oscillations limited to nanoscale volumes around the boundary of the nanoparticle, which enhance the intensity of an electromagnetic radiation with the same frequency. The core can become hollow and thus available for filling with different dielectrics after removal of the genetic material. In particular, the chilo iridescent virus has a diameter of 140 nm and contains a dsDNA–protein core surrounded by a lipid bilayer, which is sandwiched between outer and inner capsid shells, with 35-nm-long protruding fibrils on the outer surface. The virus is first seeded with gold nanoparticles in a concentrated NaCl electrolyte solution, which decreases the repulsive forces between nanoparticles and favors fibril collapse on the virus capsid, except for large NaCl concentrations, for which the gold nanoparticles aggregate on the virus surface. The seeded viruses are then introduced in a gold ion solution, and Au shells of different thickness form depending on the interaction time/concentration of gold solution. For example, a 22-nm-thick shell exhibits a strong plasmon dipole mode at about 800 nm and a quadrupole resonance at about 550 nm. The resulting gold shells are rough, as suggested also by Fig. 5.12, the surface irregularities broadening the

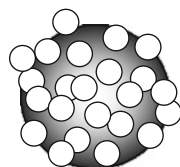


**Fig. 5.12** Gold nanoparticles on the spherical capsid of a virus

nanoshell plasmon spectrum. A recent review on the design principles of building plasmonic nanostructures on DNA scaffolds can be found in [Tan et al. \(2011\)](#).

In another virus-assisted deposition process ([Szuchmacher Blum et al. 2004](#)), gold nanoparticles with diameters of 2 and 5 nm bind via gold–sulfur links at specific sites, separated by precise distances, on a cowpea mosaic virus with an average diameter of 28.4 nm. Because the protein capsid of this virus has an icosahedral shape that results from the assembly of 60 copies of an asymmetric unit, only multiple-of-60 numbers of gold nanoparticles can be attached on the capsid. Gold attachment is only possible if cysteine groups are introduced at designed locations on the virus capsid, on which thiol-reactive nanoparticles are linked by sulfur–gold covalent bonds. The cysteine groups can be arranged in various symmetric patterns, which correspond to different distances between gold nanoparticles that can vary from 5.3 to 8.4 nm.

Viruses such as M13 are real toolkits for synthesizing semiconducting nanowires from materials like ZnS and CdS, as well as magnetic nanowires from CoPt and FePt ferromagnetic alloys, by incorporating specific nucleating peptides into its highly ordered capsid ([Mao et al. 2004](#)). The filamentous viral template can afterwards be removed by an annealing process, which also promoted transformation of polycrystalline into single-crystal nanowires. Modified M13 scaffolds have been used to genetically engineer high-power lithium-ion batteries ([Lee et al. 2009](#)). In such batteries, nanostructured composite electrodes are essential to enhance the transfer of electrons and  $\text{Li}^+$  ions through the structure. Amorphous anhydrous  $\text{FePO}_4$  nanowires that act as cathodes for batteries have been templated on modified M13 viruses loaded with uniformly distributed silver nanoparticles to enhance conductivity. A further increase in performance of lithium-based batteries implies good electrical contact between the active materials, which could be achieved by a percolating network throughout electrodes. An additional genetic modification of M13 allows conducting CNT to bind on the virus and thus to produce nanoscale wiring to the active material.

A similar hybrid structure forms when a semiconducting polymer is encapsulated in a self-assembled protein vault ([Ng et al. 2008](#)). Such filled nanocapsules exist in large numbers in human cells but can be engineered to contain fluorescent nanoparticles useful in nanotechnology, for example, or nanoscale deliverable drugs. Natural vaults are cylindrical structures that resemble a capped barrel, with typical diameters and lengths of 41 and 72 nm, respectively, composed of two identical cuplike halves. When deposited on functionalized mica surface, the vaults can adopt the closed and open conformations, the latter referring to separated halves that assume a flower-like shape with eight petals. In solution, the vaults dissociate for  $\text{pH} < 4$ . After encapsulation in a protein vault in an acid buffer solution with  $\text{pH} = 6.5$ , the environment of an MPS-PPV [poly(2-methoxy-5-propyloxy sulfonate phenylene vinylene)] fluorescent polymer changes and its emission spectrum becomes more intense and red-shifted.

It should be mentioned that in some cases, the biological scaffolds should be alive during the growth process. For example, when a percolating gold monolayer with a thickness of 30 nm is selectively deposited on rod-shaped *Bacillus cereus*

bacteria to bridge a distance of 12  $\mu\text{m}$  between Au electrodes deposited on an oxidized Si wafer, it is essentially that the bacteria are alive, at least during a part of the deposition process (Berry et al. 2004). Lysine-coated gold nanoparticles with diameters of 30 nm in a solution of  $\text{pH} = 7$  can be deposited on bacteria, which have diameters and lengths of 0.9 and 5  $\mu\text{m}$ , respectively, due to the high specific affinity of live bacteria to lysine; this affinity degrades significantly for dead bacteria. The span between the gold electrodes can be bridged by two bacteria covered with gold nanoparticles. A single gold monolayer forms because electrostatic repulsion between positively charged nanoparticles prevents the deposition of following layers. After deposition of the gold nanoparticles, an electric field rearranges the morphology of the metal monolayer such that its electrical conductivity is enhanced more than ten times. The increase in conductivity can be explained by an increase in the number of branching/parallel current pathways in the percolating network.

## 5.4 Nonperiodic Biological Scaffolds for Inorganic Structures

In many cases, inorganic structures, in particular inorganic nanoparticles, use biological molecules as templates, even if the latter show no specific pattern. Individual biomolecular scaffolds can be seen as zero-dimensional templates. For example, biological scaffolds for colloidal quantum dot synthesis can determine and tune their optical properties. In this case,  $\text{Pb}^{2+}$  ions seed a nucleotide ligand, which hinders the growth of a bulk semiconductor if  $\text{S}^{2-}$  ions are added afterwards to the solution (Hinds et al. 2006). In the growth process, the nucleotide binds the precursor metal cation, caps the nanoparticles when the reagents are consumed, passivates the eventual defect states on the surface of the nanoparticle, and favors the formation of stable dispersed nanoparticles in solution. The process takes place for a molecular ratio nucleotide: $\text{Pb}^{2+}$  :  $\text{S}^{2-}$  of 3:1:1. The spherical PbS nanocrystals obtained using the GTP nucleotide have a diameter of 4 nm and show photoluminescence with a quantum efficiency of 1–2%.

CdS semiconductor nanocrystals can be also fabricated using transfer RNA (tRNA) polynucleotides from *E. coli* with a cloverleaf secondary structure as template and nanocrystal ligands (Ma et al. 2006). In this case, no additional ligand or functionalization is needed for the aqueous synthesis of CdS. The spherical CdS particles synthesized with this tRNS from ions of  $\text{Cd}^{2+}$  and  $\text{S}^{2-}$  have mean diameters of  $4.4 \pm 0.4$  nm, whereas semiconductor nanoparticle diameters obtained with a mutant tRNA had larger values, of  $5.5 \pm 1.0$  nm.

Biomolecules can also act as active templates for the growth of inorganic architectures. For example, enzymes modified with gold nanoparticles catalyze the formation of metallic nanowires and nanoparticles with different morphologies (triangular, spherical, prismatic, etc.) and allow the orthogonal growth of nanowires from different metals if immobilized on Si surfaces (Willner et al. 2006).

Although plasmonics usually requires linear chains of metallic nanoparticles to guide surface plasmon resonances along the regions with enhanced electromagnetic

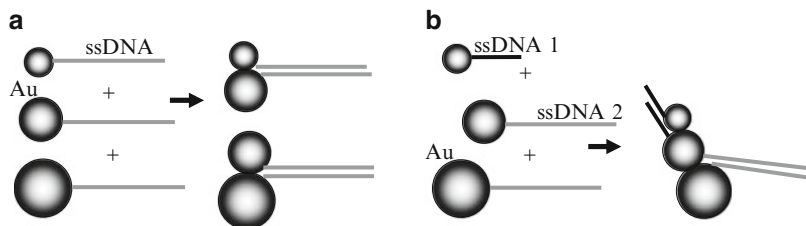


**Fig. 5.13** Self-assembled groups for plasmonic applications containing (a) two and (b) three nanoparticles with different diameters

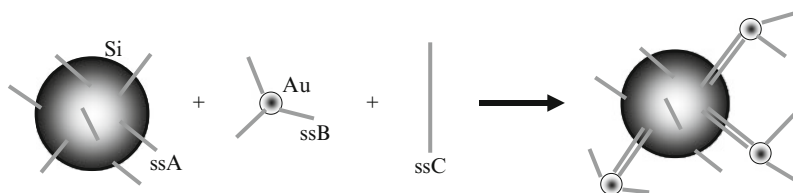


**Fig. 5.14** Formation of satellite structures

field, nonperiodic assembly of nanoparticles can show also plasmon resonances if the distances between particles are of only few nanometers. In this case, the plasmonic modes of individual nanoparticles hybridize analogously to hybridization of electron orbitals in molecules. Such groups of nanoparticles, consisting of groups of Au particles with diameters of 5, 8, and 18 nm, can be obtained by self-assembling on a DNA scaffold (Bidault et al. 2008). More precisely, if phosphine-coated gold nanoparticles with different diameters are functionalized either with a 5'-thiolated ssDNA or with a 3'-thiolated ssDNA with complementary strands, strand hybridization forms asymmetric groups of two particles, whereas a group of three particles forms when one type of nanoparticle is sequentially functionalized with different ssDNA molecules (see Fig. 5.13). Estimates show that these groups of particles locally enhance electromagnetic fields up to four orders of magnitude, depending on the interparticle spacing, particle diameters, and the angle between the particles in the three-particle group.

One of the successes of DNA-driven self-assembly processes is the fabrication of congregations of nanoparticles with different properties and sizes. In particular, small metallic particles, with a diameter of 11 nm, can link to the surface of large, mesoporous silica, with diameters of 100 nm, such that a satellite structure forms (Sadasivan et al. 2005). In this assembly, shown schematically in Fig. 5.14, both components can be accessed and multifunctionality can be achieved. Moreover, the structure is reversible. To form satellite nanostructures, the mesoporous silica particles are functionalized with a 12-bp single-strand oligonucleotide ssA and the gold particles are functionalized by another 12-bp ssDNA, ssB, self-assembly being initiated when a target 24-bp single-strand nucleotide ssC, complementary with both ssA and ssB, is introduced in the solution containing the functionalized gold and

mesoporous silica particles. More than 50% of gold nanoparticles are conjugated on the surface of the bigger spheres but remain well separated from the surface, a mesoporous silica particle containing 5–10 gold nanoparticles, while retaining its mesopores, which are hexagonally arranged open channels with a 3 nm width.

The DNA-templated arrangement of nanoparticle arrays is not always restraint to small sizes, such as a DNA strand or even a DNA architectural pattern. For patterning self-assembly structures on large areas, the assembly technique can be combined with lithography. In particular, electron-beam lithography can be used to define with high-resolution domains on which self-assembly of specific biological molecules from solution occurs (Sabella et al. 2009). A functionalized substrate with a desired pattern is thus obtained after the removal of the resist and can be used as template in a further site-specific assembly of probe species by hybridization with a complementary DNA strand, for example, which become immobilized on desired areas of the substrate. The remaining substrate area can be used to immobilize another type of molecule, for example, a fluorophore which emits in another spectral range than the initial probe fluorophore. The resolution of e-beam lithography and thus of the DNA patterns is of the order of nanometers, but the method is costly and time-consuming.

An inexpensive, large-area printing technique of DNA patterns called subtractive printing has been developed in Noh et al. (2009) and is schematically represented in Fig. 5.15. Using this method, which involves adsorption of ssDNA solutions on a polydimethylsiloxane (PDMS) substrate, followed by drying in a humidified atmosphere, subtraction printing of DNA films on a silicon master, and finally transfer of the remaining DNA on silicon substrates, it is possible to pattern DNA

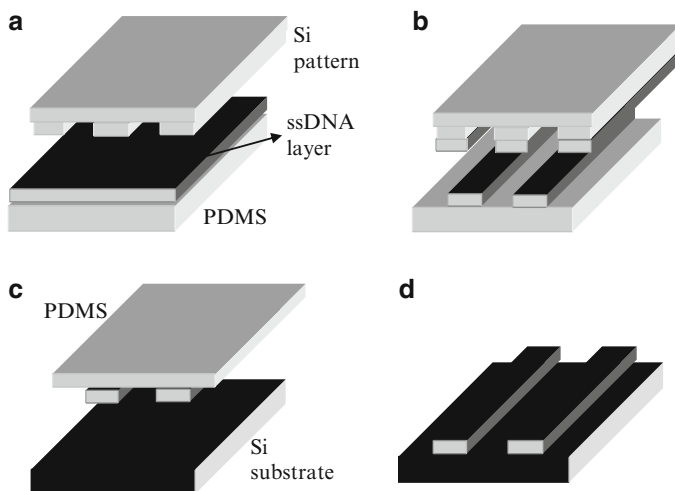


**Fig. 5.15** Subtractive printing: (a) DNA film and the Si master, (b) subtraction printing of DNA films on the silicon master, (c) transfer of the remaining DNA on silicon substrates, (d) the transferred pattern

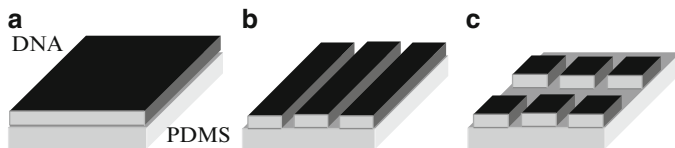
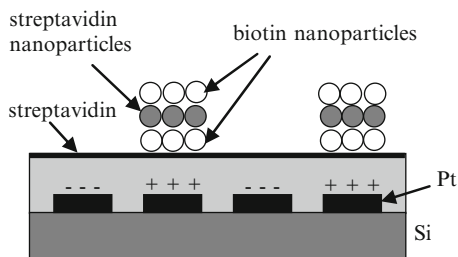


**Fig. 5.16** Double subtraction method: (a) initial DNA layer on PDMS, (b) the pattern after the first subtraction and (c) after the second subtraction process

**Fig. 5.17** Electric-field-directed self-assembly



strands over areas of 4 mm, with a resolution of 50 nm. Colloidal conjugated gold nanoparticles with dimensions of 10 nm can then bind on the DNA patterns and show long-range order if confined in sub-100-nm domains. The method relies on the fact that DNA is transferred to the silicon master only when there is conformal contact between DNA and the master surface. In particular, it was shown that silicon masters with holes with diameters of 180 nm produce dot patterns of ssDNA with the same diameter on silicon, arrays of ssDNA lines with widths of 50 nm, and crossed ssDNA line patterns with widths of 100 nm can be generated.

A two-dimensional large-area DNA-templated nanoparticle pattern, with long-range order over 1–2  $\mu\text{m}$ , can be obtained by confining the nanoparticles to surfaces covered by patterns of DNA molecules (Noh et al. 2010) that can be formed by the double subtraction method. This method involves a double subtraction printing on two silicon masters with orthogonal groove directions (see Fig. 5.16). Such two-dimensional DNA patterns have sharp edges and corners, can be as thin as 4–5 nm, and can be fabricated on PDMS substrates, with a resolution better than 200 nm. Inside such parallelogram-shape DNA features with dimensions ranging from 3 to 200 nm, 10-nm functionalized gold nanoparticles are arranged in hexagonally packed superlattices due to a combination of thermal annealing and interparticle DNA hybridization.

One of the problems of self-assembly is the formation of undesired nonspecific binding, particularly important for high concentrations of analytes which, however, speed the assembly process. A solution to avoid nonspecific binding and to fabricate multilayer structures in a relatively short time interval is the electric-field-directed self-assembly (Dehlinger et al. 2007). In this case, positive and negative voltages are applied on adjacent Pt electrodes patterned over a Si substrate, as shown in Fig. 5.17, the electrodes being embedded in a covering layer that contains streptavidin on

top of it. Then, if negatively charged biotinylated nanoparticles in solution are placed over the structure, these concentrate above the positively charged electrodes and bind to the streptavidin layer. A further nanoparticle layer can be added if negatively charged streptavidin-coated nanoparticles are introduced, which bind with the previous immobilized biotin-coated nanoparticles, and so on. A single layer of 40-nm fluorescent particles can form in 15 s and 50 alternate layers need only 1 h for completion, fractures appearing after more than 50 deposited layers. The structure can then be lifted-off and float freely in the solution, if desired. More complex structures, consisting of six layers of 40-nm particles followed by four layers of 200-nm particles and a final six layers of 40-nm particles can be assembled in this way.

## 5.5 Inorganic Scaffolds for Biomolecules

CNTs are ideal for scaffolds for tissue regeneration due to their mechanical strength, flexibility, and low density compared to other ceramic-based or metallic scaffolds. In addition, CNTs are not biodegradable, so that can be used as long-term implants, and have the right dimension for scaffolds aimed at bone or neural regeneration. A review of CNT and carbon nanofiber applications in regenerative medicine and, in particular, in bone and tissue regeneration, can be found in [Tran et al. \(2009\)](#).

The length and diameter of a single-walled CNT, with values between 100 and 300 nm and, respectively, 0.5 and 1.5 nm, are comparable to the size of collagen fibrils and thus can easily mimic collagen as a scaffold on which hydroxyapatite (HA), the major component of bone, grows. However, to attract calcium cations that initiate HA crystallization, and thus mineralizes the bone matrix proteins produced by osteoblasts, CNTs must first be functionalized.

Analogously, CNT functionalized with bioactive molecules is appropriate for neural regeneration due to its electrical conductivity and dimensions similar to that of small nerve fibers. As extracellular scaffold for neural growth, CNTs can also control neurite branching and outgrowth if properly chemically modified. In particular, the surface charge of CNTs affects neurite control. At a physiological pH of 7.35, hippocampal neuronal cultures from rats grew well on neutral, positively and negatively charged multiwalled CNTs, and zwitterionic CNTs, with almost the same concentration of positive and negative charged groups, no difference being observed in the number of neurites per neuron ([Hu et al. 2004](#)). However, the neurite branching and outgrowth, characterized by the number of growth cones and neurite length, is most developed in positively charged CNTs, moderate in zwitterionic and neutral CNTs and least developed in negatively charged CNTs. The surface charge density of chemically modified single- and multiwalled CNTs influence also the rate of cell growth and the osteoblast morphology when CNTs are used as scaffolds for proliferation of osteosarcoma rat cells and formation of bone-like tissues ([Zanello et al. 2006](#)).

Three-dimensional networks of multiwalled CNTs comprising interconnected cavities are ideal scaffolds for seeding and growth of biological cells, in particular mouse fibroblast cells (Correa-Duarte et al. 2004). This particular architecture of CNTs forms from vertically aligned arrays of MWCNTs, which are subjected to an oxidation process that generates carboxylic groups at the ends of MWCNT as well as at the sidewall defects. This functionalization process of MWCNT takes place in acid solution, which generates tensile and capillary forces between the aligned tubes that lead to their flattening at positions on the array with higher densities. A three-dimensional structure consisting of polygon cavities with almost honeycomb shapes separated by perpendicular walls forms when nanotubes collapse from opposite directions. The spatial distribution of structure can be controlled by the lengths of the aligned MWCNTs: pyramid-like structure form for shorter nanotubes and interconnected cavities for longer MWCNTs, the average diameters of the cavities being shorter for shorter nanotubes. This cross-linking of MWCNTs provides a larger surface for cell attachment and improves the mechanical properties of the structure.

## References

- Berry V, Rangaswamy S, Saraf RF (2004) Highly selective, electrically conductive monolayer of nanoparticles on live bacteria. *Nano Lett* 4:939–942
- Bidault S, García de Abajo GJ, Polman A (2008) Plasmon-based nanolenses assembled on a well-defined DNA template. *J Am Chem Soc* 130:2750–2751
- Bui H, Onodera C, Kidwell C, Tan YP, Graugnard E, Kuang W, Lee J, Knowlton WB, Yurke B, Hughes WL (2010) Programmable periodicity of quantum dot arrays with DNA origami nanotubes. *Nano Lett* 10:3367–3372
- Burley GA, Gierlich J, Mofid MR, Nir H, Tal S, Eichen Y, Carell T (2006) Directed DNA metallization. *J Am Chem Soc* 128:1398–1399
- Carny O, Shalev DE, Gazit E (2006) Fabrication of coaxial metal nanocables using a self-assembled peptide nanotube scaffold. *Nano Lett* 6:1594–1597
- Correa-Duarte MA, Wagner N, Rojas-Chapana J, Morszeck C, Thie M, Giersig M (2004) Fabrication and biocompatibility of carbon nanotube-based 3D networks as scaffolds for cell seeding and growth. *Nano Lett* 4:2233–2236
- Dehlinger DA, Sullivan BD, Esener S, Heller MJ (2007) Electric-field-directed assembly of biomolecular-derivatized nanoparticles into higher-order structures. *Small* 3:1237–1244
- Deng Z, Mao C (2004) Molecular lithography with DNA nanostructures. *Angew Chem Int Ed* 43:4068–4070
- Feldkamp U, Niemeyer CM (2006) Rational design of DNA nanoarchitectures. *Angew Chem Int Ed* 45:1856–1876
- Gu Q, Cheng C, Gonela R, Suryanarayanan S, Anabathula S, Dai K, Haynie DT (2006) DNA nanowire fabrication. *Nanotechnology* 17:R14–R25
- Han TH, Moon H-S, Hwang JO, Seok SI, Im SH, Kim SO (2010) Peptide-templating dye-sensitized solar cells. *Nanotechnology* 21:185601
- Hinds S, Taft BJ, Levina L, Sukhovatkin V, Dooley CJ, Roy MD, MacNeil DD, Sargent EH, Kelley SO (2006) Nucleotide-directed growth of semiconductor nanocrystals. *J Am Chem Soc* 128:64–65

- Hu H, Ni Y, Montana V, Haddon RC, Parpura V (2004) Chemically functionalized carbon nanotubes as substrates for neuronal growth. *Nano Lett* 4:507–511
- Jaeger L, Chworos A (2006) The architectonics of programmable RNA and DNA nanostructures. *Curr Opin Struct Biol* 16:531–543
- Keren K, Berman RS, Braun E (2004) Patterned DNA metallization by sequence-specific localization of a reducing agent. *Nano Lett* 4:323–326
- Keren K, Krueger M, Gilad R, Ben-Yoseph G, Sivan U, Braun E (2002) Sequence-specific molecular lithography on single DNA molecules. *Science* 297:72–75
- Keren K, Berman RS, Buchstab E, Sivan U, Braun E (2003) DNA-templated carbon nanotube field-effect transistor. *Science* 302:1380–1382
- Kershner RJ, Bozano LD, Micheel CM, Hung AM, Fornof AR, Cha JN, Rettner CT, Bersani M, Frommer J, Rothmund PWK, Wallraff GM (2009) Placement and orientation of individual DNA shapes on lithographically patterned surfaces. *Nat Nanotechnol* 4:557–561
- Kuzuya A, Komiyama M (2010) DNA origami: fold, stick and beyond. *Nanoscale* 2:310–322
- Le JD, Pinto Y, Seeman NC, Musier-Forsyth K, Taton TA, Kiehl RA (2004) DNA-templated self-assembly of metallic nanocomponent arrays on a surface. *Nano Lett* 4:2343–2347
- Lee YJ, Yi H, Kim W-J, Kang K, Yun DS, Strano MS, Ceder G, Belcher AM (2009) Fabricating genetically engineered high-power lithium-ion batteries using multiple virus genes. *Science* 324:1051–1055
- Li H, Carter JD, LaBean ThH (2009) Nanofabrication by DNA self-assembly. *Mater Today* 12: 24–32
- Liang H, Angelini TE, Ho J, Braun PV, Wong GCL (2003) Molecular imprinting of biomineralized CdS nanostructures: crystallographic control using self-assembled DNA-membrane templates. *J Am Chem Soc* 125:11786–11787
- Lin C, Liu Y, Yan H (2009) Designer DNA nanoarchitectures. *Biochemistry* 48:1663–1674
- Lu Y, Yeung N, Sieracki N, Marshall NM (2009) Design of functional metalloproteins. *Nature* 460:855–862
- Ma N, Dooley CJ, Kelley SO (2006) RNA-templated semiconductor nanocrystals. *J Am Chem Soc* 128:12598–12599
- Mao C, Solis DJ, Reiss BD, Kottman ST, Sweeney RY, Hayhurst A, Georgiou G, Iverson B, Belcher AM (2004) Virus-based toolkit for the directed synthesis of magnetic and semiconducting nanowires. *Science* 303:213–217
- Maune HT, Han S, Barish RD, Bockrath M, Goddard III WA, Rothmund PWK, Winfree E (2010) Self-assembly of carbon nanotubes into two-dimensional geometries using DNA origami templates. *Nat Nanotechnol* 5:61–66
- Ng BC, Yu M, Gopal A, Rome LH, Monbouquette HG, Tolbert SH (2008) Encapsulation of semiconducting polymers in vault protein cages. *Nano Lett* 8:3503–3509
- Noh H, Hung AM, Choi C, Lee JH, Kim J-Y, Jin S, Cha JN (2009) 50 nm DNA nanoarrays generated from uniform oligonucleotide films. *ACS Nano* 3:2376–2382
- Noh H, Choi C, Hung AM, Jin S, Cha JN (2010) Site-specific patterning of highly ordered nanocrystal superlattices through biomolecular surface confinement. *ACS Nano* 28:5076–5080
- Pinto YY, Le JD, Seeman NC, Musier-Forsyth K, Taton TA, Kiehl RA (2005) Sequence-encoded self-assembly of multiple-nanocomponent arrays by 2D DNA scaffolding. *Nano Lett* 5: 2399–2402
- Prasad T, Turner M, Falkner J, Mittleman D, Johnson J, Lin T, Colvin V (2006) Nanostructured virus crystals for X-ray optics. *IEEE Trans Nanotechnol* 5, 93–96
- Puchner EM, Kufer SK, Strackharn M, Stahl SW, Gaub HE (2008) Nanoparticle self-assembly on a DNA-scaffold written by single-molecule cut-and-paste. *Nano Lett* 8:3692–3695
- Radloff C, Vaia RA, Brunton J, Bouwer GT, Ward VK (2005) Metal nanoshell assembly on a virus bioscaffold. *Nano Lett* 5:1187–1191
- Rakitin A, Aich P, Papadopoulos C, Kobzar Yu, Vedenev AS, Lee JS, Xu JM (2001) Metallic conduction through engineered DNA: DNA nanoelectronic building blocks. *Phys Rev Lett* 86:3670–3673

- Sabella S, Brunetti V, Vecchio G, Della Torre A, Rinaldi R, Cingolani R, Pompa PP (2009) Micro/nanoscale parallel patterning of functional biomolecules, organic fluorophores and colloidal nanocrystals. *Nanoscale Res Lett* 4:1222–1229
- Sadasivan S, Dujardin E, Li M, Johnson CJ, Mann S (2005) DNA-driven assembly of mesoporous silica/gold satellite nanostructures. *Small* 1:103–106
- Seeman NC (1998) Nucleic acid nanostructures and topology. *Angew Chem Int Ed* 37:3220–3238
- Sharma J, Chhabra R, Liu Y, Ke Y, Yan H (2006) DNA-templated self-assembly of two-dimensional and periodical gold nanoparticle arrays. *Angew Chem Int Ed* 45:730–735
- Szuchmacher Blum A, Soto CM, Wilson CD, Cole JD, Kim M, Gnade B, Chatterji A, Ochoa WF, Lin T, Johnson JE, Ratna BR (2004) Cowpea mosaic virus as a scaffold for 3-D patterning of gold nanoparticles. *Nano Lett* 4:867–870
- Tan SJ, Campolongo MJ, Luo D, Cheng W (2011) Building plasmonic nanostructures with DNA. *Nat Nanotechnol* 6:268–276
- Tran PA, Zhang L, Webster TJ (2009) Carbon nanofibers and carbon nanotubes in regenerative medicine. *Adv Drug Deliv Rev* 61:1097–1114
- Willner I, Baron R, Willner B (2006) Growing metal nanoparticles by enzymes. *Adv Mater* 18:1109–1120
- Yan H, Park SH, Finkelstein G, Reif JH, LaBean TH (2003) DNA-templated self-assembly of protein arrays and highly conductive nanowires. *Science* 301:1882–1884
- Zanello LP, Zhao B, Hu H, Haddon RC (2006) Bone cell proliferation on carbon nanotubes. *Nano Lett* 6:562–567
- Zheng J, Constantinou PE, Micheel C, Alivisatos AP, Kiehl RA, Seeman NC (2006) Two-dimensional nanoparticle arrays show the organizational power of robust DNA motifs. *Nano Lett* 6:1502–1504
- Zhou JC, Gao Y, Martinez-Molares AA, Jing X, Yan D, Lau J, Hamasaki T, Ozkan CS, Ozkan M, Hu E, Dunn B (2008) Microtubule-based gold nanowires and nanowire arrays. *Small* 4:1507–1515

## Chapter 6

# Biomolecular Machines

**Abstract** This chapter presents several devices, such as actuators and switches, based on conformational changes in biomolecules, as well as biomolecular walkers and motors, which change their spatial position and can also carry cargoes from one point to another.

The biomolecular machines described in this chapter are based either on conformation changes of a biological molecule or on its motility. Reviews on DNA nanomachines that address the problems of the different driven mechanisms and waste products can be found in [Liu and Liu \(2009\)](#), [Simmel and Dittmer \(2005\)](#), and [Dragoman and Dragoman \(2009\)](#).

In the vast majority of cases, the conformation change is due to hybridization of DNA, which changes its state from the nonstiff ssDNA to much stiffer dsDNA, although different conformations of dsDNA can also be involved in these devices. Not all conformation changes result in modifications of the dimensions of a molecule. For example, the transition between right-handed to left-handed DNA and RNA, known respectively as the B–Z and A–Z transitions, do not change the dimensions of the molecules but influence the fluorescent signal of aminopurine, attached to DNA or RNA; the fluorescence is high in the left-handed form and low in the right-handed form ([Tashiro and Sugiyama 2005](#)). These transitions are controlled by salt concentration or temperature: the left-handed state of DNA is stable at lower temperatures, while for RNA, the thermal response is different, i.e., the left-handed state is favored at high temperatures. We are interest here only in the conformation changes related to modifications of biomolecule dimensions.

Motile biological molecules are called motors because they convert one form of energy, generally chemical, into mechanical energy. Biological motors, perfected in millions of years of evolution, are in many ways superior to man-made motors because they are smaller (have nanometer to micrometer sizes), highly specialized, and, generally, convert other forms of energy into mechanical energy with better efficiency. Nature had perfected a number of biomolecular motors. There are linear motors, which are protein machines that step along protein tracks in the cytoplasm

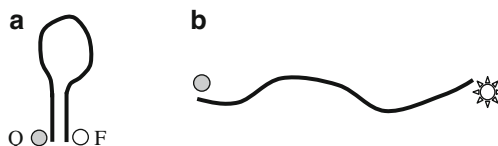
using ATP hydrolysis as fuel, and rotary motors. Examples of rotary motors are flagella, which are complex structures that contain approximately 20 parts and propel bacteria fueled by an ion flux (Berg 2003), and the  $F_1F_0$ -type ATP synthase enzyme, which controls energy interconversion in cells and consists of two interconnected rotary motors (Capaldi and Aggeler 2002). Linear motors include myosins, which glide on actin filaments, and kinesins and dyneins, which move on microtubules (Schliwa and Woehlke 2003). Myosin is involved in muscle contraction. To provide the large forces needed to contract skeletal muscles, for example, myosin motors and actin filaments work collectively. Kinesin motors transport cargoes in the form of vesicles or organelles within a biological cell along microtubule filaments, toward their plus ends, in 8-nm steps resulting from an asymmetric hand-over-hand mechanism that involves an alternation between two conformational states (Yildiz and Selvin 2005). The mechanical energy necessary for these enzymatic biomotors, each generating forces of 5–6 pN, is provided by conversion of the chemical energy derived from adenosine triphosphate. The interest for kinesin motors in nanotechnology derives from their ability to work outside biological cells, in solutions with controlled temperature and pH. Microtubules, which are cylindrical hollow protein filaments with an outer diameter of 24 nm and a length of a few micrometers, can also self-assemble in vitro from tubulin heterodimers.

Artificial molecular motors constitute an emerging research area. In many cases, artificial motors do not involve biological molecules [see Kay et al. (2007) for a review], but the focus of this chapter is on synthetic biomolecular motors. These motors should benefit from a detailed theoretical study of the natural biological motors. A common denominator of the latter is that they are small, out-of-equilibrium, and stochastic systems. Several models have been devised to study the operation modes and thermodynamics of biomolecular motors, with particular emphasis on kinesin. Among these, we mention the minimal ratchet model for fluctuating systems (Lacoste et al. 2008), a model that uses the general network representation for the motor and includes the energetics of ATP hydrolysis and the separation of time scales of mechanical and chemical processes (Liepelt and Lipowsky 2009), and a model based on the overdamped Langevin equation that incorporates experimentally accessible parameters such as ATP concentration, the external load, or the step of the motor (Ciudad et al. 2005). The collective dynamics of kinesin motors has been detailed in Hendricks et al. (2009). Rotary biomotors have also received attention, being modeled as nanoelectromechanical systems that convert the transmembrane electrochemical proton gradient into mechanical energy (Smirnov et al. 2008).

## 6.1 Biological Actuators and Switches

The biological machines included in this section are based on conformation changes. An example of a photon-driven nanomotor consisting of a single molecule that contains a hairpin DNA structure, which incorporates azobenzene moiety, has been

**Fig. 6.1** Photon-driven nanomotor in the closed state (a) and the opened state (b)



described in Kang et al. (2009). The hairpin is formed from a 19-base loop and a 6-base pair (bp) stem section. This nanomotor generates no waste and operates under UV irradiation based on the isomerization between the *trans* and *cis* forms of azobenzene, which have planar and nonplanar conformations. As shown in Fig. 6.1, in the closed state, the azobenzene moiety tethered on one end of the hairpin backbone is in the *trans* form, and the DNA molecule is in the hairpin structure, conformation that changes to *cis* under the action of UV light and transition that destabilizes the stem duplex and disrupts the hairpin structure; the DNA adopts in this case a linear form. The operation of the nanomotor can be monitored by observing the fluorescence of a fluorophore F bound at the end of the hairpin structure opposed to that where azobenzene moieties are tethered, which can be quenched or not by a quencher Q attached to the other end depending on the distance between F and Q. In the closed state, the fluorescence is quenched since F and Q are in close proximity, while in the opened state, the fluorescence increases. The nanomotor is fully reversible; the inverse transition, between *cis* and *trans* azobenzene, implies a transition between opened and closed states, occurring under illumination with visible light. The distance between the two ends of the DNA molecule increases from 2.2 nm in the closed state to 10.2 nm in the opened configuration, these values corresponding to estimated forces of 3.1 pN and 1.5 pN, respectively. Regarding the work needed to extend the molecule as the output mechanical energy, the conversion efficiency of the energy provided by UV photons is of the order of  $10^{-7}$ – $10^{-6}$ . A similar photon-driven switching of RNA digestion based on changes in topological confirmation of a photoresponsive DNAzyme, containing azobenzene-modified sequences at its ends, has been detailed in Zhou et al. (2010).

RNA control of DNA rotary machines that rely on conformation changes has been reported in Zhong and Seeman (2006). Rotary devices such as PX-JX<sub>2</sub> can convert DNA sequences in instructions for polymer assembly when controlled by DNA strands in solution, RNA control allowing device response to signals originating by transcriptional logic circuits.

Conformation change of a DNA molecule in response to pH modification has been reported in Liu et al. (2006). In this case, the nanomachine is fueled by protons and switches its conformation between a closed, quadruplex state, called *i*-motif, stable for pH < 6.5, and an open, rigid double-stranded structure, which is stable for pH > 6.5; no waste products exist that could limit the lifetime of the machine. Figure 6.2 illustrates this conformation change. The quadruplex state forms due to noncanonical base pairs between cytosine C and protonated cytosine, CH<sup>+</sup> (denoted also as C<sup>+</sup>), the *i*-motif DNA folding at the locations of the four CCC

**Fig. 6.2** pH-driven conformation change of a DNA molecule between a quadruples state (a) and a rigid state (b)

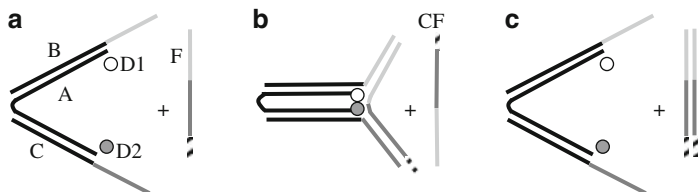
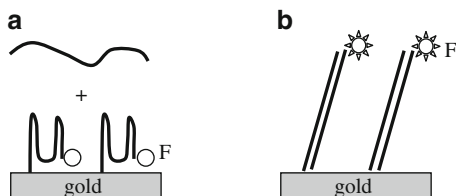


**Fig. 6.3** Conformation changes of a DNA tweezer from the opened state (a) into the closed state (b) and back again (c)

cytosine stretches. The  $\text{CH}^+$  complexes are absent in basic pH solutions when, in the presence of complementary strands, DNA hybridizes into a straight, linear structure.

To monitor the nanomotor, a rhodamine green fluorophore F is attached at the 3' end of the DNA strand, which is immobilized via gold/thiol self-assembly on precise locations on a microstructured gold layer deposited on a glass substrate. In the quadruplex state, F is quenched by the nearby gold surface due to the efficient energy transfer mechanism, while in the hybridized state, F is lifted up with about 2.5 nm and emits a green fluorescent signal four times stronger than in the closed state. The nanomachine is highly reversible upon cyclic pH changes that transition from one state to another, taking place in less than 5 min. If the DNA molecules are immobilized on the surface of a cantilever, it is possible to measure the force exerted during the conformation change. It was found that the open-to-close stroke of a single motor induced a force of about  $11 \text{ pN m}^{-1}$ , which corresponds to  $32 \text{ mN m}^{-1}$  compressive stress on the surface of a silicon cantilever with length, width, and thickness of  $500 \mu\text{m}$ ,  $100 \mu\text{m}$ , and  $1 \mu\text{m}$ , respectively (Shu et al. 2005). Oscillations of the pH value can be produced by a nonequilibrium chemical reaction involving oxidation of sulfite, which generates protons, and oxidation of thiosulfate, which consumes protons, in a solution of sodium iodate (Liedl and Simmel 2005). The pH-driven conformational switch between quadruplex and straight DNA molecules is more stable, in the sense that the closed and open states become strongly locked, if  $\text{C}_{60}$  fullerenes are attached to both 5' and 3' ends of DNA (Shin et al. 2009). The closed state is also more compact in this case, and the force and power stroke generated by the nanomachine increase.

Among the first molecular machines ever fabricated is that in Yurke et al. (2000). In this conformational switch, DNA is both fuel and machine material. As shown in Fig. 6.3, the switch commutes between opened and closed states if ssDNA fuel strand F and its complementary CF are introduced, respectively, the waste duplex

F/CF being produced at each cycle. Complementary strands are depicted with the same color/line type. In the opened state, the tweezer-like machine consists of a 40-base A strand that hybridize with complementary sequences in the 42-base B and C strands, resulting in two stiff arms connected by a 4-base ssDNA hinge. To monitor the evolution of the device, TET and TAMRA dyes (denoted by D1 and D2 in Fig. 6.3) are attached at the 5' and 3' ends of strand A, the green fluorescence emission of TET ( $\lambda = 536$  nm) being quenched by TAMRA due to resonant intramolecular energy transfer if the two dyes are in close proximity; TET is a donor and TAMRA is an acceptor in the energy transfer process. More precisely, the efficiency of the energy transfer depends on the distance  $R$  between the two dyes as  $1/[1 + (R/R_0)^6]$ , with  $R_0 \cong 5$  nm. The remaining unhybridized 24-base regions of B and C form a duplex with the complementary region of the F fuel strand, to reach the close state. The 8-base overhang of F binds and fully hybridizes to the complementary CF strand following branch migration, forming a waste product when returning in the opened state. The observed fluorescence intensity is high in the open state, when the two dyes are far apart, and decreases six times when the tweezer is closed and the dyes are separated by a distance 6 nm shorter than in the opened state. The average closing force of the tweezer is 15 pN, and the rate of the conformational change is limited by the endothermic nucleation of regions in which complementary bases hybridize; the tweezer switches in about 13 s. Cycling is possible for this machine, but repeated addition of F and CF strands yield a decrease of fluorescence in time due probably to a decrease in solution concentration caused by successive input strands addition.

The tweezer described above cannot work *in vivo* since it requires addition of input F or CF strands. However, an autonomous response of this device under environmental stimuli can be achieved by integrating the instructions for its operation into a DNA gene. *In vitro* control of the tweezer with the help of *Escherichia coli* genes has been demonstrated in [Dittmer et al. \(2005\)](#). The genes can alter their expression in response to changes in the environment, for example, to changes in lactose levels, so that the instructions for opening and closing of the tweezer can be programmed in a synthetic gene.

A theoretical coarse-grained model of DNA nanotweezers is detailed in [Ouldridge et al. \(2010\)](#). This model recovers basic thermodynamic processes of short strands such as hairpin formation, stacking, and hybridization of duplex structures. The nanotweezer in Fig. 6.3 has inspired related configurations of nanoactuators relying on the same TET and TAMRA pair of dyes for monitoring their operation. An example of the conformational changes of such a related machine is schematically represented in Fig. 6.4 ([Simmel and Yurke 2001](#)). In this configuration, the nanomachine is less susceptible to form dimmers. Unlike in the previous nanotweezer, DNA hybridization pushes apart the two dyes instead of bringing them in close proximity. In the relaxed state, the A and B ssDNA strands hybridize to form 18-bp stiff arms, connected by a 4-bp hinge in the A strand and a 48-bp loop in the B strand, which consists of a 40-bp active region surrounded by two 4-bp spacers. The active region can hybridize with the fuel strand F leaving an unhybridized toehold in F, the pushing forces necessary to form

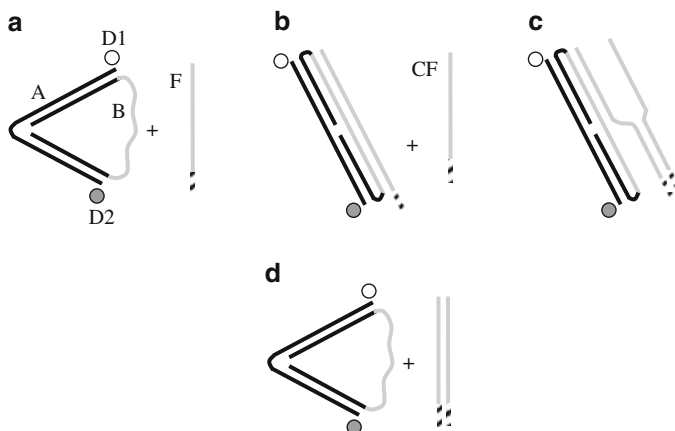
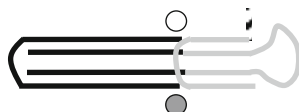


**Fig. 6.4** Conformation changes of a DNA actuator from the relaxed state (a) into the straightened state (b). A branch migration process (c) returns the machine in the original relaxed state (d)

**Fig. 6.5** Closed state of the actuator in Fig. 6.4



the resulting straightened configuration being of about 37 pN. The initial, relaxed state is recovered by addition of a complementary strand to F, denoted CF, which removes F by hybridization after toehold binding followed by branch migration. Breaking of base pair bonds due to thermal fluctuations occurs in a time interval of about 10  $\mu$ s. The nanoactuator can be repeatedly cycled between the relaxed and straightened configurations, the fluorescence intensity that signals the straightened state decreasing in time due to the decrease of the concentration of actuators in solution caused by F and CF strands addition.

The nanoactuator in Fig. 6.4 can be developed into a more complex, three-state machine, acquiring a new stable closed form, besides the relaxed and straightened conformations (Simmel and Yurke 2002). This rigid closed form is represented in Fig. 6.5, the state of the device changing between the three alternatives depending on the fuel strand added in the solution. Compared to the relaxed state, the fluorescence decreases by half in the closed state and increases with 40% in the straightened state since the average distance between the dyes is 5.1 nm in the relaxed state, 2.3 nm in the closed state, and 13 nm in the straightened state. The transitions between different states occur in tens of seconds.

An autonomous DNA nanomotor that does not require fuel strands to change its configuration, but RNA-cleaving DNA enzymes, has been demonstrated in Chen et al. (2004). It extracts chemical energy from the covalent bonds of a DNA/RNA chimera substrate to which it binds and converts it into mechanical motion, as do natural protein motors. The sequence of processes that lead from the closed to the opened state is represented schematically in Fig. 6.6.

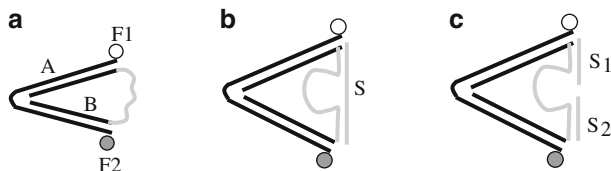
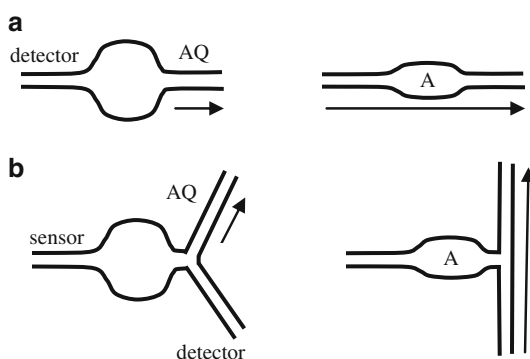


**Fig. 6.6** Conformation changes in a nanomotor: (a) closed state, (b) opened state, and (c) substrate cleaving for return in the closed state

**Fig. 6.7** Analyte sensing through conformation changes: (a) integrated-ligand sensor and (b) coupled-ligand sensor. The direction of current flow by the arrow



The DNA nanomotor consists of the A strand terminated with two fluorophores, FAM and TAMRA (denoted by F1 and F2 in Fig. 6.6), and the B strand, which contains an RNA-cleaving 10–23-DNA enzyme that binds to the DNA/RNA chimera substrate S and cleaves it into the fragments S<sub>1</sub> and S<sub>2</sub>. When not in contact with the substrate, the B strand is in collapsed state, and the nanomotor takes its closed conformation. Because of the resonance energy transfer between FAM and TAMRA, the green FAM signal at 520 nm has a low intensity in this state, and the yellow TAMRA signal at 568 nm is high. When it binds to S, the DNA enzyme takes a bulged duplex form pushing apart the rigid parts and adopting the open state. Now, the FAM signal increases, and the TAMRA signal decreases. Subsequently, the bounded enzyme cleaves the substrate in smaller parts with a lower affinity for the enzyme, which can therefore dissociate from the nanomotor. The DNA nanomotor returns thus to the closed state, ready for a new cycle, and its autonomous operation lasting as long as the substrate, which acts as fuel, is not fully consumed. On average, 20 substrate molecules are consumed each half hour. As the motor cycled, the fluorescence signals decrease due to dye photobleaching.

Conformational changes of DNA strands can be exploited for sensing specific analytes. Examples of such electrical sensors are described in [Fahlman and Sen \(2002\)](#) and illustrated in Fig. 6.7. The sensing principle is based on the finding that the electrical transport in DNA, which is a multistep hopping process, is hindered by mismatches and bulges in double-strand molecules. In particular, a bulge can be caused by aptamer sequences in dsDNA. In the presence of the adenosine analyte (denoted by (a) in Fig. 6.7), however, which binds strongly to the aptamer but not to

the dsDNA, the bulge distortion lessens due to internal stacking and folding of the aptamer loop and allows electron flow to occur along the duplex structure, between the anthraquinone oxidant AQ, tethered at one end of the molecule, and the detector stem. The configuration in Fig. 6.7a is called integrated-ligand sensor, while that in Fig. 6.7b is the coupled-ligand sensor. The properties of the latter sensor are independent of the conductivity of the folded aptamer domain.

## 6.2 Biological Walkers

This section focuses on biological machines able to change their position along a track, which is typically a DNA molecule, mostly by conformation changes. A DNA biped walker that can move along a track in both, forward and backward, direction has been demonstrated in [Sherman and Seeman \(2004\)](#). A schematic description of its stepped movement is illustrated in Fig. 6.8, where W denotes the biped walker, T is the track, consisting of a triple-crossover molecule with footholds FH, and P are psoralen molecules, which cross-link DNA strands covalently if irradiated. In Fig. 6.8, the double-stranded parts of W and T are represented by thicker regions.

The walker contains two double-helical rigid parts connected by flexible strands of ssDNA, consisting of nine nucleotides, each rigid part terminating with a ssDNA foot. The foot can attach to a foothold in the presence of strands  $S_i$ ,  $i = 1, 2, 3$ , that are complementary to both of them and have an additional 8-base toehold, which allows removal of the strand by a complementary strand  $CS_i$  in the solution. If one of the feet is released from the corresponding foothold due to the presence of  $CS_i$ , which completely hybridize to the strand  $S_i$  following branch migration, it can extend to the adjacent foothold to which it becomes attached with the help

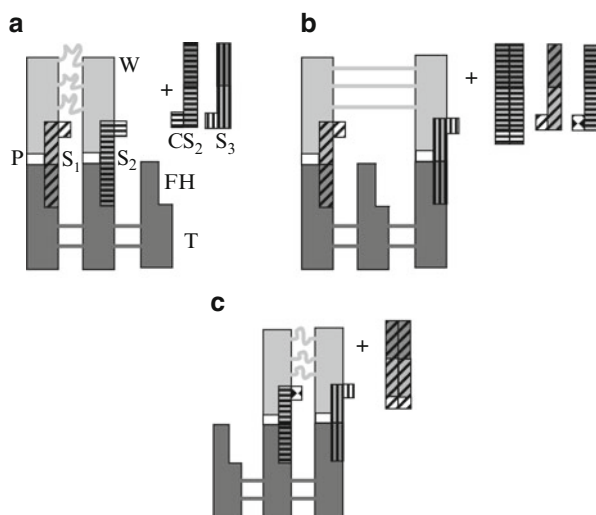
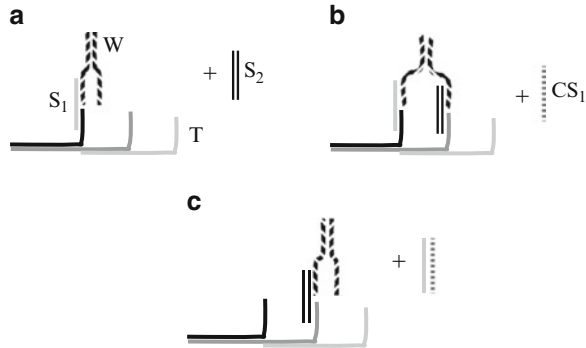


**Fig. 6.8** DNA biped walker: (a) the two feet are attached to the track, (b) the leading foot moves to the next position, and (c) the trailing foot follows

**Fig. 6.9** DNA biped walker: (a) one foot is attached to the track, (b) the leading foot moves to the next position, and (c) the trailing foot becomes the new leading foot



of strand  $S_j$ . This first step of the biped walker is completed if the remaining foot performs the same sequence of operations. The direction of movement is controlled by the complementary input strands introduced in the solution. In this walker configuration, one foot always trails the other.

A DNA walker that moves similar to the kinesin motor along a microtubule, i.e., by advancing the trailing foot to the lead, is described in [Shin and Pierce \(2004\)](#) and represented schematically in [Fig. 6.9](#). The walker  $W$ , which consists of partially complementary ssDNA strands composed of a 20-bp helix section that joins two 23-bp legs, moves along a DNA track  $T$  containing protruding 20-bp ssDNA branches (three such branches are shown in [Fig. 6.9](#)) separated by scaffold helices with a length of 15 bp. An input strand  $S_1$  forms a 18-bp helix with one leg of the walker and another 17-bp helix with one protruding branch, anchoring the walker to the track. In the presence of another strand  $S_2$ , the other leg of the walker is anchored to the neighboring protruding branch, while the addition of the  $CS_1$  strand, complementary to  $S_1$ , releases the initially bound/leading leg of the walker and forms the waste  $S_1$ - $CS_1$  double strand; the initial leading leg becomes a trailing leg.  $CS_1$  initially binds to  $S_1$  at a 10-bp overhang, a following strand displacement process completing the generation of the waste product. The walker locomotion, which proceeds in 5-nm steps, can be monitored by end-labeling the protruding branches with different dyes and the walker legs with quenchers.

An addressable molecular tweezer somewhat similar to the walker in [Shin and Pierce \(2004\)](#) contains a set of immobilized footer tweezers that self-assemble on a DNA track and a free header tweezer that floats in solution such that it can close any footer tweezer in the presence of a specific pair of fuel input ssDNA strand ([Chhabra et al. 2006](#)). All tweezers are branched DNA junctions with four rigid arms forming an X-shaped structure with an acute angle that has an average value of  $60^\circ$ . Two arms which enclose the acute angle are terminated with single-stranded sticky ends. In addition, the arms of footer tweezers with sticky ends contain also coupling reactants. Then, when the sticky ends of the header and footer tweezers hybridize with parts of the input strands, the footer tweezer is pinched. As a result, the two reactants are brought close enough to trigger a coupling reaction that leads to an amine bond, which covalently joins the two strands on the footer into a single strand.

Complementary strands to the input ssDNA remove the header from the footer because the input strands hybridize with their complementary DNA sequences. A new cycle of events can start.

Another DNA-based walker that can move forward or backward on a ssDNA track depending on the sequence of the ssDNA fuel is described in Bath et al. (2009). As for a kinesin motor, its movement is based on the coordination between two identical single-stranded DNA feet attached to the 3' end of a double-stranded spacer. The track consists of a sequence of ten nucleotide-binding domains and six nucleotide competition regions, the feet competing for hybridization to the competition domain. When the 5' end of one foot is lifted from the track as a result of this competition, it can bind to the fuel, which initiates the next step by a series of strand displacement, strand cutting by a nicking enzyme, dissociation, and rehybridization to the track processes. The directional bias of the walker relies on a ratchet mechanism determined by the preferential interaction of the fuel strand with one of the two feet.

An example of a unidirectional DNA walker that moves along a DNA track can be found in Yin et al. (2004), and the processes involved in a single step (two consecutive steps are detailed in Yin et al. (2004)) are illustrated schematically in Fig. 6.10. The track contains anchorage sites denoted by A and B on which the six-nucleotide walker, indicated by \*, can bind. Initially, the walker is positioned at A, forming the A\* complex. Then, anchorages A\* and B ligate, because they have complementary sticky ends, form the A\*B molecule in an irreversible energy-consuming process and create a recognition site for a cutting enzyme, which cleaves the structure and transfers the walker to the anchorage site B. The newly formed complex, B\*, can be transferred to another anchorage site if the sequence of processes described above are enabled; the cutting enzymes (endonucleases) involved in subsequent steps can be different. Backward movement is not possible since the previous restriction site is destroyed by the cut and a new site is created at each ligation. The energy source is the hydrolysis of adenosine triphosphate, and the motion of the walker can be monitored by gel electrophoresis.

DNA displacements on a DNA track can also be driven by polymerase  $\phi 29$ , which is an enzyme that replicates DNA or RNA templates (Sahu et al. 2008). DNA displacement from its template or cargo transport occurs in this case by extension of a primer hybridized to the template. Transportation by polymerase-driven processes takes place at a relatively high speed of  $680 \text{ nm min}^{-1}$ .

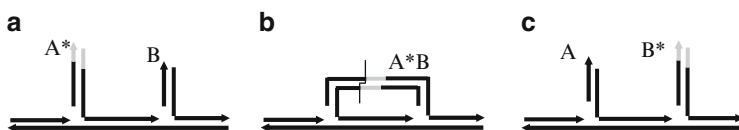


**Fig. 6.10** Unidirectional DNA walker: (a) the walker \* is positioned at A, (b) the A\*B molecule is cut by an enzyme, and (c) the walker is positioned at B

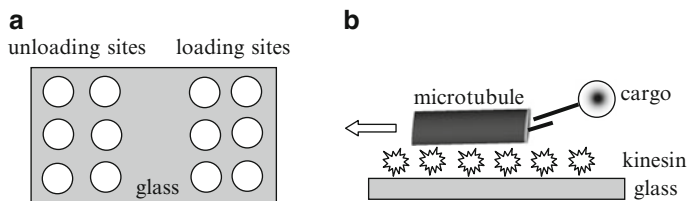


**Fig. 6.11** (a) Loading and unloading sites on a kinesin-coated glass substrate. (b) Cargo-carrying microtubule that glides on kinesin

### 6.3 Biological Motors

In this section, we deal with machines based on biological motility that can transport cargo molecules from one position to another. For future bionanotechnologies, it would be of interest to be able to selectively translocate nanoparticles in parallel by autonomous on-chip systems. This task can be performed by microtubules labeled by ssDNA strands that glide on surfaces coated with kinesin, as described in [Hiyama et al. \(2009\)](#). Nanoparticle cargoes labeled by ssDNA strings that have a common sequence with that of the microtubule can then be loaded on the microtubule from a loading site specified by a certain DNA base sequence and transported to an unloading site. In the experiment described in [Hiyama et al. \(2009\)](#) and schematically illustrated in Fig. 6.11, the cargoes were fluorescent polystyrene microspheres with a diameter of 200 nm labeled with a 23-base ssDNA, which become trapped at specific loading sites micropatterned on a glass substrate and containing 10-base ssDNA that hybridizes with the ssDNA on the cargo. Outside the loading and unloading sites, the glass substrate is covered with immobilized kinesin, on which microtubules labeled with 15-base ssDNA can glide with an average speed of  $0.35 \mu\text{m s}^{-1}$ . When a microtubule encounters a cargo, the latter is loaded on the microtubule following a DNA hybridization/strand exchange mechanism with the longer complementary strand on the microtubule; the state of cargo on microtubule is more stable than that of cargo on loading site. Upon loading, the microtubules continue to glide with similar speeds until they reach the unloading sites on which 23-base ssDNAs, complementary to that on the cargo, are immobilized. Complete hybridization of ssDNA on cargo and unloading sites allows cargoes to be unloaded (to reach more stable states than on microtubules). The operation of this autonomous loading/unloading system is observed via fluorescence, which shows that in time (over about 1 h), the cargoes are transported to and accumulate on the unloading sites.

When active transport of cargoes attached on microtubules that glide on kinesin is desired, the microtubule/kinesin interaction is preserved if the cargo is confined to the central region of the microtubule ([Bachand et al. 2004](#)). Cargo transport and self-assembly processes can be performed in the same system when biotinylated microtubules are used as scaffolds for streptavidin-coated nanocrystal CdSe

quantum dots, for example. It was found that kinesin binding, needed to transport the cargo-microtubule system, is inhibited if the microtubule filaments are uniformly functionalized with quantum dots, whereas for microtubules functionalized only in the central region, the translational velocities attain  $0.3 \mu\text{m s}^{-1}$ .

Because of the glue-like character of the biotin–streptavidin bond, efficient cargo attachment occurs for optimized gliding velocities of microtubules, which can be controlled between  $50$  and  $450 \text{ nm s}^{-1}$  by modifying the concentration of kinesin substrate ATP (Agarwal et al. 2009). For biotinylated 4-nm polystyrene nanospheres that attach to streptavidin-coated microtubules, which move on a surface coated with kinesin, the optimum gliding velocity of microtubules for loading was found to be  $200 \text{ nm s}^{-1}$ .

There is also an inverse configuration, in which kinesin motors walk along microtubules, preferred in some applications because the microtubules can be oriented along certain directions. In addition, cargoes can be attached to kinesin motors in the same way as to microtubules. In this inverse configuration, an array of long and properly aligned microtubules is required for motor displacements along desired directions. Such an array can be fabricated by immobilizing first microtubule seeds, then polymerizing the microtubules only from the plus ends of the seeds to obtain long structures of about  $50 \mu\text{m}$ , and, finally, attaching the microtubule filaments to the surface (Brown and Hancock 2002). Microtubule alignment along a certain direction was achieved by allowing a solution of buffer to flow, which causes microtubules to align downstream, while microtubule attachment to the surface by a solution of glutaraldehyde or by binding to mutant kinesins cannot harness ATP hydrolysis.

Bifunctional DNA molecules with a biotinylated end attached to a microtubule that glides over kinesin immobilized on a surface and with a thiolated end to a patterned gold pad can be (over)stretched between the motile microtubule and the pads (Dinu et al. 2006). This stretching method manipulates many DNA molecules in parallel and can help construct dynamic networks. In particular,  $\lambda$ -phage DNA can be stretched to more than  $18.6 \mu\text{m}$ , which is the full contour length of DNA. However, as yet, the stretching process can be only observed but not controlled.

Control of microtubule/kinesin interactions has been reported in Ionov et al. (2006). In this work, as shown in Fig. 6.12, kinesin molecules were adsorbed on Si between chains of the poly(N-isopropylacrylamide) thermoresponsive polymer,

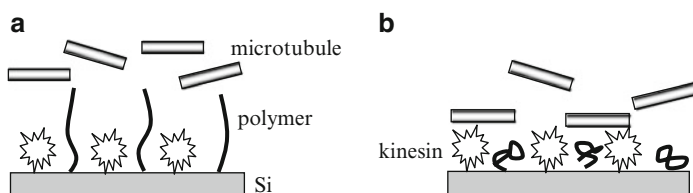


**Fig. 6.12** Controlled microtubule/kinesin interactions via conformation changes of a thermoresponsive polymer: (a) inhibited interaction and (b) allowed interactions

which hydrate in an aqueous solution at temperatures below the lower critical solution temperature (LCST). When hydrated, the polymer chains form extended structures, while above LCST, which is about 32 °C, the polymer chains dehydrate and collapse. So, below LCST, microtubules are prevented from binding to kinesin motors and diffusing in solution while binding, and hence, microtubule gliding on kinesin is allowed above LCST. The switching of the microtubule motility is reversible. However, not all microtubules behave in the same way when the temperature is cyclically changed. At cooling, the shorter microtubules are predominantly released since polymer chain hydration is accompanied by partial screening of kinesin molecules so that the effective distance between adjacent kinesin motors increases. Therefore, continuous microtubule gliding, which implies contact with at least two kinesin molecules at any given moment, is possible only for longer microtubules; this device sorts the molecules according to their lengths as temperature varies.

Although most artificial biomotors rely on the kinesin/microtubule interactions, there are also nanomotors involving myosin and actin filaments. In particular, silicon nanowires functionalized with the myosin motor domain and dispersed in aqueous solution confine the motion of actin filaments along their circumference (Byun et al. 2009). These filaments move ballistically on the silicon nanowires over distances as long as 100  $\mu\text{m}$ .

Guided unidirectional movement of microtubules gliding on kinesin can be achieved in microfabricated channels, as those in Fig. 6.13 (Lin et al. 2006). Although initially moving diffusively in solution, all microtubules placed on the structure acquire a rotational movement in the same direction, the arrowhead or rounded corners acting as motion rectifiers for the microtubules that follow the kinesin-coated sidewalls of the channel. When a microtubule encounters a sidewall, it must locally bend to glide along the sidewall and tends to reach the outer sidewall of the channel, the bending energy increasing with the sharpness of the channel edges. For bending energies larger than the binding energy between microtubule and kinesin, the former can detach. On the contrary, curved ends of the rectifier regions, such as those in Fig. 6.13b, c, redirect more efficiently the gliding microtubules toward the circular channel. The configuration in Fig. 6.13c is the most effective in collecting microtubules in the channel and thus sorting them from solution since the

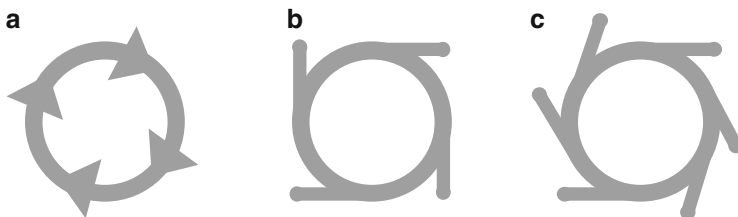
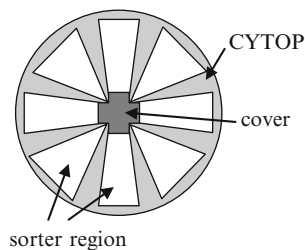


**Fig. 6.13** Microfabricated channel geometries that rectify the motion of microtubules: (a) arrow-headed and (b, c) rounded corner rectifiers

**Fig. 6.14** Undercut geometry of microchannel for efficient microtubule guiding



**Fig. 6.15** Biomolecular sorter



geometrical constraints for diffusing into the channel are the least restrictive. The guiding efficiency of microtubules along kinesin-coated channels increases for a channel geometry that includes an undercut, which prevents microtubules to climb the sidewalls (see Fig. 6.14) (Hess et al. 2003). The height and depth of such an undercut are 200 nm and 1  $\mu\text{m}$ , respectively.

An autonomous highly selective biomolecular sorter based on kinesin/microtubule interactions has been shown in Lin et al. (2008). The device, represented schematically in Fig. 6.15, consists of functionalized microtubules that move along kinesin-coated petal-shaped microchannels etched in the CYTOP polymer film. CYTOP surfaces inhibit the displacement of kinesin-driven microtubules, providing selective confining of the microtubules in the channels. The microtubules bind to a specific cargo protein from a dilute solution and are guided by the sorting channels to a collector region in the center of the structure, in which they become trapped. The channel petal shape avoids microtubule loss at sharp corners, while arrow-shaped patterns in the collector region prevent microtubule escape from the trap. The collector region is protected by a parylene cover, which increases the trapping efficiency. Experiments with microtubules labeled with the fluorescent dye TMR showed that the intensity of the fluorescent signal increases rapidly and then saturates after 45 min, the density of trapped microtubules in the collector being 100 times higher than in other parts of the device. Analyte sorting can be achieved by binding microtubules to specific molecules.

DNA machines are not only passive, in the sense that they process, detect, or transport other molecules, but can be also active, multiplying the amount of molecules in a solution. For instance, an autonomous isothermic DNA machine can amplify the detection of M13 phage ssDNA sequences (Weizmann et al. 2006). In this case, the machine is activated upon recognition of the viral DNA that must be analyzed and synthesizes a DNzyme, which allows visual monitoring of the reaction by chemiluminescent or colorimetric imaging. The peroxidase-mimicking enzyme is synthesized on a DNA template. The sensitivity level of virus detection is  $10^{-14}$  M.

Another autonomous DNA motor is fuelled by the noncovalent polymerization of a double-helical DNA tail when encountering a target molecule (Venkataraman et al. 2007). As a result, an initially anchored Rickettsia strand is propelled with about 8 nm per polymerization step at the living end of the polymer. At each such step, a metastable polymerizing hairpin inserts between the polymer tail and the Rickettsia strand by a four-branch migration mechanism, so that the Rickettsia strand remains attached to the growing polymer by about 20 bp and is transferred to the new living end.

## References

- Agarwal A, Katira P, Hess H (2009) Millisecond curing time of a molecular adhesive causes velocity-dependent cargo-loading of molecular shuttles. *Nano Lett* 9:1170–1175
- Bachand GD, Rivera SB, Boal AK, Gaudioso J, Liu J, Bunker BC (2004) Assembly and transport of nanocrystal CdSe quantum dot nanocomposites using microtubules and kinesin motor proteins. *Nano Lett* 4:817–821
- Bath J, Green SJ, Allen KE, Turberfield AJ (2009) Mechanism for a directional, processive, and reversible DNA motor. *Small* 5:1513–1516
- Berg HC (2003) The rotary motor of bacterial flagella. *Annu Rev Biochem* 72:19–54
- Brown TB, Hancock WO (2002) A polarized microtubule array for kinesin-powered nanoscale assembly and force generation. *Nano Lett* 2:1131–1135
- Byun K-E, Heo K, Shim S, Choi H-J, Hong S (2009) Functionalization of silicon nanowires with actomyosin motor protein for bioinspired nanomechanical applications. *Small* 5:2659–2664
- Capaldi RA, Aggeler R (2002) Mechanism of the  $F_1F_0$ -type ATP synthase, a biological rotary motor. *Trends Biochem Sci* 27:154–160
- Chen Y, Wang M, Mao C (2004) An autonomous DNA nanomotor powered by a DNA enzyme. *Angew Chem Int Ed Engl* 43:3554–3557
- Chhabra R, Sharma J, Liu Y, Yan H (2006) Addressable molecular tweezers for DNA-templated coupling reactions. *Nano Lett* 6:978–983.
- Ciudad A, Lacast AM, Sanch JM (2005) Physical analysis of a processive molecular motor: the conventional kinesin. *Phys Rev E* 72:031918
- Dinu CZ, Opitz J, Pompe W, Howard J, Mertig M, Diez S (2006) Parallel manipulation of bifunctional DNA molecules on structured surfaces using kinesin-driven microtubules. *Small* 2:1090–1098
- Dittmer WU, Kempter S, Rädler JO, Simmel FC (2005) Using gene regulation to program DNA-based molecular devices. *Small* 1:709–712
- Dragoman M, Dragoman D (2009) *Nanoelectronics. Principles and devices*, 2nd edn. Artech House, Boston, Chapter 7
- Fahlman RP, Sen D (2002) DNA conformational switches as sensitive electronic sensors of analytes. *J Am Chem Soc* 124:4610–4616
- Hendricks AG, Epureanu BI, Meyhöfer E (2009) Collective dynamics of kinesin. *Phys Rev E* 79:031929
- Hess H et al (2003) Molecular shuttles operating undercover: a new photolithographic approach for the fabrication of structured surfaces supporting directed motility. *Nano Lett* 3:1651–1655
- Hiyama S, Gojo R, Shima T, Takeuchi S, Sutoh K (2009) Biomolecular-motor-based nano- or microscale particle translocations on DNA microarrays. *Nano Lett* 9:2407–2413
- Ionov L, Stamm M, Diez S (2006) Reversible switching of microtubule motility using thermoresponsive polymer surfaces. *Nano Lett* 6:1982–1987

- Kay ER, Leigh DA, Zerbetto F (2007) Synthetic molecular motors and mechanical machines. *Angew Chem Int Ed Engl* 46:72–191
- Kang H et al (2009) Single-DNA molecule nanomotor regulated by photons. *Nano Lett* 9: 2690–2696
- Lacoste D, Lau AWC, Mallick K (2008) Fluctuation theorem and large deviation function for a solvable model of a molecular motor. *Phys Rev E* 78:011915
- Liedl T, Simmel FC (2005) Switching the conformation of a DNA molecule with a chemical oscillator. *Nano Lett* 5:1894–1898
- Liepelt S, Lipowsky R (2009) Operation modes of the molecular motor kinesin. *Phys Rev E* 79:011917
- Lin C-T, Kao M-T, Kurabayashi K, Meyhöfer E (2006) Efficient designs for powering microscale devices with nanoscale biomolecular motors. *Small* 2:281–287
- Lin C-T, Kao M-T, Kurabayashi K, Meyhofer E (2008) Self-contained, biomolecular motor-driven protein sorting and concentrating in an ultrasensitive microfluidic chip. *Nano Lett* 8:1041–1046
- Liu H, Liu D (2009) DNA nanomachines and their functional evolution. *Chem Commun* 2625–2636
- Liu D, Bruckbauer A, Abell C, Balasubramian S, Kang D-J, Klenerman D, Zhou D (2006) A reversible pH-driven DNA nanoswitch array. *J Am Chem Soc* 128:2067–2071
- Ouldridge TE, Louis AA, Doye JPK (2010) DNA nanotweezers studied with a coarse-grained model of DNA. *Phys Rev Lett* 104:178101
- Sahu S, LaBean TH, Reif JH (2008) A DNA nanotransport device powered by polymerase  $\phi$ 29. *Nano Lett* 8:3870–3878
- Schliwa M, Woehlke G (2003) Molecular motors. *Nature* 422:759–765
- Sherman WB, Seeman NC (2004) A precisely controlled DNA biped walking device. *Nano Lett* 4:1203–1207
- Shin J-S, Pierce NA (2004) A synthetic DNA walker for molecular transport. *J Am Chem Soc* 126:10834–10835
- Shin SR et al (2009) Fullerene attachment enhances performance of a DNA nanomachine. *Adv Mater* 21:1907–1910
- Shu W et al (2005) DNA molecular motor driven micromechanical cantilever arrays. *J Am Chem Soc* 127:17054–17060
- Simmel FC, Dittmer WU (2005) DNA nanodevices. *Small* 1:284–299
- Simmel FC, Yurke B (2001) Using DNA to construct and power a nanoactuator. *Phys Rev E* 63:041913
- Simmel FC, Yurke B (2002) A DNA-based molecular device switchable between three distinct mechanical state. *Appl Phys Lett* 80:883–885
- Smirnov AYu, Savel'ev S, Mourokh LG, Nori F (2008) Proton transport and torque generation in rotary biomotors. *Phys Rev E* 78:031921
- Tashiro R, Sugiyama H (2005) Biomolecule-based switching devices that respond inversely to thermal stimuli. *J Am Chem Soc* 127:2094–2097
- Venkataraman S, Dirks RM, Rothemund PWK, Winfree E, Pierce NA (2007) An autonomous polymerization motor powered by DNA hybridization. *Nat Nanotechnol* 2:490–494
- Weizmann Y, Beissenhirtz MK, Cheglakov Z, Nowarski R, Kotler M, Willner I (2006) A virus spotlighted by an autonomous DNA machine. *Angew Chem Int Ed Engl* 45:7384–7388
- Yildiz A, Selvin PR (2005) Kinesin: walking, crawling or sliding along? *Trends Cell Biol* 15: 112–120
- Yin P, Yan H, Daniell XG, Turberfield AJ, Reif JH (2004) A unidirectional DNA walker that moves autonomously along a track. *Angew Chem Int Ed Engl* 43:4906–4911
- Yurke B, Turberfield AJ, Mills, Jr AP, Simmel FC, Neumann JL (2000) A DNA-fuelled molecular machine made of DNA. *Nature* 406:605–608
- Zhong H, Seeman NC (2006) RNA used to control a DNA rotary nanomachine. *Nano Lett* 6: 2899–2903
- Zhou M, Liang X, Mochizuki T, Asanuma H (2010) A light-driven DNA nanomachine for the efficient photoswitching of RNA digestion. *Angew Chem Int Ed Engl* 122:2213–2216

# Chapter 7

## Biomolecular Computing

**Abstract** This chapter focuses on biomolecular computing, emphasizing the advantages and disadvantages of this computational method. Examples of biomolecular systems that work as memory or that perform Boolean computation, self-assembly, and logical computations are given.

Because of the recent technological progress in the semiconductor industry, alternatives to electronic computations could be of interest only if (1) the computation speed increases, which implies parallel computation and/or development of more efficient computing algorithms, or (2) the heat problem, especially relevant in miniaturized components, can be alleviated. In this chapter, we will address the issue of biomolecular computing from this perspective.

### 7.1 Principles of Biomolecular Computing

Biomolecular computing is an appealing candidate for efficient computation since information processing and memory are common to all life forms and take place with great reliability in the world around us. The original incentive for developing biomolecular computation was the expected parallelism and the potential high-density storage characteristic of biomolecules. Although biomolecular computing is a parallel process and, therefore, the computation time increases only polynomially with the number of variables and not exponentially, as in standard computers, the number of strands involved in the computation that must be prepared increases exponentially with the number of variables. This is a disadvantage, which implies an additional time for preparing the strands, which increases exponentially with the number of variables, and cannot be avoided since it is caused by the still classical way in which biomolecular computing works (Feldkamp and Niemeyer 2006). In fact, biomolecular computing experiences the same exponential scaling of the solution space as electronic computers. The 200-city traveling salesmen problem

would require DNA molecules that would weigh more than the earth (Ezziane 2006). A possible solution to the exponential scaling could be the development of genetic algorithms, which are also more tolerant to errors, or the use of swarm intelligence based on complex collaborative behaviors (Ezziane 2006).

The computation parallelism is inherent also in quantum computation. In fact, a DNA-based proposal of implementing a quantum bit relied on the electronic quantum tunneling phenomenon in the bond connecting different phosphorus bridges in a DNA strand, which mimicked a Josephson junction qubit (Ben-Jacob et al. 1999). This proposal would not have led, however, to a true biomolecular computer, whether classical or quantum, since it required external voltage sources to connect conductive DNA strands; these strands would become conductive via self-assembly, except for the phosphorus bridge bonds involved in tunneling. Biomolecular and quantum computing share another property: the computation process alters the device. Biomolecular computing, on the other hand, as revealed by all life forms, can operate in natural noisy environments at room temperature, whereas quantum computing needs and is limited by the isolation from the environment, usually favored at very low temperatures.

Biomolecular computers are autonomous, programmable devices in which the hardware, software, and input and output consist of biological molecules. In most cases, active computation is performed with single-stranded molecules, which can link to complementary strands, the double-stranded sequences being inert. In general, biomolecular computing is stochastic, each computing step involving two or more competing transitions/chemical processes. The result of computation depends on the relative probability of alternative paths. Molecular logic gates are in fact analog approximations of the corresponding electronic gates. In an analog system, the information is no longer contained in series of 0 and 1 logic states, but all intermediate values must be considered. However, in most cases, the result of biomolecular computation can be described by a series of logic gates.

DNA chemistry, which is at the basis of any DNA computer, is not an accurate process; it is extremely sensitive to the chemical and environmental conditions. DNA computers rely on enzymes to process information through denaturation, replication, and annealing, while DNA strings act as input, output, and storage units. Cutting (denaturation) of DNA strands is performed with restriction enzymes, which recognize a specific nucleotide sequence (restriction site) that is typically 4–8 base pairs (bp) long, attaches itself at/near this sequence, and cuts the DNA strand at that point. The process of denaturation is accompanied by the release of energy, energy that can be harnessed to power the next computation step. Replication rates can be as fast as 500 bp/s or 1,000 b/s. Parallelism in DNA computing appears when enzymes work simultaneously on multiple DNA strands. This is a typical situation in solution-based DNA computation.

One advantage of biomolecular computation over electronic computation is the very low energy dissipation encountered in reversible DNA processing. For example, a DNA programmable automaton implemented in 120- $\mu$ l solution at room temperature, able to perform  $10^9$  transitions/s with high fidelity, consumes only  $10^{-10}$  W (Benenson et al. 2001), while a single DNA molecule acting as

input data provides at the same time the energy necessary for a biomolecular automaton performing  $6.6 \times 10^{10}$  transitions/s  $\mu\text{l}$  and dissipates  $5 \times 10^{-9}$  W  $\mu\text{l}^{-1}$  as heat (Benenson et al. 2003). This energy stored in the bonds of the biomolecule is released as the input data are destroyed during computation. Such a process has no correspondent in electronic computation. The key for understanding the low energy consumption of reversible biomolecular computers is the fact that, at each computation step, a state of equilibrium is reached between reactants and products, which assures thermodynamic (and logical) reversibility. In electronic, digital computation, the minimum energy required to transfer or delete one bit of information is  $E = k_B T \ln 2$  (Szaciłowski 2008); in standard silicon switching devices operating in hard drives, the energy cost per computational step could be orders of magnitude higher than this minimum value. The energy cost is related to the irreversibility of logical gates. In reversible logic operations, which can take place in biomolecular computers when operated at or near thermodynamic equilibrium, the energy cost per computational step can decrease up to  $0.01 k_B T$  (in perfect equilibrium this energy cost should vanish).

However, no biologic circuit reaches yet the reliability and complexity of silicon-based electronics. In addition, unlike electronic computers, biomolecular computation is certainly not fast. The results of chemical processes catalyzed by enzymes reveal themselves in several minutes or hours. Therefore, biomolecular computing will probably not replace electronic computing; it is much more suitable for analyzing biological/stochastic information rather than deterministic information (Ezziane 2006). The applications of biomolecular computation tend to focus not so much on in vitro (inside a recipient) but on in vivo (inside the cell) operations, with the ultimate goal of smart diagnosis and drug delivery.

One of the still-standing issues of biomolecular computing is the efficient cascading of several logic gates. Unlike in electronic systems, where both the input and output signals are of the same (electronic) nature, in biomolecular logic input/output incompatibilities can arise. In many cases, the logic gates are “single-use” devices. Ideally, the output of a gate should act as input for the next logic gate. Important for implementing logical gates but also to concatenate such gates are the sticky ends. Matching sticky ends from DNA molecules cut by the same restriction enzyme can be joined by ligase.

The different mechanisms at work in electronic processors and biological computers justify the search for specific algorithms for the latter, which would enable the implementation of logical circuits in only one molecule. An example of such a molculator, i.e., a molecular computer on a truly molecular scale, is the fluorescent molecule known as fluorescein in which advanced arithmetic operations such as full-adder and full-subtractor can be implemented. Fluorescein exists in four ionization forms with different spectral properties: F(-1), F(0), F(+1), and F(+2). In solution, logic operations can be implemented by switching between these states through a controlled change of the pH (Margulies et al. 2006). Input signals are acids and/or bases, which change the predominant F(0) form of a neutral solution in cations F(+1) and/or anions F(-1) and F(-2), both types of inputs annihilating each other. The output is read by monitoring the transmittance or absorbance at

different wavelengths: 447 nm and 474 nm. Of course, only a small number of bits can be encoded in the fluorescein molecule, and the computation rate is determined by the (slow) diffusion rate of the inputs. However, this example reveals that biological computers are fundamentally different than their electronic counterparts. Therefore, besides searching for true biological computers, an alternative route to increase the computational power of present-day computers is to mimic nature and, in particular, the highly interconnected and reconfigurable biological neural networks, by creating programmable neural network architectures; an example of such an approach can be found in [Harkin et al. \(2009\)](#).

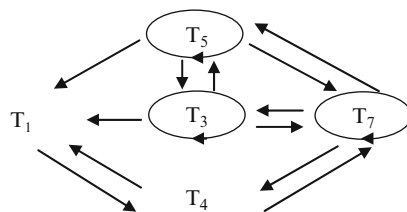
Reviews on biological computations can be found in [Ezziane \(2006\)](#), [Szaciłowski \(2008\)](#), [Sager et al. \(2008\)](#), and [Dragoman and Dragoman \(2009\)](#). There is a recent surge in interest in this subject. This chapter is by no means a comprehensive review of the field, but offers some insights in this fascinating subject.

## 7.2 Boolean Biomolecular Computing

Boolean computing is performed in digital systems, where the information is encoded in bits with logical values 0 and 1, which are represented in electronic systems as low and high voltages on circuit elements such as transistors or capacitances. Biomolecular computing, and in particular, DNA computation, is based on encoding information in the sequence of nucleotides and developing algorithms to operate with these bits of information. A single-stranded DNA (ssDNA) molecule has the potentiality of high data density of  $10^{22}$  by/g since the nucleotides are separated by only 0.35 nm; in two dimensions, the data density stored in DNA would be  $10^6$  Gb/in<sup>2</sup>, whereas in a typical hard drive, it is of the order of 10 Gb/in<sup>2</sup> ([Ezziane 2006](#)). DNA computers are comparable to teraflop supercomputers in terms of parallelism, which can reach  $10^{20}$  operations/s, but scores quite poorly in error correction performances. Despite the sequence specificity of DNA hybridization and the repair enzymes that can correct the eventual errors, in DNA replication one error occurs at about  $10^9$  copied bases, while in electronic computers performant correction algorithms reduce errors to one at every  $10^{13}$  operations ([Ezziane 2006](#)).

The first demonstration of biomolecular computing took place in 1994 ([Adleman 1994](#)) when the problem that was tackled was that of the directed traveling salesman (also known as the Hamilton path problem), which involves finding a path that connects several cities without going through any city twice. In this case, each city was encoded in a ssDNA molecule composed of 20 nucleotides (nt), and the possible connections/paths between cities was encoded as a ssDNA consisting of the last 10 nt of the starting city and the first 10 nt of the finishing city. Although apparently trivial, the traveling salesmen problem is of the NP (nondeterministic polynomial time)-type, and the optimal route through 50 cities is a task that can only be solved in few years by electronic computers. [Adleman \(1994\)](#) solved the 7-city problem by hybridization and ligation, i.e., by mixing the DNA strands with ligase, adding adenosine triphosphate (ATP), and finally filtering out the incorrect

**Fig. 7.1** Network of synthetic peptides forming a graph



paths which were too short, too long, or had wrong departure and arrival cities. The remaining DNA molecules form the solution. The parallelism was ensured by the large number of ssDNA strands in the reaction ( $3 \times 10^{13}$  copies of each).

An illustrative example of the statistical nature of biomolecular logic is the Boolean functions implementation by segments of small network of synthetic peptides that form a graph with 5 nodes and 15 directed edges (Ashkenasy and Ghadiri 2004). This graph is represented in Fig. 7.1. The system operates in neutral aqueous solutions and consists of synthetic peptides denoted by  $T_i$  in Fig. 7.1 that form a network and that differ from one another through amino acids. A peptide  $T_i$  can transform into another peptide  $T_j$  in the presence of template-directed cross-catalytic reactions consisting of condensation of nucleophilic N and electrophilic  $E_j$  fragments or can undergo autocatalytic reactions if  $T_j = T_i$ .

The transformation directions are represented by arrows in Fig. 7.1, the autocatalytic reactions by circles, and the reaction rates for transforming peptide  $T_i$  into peptide  $T_j$ ,  $R_{ij}$ , satisfy the following relation:  $R_{77} = R_{33} < R_{47} < R_{37} = R_{73} < R_{31} = R_{41} < R_{35} = R_{57} < R_{14} < R_{74} < R_{51} < R_{53} = R_{75} < R_{55}$ . Under these circumstances, the subnetwork  $T_3 \leftrightarrow T_7 \leftrightarrow T_4$  can implement an OR logic gate with  $T_3$  and  $T_4$  as inputs and  $T_7$  as output. More precisely, when  $T_3$  and  $T_4$  are absent, the autocatalytic production rate of  $T_7$  in the presence of N and  $E_7$  is low, while in the presence of either of the two inputs in the reaction mixture the production rate of  $T_7$  increases. A NOT gate can be implemented as the autocatalytic reaction of  $T_3$  in a mixture containing N and  $E_3$ . When  $E_5$  is added, the production of  $T_5$  is encouraged by the more efficient  $T_3 \rightarrow T_5$  reaction, and thus the autocatalytic reaction of  $T_3$  is negatively affected. The NOR gate involves the circular subnetwork  $T_3 \leftrightarrow T_5 \leftrightarrow T_7$ , with  $T_3$  as output. Its autocatalytic production rate in the presence of N and  $E_3$  is diminished if  $E_5$  and/or  $E_7$  is added since the transformation  $T_3 \rightarrow T_5$  and/or  $T_3 \rightarrow T_7$  are more efficient. Similarly, the NOTIF gate can be implemented by the transformation  $T_3 \rightarrow T_1$ , with  $T_3$  as output. The strong autocatalytic reaction of  $T_3$  is inhibited by the presence of  $E_1$ , which induces the  $T_3 \rightarrow T_1$  reaction.  $T_1$  cannot back-catalyze to form  $T_3$  and is not an autocatalyst.

An interesting approach to Boolean biomolecular computing was reported in Frezza et al. (2007). It involves solid-supported DNA gates emerged in solution and input and output ssDNA molecules. The solid-supported gates provide enhanced modularity since the task of choosing suitable input and output DNA strands for cascaded operation is much simplified. The device in Frezza et al. (2007) is based on the strand displacement process in which a full-length input complementary strand

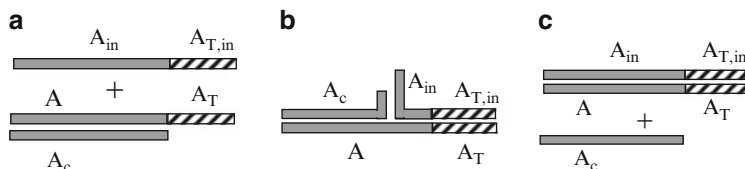


**Fig. 7.2** Strand displacement mechanism: (a) A double-stranded molecule with a toehold and the input strand. (b) The input complementary strand binds to the toehold  $A_T$  and displaces shorter hybridized sequences. (c) The resulting molecules

binds to a toehold  $A_T$ , which is a single-stranded overhang, and then invades and displaces shorter hybridized sequences by a mechanism known as three-way branch migration. The sequence of processes involved in strand displacement is illustrated in Fig. 7.2.

The 0 and 1 logic values are represented, respectively, by high and low concentrations of each ssDNA molecules. The output strand of a gate ( $A_c$ ) is complementary to and hybridizes with a ssDNA molecule ( $A + A_T$ ) immobilized on a substrate by T, such that different logic gates are immobilized on different supports. Successfully cascading logic operations implies that the toehold region of a certain gate can bind only to the output strand of the preceding gate, which is released only when the latter gate is executed by a suitable combination of its inputs. This gate executed operations such as AND, OR, and AND-NOT, the final output being reported by a REPORT gate, which emitted a fluorescent signal for an appropriate input, by releasing/displacing a fluorescent molecule into solution. This molecule fluoresce only in solution since on support is preventing of doing so by the action of an immobilized quencher. An AND gate is implemented such that either one of the  $XX_T$  or  $YY_T$  input sequences displaces a single duplex region ( $X$  or  $Y$ ) of an anchored molecule, the resulting  $XYZZ_T$  strand remaining anchored, while both inputs release the output strand  $XYZZ_T$  into solution. In an OR gate, the inputs  $XX_T$  or  $YY_T$  displace the respective strands  $XZZ_T$  or  $YZZ_T$ , whereas both inputs double the effective output  $ZZ_T$ . Other logic circuits or combinations of them are implemented in a similar way (Frezza et al. 2007). Rewiring implies a modification of the output sequences of logic gates. Successful cascading requires taking into account that differences in gate output levels amplifies in a multilevel circuit so that corrections are needed.

An example of a sequence-addressable DNA logic device is presented in Voelcker et al. (2008). It can implement in solution simple logic gates (AND, OR, XOR) and can combine them in a half-adder, which consists of an AND gate and a XOR gate that implement, respectively, the carry and the sum bit. The working principle of the device is based on the fact that ssDNA molecules can invade and displace shorter sections of a matching double-stranded DNA (dsDNA). These ssDNA attach first to short single-stranded toehold regions and then replace the base pairing in a smaller duplex, the thermodynamic driving force for the displacement being the longer duplex that the input DNA forms in the toehold region.

An example of the implementation of the AND gate utilizes as inputs two 24-nt sequences designed to bind to one 10-nt toehold end of a stationary 55-nt sequence immobilized on functionalized silica beads. As a result of this binding, the three-way branch migration mechanism induces a displacement of 14 bp of the 28-nt output strand which is duplexed to the center of the stationary strand. The output strand, labeled with a fluorescent molecule, is bounded to the immobilized stationary strand as long as no input or only one input is present, in the second case the binding becoming weaker. The result of computation is followed monitoring the release of the fluorescent molecule into the supernatant. This release occurs only in the presence of both inputs. A similar OR gate can be implemented if the 14-nt output strand is bound to the 30-nt immobilized stationary strand, both strands having ssDNA overhang regions. Either one of the 24-nt inputs can displace the output strand by binding to output strand itself or to the toehold region of the stationary strand first. In both case, the fluorescent molecule is released in the supernatant. Several logic gates can be cascaded if the output of a gate acts as input for the subsequent gate and if the sequence of reactions is implemented such that cross contamination is avoided.

A digital biomolecular circuit with a modular construction, which implements logic gates, as well as signal amplification and restoration, feedback, and cascaded operation, is described in Seelig et al. (2006). This enzyme-free circuit uses short oligonucleotides as input and output, the logic values 0 and 1 being assigned, respectively, to low and high concentrations. The gates operate based on Watson–Crick interactions/base pairing and breaking, which is used also for cascading several gates. A gate is composed of one or more gate strands, A and B in Fig. 7.3, which contain recognition regions complementary to the input and one output strand, O, which can either act as input for the next gate or can be labeled by a fluorescent molecule. As shown in Fig. 7.3, for an AND gate, computation begins when input strands are added in the solution containing the gate. The input strands  $A_{in}$  binds to the toehold region (gray) of the double-stranded gate, displacing the first gate strand by the mechanism of three-way branch migration and releasing a double-stranded waste. The toehold is thus ready for the next input,  $B_{in}$ , which induces similar processes. The output strand is released in the solution only in the presence of both inputs, and the result of computation is read by fluorescence experiments. In a similar manner, OR and NOT circuits can be implemented.

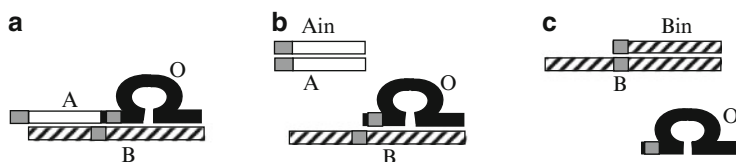


**Fig. 7.3** Implementation of an AND gate: (a) gate and output strands, (b) displacement of the A strands, and (c) displacement of the B strand

Cascading several gates is successful if the toehold-binding region of output strands is protected in upstream gates. Translator gates, which consist of single-input AND gates and convert the input to the output signal are useful in cascading circuits that have different toehold and recognition sequences. If the output signal level is not that required to act as input in the next operation, restoration can be achieved by thresholding, implemented as a three-input AND gate, and amplification, based on feedback reactions. The last gates prevented a 25% output leak in an 11-gate circuit, but slowed the operation from 2 to 10 h.

Photonic Boolean computing with DNA aptamers has been demonstrated in [Yoshida and Yokobayashi \(2007\)](#). These logic gates sense ssDNA molecules and aptamer ligands (adenosine and thrombin) as inputs and generate fluorescent signals as output. AND and OR logic gates have been implemented based on the reversible structure-switching mechanism of signaling aptamers, based on the equilibrium hybridization shift between an aptamer and a partially complementary oligonucleotide in the absence or presence of a ligand.

Besides DNA-based logic gates, ribozyme-based gates working in solution with short ssDNA strands as inputs have been extensively studied. Boolean logic is implemented in this case by an appropriate cleavage of a fluorogenic substrate sequence. For example, logic gates assembled from ligase units have been reported in [Stojanovic et al. \(2005\)](#), the ligase processes being controlled by stem-loop attachment. In another work, a molecular full-adder has been demonstrated ([Lederman et al. 2006](#)), which consists of an array of seven stem-loop-controlled deoxyribozyme-based logic gates using as inputs and three oligonucleotides and as carry and sum outputs two fluorogenic cleavage/cutting reactions with green and red emissions, respectively. Finally, a second-generation functional automaton able to play a complete game of tic-tac-toe according to a perfect strategy has been described in [Macdonald et al. \(2006\)](#). This medium-scale integrated automaton, called MAYA-II (Molecular Array of YES and AND gates), consists of 128 stem-loop-controlled deoxyribozyme-based logic gates, is operated by 32 oligonucleotide input, and yields 8 two-channel fluorescent outputs across 8 wells. It is assembled from three classes of logic gates: YES<sub>x</sub>, activated by one input, *x*; xAND<sub>y</sub> gates, activated by two inputs, *x* and *y*; and xAND<sub>y</sub>AND-NOT<sub>z</sub> gates that require three inputs, *x*, *y*, and *z*.

Another remarkable realization of biomolecular computing is the development of a biomolecular keypad lock based on enzyme logic gates ([Strack et al. 2008](#)) in which the output signals depend not only on the proper inputs but also on the order in which these are introduced. This keypad is based on a model biochemical reaction chain, represented schematically in Fig. 7.4 as a succession of three AND

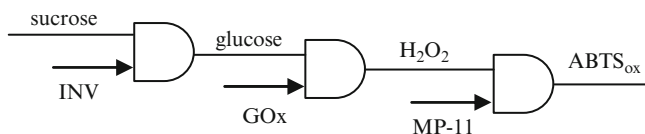


**Fig. 7.4** Biomolecular keypad

gates in solution, which results in a colored product. This device secures a code of three inputs.

The chain reaction involves the hydrolysis of sucrose to glucose, reaction that takes place only in the presence of the enzyme invertase INV, which is the first input, followed by the oxidation of glucose to hydrogen peroxide, which occurs only in the presence of the enzyme glucose oxidase (GOx), which represents the second input, the final reaction being the oxidation of a synthetic dye ABTS (2, 2'-azino-bis(3-ethylbenzthiazoline-6-sulfonic acid) in the presence of the third input enzyme, microperoxidase-11 (MP-11). All enzymes were immobilized on glass beads. The final oxidized product, ABTSox, was detected by monitoring the absorbance change at 415 nm. These measurements revealed that the correct output (a significant enhancement in absorption) occurs only when the three inputs are introduced in the correct order: INV, GOx, and MP-11. For any other order, the absorption change is minor, if at all.

A significant increase in the interest in DNA-based computing would be the ability to assemble at will logic circuits using a universal set of logic gates. This idea prompted the research for libraries of predesigned DNAzymes subunits, and their respective substrates that would perform logical operations in the presence of fitting nucleic acid inputs (Elbaz et al. 2010). If such libraries would be available, a computational unit would be assembled from two independent modules: an input module, consisting of input strands and recognition arms of the DNAzymes, and a processing module, which contains the cores of the catalytic DNAzymes that bind to the substrate. Then, inputs would guide the assembly of gate units by cleaving the substrate and releasing the output strand, conferring diversity and modularity to the design of computational units. Moreover, it is possible to choose a suitable substrate to enhance a gate output by feedback. Different gates would be formed by selecting individual subunits, while parallel gates could be assembled by choosing as input a combination of inputs of the individual gates. Initial attempts succeeded to assembly in this way XOR gates, half-adders and half-subtractors, as well as a YES gate that releases drugs, for example, a thrombin-binding aptamer, if a certain nucleic acid input is present (Elbaz et al. 2010). Such a modular design would encourage smart drug release procedures. However, much work is yet to be done since at present the inputs generated by cascades of gates weaken as the depth of the circuit increases, while interinput hybridization necessary in some computation and nonstoichiometric generation of inputs can prevent cascaded operation.

Several other biomolecular systems can be used to implement logic operations. For example, pairs of orthogonal ribosome-orthogonal mRNA in *Escherichia coli* can be used to implement posttranscriptional combinatorial logic in living cells (Rackham and Chin 2005), while the folding process of proteins in response input stimuli such as light and ATP (adenosine triphosphate) can be controlled by a genetically engineered chaperonin azo-GroEL, which originates from a GroEL protein in *Escherichia coli* functionalized by an azobenzene derivative. GroEL has a cylindrical cavity, which can trap a denatured green fluorescent protein, preventing its folding, but releases the protein (thus, allowing its folding) in the present of

both input stimuli (Muramatsu et al. 2006). This AND gate implementation could mechanically drive biomolecular devices.

### 7.3 Self-Assembly Biomolecular Computing

Biomolecular computing can help build complex two- or three-dimensional self-assembled or self-replicating structures, illustrating a bottom-up approach for nanoscale technology. Self-assembling, as discussed in Chap. 5, can be done with nanometer precision. A modular way of programmable assembly of nanostructures involves DNA tiles that have sticky ends that match the corresponding sticky ends of other tiles. The net result is a tiling lattice (Ezziane 2006). Examples of DNA computation using self-assembled tiles are given in Feldkamp and Niemeyer (2006), and a detailed discussion of error corrections can be found in Sager et al. (2008).

An illustration of biomolecular computation based on shape processing is the problem of three-vertex colorability for a graph with six vertices and nine edges, which can be solved by self-assembly of DNA strands (Wu et al. 2009). In this case, stable-branched DNA molecules are used to encrypt the solution as a nanoobject with a connectivity resembling that of the graph and not as sets of symbols encoded in DNA base pair sequence. The computation is performed in the presence of enzymes, which catalyze ligation and restriction reactions. Each vertex is embodied by a branched junction molecule with a number of arms equal to the number of connections it must establish with its adjacent vertices. Each arm has an extended single-strand 5' end, composed of 24 nt, each color being represented by different shades of gray in Fig. 7.5. The 5' ends identify unambiguously each edge that connects two neighboring vertices through three specific parts that enter their composition.

These parts, denoted by  $x$ ,  $y$ , and  $z$ , encode the edge information in the  $x$  and  $z$  portions and the color in  $y$ , so that all three arms of a branched junction have the same  $y$  parts on their 5' ends and the portions  $x$  and  $z$  on one arm of the molecule that represent vertex  $i$ , for example, are complementary to the  $x$  and  $z$  parts of the single-strand extensions of one of the arms representing the adjacent vortex  $j$  (their  $y$  portions are not complementary in this case, since the colors of adjacent vertices

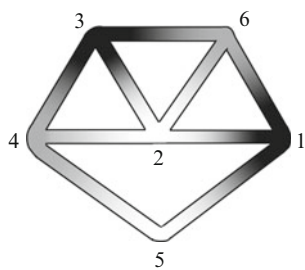


**Fig. 7.5** DNA graph that encrypts the solution of the three-vertex colorability problem

must differ). All three x, y, and z parts are encoded in 8 nt. When two arms of vertices with the same color hybridize, they form a restriction site allowing molecule cutting by a specific enzyme, associated to that specific color. On the contrary, when vertices with different colors join, the y parts of the sticky ends contain despaired restriction sites and the resulting edge is not destroyed by the restriction enzymes. The algorithm that solves the problem of three-vertex colorability involves the operations of annealing, during which the sticky ends hybridize, ligation, cleavage/cutting, during which the structures with joined identical-colored vertices are destroyed by the action of restriction enzymes, and extraction, which identifies the solution to the problem by the size of the remaining graphs. Three copies of each vertex, one for each color, are initially placed in solution, and the biomolecules are selected such that the optimal temperatures for ligation and restriction are different enough so that they take place separately as the temperature varies. The nanoobject that results after hybridization consists of a single strand that traverses twice the graph, each edge being a dsDNA molecule. The mathematical model of bidimensional shapes with colored edges is called Wang tile.

Biomolecular computing can also control the reversible self-assembly of nanoparticles into structural aggregates. For example, it is possible to couple 200-nm silica nanoparticles with pH-sensitive polymer shells with enzyme-base logic gates (Motornov et al. 2008). For  $\text{pH} < 5$ , the nanoparticle dispersion is stabilized by the charged polymer molecules, whereas for  $\text{pH} > 5$  the nanoparticles aggregate into structures with dimensions of  $3 \mu\text{m}$  because hydrophobic interactions between polymer chains dominate. To reversibly control the self-assembly process, pH changes must occur as a result of enzyme-based computing systems that generate biocatalytic reactions. If the pH-changing reaction occurs only in the presence of two input enzymes, the system implements the AND operation, the 0 and 1 logic states being encoded in the absence and presence, respectively, of each enzyme. Similarly, an OR logic gate is implemented if a pH change takes place in the presence of either one of two enzymes, which activate independent biocatalytic reactions. After completion of these reactions, the state of the system can be reset by another enzyme, which restores the pH value.

Other applications make use of DNA-patterned scaffolds or templates for targeted deposition of specific biomolecules that are part of computing protocols. Biomolecular logic circuits based on DNA self-assembly can identify femtomole quantities of analytes, such as short nucleic acids or proteins, in solution by encoding the optical response of arrangements of chromophores (Pistol et al. 2010). This sensor consists of a  $2 \times 80 \times 80\text{-nm}^3$  DNA grid, assembled as a  $4 \times 4$ -tile motif, on which input chromophores are attached at precise locations on one tile and the output chromophores on the neighboring tile. The resonance energy transfer of bound chromophores generates constrained pathways for excitons, which transfer between donors and acceptors, such that a multidonor resonance energy transfer index due to denaturation of the gate or input excitation designates the output. Chromophore triplets, consisting of two donors and one acceptor, are particularly well suited for logic and sensing since their optical responses can be changed by tuning the donor–acceptor separations.

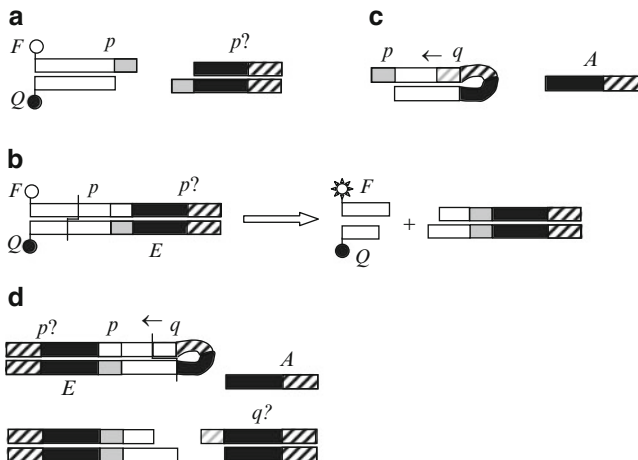


**Fig. 7.6** Logic DNA computation: (a) representation of a proposition (*left*) and query (*right*) molecules, (b) implementation of query reduction with a proposition, (c) representation of the implication molecule (*left*) and auxiliary strand (*right*), and (d) implementation of query reduction with an implication

## 7.4 Biomolecular Logical Deductions

Besides being able to implement complex Boolean logical circuits consisting of sequences of logic gates, biomolecules, and in particular DNA can be used to perform simple logical deductions (Ran et al. 2009). Thus, biomolecular-implemented simple programming languages can be developed in this way. In order to do this, the propositions  $p$  (“Plato is a man”) are encoded in the 4-nt sticky end of a dsDNA, one strand being the sense strand and ending with a fluorescent molecule  $F$ , while the other, antisense strand ends with a matching quencher  $Q$ , which inhibits  $F$ . Queries, denoted by  $p?$  (“Is Plato a man?”), are represented by a dsDNA with a complementary sticky end to that of  $p$  and a 5-nt recognition site for a restriction enzyme  $E$  (the enzyme  $E$  cuts the two strands at different places at a certain distance from its recognition site (dark color in Fig. 7.6)).

Then, the query  $p?$  has a positive answer (“Yes”) by the proposition  $p$ ; since their sticky ends hybridize, the enzyme  $E$  is attracted to the recognition site on  $p?$  and cuts the proposition molecule  $p$ . As a consequence, the sense and antisense strands become separated, and the fluorescent molecule emits light if excited. The light emission is interpreted as a positive response to the query. An implication, denoted by  $p \leftarrow q$  (“Plato is mortal if Plato is a man”), can be encoded in a hairpin ssDNA, which consists of a 4-nt sticky end that represents  $p$ , a 4-nt section that matches  $q$ , and a third, 5-nt section that matches an auxiliary complementary strand  $A$ , both representing the recognition site for  $E$ . Then,  $p \leftarrow q$  reduces the query  $p?$  to the query  $q?$  (“Plato is mortal”), which implies that the positive answer to  $p?$  guarantees a positive answer to  $q?$ . In solution, the sticky end of  $p?$  hybridizes with

that of  $p \leftarrow q$ ; the enzyme  $E$  cuts the implication molecule at the recognition site in the query and releases a ssDNA, which hybridizes with the auxiliary matching strand to form  $q$ ?

These simple biomolecular logical operations can be used to implement logic programs, which consists of a finite set of facts and rules (Ran et al. 2009). In this sense, a query is answered by the output of a logic program, query reduction being the basic step of logical deduction. In Ran et al. (2009), a four-step cascaded deduction experiment was implemented in which the half time of a logical deduction was 3 min and the query molecule was able to perform many cleavage operations without needing an external supply and without undergoing change. The experiment was designed such that different fluorescent molecules, with different light emission wavelengths, can signify different assumptions. Such logical programs with clear semantics can develop high-level languages, which could be compiled into executable programs.

A programmable 3-symbol-3-state automaton, consisting of biomolecules in solution that represent hardware, software, input, and output components, has been demonstrated in Soreni et al. (2005). The hardware is composed of two enzymes (a ligase and a restriction nuclease), and the software, surface-anchored input, and output molecules are dsDNA strands, the computation being implemented via cycles of restriction, hybridization, and ligation induced by the order and type of transition molecules introduced in solution. The readout of the result and the monitoring of the computation are performed by surface plasmon resonance technology. Each symbol is encoded in a 6-bp sequence, and each state is represented by the depth of the cut performed by a restriction molecule in the symbol domain. An input molecule contains a recognition site for the restriction nuclease, several symbols, and a terminator domain, the software consists of a set of nine transition molecules with a 5-bp recognition site and a unique 4-bp sticky end separated by a spacer that contains up to 4 bp. The readout is done by three detection molecules with matching sticky ends to corresponding ends generated by restriction of the terminator molecule. The detection molecules produce different surface plasmon resonance responses upon hybridization with one of the three symbol sequences. A program consists of selecting a subset from the 27 possible transition rules and choosing the accepting internal states; there are 137,781 syntactically distinct programs. The program ends when there are no transition molecules left that match the sticky end of the input or when the terminator domain is restricted, producing sticky ends that encode the final output state. Parallel computing is possible if the input molecules are immobilized.

## 7.5 Biomolecular Memory Devices

DNA scaffolds that support arrays of independently and reversibly addressable sites can be used as rewritable memories. Such a device, consisting of three independent addresses representing eight states, was demonstrated with a one-dimensional array

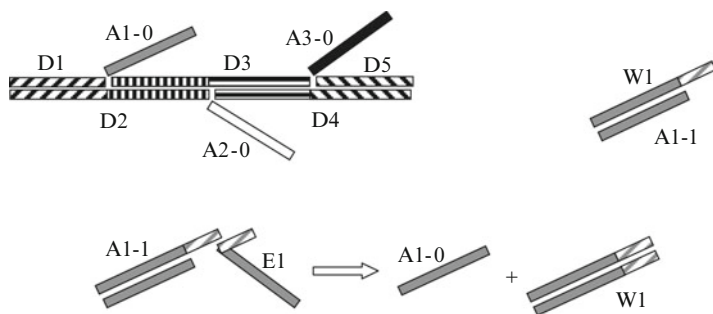


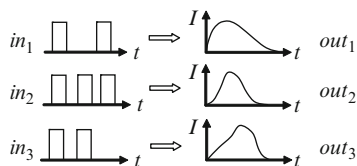
**Fig. 7.7** Biomolecular memory. *Top left* addressable branches, *top right* writing procedure, *bottom* erasing procedure

of sites spaced at 7 nm in which specific DNA strands control the bit state of each address (Shin and Pierce 2004). The readout of each state can be performed by fluorescent molecules that emit at different visible wavelengths. The biomolecular memory is formed from five single-stranded oligonucleotides denoted by  $D_i$  in Fig. 7.7, which self-assemble in a structure with three addressable branches  $A_i$  if stoichiometrically mixed.

The branches  $A_i$ , which are separated by 20 bp with a total length of 7 nm, have the logic value 0 if single stranded and the logic value 1 if double stranded. The information can be written by single-stranded writing molecules  $W_i$ , which have a complementary structure to one of the addresses, changing its logic values from 0 to 1 by hybridization. The writing strands have a 10-bp overhang, which represents the nucleation site for hybridization with a matching region of an erasing strand. The erasing strands  $E_i$  restore the initial 0 logic value of the address by hybridizing with  $W_i$  and thus forming a duplex waste product  $W_i$  and a single-stranded address with a 0 logic value. The state readout can be done by fluorescent measurements if quencher molecules for different fluorescent molecules in the vicinity of the addresses are attached to the  $W_i$  strands. Then, the 0 state is associated to no (or weak) fluorescence, and the 1 logic state corresponds to strong fluorescence. The writing and erasure processes must be implemented in a controlled sequence to avoid undesirable interactions between strands. This memory device is slow: the writing rate constants are of the order of  $10^5 \text{ s}^{-1} \text{ M}^{-1}$ , while the erasing process is governed by a fast phase with a comparable rate to the writing process and a slow phase, with a rate of  $10^{-3} \text{ s}^{-1} \text{ M}^{-1}$ . Larger memory addresses require more rigid, two-dimensional scaffolds.

Biomolecules can also be used to implement a fractal memory, which is no longer a binary-code device, but its output signal pattern depends on the pattern of the input signal. For example, for input pulses of different shapes, such as in Fig. 7.8, the output represented, for example, by the decay of a photocurrent is different. Different patterns of the input signal can represent different ASCII codes.

**Fig. 7.8** Current-time patterns in a fractal memory



Such a fractal memory photodiode can be implemented with four molecules: ferrocene, which acts as electron donor, flavin as the sensitizer, viologen as the relay, and, finally, the protein cytochrome *c* as the electron acceptor. These are deposited sequentially in this order on a substrate in a metal/insulator/metal configuration, the top electrode being an aluminum layer (Choi et al. 2003). The electron transport in this biomolecular photodiode mimics the photosynthesis process. The state of the photodiode can be preset by irradiation with a laser pulse and can be reset by applying a bias in dark/absence of light. The fractal memory effect was tested by transient photocurrent measurements for trains of input pulses that simulate the ASCII codes “U,” “T,” “Q,” and “P,” different responses/decay profiles corresponding to different inputs.

## 7.6 Logical Drug Delivery and In Vivo Computation

Biomolecular logic computation can be used in biomedicine for controlled delivery of drugs. In such a device (Shlyahovsky et al. 2009), the 0 and 1 Boolean bits are encoded as presence and absence, respectively, of aptamer substrates or a ssDNA molecule, such that for each gate a set of aptamer substrates or DNA strands representing the output release a catalytic nucleic acid that yield a fluorescent signal. Logic gates combine two DNA translators that mediate the release of certain output nucleic acid strands when the DNA input strand does not match the output. This operation, which decouples the input sequence from useful output sequences, allows information translation from one code to another. The operation of the device is based on strand displacement instigated by formation of a duplex in the loop region (see Fig. 7.9). This mechanism is based on the fact that duplex formation is favored by base-pairing of loop-bridged complementary sequences A and B, and that stability of the duplex region is dictated by the extent of base pairing.

More specifically, if one duplex region is separated by the creation of an aptamer–substrate complex or by strand displacement due to favored interactions/superior base pairing, the other weakened double-stranded region is separated in its turn in a subsequent process. The DNA logic device consists of four footholds hybridized to the same DNA scaffold that acts as a track. The outer footholds, hybridized with mediator strands, sense the input and, for appropriate input aptamers or DNA strands, translocate the mediator strands to the inner footholds. Then, the nucleic acids linked to the inner footholds are displaced by the mediator strands and form

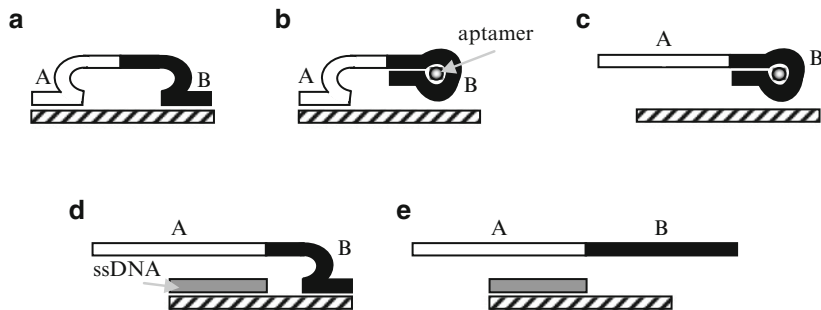


**Fig. 7.9** Logic gate for drug delivery. A stable duplex DNA (a) can be separated by interaction with an aptamer (b) or strand displacement (d). The final results of the two processes are the molecules represented in (c) and (e), respectively

the product/output strands. These can be eventually read by output-induced catalysis of a colored product. Based on these principles, logic gates such as OR, XOR, and AND were implemented (Shlyahovsky et al. 2009). In experiments, the results of these complex logic gates can be reproduced with up to 15% errors. However, these experiments suggest that the DNA-translator-based device could activate the release of nucleic acids or inhibitors of harmful enzymes. In fact, this DNA-scaffold-based device was used for the controlled release of thrombin-binding aptamers, which inhibit thrombin. Thrombin is an enzyme that participates in blood clotting and could cause inflammatory brain illness. Experiments showed that the hydrolytic activity of thrombin was inhibited by 40%.

An *in vitro* demonstration of an autonomous biomolecular computer that analyses the levels of messenger RNA and releases in response a molecule that affects the gene expression is presented in Benenson et al. (2004). The computer consists of an input module, which regulates the transition probabilities in the automaton through mRNA levels, a computation module, and an output module, which release a short ssDNA molecule depending on the input. The automaton has two possible outcomes: YES or NO (positive or negative diagnosis) depending on the concentration of certain molecule [four in Benenson et al. (2004)], which indicate a specific illness. It is a stochastic automaton, with competing transitions associated to each output, able to release a drug or its suppressor molecule in the YES or NOT state, respectively. The sensitivity of the automaton to diagnosis can be tuned by adjusting the concentrations of competing transitions so that the disease-indicative mRNA can be detected at concentrations as low as 100 nM.

An encouraging sign toward a reliable *in vivo* molecular computing is the ability to control mRNA with appropriate combinations of transcription factor, which regulate synthetic genes coding (Leisner et al. 2010). This computer consists of sensory, computational, and actuation modules, which have yet to be optimized.

Not only computations involving individual DNA strands have been demonstrated, but also collective computations in living cells. For example, a genetic circuit able to generate synchronized oscillations (genetic clocks) in a thriving

population of cells has been recently implemented; it is another example of complex cellular behavior besides that encountered in genetic circuits able to shape intracellular noise, generate designed patterns, counting cellular events, and so on [see [Danino et al. \(2010\)](#)] and the references therein). The collective synchronization is based on placing genes involved in quorum sensing machines and extracted from *Bacillus Thuringensis* and *Vibrio fischeri*, under the control of gene promoters. These genes generate synchronized oscillations in the population of *Escherichia coli* placed in a microfluidic device. These oscillations are robust, persistent, and fast, with periods as short as 13 min. The oscillation period depends on temperature, media source, and concentration of inducers in the solution [for details, see [Stricker et al. \(2008\)](#)]. It was observed that almost every *E. coli* cell oscillates and that the oscillatory phase is inherited by daughter cells.

## References

- Adleman L (1994) Molecular computation of solutions to combinatorial problems. *Science* 266:1021–1024
- Ashkenasy G, Ghadiri MR (2004) Boolean logic functions of a synthetic peptide network. *J Am Chem Soc* 126:11140–11141
- Ben-Jacob E, Hermon Z, Caspi S (1999) DNA transistor and quantum bit element: realization of nano-biomolecular logical devices. *Phys Lett A* 263:199–202
- Benenson Y, Paz-Elizur T, Adar R, Keinan E, Livneh Z, Shapiro E (2001) Programmable and autonomous computing machine made of biomolecules. *Nature* 414:430–434
- Benenson Y, Adar R, Paz-Elizur T, Livneh Z, Shapiro E (2003) DNA molecule provides a computing machine with both data and fuel. *Proc Natl Acad Sci USA* 100:2191–2196
- Benenson Y, Gil B, Ben-Dor U, Adar R, Shapiro E (2004) An autonomous molecular computer for logical control of gene expression. *Nature* 429:423–429
- Choi J-W, Nam Y-S, Cho KS, Lee W-H, Park S-Y, Fujihira M (2003) Fractal memory function of biomolecular photodiode consisting of ferrocene/flavin/viologen/cytochrome c hetero-film. *J Ind Eng Chem* 9:31–36
- Danino T, Mondragón-Palomino O, Tsimring L, Hasty J (2010) A synchronized quorum of genetic clocks. *Nature* 463:326–330
- Dragoman M, Dragoman D (2009) *Nanoelectronics. Principles and devices*, 2nd edn. Artech House, Boston, MA, Chapter 7
- Elbaz J, Lioubashevski O, Wang F, Remacle F, Levine RD, Willner I (2010) DNA computing circuits using libraries of DNAzyme subunits. *Nat Nanotechnol* 5:417–422
- Ezziane Z (2006) DNA computing: applications and challenges. *Nanotechnology* 17:R27–R39
- Feldkamp U, Niemeyer CM (2006) Rational design of DNA nanoarchitectures. *Angew Chem Int Ed Engl* 45:1856–1876
- Frezza BM, Cockroft SL, Ghadiri MR (2007) Modular multi-level circuits from immobilized DNA-based logic gates. *J Am Chem Soc* 129:14875–14879
- Harkin J, Morgan F, McDaid L, Hall S, McGinley B, Cawley S (2009) A reconfigurable and biologically inspired paradigm for computation using network-on-chip and spiking neural networks. *Int J Reconfigurable Comput* 908740
- Lederman H, Macdonald J, Stefanovic D, Stojanovic MN (2006) Deoxyribozyme-based three-input logic gates and construction of a molecular full adder. *Biochemistry* 45:1194–1199
- Leisner M, Bleris L, Lohmueller J, Xie Z, Benenson Y (2010) Rationally designed logic integration of regulatory signals in mammalian cells. *Nat Nanotechnol* 5:666–670

- Macdonald J, Li Y, Sutovic M, Lederman H, Pendri K, Lu W, Andrews BL, Stefanovic D, Stojanovic MN (2006) Medium scale integration of molecular logic gates in an automaton. *Nano Lett* 6:2598–2603
- Margulies D, Melman G, Shanzer A (2006) A molecular full-adder and full-subtractor, an additional step toward a moleculator. *J Am Chem Soc* 128:4865–4871
- Motornov M, Zhou J, Pita M, Gopishetty V, Tokarev I, Katz E, Minko S (2008) “Chemical transformers” from nanoparticle ensembles operated with logic. *Nano Lett* 8:2993–2997
- Muramatsu S, Kinbara K, Taguchi H, Ishii N, Aida T (2006) Semibiological molecular machine with an implemented “AND” logic gate for regulation of protein folding. *J Am Chem Soc* 128:3764–3769
- Pistol C, Mao V, Thusu V, Lebeck AR, Dwyer C (2010) Encoded multichromophore response for simultaneous label-free detection. *Small* 6:843–850
- Rackham O, Chin JW (2005) Cellular logic with orthogonal ribosomes. *J Am Chem Soc* 127:17584–17585
- Ran T, Kaplan S, Shapiro E (2009) Molecular implementation of simple logic programs. *Nat Nanotechnol* 4:642–648
- Sager J, Farfel J, Stefanovic D (2008) Nanocomputing. In: Shoseyov O, Levy I (eds) *Nanobiotechnology: bioinspired devices and materials of the future*. Humana Press, Totowa, NJ
- Seelig G, Soloveichik D, Zhang DY, Winfree E (2006) Enzyme-free nucleic acid logic circuits. *Science* 314:1585–1588
- Shin J-S, Pierce NA (2004) Rewritable memory by controllable nanopatterning of DNA. *Nano Lett* 4:905–909
- Shlyahovsky B, Li Y, Lioubashevski O, Elbaz J, Willner I (2009) Logic gates and antisense DNA devices operating on a translator nucleic acid scaffold. *ACS Nano* 3:1831–1843
- Soreni M, Yoge S, Kossoy E, Shoham Y, Keinan E (2005) Parallel biomolecular computation on surfaces with advanced finite automata. *J Am Chem Soc* 127:3935–3943
- Stojanovic MN, Semova S, Kolpashchikov D, Macdonald J, Morgan C, Stefanovic D (2005) Deoxyribozyme-based ligase logic gates and their initial circuits. *J Am Chem Soc* 127:6914–6915
- Strack G, Ornatska M, Pita M, Katz E (2008) Biocomputing security system: concatenated enzyme-based logic gates operating as a biomolecular keypad lock. *J Am Chem Soc* 130:4234–4235
- Stricker J, Cookson S, Bennett MR, Mather WH, Tsimring LS, Hasty J (2008) A fast, robust and tunable synthetic gene oscillator. *Nature* 456:516–519
- Szaciłowski K (2008) Digital information processing in molecular systems. *Chem Rev* 108:3481–3548
- Voelcker NH, Guckian KM, Saghatelian A, Ghadiri MR (2008) Sequence-addressable DNA logic. *Small* 4:427–431
- Wu G, Jonoska N, Seeman NC (2009) Construction of a DNA nano-object directly demonstrates computation. *BioSystems* 98:80–84
- Yoshida W, Yokobayashi Y (2007) Photonic Boolean logic gates based on DNA aptamers. *Chem Commun* 195–197

## Chapter 8

# Bioinspired Devices

**Abstract** This chapter summarizes materials and devices that were designed using nature as inspiration. These materials can incorporate multiple functionalities, while the devices improve standard human designs. In addition, bioinspired technological processes are presented, which take place in mild environmental conditions, and complex structures that mimic the functionality of organs are discussed as a first step toward a better understanding of human and animal bodies.

Bioinspired devices or, more generally, biomimetics is a growing research area driven by the belief that nature, in its long evolution, created already the most efficient and environment-friendly solutions of many of our problems. In many cases, our task is just to unravel the mechanisms of biological processes and, if possible, to copy them with the greatest possible fidelity. Indeed, aviation, car industry, and robotics are inspired by the nature's efficient solutions for movement embodied in human and animal life-forms, while innovative architecture solutions often resemble constructions made by insects, fish, or animals. Despite these timid approaches to copy nature's most successful creations, we are still far from the sophisticated hierarchy of structures of nature's designs. For example, cephalopods have both static and variable reflective tissues, incorporated in the eyes, light organ and digestive gland, and, respectively, in the skin of the mantle. The complexity of these biological nanostructures overcomes by far the man-made counterparts. These tissues are essential for camouflage and consist of flat nanometer-sized platelets with a high refractive index separated by low-refractive-index layers, which modulate light as a result of thin-film interference. They are made, generally, from purine crystals, but can consist also of proteins, as in the tissue of the *Euprymna scolopes* squid (Crookes et al. 2004).

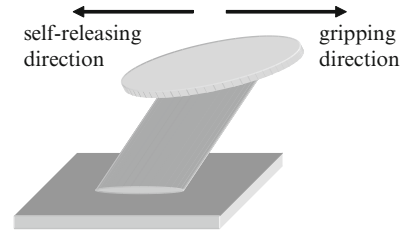
## 8.1 Bioinspired Materials

Bioinspired nanoscale surfaces and structures can lead to the development of new materials with amazing properties. In particular, spiders inspired the synthesis of flexible hair, fire beetles inspired infrared sensors based on flexible membranes (McConney et al. 2009), whereas hydrogel networks are bioinspired dynamic materials that can change their volume and shapes and can assemble and disassemble in response to external stimuli (Mohammed and Murphy 2009). Nature is also an endless source of inspiration of superantwetting interfaces with controlled liquid–solid adhesion through micro- and nanostructures (Liu et al. 2010). For instance, lotus flowers, which have the ability to maintain their cleanliness even in swampy waters due to a low-adhesion superhydrophobic surface, have inspired the production of self-cleaning paints. On lotus leaves, composed of papillae that are covered with nanohairs, the almost spherical water droplets easily roll off the surface at small tilt angles and wash away any small particles of dirt. Similar to the self-cleaning effect of lotus flowers, fishes are able to resist pollution of oil in water due to the superoleophobic water/solid interface of their rough scales. Rose petals, which consist of arrays of micropapillae, and gecko feet, covered with millions of nanohairs, are high-adhesion superhydrophobic surfaces, on which water droplets are pinned at any tilt angles, although the static contact angle is larger than  $150^\circ$ .

On superhydrophobic surfaces, for which the static contact angle is higher than  $150^\circ$ , the liquid–solid adhesion can be high or low, depending on the contact mode, which is determined by the composition and geometrical structure of the surface, and the triple-phase liquid/air/solid contact line. High adhesion corresponds to a continuous and stable triple-phase contact line and a wet contact mode, in which the water droplet penetrates the valleys of a patterned surface, while low adhesion is associated with a discontinuous triple-phase contact line and a composite contact mode, in which the droplet is suspended by air pockets trapped on a textured surface. Intermediate states also exist, in which the water droplet partially wets a superhydrophobic surface when air pockets are partially trapped in the valleys of the textured surface (Liu et al. 2010). In butterflies, for example, the surface adhesion of the wings is not fixed but can be controlled by their posture (upward or downward) and the airflow direction across the surface. Examples of synthetic bioinspired superhydrophobic surfaces with different liquid–solid adhesion are described in Liu et al. (2010).

Bioinspired surface micro- and nanostructuring changes the hydrophobicity of metallic alloys and prevents them from corrosion. For example, the ultralight, rigid, strong, and highly ductile Mg–Li alloy, with potential applications in electronics and aviation, becomes stably superhydrophobic after modifying its surface in a peony-like hierarchical structure as that in the petals of *Paeonia* roses. In fact, to obtain a static contact angle of  $160^\circ$  and a sliding angle as small as  $5^\circ$ , plates of Mg–Li alloys are ultrasonically cleaned in ethanol and doubly distilled water at room temperature, dried in  $N_2$ , immersed in 0.1 M HCl aqueous solution, rinsed in doubly distilled water and dried again in  $N_2$ , exposed to a 1% ethanol solution of fluoroalkylsilane

**Fig. 8.1** Gecko-inspired tipped fiber with anisotropic adhesion



for 12 h, and finally heated at 100 °C for 2 h. After developing random papillae with peony-like morphology, the surface energy is lowered by an additional coating with fluoroalkylsilane. The papillae are 2–3  $\mu\text{m}$  in diameter, and the 30–50-nm-thick petal-like structures are separated by interspaces with a thickness of 40–300 nm. The acquired surface roughness traps air and so minimizes the contact area between alloy and water droplets (Liu et al. 2008).

Controlled anisotropic/directional wetting, as in butterfly wings, duck feathers, or shark skin, can be achieved in periodic structures with different heights, periods, and linewidths, obtained by laser interference lithography (Wu et al. 2010). It was found that the height of the grooves mainly determines the anisotropic wetting, due to the dependence of free energy barrier on this parameter, the linewidths and periods having a much weaker influence. For example, the anisotropy of a 2- $\mu\text{m}$ -period grating, defined as the difference of contact angles in the perpendicular and parallel directions to the longitudinal axis of the grating, increases from 9° to 48° when the height of the grooves increased from 100 nm to 1.3  $\mu\text{m}$ . The height of the grooves can be controlled by varying the thickness of the resin, the period  $\Lambda = \lambda / (2 \sin \theta)$  depends on the laser wavelength  $\lambda$  and incident angle  $\theta$ , while the width of the grooves is determined by the laser exposure dosage. An increase in contact angles on both directions to values higher than 100° (131° and 108°) is achieved by fluoroalkylsilane surface modification. High contact angles are beneficial for water roll down on grass leaves, for example. In addition, the wetting anisotropy is accompanied by iridescent diffraction patterns.

The design of strong adhesive materials can get inspiration from gecko lizards, which can climb easily on vertical or even inverted surfaces, due to the attachment mechanism of their setae. (Setae are specialized keratinous foot hairs on the foot pads of geckos.) This mechanism of high interfacial shear adhesion is determined by intermolecular surface forces acting at the tips of the microscale angled keratinous fibers on the lizard feet. In fact, the adhesion strength is the result of the contribution of millions of contact points with nanometer scale. The angled fibers determine a significant frictional anisotropy, with high adhesion at dragging along the gripping direction and only weak Coulomb friction along the opposite, releasing direction, which allows also an easy detachment of gecko setae from smooth surfaces. Synthetic adhesives that mimic the behavior of gecko setae use 100- $\mu\text{m}$ -long angled fibers with diameters of 35  $\mu\text{m}$  terminated with flat, mushroomed-shaped tips to increase the contact area (Murphy et al. 2009). A singular tipped fiber is represented in Fig. 8.1.

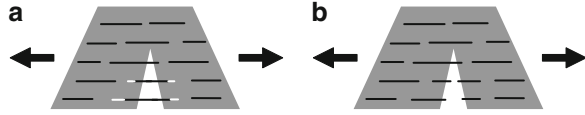
The fibers are made from polyurethane, a material with high strain before failure, high tear strength, and high Young modulus, of about 3 MPa, using lithography and molding techniques. An array of such fibers can support, through shear adhesive strength, loads of about  $1 \text{ kg cm}^{-2}$  if loaded in the gripping direction and self-releasing behavior if loaded in the opposite, shear direction, when it supports only a load of  $200 \text{ g cm}^{-2}$ . The shear anisotropy, caused by the stresses originating in the moment of the sheared tip, is controlled by the tip angle, while the interfacial shear strength is determined by the tip area. The tip angle can vary between  $0^\circ$  and  $90^\circ$ , whereas the base fiber angle can be varied between  $0^\circ$  and  $33^\circ$ . Combining the controlled fabrication of arrays of micrometer-sized angled polymer stalks with a strategy of controlling the toes' smooth attachment and detachment and the balance forces among the feet allowed the fabrication of the bioinspired Stickybot robot. Stickybot uses a hierarchy of conformable structures to climb glass, ceramic tiles, or smooth plastic surfaces at a speed of  $4 \text{ cm s}^{-1}$  (Kim et al. 2008).

Gecko-inspired synthetic materials consisting of angled nanostructures have been extensively studied. It was shown that for nanohairs fabricated from both soft and hard polymers, an increase in the leaning angle enhances significantly the shear adhesion and the adhesion hysteresis, the effect being more pronounced for soft materials (Jeong et al. 2010). The reason is that the hard polymer nanohairs make a tip contact with the substrate, while soft polymer nanohairs make a side contact. However, nanohairs with a high leaning angle have also increased difficulty to attach to rough surfaces and tend to clump on the substrate, phenomena that are avoided in gecko lizards by a multiscale, hierarchical organization of foot hairs. Bioinspired design strategies for smart multiscale interfacial materials are exemplified in Xia and Jiang (2008).

Often, gecko-inspired synthetic materials with high adhesion do not maintain this property in wet environments. To create an artificial material with comparable high adhesion in air and water, we have to look to both gecko and mussels for inspiration. Mussels are able to cling to wet surfaces due to the secretion of a specialized adhesive protein containing a catecholic amino acid. The resulting material is called geckel (Lee et al. 2007) and consists of an array of poly(dimethylsiloxane) elastomer nanopillars fabricated by electron-beam lithography coated with an ultrathin layer (with a thickness of less than 20 nm) of a synthetic polymer with similar properties as the wet adhesive proteins in the holdfasts of mussels. The geckel has superior adhesion force per pillar than gecko-inspired material in both air and water environments: 120 nN for geckel in air compared to about 40 nN for gecko-like material in air and 86.3 nN for geckel in water with respect to only about 6 nN for gecko-inspired adhesive in water. The force per pillar in water increased about 15 times, the wet adhesion properties maintaining over more than 1,000 contact cycles. It is important to emphasize that the synthetic polymer used for coating peels off quite easily if applied on flat substrates.

Nature's sophisticated architectures are also visible in the creation of hybrid flexible and strong structures starting from materials with poor qualities. Humans have long since fabricated strong and stiff clay-based nanocomposites, which lack, however, flaw tolerance and ductility encountered in the outer skeleton of

**Fig. 8.2** Bioinspired composite material exhibiting (a) plastic flow and (b) catastrophic rupture



invertebrates, for instance, in the nacreous layer of mollusk shells or in the mineralized tissues of vertebrates, exemplified by teeth or bones. These biological materials have a layered structure, which consist of an organic, soft, and ductile matrix that incorporates inorganic, strong platelets. Although the inorganic materials such as silica, phosphates, or calcium carbonates are weak, the resulting platelets are strong due to the nanoscale confinement of at least one of their dimensions. Moreover, the platelets are often arranged in a hierarchical structure over a wide range of length scales. Such hybrid structures can be described by a model (Bonderer et al. 2008) which predicts that the tensile strength of the material,  $\sigma$ , is a weighted average of the tensile strengths of the platelets,  $\sigma_p$ , and of the organic matrix,  $\sigma_m$ :

$$\sigma = \alpha V_p \sigma_p + (1 - V_p) \sigma_m. \quad (8.1)$$

In (8.1),  $V_p$  is the volume fraction of platelets and  $\alpha$  is a constant that depends on the aspect ratio of the platelets,  $r$ , on their bonding to the matrix, expressed by the interfacial strength  $\tau_i$ , as well as on the shear strength of the matrix  $\tau_m$ . If  $r < r_c$ , with  $r_c$  a critical aspect ratio, the organic matrix breaks first, and the platelets are pulled out (see Fig. 8.2a), the composite becoming tougher and ductile and exhibiting a matrix plastic flow before rupture. This is the case of biological materials discussed above. In this situation,  $\alpha = \tau_m r / (2\sigma_p)$  or  $\alpha = \tau_i r / (2\sigma_p)$  if the fracture appears first at the organic–inorganic interface and then in the organic matrix. On the contrary, when  $r > r_c$ , the platelets are fractured first and the composite undergoes a brittle catastrophic rupture, regime for which  $\alpha = 1 - \sigma_p / (2\tau_m r)$ . Synthetic materials with the same structure as nacre have been fabricated using a sequential deposition of organic and inorganic layers at ambient conditions and colloidal-based techniques for the assembly of the platelets. These artificial structures used a chitosan polymer, with a similar  $\tau_m$  value as in nacre, of 40 MPa, but alumina platelets instead of the aragonite platelets in nacre, allowing  $\sigma_p$  to become 2 GPa instead of the 360–500-MPa range of values in nacre (Bonderer et al. 2008). Thus,  $r_c$  increased from the biological value of 9–12.5 to 50 so that 200-nm-thick platelets could be used in the synthetic material, value comparable to that in nacre. The fabricated structures had a  $V_p$  value of up to 0.15, range in which a load applied parallel to the ordered platelets increases the elastic modulus of the composite from 2 to 10 GPa, and the tensile stress for plastic yielding (regime in which the mechanical behavior deviates from the linear elastic regime) augments from 50 MPa to 300 MPa. Although artificial composites have less-elaborate structure compared to their biological counterparts, synthetic materials can outperform their biological counterparts in terms of strength and ductility since the range of available materials is larger than in the natural environment.

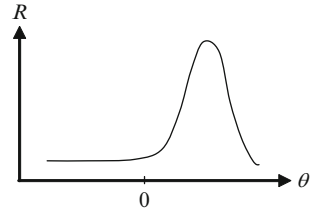
It should be mentioned that strength and flexibility are not the only characteristics of synthetic materials that can be improved by bioinspired designs. The mechanical sensing mechanism of low-frequency vibrations in spiders in the presence of significant background noise, and their ability to distinguish between air flow, for example, and signals from prey can inspire an efficient mechanical high-pass filter (Fratzl and Barth 2009). The sensory hairs on the spider's legs have both high sensitivity to small deflections and associated protection against overload. Other biological structures for interest in designing actuators and mechanical sensors are discussed in Fratzl and Barth (2009).

Structures with controlled and tunable mechanical properties often follow nature's design. For instance, scaffolds with controlled gradation of mineral contents, in particular calcium phosphate, which resemble the tendon-to-bone attachment and hence are invaluable in prosthetics and tissue regeneration, have been reported by Li et al. (2009). These structures are important since they avoid stress development at the interface between soft materials, like tendons, and stiff materials, such as bones. Calcium phosphate incorporates easily into nonwoven mats of electrospun nanofibers, which provide a large surface area and high porosity that resemble those in the extracellular matrix, the mineralization gradient being obtained by varying the immersion time of the mats into a concentrated simulated body fluid. The latter task can be achieved simply by introducing the mat into a vial and pouring the mineral solution at constant rate in the vial; the bottom part of the mat will present a larger calcium phosphate concentration because it is immersed longer in the mineral solution, the concentration decreasing linearly from the bottom to the top of the mat. The morphology of different mat regions is also different: a nanotextured mineral coating is observed near the bottom of the vial, while the porous structure of the mat is still preserved in regions near the top of the mat. Mouse preosteoblast cells deposited on regions with higher concentration of calcium phosphate showed higher levels of cell density, as expected from this functional graded material. From the point of view of material engineering, the graded scaffolds show also graded mechanical properties: the local strain under uniaxial tensile deformation was higher at the unmineralized end of the scaffold than at the mineralized end, whereas the Young modulus increased twice as the calcium phosphate covering increased by 23%. The results suggest that mineral coating stiffened the nanofibers.

Among the few bioinspired hierarchically organized materials are the scaffolds fabricated from bioactive nanotitanate grown on a three-dimensional microporous NiTi/Ti orthopedic scaffold, which are detailed in Wu et al. (2008). The NiTi/Ti scaffold is submerged in a 10-M NaOH aqueous solution and then heated, such that a titanate nanoskeleton layer appears on the surface of the scaffold, on which titanate nanowires and nanobelts nucleate in time. Such metallic Ti-based hierarchical scaffolds have great importance in tissue regeneration since, in addition to resembling the hierarchical organization of the main bone constituents collagen and hydroxyapatite, they are superhydrophilic and so enhance bone proliferation.

Light manipulation is an active direction of research, which profit from bioinspired structures to produce pigment-free colors, for example. Few life-forms have

**Fig. 8.3** Angular dependence of reflection for iridescent structures

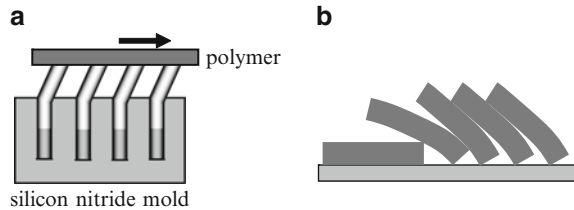


a more amazing capacity of light modulation by periodic micro- and nanostructures than butterflies. In particular, the wings of *Ancyluris meliboeus* consist of 50- $\mu\text{m}$ -wide and 100- $\mu\text{m}$ -long overlapping scales arranged like roof tiles with a density of 500–600 scales  $\text{mm}^{-2}$ . Each scale is made of layers of 150-nm-thick, 200-nm-wide, and 1.5- $\mu\text{m}$ -long cuticles separated by air spaces; the rows of cuticles are tilted at  $30^\circ$  with respect to the scale substrate. These structures produce bright iridescence, characterized by an angle-dependent reflection, as shown in Fig. 8.3.

A nanoengineering approach to reproduce the structure and the angle-dependent reflectivity of this butterfly wing, which involves nanoimprint lithography and shear patterning, is described in Kustandi et al. (2009). A silicon nitride mold containing nanosized trenches is pressed at high temperature against a polymer, which fills the trenches under external imprint pressure. After cooling, a controlled lateral collapse of the high-aspect-ratio polymer nanostructures obtained after releasing the mold can be achieved by applying a horizontal force during the release process; as shown in Fig. 8.4, nanostructures of similar dimensions and tilting as in butterfly wings can be achieved with polycarbonate, which is a material that has sufficient mechanical stability to obtain periodic patterns of collapsed nanopillars, low elastic modulus at high temperatures to fill the mold trenches, and high elongation break and tensile strength necessary to produce uniform arrays of sheared nanostructures. In addition, polycarbonate, as well as the chitin in the butterfly wings, is hydrophobic, which prevents matting between neighboring pillars and maintains the air gaps between nanostructures. The sheared pillars do not fracture from the substrate, but arrange as shown in Fig. 8.4, where the separation of adjacent pillars varies gradually, the observed colors, color intensity, and color patterns of the structure varying in a broad range. The structure is periodic, acting as a grating while producing interference and scattering for illumination normal to the substrate due to the inclination of the pillars. Rainbow patterns appear for incident light normal to the ridge lines, and dominant colors are observed for other light directions. Unlike in butterfly wings, rainbow patterns in multiple directions could be observed in the synthetic structure if the polymer pillars are pulled from the mold in several steps, each with a different pulling direction.

Structures that simulate the color mixing effect of the *Papilio blumei* wings have been described in Kolle et al. (2010). The color of these butterfly wings results from juxtaposing yellow-green and blue colors obtained by light reflection on the centers and edges of concavities on wing scales, respectively. These concavities have widths of 5–10  $\mu\text{m}$  and are clad with a multilayer perforated cuticle, which reflects light at 525 nm at normal incidence and at 477 nm at  $45^\circ$  incidence. In addition, light

**Fig. 8.4** Fabrication of arrays of polymer nanopillars with iridescent colors: (a) nanoimprint lithography and shear patterning and (b) the collapsed array of nanopillars



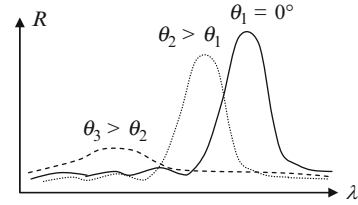
retroreflection from the edges of the multilayer cavity leads to polarization rotation of the incident electromagnetic field. This retroreflection is at the origin of color mixing. The optical characteristics of the *Papilio blumei* wings have been replicated by a multilayer structure consisting of hexagonally arranged concavities, with a diameter of  $4.5\ \mu\text{m}$  and a height of  $2.3\ \mu\text{m}$ , fabricated by replicating spherical polystyrene colloids with  $5\text{-}\mu\text{m}$  diameter by gold or platinum electroplating of the interstices in the colloid array. A multilayer consisting of alternating alumina and titania layers, with average widths of 82 and 57 nm, respectively, is then deposited directly on the template after colloid removal or forms a planar structure on top of the template covered by molten polystyrene colloids. Although the color creation mechanism is different in the two cases, both structures mimic well the butterfly wings.

Besides angle-dependent, iridescent colors, (almost) angle-independent structural colors can be found in nature, for instance, in bird feathers, which originate from light scattering from isotropic structures. One of the methods to mimic structural colors involves mixing two self-assembled colloidal polymer nanoparticles with different sizes [see (Forster et al. 2010) and the references therein]. For example, a mixture of such spherical polystyrene nanoparticles with mean diameters of 226 and 271 nm shows reduced angle dependence, the perceived color being determined by the thickness of the colloidal film and/or by the concentration of an added broadband absorber [carbon black in (Forster et al. 2010)]. These synthetic mixtures can be considered as biomimetic since they consist of high refractive index spheres in air, while the bird feathers of *Lepidothrix coronata*, for example, incorporate spheres of air in a background with a high index of refraction.

Many insects show varying hues as the incidence angle of light changes from normal to grazing as well as metallic colors that originate from specular light reflection. For example, the cuticles of *Chrysochroa vittata*, also known as the woodboring beetles, display red iridescence at normal incidence and green iridescence at illumination close to the grazing angle (see Fig. 8.5). This color change can be explained modeling the stacks of about 20 chitin layers with a thickness of 194 nm separated by 10-nm-thick and irregular air gaps that form the cuticle as part of a periodic infinite structure/photonic bandgap (Vigneron et al. 2006).

If the refractive index contrast between the layers that make up the photonic bandgap is not too high (1.56 in chitin and 1 in air in the woodboring beetle), the dominant colors in the reflection spectrum (those at which the reflection coefficient

**Fig. 8.5** Reflection spectra of materials with angle-dependent hues



$R$  is maximum) occur at the gap wavelengths:

$$\lambda = 2\Lambda \sqrt{n^2 - \sin^2 \theta} / m, \quad (8.2)$$

where  $\Lambda = l_1 + l_2$  is the period of the structure composed of layers with widths  $l_i$  and refractive indices  $n_i$ ,  $i = 1, 2$ ;  $\theta$  is the incidence angle;  $m$  is an integer; and  $n$  is the average refractive index given by

$$n^2 = (l_1 n_1^2 + l_2 n_2^2) / \Lambda \quad (8.3)$$

for transverse electric waves and

$$1/n^2 = [l_1 (1/n_1^2) + l_2 (1/n_2^2)] / \Lambda \quad (8.4)$$

for transverse magnetic radiation. In the case of woodboring beetle, for  $m = 1$ , this model predicts  $\lambda = 627$  nm (red) at normal incidence ( $\theta = 0^\circ$ ),  $\lambda = 593$  nm for TE and 588 nm for TM polarized waves (yellow) at  $\theta = 30^\circ$ , and  $\lambda = 488$  nm for TE waves and 472 nm for TM radiation (green) at  $\theta = 75^\circ$ . The values are in agreement with the observed  $\lambda = 639$  nm (red) at normal incidence,  $\lambda = 600$  nm (yellow) at  $\theta = 30^\circ$ , and  $\lambda = 505$  nm (green) at  $\theta = 75^\circ$ . An artificial structure designed according to this simple model, with SiO layers with a refractive index of 1.9 replacing chitin and Ni layers with a complex index of refraction  $1.85 + i 3.48$  replacing air, was fabricated. The bioinspired structure showed similar angle dependence of the dominant color since the thicknesses of the SiO and Ni layers were chosen to obtain almost the same average refractive index as in the beetle cuticle: 170 nm and 10 nm, respectively. The dominant wavelengths of the artificial structure consisting of six periods were  $\lambda = 702$  nm (red) at normal incidence,  $\lambda = 662$  nm at  $\theta = 30^\circ$ , and  $\lambda = 495$  nm (green) at  $\theta = 75^\circ$  when illuminated with unpolarized white light.

## 8.2 Bioinspired Devices

Light manipulation by bioinspired devices has many applications in optoelectronics, especially in nanoscale lasers, photodetectors, and photovoltaic cells. For instance, broadband antireflection coatings for use in solar cells can be designed by drawing

inspiration from moth eye corneas, which consist of a hexagonal non-close-packed arrays of conical nipples (Min et al. 2008). The latter have subwavelength sizes so that they do not scatter the incident light but rather modify the refractive index profile, inducing a gradual variation of this parameter at the interface between cornea and air. This principle has been demonstrated experimentally by fabricating a similar pattern of GaSb nipple arrays, by first inserting a hexagonal non-close-packed colloidal layer of silica particles in a polymer matrix deposited on a GaSb wafer followed by removing the polymer matrix by oxygen plasma etching and using the released colloidal array, which is removed in the final step, as etching mask in a subsequent chlorine RIE process. As a result, the effective refractive index increases with the depth  $z$  in the material as

$$n(z) = \left\{ f(z)n_{\text{GaSb}}^{2/3} + [1 - f(z)]n_{\text{air}}^{2/3} \right\}^{3/2}, \quad (8.5)$$

where  $f$  is the fraction of GaSb, and  $n_{\text{GaSb}}$  and  $n_{\text{air}}$  are the refractive indices of the wafer material and air, respectively. The nipple geometry, and thus the form of the refractive index and of the  $f$  change with  $z$  depends on the etching conditions, simulations showing that pyramidal and paraboloid nipples are more efficient as broadband antireflection coatings than half-ellipsoid nipples. These structures can also be used in thermophotovoltaic cells since they have excellent thermal stability.

Although most bioinspired materials and devices reproduce a single dominant characteristic of a biological system, multifunctionality can be achieved combining characteristics of different life-forms. For example, an optical coating that is at the same time antireflective and superhydrophobic/self-cleaning can be fabricated, reproducing the functionalities of moth eyes and cicada wings, respectively (Sun et al. 2008). The antireflection effect of nocturnal moths is determined by the refractive index gradient across the interface between their cornea and air, while the self-cleaning property of cicada wings is due to surface microstructures. These biological structures are similar, consisting of hexagonally ordered, non-close-packed protrusions in the shape of nipples with dimensions of about 300 nm. Synthetic structures that mimic the biological ones and fabricated by a scalable templating technique, can be used as broadband antireflection coatings. More precisely, a process that involves transferring with the help of a mold of the periodic surface protrusions of non-close-packed 360-nm colloidal silica spheres to perfluoroacrylate polymers, which have a low index of refraction and a low surface energy, was used to fabricate self-cleaning broadband antireflection coatings. The fluoropolymer nipple arrays were then replicated on glass substrates and shown to exhibit Bragg diffraction, i.e., angle-dependent colors, specific for periodic structures. In addition, the reflectivity decreased with increasing nipple heights, which can be controlled by oxygen plasma etching, the hemispherical nipple arrays showing relatively high reflectivities (around 1%) at long wavelengths if templated from small particles (with diameters in the 200–250 nm range) and at short wavelengths if templated from particles with a diameter between 450 and 500 nm.

Not only periodic biological structures achieve light modulation but also photonic amorphous structures, in which only short-range order but no long-range order exist. These structures are at the origin of noniridescent colors in nature. A biomimetic photonic amorphous structure, consisting of holes with a radius of about 76 nm and an average distance of 255 nm in a freestanding 190-nm-thick GaAs membrane containing InAs quantum dots as active media, has been shown to produce laser radiation at frequencies for which the short-range order enhance optical confinement (Noh et al. 2011). The emission frequency of photonic amorphous laser structures can be tuned by modifying its structural parameters. This type of optically pumped laser is intermediate between photonic crystal lasers, characterized by long-range periodicity and frequency bandgaps used to confine light and random lasers, in which the feedback mechanism is multiple light scattering in a disordered medium.

Apart from light modulation, nature teaches us how to efficiently collect light through highly specialized mechanisms of eye sight which, depending on the animal species, are optimized for different illumination conditions: near/far, day/night, and wide/narrow field of view (Lee and Szema 2005). In applications, we often need to design optical devices with large field of views and small volumes, the design of which can be inspired from flies since their compound eyes have exactly these desired features.

The fabrication of a three-dimensional compound eye consisting of 601 channels/microassemblies of microprisms and microlenses, ultraprecisely machined with diamond on curved and flat surfaces, respectively, in an area with a 20-mm diameter, has been reported in Li and Yi (2010). Cross talking between channels is eliminated by an aperture array. This system, represented schematically in Fig. 8.6, allows for a maximum light deviation angle of  $18.43^\circ$ . It is a replica of the eye of a fly, which is composed of basic imaging unit, called ommatidia, implemented as individual channels. The optical components on the curved surface generate an image on a flat plane, which can be sensed with commercially available photodetectors. All microlenses have an aperture of 0.58 mm and a curvature radius of 4 mm, while the microprisms arranged on 12 layers/circles have the same width of 0.6 mm, but different refracting angles depending on their location. The prism at the vertex is planar and is the only one to be associated with more than one (with six) microlens(es).

The photodetectors in the previous compound eye could have been placed on the imaging plane. However, it is possible to fabricate a hemispherical electronic

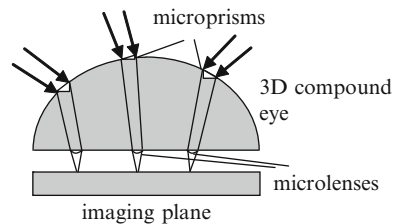


**Fig. 8.6** Artificial three-dimensional compound eye

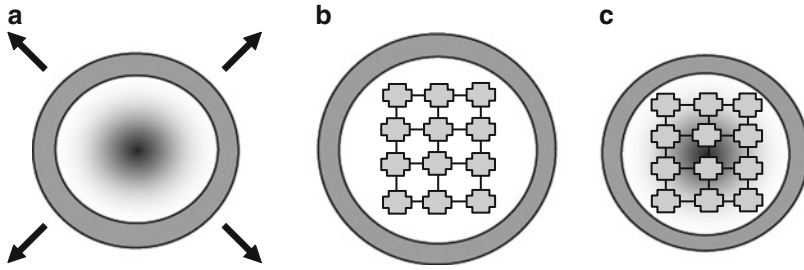


**Fig. 8.7** Fabrication of a hemispherical electronic eye: (a) stretched hemispherical elastomer, (b) array of detectors on the flattened elastomer, and (c) hemispherical electronic eye obtained after releasing the elastomer

eye that has not only a three-dimensional refracting element but also a three-dimensional arrangement of its detectors (Ko et al. 2008). This electronic eye is illustrated in Fig. 8.7. The hemispherical geometry, although suitable for a wide field of view and low aberrations, is not compatible to the planar nanofabrication techniques. Let us suppose that we want to fabricate a hemispherical eye camera similar to the human eye, consisting of a number of pixels, the electronic part of each pixel, referred to as silicon device, containing a photodiode and a blocking diode monolithically integrated in a  $500 \times 500 \mu\text{m}^2$  crystalline silicon and capped with a micrometer thin polyimide layer. An ingenious trick is needed to place the silicon devices manufactured using the usual wafer-scale two-dimensional technology on a hemisphere: place first the two-dimensional array of Si devices on a flattened, drumhead-like, radially stretched hemispherical elastomeric transfer element and then release the elastomer to regain its hemispherical shape. The Si device array adopts the same hemispherical shape due to van der Waals interactions with the elastomer surface, but suffers no distortions if the interconnects between adjacent Si devices are thin and narrow enough and have high elastic compressibility. In (Ko et al. 2008), the interconnects were made from  $50\text{-}\mu\text{m}$ -wide,  $360\text{-}\mu\text{m}$ -long, and  $3:150:3\text{-nm}$ -thick Cr: Au: Cr metal layers patterned on polyimide. These stages of fabrication are illustrated in Fig. 8.7. Afterward, the Si device array is transferred onto a hemispherical glass substrate with the same radius of curvature and is finally coated with a photocurable adhesive. Such a  $16 \times 16$  pixels eye camera was successfully fabricated and shown to function properly, and the poor image quality due to the small number of pixels could be improved by collecting sequences of images rotated in the azimuthal and polar directions by small increments and then reconstructing the image (Ko et al. 2008); this strategy is also adopted in biological systems.

In contrast to human and insect eyes, fish and octopus eyes use gradient index biological structures to increase their focusing power and to correct spherical aberrations. In particular, the octopus has no cornea so that it can see only with the help of a spherical lens with an almost parabolic distribution of the refractive index, obtained by a corresponding change of the water and protein concentrations.

**Fig. 8.8** Gradient index lens with minimized spherical aberrations



This concept has been exploited in the design of a lens with a graded refracted index distribution fabricated, as illustrated in Fig. 8.8, by pressing an planar graded index polymer film between two molds, M1 and M2, with different radii of curvature,  $R_1$  and  $R_2$ , respectively (Jin et al. 2007). The graded index distribution is preserved in the process and a plano-convex lens with a graded index can be obtained after subsequent polishing the shaped film along a horizontal plane. The planar 4-mm-thick polymer film consists of 20,000 layers that induce a total index of refraction gradient across the structure of  $\Delta n = 0.08$ . Refractive index differences between nanolayers as small as 0.0009 can be obtained by varying the ratios of polycarbonate (with an index of 1.58) and poly(methyl methacrylate) with a refractive index of 1.49 in the material. These ultrathin layers do not scatter light since they are thinner than a quarter wavelength, their effect on the incident radiation being to modulate the effective index of refraction. The focal lengths of the lenses fabricated in this way are of tens of millimeters.

Nature is a source of inspiration not only for efficient gathering of ambient light but also for configurations of solar cells. For example, the so-called Grätzel or dye-sensitized solar cell is a photoelectrochemical system that mimics the photosynthesis process of chlorophyll in green leaves (O'Regan and Grätzel 1991). It consists of a porous layer of  $\text{TiO}_2$  nanoparticles surrounded by an absorbing dye, which replaces the organic dye porphyrin, found in plants as chlorophyll and in animals as hemoglobin. The nanoparticles, in contact with a transparent anode, are immersed in an electrolyte solution containing a platinum cathode. The photogenerated electrons are injected in the conduction band of wide-bandgap  $\text{TiO}_2$  nanoparticles and subsequently collected by the anode, the electrolyte having the role of regenerating the electrons in dye, and thus closing the electrical circuit, through redox reactions.

Irrespective of the type of solar cell, the conversion efficiency can be greatly improved if the number of incident photons is maximized. A wide field of view certainly improves light collection. The common housefly *Musca domestica*, for example, has a field of view of  $270^\circ$ , its compound eyes consisting of cylindrical ommatidia with a diameter of  $20\ \mu\text{m}$ , positioned on a curved surface. Prismatic compound lenses, inspired from the housefly and made from silicon and silicon dioxide, were studied in Chiadini et al. (2010). A detailed fractal model was considered for their design, the original zeroth-stage cross section of the lens, in the form of a segment of a circle being decorated in the first stage by a number of circular segments with decreasing radii, which are decorated in the second stage with circular segments with still smaller radii, and so on. The zeroth and first stages of the cross section of the prismatic lens, which is constant along the  $y$  direction, are shown in Fig. 8.9. Extended ray-tracing simulations have confirmed

**Fig. 8.9** Cross section of a bioinspired compound lens with fractal design

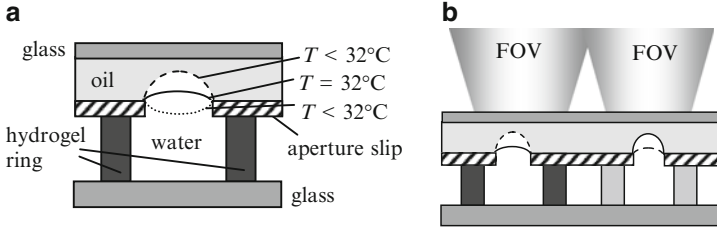
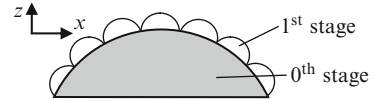


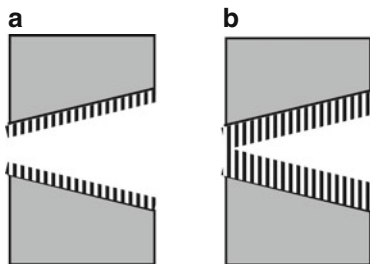
**Fig. 8.10** (a) Bioinspired lens with adjustable focus. (b) Overlapping field of views of two such lenses.

the superiority of nature's design: for an incident wavelength of 600 nm, the zeroth-stage design of silicon dioxide bioinspired compound lenses has a higher light coupling efficiency than antireflection layers, especially for large angles, the first stage structure improves the performance of direct-illuminated lenses but not that of diffused-illuminated lenses, while second-order structures do not further improve the performances. For silicon compound lenses, the zeroth-stage design outperforms antireflection-coated structures only for diffused light illumination, the first-order stage is more performant than the zero-order stage, whereas the second-order stage does not improve significantly the light coupling efficiency. Note that only the first stage is encountered in nature.

Not only have the compound eyes of insects inspired innovative devices, but the human eye is also worth copying. What makes human eye special is its ability to focus on different distances by modifying the shape of its lens through the action of ciliary muscles. On the contrary, man-made optical lenses can adjust their focal distance by a refraction index change induced by the electro-optic effect, for example, or by varying their position. A lens that can autonomously adjust its focal length by changing its shape in response to external stimuli has been demonstrated in [Dong et al. \(2006\)](#). It consists of a cylinder-shaped liquid droplet container surrounded by a hydrogel ring and integrated into a microfluidic system (see Fig. 8.10a). The optical lens is the meniscus between water and oil, which is pinned at the top edge of the aperture slip due to the different properties of its top surface and sidewall and bottom surface: hydrophobic and hydrophilic, respectively.

If fabricated from a temperature-sensitive NIPAAm hydrogel, the hydrogel ring expands when the temperature decreases below 32 °C due to water absorption in its network interstitials, such that the available container volume for the water droplet decreases, the pressure difference across the water–oil interface changes and the meniscus curvature grows. On the contrary, at temperatures above 32 °C, the meniscus first retreats and then changes sign. Thus, the focal length of the microlens changes: it is divergent for temperatures below 33 °C, attaining a focal

**Fig. 8.11** Biomimetic nanopore in the (a) opened and (b) closed state.



length of  $-11.7$  mm at  $23^\circ\text{C}$ , and becomes convergent for higher temperatures, reaching  $22.8$  mm at  $47^\circ\text{C}$ . The response time is about  $20$  s. This principle can be used for implementation of lenses that autoadjust at variations of other parameters. For example, for pH-sensitive AA hydrogel rings, which contracts for  $\text{pH} < 5.5$  and expands for  $\text{pH} > 5.5$ , the divergent focal length changes from  $-6$  mm to  $-2.5$  mm when the pH changes from 2 to 8 and remains almost constant for a further increase in the pH; the response time in this case is about  $12$  s. Arrays of microfluidic lenses can be fabricated that resemble the compound eyes of *Drosophila* insects, in which each ommatidium senses one area in space and can track spatial movements across the field of view of the eye. For example, two liquid microlenses with different hydrogel rings, which have opposite responses to pH, for example, such that one expands and the other contracts at a pH change, mimic two compound eyes with possible overlapping field of views, FOVs, and tunable focal lengths, which autoadjust at specific environmental conditions. An array consisting of two such microlenses is shown in Fig. 8.10b.

Biomimetic nanopores that resemble biological ion channels have also been fabricated. A stimuli-activated change in conformation of molecules can close or open solid-state nanopores, preventing or allowing ions to pass through (Yameen et al. 2009). If the surface of a conical nanopore etched in a polyimide membrane is covered with temperature-sensitive N-isopropylacrylamide (NIPAM) polymer brushes covalently tethered at one end, as illustrated in Fig. 8.11, the small opening of the nanopore remains open at temperatures higher than the critical solubility temperature of the polymer since the brushes are in a collapsed state (Fig. 8.11a). On the contrary, at lower temperatures, in particular at room temperature, NIPAM polymerizes, takes a swollen/stiffer form and the small opening, with a diameter of about  $8$  nm, becomes partially or even completely obstructed, and the ionic current through the nanopore decreases significantly compared to the previous situation (see Fig. 8.11b). In particular, the effective diameter of the small opening decreases  $3.4$  times if the temperature changes from  $40^\circ\text{C}$  to  $23^\circ\text{C}$ . NIPAM can be considered as thermally driven molecular gate that controls the ionic current through the nanopore in a physiologic range of temperatures. The change in diameter/current is not abrupt since the polymer brushes exhibit intermediate conformational states between collapsed and swollen; the conformational changes are completely reversible.

### 8.3 Bioinspired Technological Processes

Not only innovative devices and materials mimic the biological world, but efficient catalytic reactions (Que and Tolman 2008) and technological processes for nano- or micrometer-size structures that could take place at nonextremal temperature, pressure, and/or chemical conditions are sometimes inspired from nature. Present-day nanotechnology relies heavily on silicon or silica nanostructures of various shapes and sizes (Losic et al. 2009). Biosilica is also found in nature, porous silica shells, for example, being encountered in the frustules of microscopic unicellular algae called diatoms. The frustules consist of two valves connected by girdle bands, each valve being composed of silica plates that separate stacked hexagonal chambers. There is a huge variety of shapes in the diatom frustules determined by the structural diversity of the groups of nanosized pores in the plates, each diatom from the 100,000 existing species being characterized by a distinctive frustule morphology (Losic et al. 2009). Since biosilica in diatoms forms in specialized compartments, in mild acidic environment, and at moderate temperatures and pressures, bioinspired silica production could have advantages over common technologies.

For example, a controlled bioinspired growth of silica nanoparticles has been reported in Bauer et al. (2007). It occurs in confined environments containing monosilicic acids and spherical reverse micelles in the presence of a branched polyamine, which is structurally similar to polyamines isolated from unicellular marine algae *Cylindrotheca fusiformis* and *Stephanopyxis turris*, various morphologies and particle sizes being obtained by changing the ratio of water and reverse micelles in the container. In a similar manner, silica structures synthesized from a mixture of chitosan solution previously incubated for different times and in the presence of prehydrolyzed tetraethylorthosilicate showed a spherical shape with a diameter of 40 nm for a chitosan solution incubation time of 56 h and appeared as sheets of carambola-like silica particles with diameters of 20–40 nm for incubation times of 150 h; after 280 h incubation times, the chitosan solution precipitates (Leng et al. 2008). For instance, solid particles with a trimodal size distribution, having diameters ranging from 56 to 500 nm, are obtained for smaller water-to-micelles ratios, while hollow and robust micrometer-sized silica shells are produced for larger values of this ratio. More complex structures, consisting of hollow silica capsules, which are reinforced with carbon nanotubes, have been inspired by sea anemones (Sanles-Sobrido et al. 2008). These rigid structures can be assembled by an applied magnetic field if the capsules are loaded with  $\text{Fe}_3\text{O}_4$  magnetic nanoparticles.

Besides silica, sulfide semiconductor nanocrystals such as CuS, CdS, PbS, or  $\text{Ag}_2\text{S}$  can be fabricated using bioinspired techniques, which produce them in aqueous solution without toxic ligands (Pejoux et al. 2010). The inspiration comes this time from mollusks, which synthesize complex calcium carbonate crystals in mild conditions on nucleating sheets of proteins from precursors with low solubility in water. In a similar manner, core/shell enzyme/ $\text{Ag}_2\text{S}$  sulfide semiconductors are grown in mild conditions on an enzyme nucleating template in the presence of a controlled concentration gradient of  $\text{S}^{2-}$  ions. Crystalline nanoparticles with a

mean diameter of 35 nm are obtained if the synthesized enzyme urease, which is a powerful catalyst, is moderately inhibited by the concentration of the  $\text{Ag}^+$  ions so that the  $\text{S}^{2-}$  concentration gradient determined by the catalytic activity of the enzyme reaches the supersaturation regime close to the enzyme surface. On the contrary, when the enzyme is only slightly inhibited, the  $\text{S}^{2-}$  gradient is higher and the supersaturation regime is attained in a larger volume around the enzyme, the result being amorphous particles with 142-nm average diameter because the enzyme cannot control the crystallization process that takes place far away from its surface. A fully inhibited enzyme is not able to produce  $\text{S}^{2-}$  ion precursors and thus to template the insoluble  $\text{Ag}_2\text{S}$  particles. The enzyme is moderately, slightly, and fully inhibited for  $\text{Ag}^+$  ion concentrations of  $10^{-13}$  M,  $10^{-7}$  M, and  $10^{-4}$  M, respectively.

Useful light manipulating two- or three-dimensional photonic crystals are difficult to fabricate. Biology can help construct such structures in a more direct way than through inspiration. In fact, wings of the *Papilio blumei* butterfly, for example, which are covered by millions of scales with a length of about 100  $\mu\text{m}$  that consist of arrays of concavities with a diameter of 5–10  $\mu\text{m}$  and contain nanometer scale air chambers separated by chitin laminae, can be used for producing artificial photonic structures (Gaillot et al. 2008). More precisely, up to 50-nm-thick  $\text{TiO}_2$  layers can be deposited on parts of butterfly wings by the low-temperature atomic layer deposition technique either as a skin that coats only the outer part of the wing or both inner and outer parts, if penetrating through microcracks on the surface. In the first case, the dominant reflection peak of the wing, at 524 nm, is preserved, and additional peaks at 652, 742, 850, and 1,054 appear with an intensity that increases with the coating thickness due to the Fabry–Perot-type behavior of the coated wing. In the second case, the dominant color changes from green (524 nm) to red (648 nm) as the coating thickness increases to 10 nm and the intensity of the dominant reflection peak decreases in comparison to the intensities of the Fabry–Perot peaks mentioned before because the air trapped in the wing concavities is partially replaced with  $\text{TiO}_2$  with a higher refractive index. So, the chromaticity and intensity of the reflected light of this periodic hybrid inorganic–organic structure is controlled by the thickness of the coating layer.

Recently, a mass fabrication technique for replicating insect corneas, with the aim of reflection reduction for obliquely illuminated solar cells, has been reported in Pulsifer et al. (2010). It has the advantage of sacrificing only a single biotemplate, in this case, containing several corneas of blowflies, to produce a master negative of nickel, which can be used subsequently either as a stamping die or as a casting mold for multiple replicas. In order to capture the fine surface features of the corneas, a 250-nm-thick Ni film is first deposited on an array of corneas using the conformal-evaporated-film-by-rotation method, followed by electroforming of a 60- $\mu\text{m}$ -thick nickel layer, which strengthens the conformal coating, the processing ending, finally, with the removal of the blowfly corneas. Features down to 200 nm in size, including the 20- $\mu\text{m}$ -diameter individual lenslets of the compound eye, are captured with high fidelity.

## 8.4 Devices Mimicking Biological Organs/Functionalities

Several human organs have been mimicked in man-made devices that try to match the sensitivity of the natural counterparts. One example is the nose. Owing to the extensive research in nanosensors able to detect minute concentrations of several gases, one would expect that an array of specialized/appropriately functionalized sensors can easily replace the nose as gas (odor) sensor. However, a true biomimetic nanotechnology olfactory sensor (NOSE) does not consist of an array of sensors in which each sensor detects a single analyte but of an array of sensors that respond to several gases, such that identification of a particular gas reduces to identifying the distinct signature of that gas on the entire array of cross-reactive sensors. So, whether it is not difficult to fabricate bioinspired sensors, it is also important to understand the sensing mechanism of the biological organ in order to produce biomimetic NOSEs. For detection and identification of gases in biomimetic NOSEs, one should first collect the simultaneous responses from all sensors in the array and then to apply pattern recognition algorithms such as artificial neural network techniques or principal component analysis to determine the combination of sensor values for which one can obtain the maximum variance of data points in mutually orthogonal directions. The gases are identified by their signatures in the planes/volumes spanned by these orthogonal directions, as illustrated in Fig. 8.12. The nature of the sensors is not relevant. The detection can be made by arrays of micrometer-scale silicon cantilevers (Baller et al. 2000) functionalized with different polymers that swell when exposed to analytes, case in which the fingerprint of different odors is extracted from sets of deflection data collected from all cantilevers at different times, or one can detect gases via electrical signals recorded by an array of percolating SnO<sub>2</sub> nanowires (Sysoev et al. 2007). In the last case, the discriminating power of the sensor increases by inducing a temperature array across the nanowire layer deposited on top of an array of Pt strips, the detection limit for CO, for example, reaching 150–200 ppb in a response time of less than 30 s. Again, this low detection limit can only be achieved by recording conductivity patterns across the nanowire array and employing multivariate pattern recognition methods for signal processing in an optimized coordinate system with a number of dimension equal to the number of gases in a mixture minus one. In a similar manner, a functional electronic nose can be implemented in a single crystal SnO<sub>2</sub> wedge-like nanobelt, with a variable diameter, on which an array of Pt nanoelectrodes is patterned (Sysoev et al. 2010). In addition to different dimensions of the nanobelt sensing element seen by the cross-sensing detectors in the array, the nanobelt could

**Fig. 8.12** Signatures of different gases in the planes/volumes spanned by orthogonal directions defined by pattern recognition algorithms

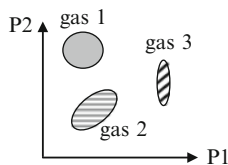
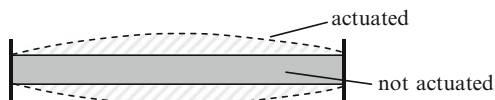


**Fig. 8.13** Flexible polymer matrix with muscle-like properties



be differently functionalized with a Pd catalyst. In the latter case, the aroma from the vapors of different alcoholic beverages was sensed, and the beverages were identified. The response of electronic noses can be so reliably and sensitive that it can even be used to detect chronic renal failure in rats from the analysis of their exhaled breath (Haick et al. 2009). A random network of single-walled CNTs coated with different organic materials was used in this case.

Muscles have the ability to repeatedly stretch and exert mechanical power. Therefore, artificial muscles could generate force and move objects. An electrically powered artificial muscle fabricated from carbon nanotube aerogel sheets has been reported in Aliev et al. (2009) and is illustrated in Fig. 8.13. The artificial muscle is actuated by applying a positive voltage to the nanotube sheet electrode with respect to a distant ground plane. It works in a temperature range that extends between 80 and 1,900 K and shows huge elongation rates, of  $(3.7 \times 10^4)\%$  per second, and giant elongations, of 220%, which can be frozen by van der Waals forces acting between the expanded sheet and a substrate. The observed giant elongations are in the width direction and are caused by the periodic corrugation in this direction during cycling of the nanotube sheet, with similar actuator strokes of 200% in the thickness direction, which implies that the sheet contracts a few percent in length when actuated. In fact, in this composite material, the Poisson's ratios have opposite signs along the width and length directions and lead to a negative linear compressibility and densification of the actuated artificial muscle. Such densified sheets have a stress-generation capability 32 times larger than the natural skeletal muscle.

The skin is a very sensitive tissue, able to sense pressure and temperature. An artificial skin has been reported in Graz et al. (2009), which consists of a flexible 30- $\mu\text{m}$ -thick foil of ferroelectric polymer matrix that incorporates piezoelectric ceramic lead titanate nanoparticles with an average diameter of 100 nm. Both pressure and temperature can be sensed since the polarization directions of the ferroelectric polymer and nanoparticles can be adjusted independently by an area-selective, sequential two-step poling technique. Thus, the same material accommodates two sensory modes, the electronic skin consisting of arrays of bifunctional sensory cells composed of two subcells, each reacting to changes in pressure or temperature. Temperature is measured in the pyroelectric subcell, obtained when the polarizations of polymer and ceramic nanoparticles are parallel, whereas an antiparallel polarization orientation corresponds to a piezoelectric subcell, which senses pressure. A controlled manipulation of the polarization directions of the polymer and nanoparticles is possible since their piezoelectric coefficient has a different sign and their Curie temperatures are different. Then, rendering the material pyroelectric or piezoelectric implies a sequential poling

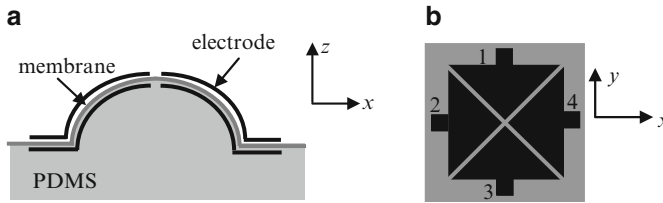


**Fig. 8.14** (a) Side view (cross section) and (b) top view of a detector of three-dimensional forces

process that takes place first at high temperatures (higher than the Curie temperature of the polymer) in a DC field, stage at which only the nanoparticles are poled, and then at low temperatures in an AC field, which poles the polymer matrix and can be interrupted when the polarization of the matrix becomes parallel or antiparallel to that of the nanoparticles. An appropriate formulation and poling minimizes the cross-sensitivities between these subcells. Electrical transduction of the signals is achieved by aligning each subcell on the frontplane foil with an amorphous-silicon thin-film transistor placed on the flexible backplane.

Animal skin contains very sensitive tactile sensors. Such sensors based on ionic membranes and capable of detecting three-dimensional forces, i.e., can detect the direction of the applied forces, are described in Wang et al. (2009). In the skin of a cucumber tendril, tactile sensors of three-dimensional forces are shaped as extruded papillae positioned on the inner surface. A similarly shaped tactile sensor has been fabricated in a light and flexible ionic polymer metal composite (Wang et al. 2009). The induced stress is proportional to the charge density accumulated at the polymer surface as a result of water uptake at the interface between the polymer and metal electrode at actuation, while the direction of applied force is determined by a special, dome-shaped design of the sensor. More precisely, the dome, with a diameter of 9 mm and a height of 3 mm, consists of a sheet of Flemion polymer sandwiched between 8- and 10- $\mu\text{m}$ -thick gold electrodes and is positioned over a layer of soft elastomer polydimethylsiloxane (PDMS). Viewed from above, the sensor consists of four segments, denoted by 1, 2, 3, and 4 in Fig. 8.14, the comparison of the current/voltage signals of all segments determining the direction of the applied force. For instance, for a force applied along  $z$ , all four signals are equal, whereas for a force applied along the positive  $x$  axis, only sensor 2 has a significant response.

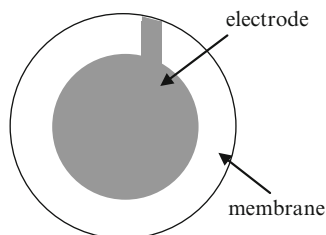
Even such delicate organs as lungs can be mimicked in microdevices that reproduce the critical functionality of the alveolar–capillary interface of the human organ. Such a microdevice is, by necessity, a microfluidic system, which consists of two microchannels separated by a porous and flexible membrane of poly(dimethylsiloxane) with a thickness of only 10  $\mu\text{m}$  (Huh et al. 2010). If the membrane is coated with extracellular matrix such as collagen or fibronectin, which provides structural support to animal cells, and if human pulmonary microvascular endothelial and alveolar epithelial cells are cultured on opposite sides of the membrane, the resulting structure closely resembles a human lung, the microchambers

assuring the pressure-driven stretching of the thin wall that mimics the intrapleural pressure in lungs.

Bioinspired nanoengineering of surfaces can also reduce the thermal shock resistance in ceramic materials (Song et al. 2010). The poor resistance of ceramics to thermal shock, which decreases their strength with respect to the melting point value, is the main disadvantage of this otherwise high-temperature-resistant material. The failure mechanism in ceramics subjected to thermal shocks is crack initiation due to the thermal gradient and stresses on the surface. However, inspired by dragonfly wing membranes, ceramics can be rendered insensitive to thermal shock up to the melting temperature by roughening their surface, such that thin air layers can envelope the nanofinned surface and increase the heat transfer resistance with several orders of magnitude. Surface roughening is achieved by high-temperature plasma etching and chemical corrosion in a mixed solution of HF and HNO<sub>3</sub>, the result being the appearance of randomly distributed circular nanoscale rod fins that stand up nearly vertically. These nanofins occupy an areal fraction of 0.37 with a density of 71  $\mu\text{m}^{-2}$  and have average thicknesses and diameter values of 375 nm and 81 nm, respectively. Their action is to dramatically increase the heat transfer resistance for heated ceramics quenched in water and thus to prevent crack appearance, by rendering the surface hydrophobic and hence able to trap a thin air layer between nanofins when quenched. The heat transfer resistance at the interface increased from about  $10^{-4} \text{ m}^2\text{K W}^{-1}$ , without nanofins, to  $0.63 \text{ m}^2\text{K W}^{-1}$  with nanofins for the refractory ceramic ZrB<sub>2</sub>-20%SiC<sub>p</sub>-5%AlN because the steep temperature difference at quenching acts on the nanofins and no longer on the ceramic.

Bioinspired artificial bacterial flagella, which could be used as micro-/nanomanipulators with six degrees of freedom or as in vivo medical micro- or nanorobots, which can sense and deliver chemical and biological substances, can be fabricated by self-scrolling of helical nanobelts and Cr/Ni/Au soft-magnetic heads (Zhang et al. 2009). The flagella swimming mechanism depends on the cell type: eukaryotic flagella create paddling motions, while prokaryotic (bacterial) flagella turn the base or bundle of the helical flagella with the help of a molecular motor. Self-propelled artificial bacterial flagella can be controlled by a weak rotating magnetic field, the frequency of which is directly proportional to the translational velocity of the device, as long as it is lower than the step-out frequency. A velocity of  $18 \mu\text{m s}^{-1}$ , comparable to that of the *E. coli* bacteria, can be obtained with a magnetic field of 2 mT rotating at a frequency of 30 Hz. Such swimmers are fabricated by patterning a 1.8- $\mu\text{m}$ -wide ribbon-like InGaAs/GaAs/Cr trilayer, with 11/16/15 nm thicknesses, terminated with a 10/180/10-nm Cr/Ni/Au soft-magnetic head on a sacrificial layer, which is wet etched releasing the 2D mesa, which self-organizes as a tethered artificial flagella with a diameter of 2.8  $\mu\text{m}$ . The artificial flagella with smaller heads swim faster at low frequency due to the smaller viscous drag, but swimmers with larger heads have larger maximum velocity and step-out frequency since the exerted magnetic torque is larger. The swimming direction, upward or downward, which depends on the sum of the gravitational, propulsive,

**Fig. 8.15** Bioinspired self-pumping membrane

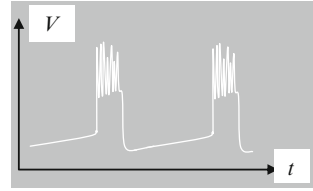


and buoyancy forces, can be tuned by the rotation frequency of the magnetic field. Moreover, several artificial flagella swim in a swarm-like, coordinated fashion and can be controlled as a single unit.

A bioinspired self-pumping membrane, which integrates a chemical-driven electroosmotic pump into a synthetic track-etched polycarbonate membrane with a pore diameter of  $1\ \mu\text{m}$ , has been described in [Jun and Hess \(2010\)](#). Such a membrane mimics material exchange across biological membranes by specialized channel proteins using ATP as fuel. As shown in [Fig. 8.15](#), Au and Pt electrodes are deposited on opposite faces of the membrane and produce a transmembrane potential due to the different abilities of the electrodes to catalyze the anodic and cathodic reaction. When an electric field is applied across the pore, the counterions attracted by the surface charges within the pore experience a force, while a plug-like flow of the fluid at the channel wall is caused by the viscous drag between fluid and counterions. Hydrogen peroxide acts as fuel for the electroosmotic flow, its hydrolysis in aqueous environment generating an ionic current flow between electrodes if they are short-circuited. More exactly, hydrogen peroxide transforms into oxygen, electrons, and protons on the platinum electrode, the resulting electrons passing into and closing the external electrical circuit, while the protons flow through the membrane pore. The electrons and protons meet again at the gold electrode, where they produce water after reacting with hydrogen peroxide. For instance, in an aqueous solution, the current generated at an applied voltage of  $1\ \text{V}$  is  $-1.9\ \mu\text{A}$ , the corresponding flow rate being  $-0.94\ \text{nL s}^{-1}$ . The negative current and flow rate values indicate that the current/flow direction is from the platinum to the gold electrode. Pumping can occur when no external voltage is applied if hydrogen peroxide is added to the solution at a  $0.01\ \text{wt}\%$  concentration. In this case, at short circuit, the flow across the membrane is directed from the platinum to the gold electrode, no flow being observed when the external circuit is open. The current and flow decrease in time from values of  $0.26\ \mu\text{A}$  and  $0.9\ \text{nL s}^{-1}$  if hydrogen peroxide concentration, consumed at the electrodes, is not maintained at the same value.

Metabolic biological functions can also be mimicked with integrated nanodevices. For example, the response of beta cell at glucose can be reproduced with ion-sensitive field-effect transistors ([Georgiou and Toumazou 2007](#)). The beta cells in pancreas sense the blood glucose originating from food intake and release the insulin hormone, which helps glucose assimilation in cells and the subsequent energy production. Faulty functioning of beta cells can lead to diabetes, which

**Fig. 8.16** Response of an ion-sensitive field-effect transistor that mimics beta cells



manifests in increased blood glucose. Beta cells are electrically excitable, their membrane potential showing slow wave bursts at high blood glucose levels, as shown in Fig. 8.16, which signal the release of insulin. In the active phase, action potentials are superimposed on these bursts. The delicate mechanisms of the beta cells, consisting of a membrane pierced by ion channels that allow the inward and outward flow of various ions, in particular  $K^+$  and  $Ca^{2+}$ , were reproduced in silicon cells, using an electrical model, in which the membrane capacitance is associated to an electrical capacitor and the gated ionic channels in the membrane, which open or close as a function of the membrane voltage value, are represented by variable conductances. Using a Hodgkin–Huxley formalism, developed for modeling neuronal electrical activity, the burst sequence could be reproduced in silicon transistors biased in the subthreshold regime, if the activation function of gating parameters has a sigmoid form. Each ionic channel was implemented using a sigmoid function generator for the activation variable, a log domain filter, and a variable linear transconductance. This implementation of a device with the same characteristics as pancreatic cells helps to understand better the functioning of our body and to design more efficient treatment of diabetes.

Recently, a synaptic transistor was fabricated by embedding a layer of ion-doped conjugated polymer and another layer of ionic conductor into the gate of a metal-oxide-semiconductor transistor based on silicon (Lai et al. 2010). The device mimics the behavior of a synapse, more precisely the ionic excitatory postsynaptic current (EPSC) in a neuron, since ionic fluxes with temporal delays of few milliseconds are triggered in the polymer by a potential spike applied on the gate and then generate spontaneous EPSC in Si during the positive pulse of the spike, which is then turned off during the negative spike pulse. The synaptic transistor showed learning function when pairs of temporally correlated pre- and postsynaptic spikes are applied, and spike-timing-dependent plasticity effects.

## References

- Aliev AE, Oh J, Kozlov ME, Kuznetsov AA, Fang S, Fonseca AF, Ovalle R, Lima MD, Haque MH, Gartstein YN, Zhang M, Zakhidov AA, Baughman RH (2009) Giant-stroke, superelastic carbon nanotube aerogel muscles. *Science* 323:1,575–1,578
- Baller MK, Lang HP, Fritz J, Gerber Ch, Gimzewski JK, Drechsler U, Rothuizen H, Despont M, Vettiger P, Battiston FM, Ramseyer JP, Fornaro P, Meyer E, Güntherodt H-J (2000) A cantilever array-based artificial nose. *Ultramicroscopy* 82:1–9

- Bauer CA, Robinson DB, Simmons BA (2007) Silica particle formation in confined environments via bioinspired polyamine catalysis at near-neutral pH. *Small* 3:58–62
- Bonderer LJ, Studart AR, Gauckler LJ (2008) Bioinspired design and assembly of platelet reinforced polymer films. *Science* 319:1069–1073
- Chiadini F, Fiumara V, Scaglione A, Lakhtakia A (2010) Simulation and analysis of prismatic bioinspired compound lenses for solar cells. *Bioinspir Biomim* 5:026002
- Crookes WJ, Ding L-L, Huang QL, Kimbell JR, Horwitz J, McFall-Ngai MJ (2004) Reflectins: the unusual proteins of squid reflective tissues. *Science* 303:235–238
- Dong L, Agarwal AK, Beebe DJ, Jiang H (2006) Adaptive liquid microlenses activated by stimuli-responsive hydrogels. *Nature* 442:551–554
- Forster JD, Noh H, Liew SF, Saranathan V, Schreck CF, Yang L, Park J-G, Prum RO, Mochrie SGJ, O'Hern CS, Cao H, Dufresne ER (2010) Biomimetic isotropic nanostructures for structural coloration. *Adv Mater* 22:2,939–2,944
- Fratzl P and Barth FG (2009) Biomaterial systems for mechanosensing and actuation. *Nature* 462:442–448.
- Gaillot DP, DeParis O, Welch V, Wagner BK, Vigneron JP, Summers CJ (2008) Composite organic-inorganic butterfly scales: production of photonic structures with atomic layer deposition. *Phys Rev E* 78:031922
- Georgiou P, Toumazou C (2007) A silicon pancreatic beta cell for diabetes. *IEEE Trans Biomed Circuits Syst* 1:39–49
- Graz I, Krause M, Bauer-Gogonea S, Bauer S, Lacour SP, Ploss B, Zirkl M, Stadlober B, Wagner S (2009) Flexible active-matrix cells with selectively poled bifunctional polymer-ceramic nanocomposite for pressure and temperature sensing skin. *J Appl Phys* 106:034503
- Haick H, Hakim M, Patrascu M, Levenberg C, Shehada N, Nakhoul F, Abassi Z (2009) Sniffing chronic renal failure in rat model by an array of random networks of single-walled carbon nanotubes. *ACS Nano* 3:1,258–1,266
- Huh D, Matthews BD, Mammoto A, Montoya-Zavala M, Hsin HY, Ingber DE (2010) Reconstituting organ-level lung functions on a chip. *Science* 328:1,662–1,668
- Jeong HE, Lee J-K, Kwak MK, Moon SH, Suh KY (2010) Effect of leaning angle of gecko-inspired slanted polymer nanohairs on dry adhesion. *Appl Phys Lett* 96:043704
- Kim S, Spenko M, Trujillo S, Heyneman B, Santos D, Cutosky MR (2008) Smooth vertical surface climbing with directional adhesion. *IEEE Trans Robot* 24:65–74
- Ko HC, Stoykovich MP, Song J, Malyarchuk V, Choi WM, Yu C-J, Geddes JB III, Xiao J, Wang S, Huang Y, Rogers JA (2008) A hemispherical electronic eye camera based on compressible silicon optoelectronics. *Nature* 454:748–753
- Kolle M, Salgard-Cunha PM, Scherer MRJ, Huang F, Vukusic P, Mahajan S, Baumberg JJ, Steiner U (2010) Mimicking the colourful wing scale structure of the *Papilio blumei* butterfly. *Nat Nanotechnol* 5:511–515
- Kustandi TS, Low HY, Teng JH, Rodriguez I, Yin R (2009) Mimicking domino-like photonic nanostructures on butterfly wings. *Small* 5:574–578
- Jin Y, Tai H, Hiltner A, Baer E, Shirk JS (2007) New class of bioinspired lenses with a gradient refractive index. *J Appl Polymer Sci* 103:1,834–1,841
- Jun I-K, Hess H (2010) A biomimetic, self-pumping membrane. *Adv Mater* 22:4,823–4,825
- Lai Q, Zhang L, Li Z, Stickle WF, Williams RS, Chen Y (2010) Ionic/electronic hybrid materials integrated in a synaptic transistor with signal processing and learning functions. *Adv Mater* 22:2,448–2,453
- Lee LP, Szema R (2005) Inspirations from biological optics for advanced photonic systems. *Science* 310:1,148–1,150
- Lee H, Lee BP, Messersmith PB (2007) A reversible wet/dry adhesive inspired by mussels and geckos. *Nature* 448:338–341
- Leng B, Chen X, Shao Z, Ming W (2008) Biomimetic synthesis of silica with chitosan-mediated morphology. *Small* 4:755–758
- Li L, Yi AY (2010) Development of a 3D artificial compound eye. *Opt Exp* 18:18,125–18,137

- Li X, Xie J, Lipner J, Yuan X, Thomopoulos S, Xia Y (2009) Nanofiber scaffolds with gradations in mineral content for mimicking the tendon-to-bone insertion site. *Nano Lett* 9:2,763–2,768
- Liu K, Zhang M, Zhai J, Wang J, Jiang L (2008) Bioinspired construction of Mg-Li alloys surfaces with stable superhydrophobicity and improved corrosion resistance. *Appl Phys Lett* 92:183103
- Liu M, Zheng Y, Zhai J, Jiang L (2010) Bioinspired super-antiwetting interfaces with special liquid-solid adhesion. *Acc Chem Res* 43:368–377
- Losic D, Mitchell JG, Voelcker NH (2009) Diatomaceous lessons in nanotechnology and advanced materials. *Adv Mater* 21:2,947–2,958
- McConney ME, Anderson KD, Brott LL, Naik RR, Tsukruk VV (2009) Bioinspired material approaches to sensing. *Adv Funct Mater* 19:2,527–2,544
- Min W-L, Betancourt AP, Jiang P, Jiang B (2008) Bioinspired broadband antireflection coatings on GaSb. *Appl Phys Lett* 92:141109
- Mohammed JS, Murphy WL (2009) Bioinspired design of dynamic materials. *Adv Mater* 21:2,361–2,374
- Murphy MP, Aksak B, Sitti M (2009) Gecko-inspired directional and controllable adhesion. *Small* 5:170–175
- Noh H, Yang J-K, Liew SF, Rooks MJ, Solomon GS, Cao H (2011) Control of lasing in biomimetic structures with short-range order. *Phys Rev Lett* 106:183901
- O'Regan B, Grätzel M (1991) A low-cost, high-efficiency solar cell based on dye-sensitized colloidal TiO<sub>2</sub> films. *Nature* 353:737–740
- Pejoux C, de la Rica R, Matsui H (2010) Biomimetic crystallization of sulfide semiconductor nanoparticles in aqueous solution. *Small* 6:999–1,002
- Pulsifer DP, Lakhtakia A, Martín-Palma RJ, Pantano CG (2010) Mass fabrication technique for polymeric replicas of arrays of insect corneas. *Bioinspir Biomim*. 5:036001.
- Que L, Tolman WB (2008) Biologically inspired oxidation catalysis. *Nature* 455:333–340
- Sanles-Sobrido M, Salgueiriño-Maceira V, Correa-Duarte MA, Liz-Marzán LM (2008) Magnificent sea-anemone-like magnetic silica capsules reinforced with carbon nanotubes. *Small* 4:583–586
- Song F, Meng S, Xu X, Shao Y (2010) Enhanced thermal shock resistance of ceramics through biomimetically inspired nanofins. *Phys Rev Lett* 104:125502
- Sun C-H, Gonzalez A, Linn NC, Jiang P, Jiang B (2008) Templated biomimetic multifunctional coatings. *Appl Phys Lett* 92:051107
- Sysoev VV, Goschnick J, Schneider T, Strelcov E, Kolmakov A (2007) A gradient microarray electronic nose based on percolating SnO<sub>2</sub> nanowire sensing elements. *Nano Lett* 7:3,182–3,188
- Sysoev VV et al (2010) Single-belt electronic nose: engineering and tests of the simplest analytical element. *ACS Nano* 4:4,487–4,494
- Vigneron JP, Rassart M, Vandembem C, Lousse V, Deparis O, Biró LP, Dedouaire D, Cornet A, Defrance P (2006) Spectral filtering of visible light by the cuticle of metallic woodboring beetles and microfabrication of a matching bioinspired material. *Phys Rev E* 73:041905
- Wang J, Sato H, Xu C, Taya M (2009) Bioinspired design of tactile sensors based on Flemion. *J Appl Phys* 105:083515
- Wu S et al (2008) A biomimetic hierarchical scaffold: natural growth of nanotitanates on three-dimensional microporous Ti-based metals. *Nano Lett* 8:3,803–3,808
- Wu D, Chen Q-D, Yao J, Guan Y-C, Wang J-N, Niu L-G, Fang H-H, Sun H-B (2010) A simple strategy to realize biomimetic surfaces with controlled anisotropic wetting. *Appl Phys Lett* 96:053704
- Xia F, Jiang L (2008) Bio-inspired, smart, multiscale interfacial materials. *Adv Mater* 20:2,842–2,858
- Yameen B, Ali M, Neumann R, Ensinger W, Knoll W, Azzaroni O (2009) Ionic transport through single solid-state nanopores controlled with thermally nanoactuated macromolecular gates. *Small* 5:1,287–1,291
- Zhang L, Abbott JJ, Dong L, Peyer KE, Kratochvil BE, Zhang H, Bergeles C, Nelson BJ (2009) Characterizing the swimming properties of artificial bacterial flagella. *Nano Lett* 9:3,663–3,667

## Chapter 9

# Nano-Bio Integration

**Abstract** The aim of nanobiotechnology is the integration of nanodevices with biological molecules, such that both components maintain their functionalities. This chapter provides examples of such hybrid materials and devices.

The issue of nano-bio integration, which bridges the fields of nanotechnology and molecular biology, can be seen from two perspectives: biological/medical or technological. Successful examples of nano-bio integration related to the first perspective include tissue engineering using nanoscale scaffolds and drug delivery using nano-sized devices, presented in Chap. 4, as well as the search for nanomaterials for neural interfaces (Kotov et al. 2009), for example. The second perspective is the focus of this chapter. More precisely, we provide examples of hybrid materials and devices that take advantage from nanotechnology, as developed for inorganic materials, and the recognition and self-organization properties of biological molecules.

### 9.1 Nano-bio Materials for Electronics and Optoelectronics

The combination of biological molecules with nanosized inorganic solids is expected to render composites with properties that are found in one of their constituents. In biological applications, properties such as biocompatibility, biodegradability, and hierarchical organization are highly desired, as discussed previously with respect to tissue engineering and implants, while in technological applications, tunability of electrical, optical, or mechanical properties is an advantage. In this respect, biomolecules can become active parts in electrochemical sensors based on chitosan-montmorillonite clay intercalation compounds, for example, since chitosan chains arrange in mono- or bilayer configurations between clay layers depending on its concentration, the two configurations showing different properties. Bio-nano hybrid materials can also exhibit multifunctionality as, for instance, the sucrose-sepiolite mixture, which is at the same time the sensing

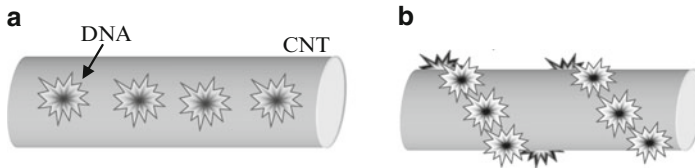


**Fig. 9.1** (a) CNTs that incorporate DNA molecules. (b) DNA molecules wrapped around a CNT

phase in potentiometric sensors and electronic collector. Additional examples of the properties of bionanocomposites can be found in [Darder et al. \(2007\)](#).

Biomaterials are reversibly tunable conductors. Hybrid structures that integrate biological molecules and nanosized conductors include carbon nanotubes (CNTs) that incorporate single-stranded DNA (ssDNA) or double-stranded DNA (dsDNA) molecules wrapped around CNTs, as illustrated in Fig. 9.1a, b, respectively. For example, ssDNA encapsulated inside double-wall CNTs with inner diameters of about 4 nm modify selectively their properties depending on the base sequence ([Li et al. 2010a](#)). More precisely, after incorporating a sequence of 30 bases, the semiconducting ambipolar behavior of pristine double-wall CNTs changes into a p-type or an n-type characteristic for C or G bases, respectively, while the resulting structure remains ambipolar after encapsulating sequences of A or T bases, the gate voltage determining whether electrons or holes transport electric charges. The ambipolar behaviors of pristine and A- or T-encapsulated double-wall CNTs are, however, different. The hybrid ssDNA–CNT conductors are stable, and the change in conduction is caused by charge transfer through  $\pi - \pi$  stacking from the CNT to DNA bases, the direction of the charge transfer being determined by reduction/oxidation potentials of the DNA bases. In particular, C has the lowest reduction potential, and G has the lowest oxidation potential of all bases.

On the contrary, metal single-wall CNTs can become p-type semiconductors if an ssDNA molecule is wrapped around them, irrespective of the homo- or heteropolymeric nature of the base sequence ([Cha et al. 2009](#)). The same  $\pi$ -stacking interactions between the side wall of the CNT and DNA bases render these structures stable, the hydrophilic sugar–phosphate backbone being positioned at the exterior. The metal–semiconductor transition takes place only in the presence of water, which screens the negative charges in the phosphate group of DNA. In fact, the metal–semiconductor transition is reversible at repeated hydration–dehydration cycles, no such effect being observed for metallic CNTs without DNA wrapping. The reason is that the phosphate groups of DNA are negatively charged only in water and not in the dry state, and in the presence of polar water, molecules move closer to the surface of the single-wall CNT, facilitating a charge transfer between CNT and DNA. In addition, the wrapped DNA molecule acts as a helical perturbation to the charge carriers in CNT, the net result of these effects being the opening of an energy band gap. The width of the gap is estimated to be 30 meV for a (6,6) single-walled CNT wrapped with adeno monophosphate, case in which the CNT donates

about  $0.2e$  to the biological molecule, the resulting local electric field breaking the cylindrical symmetry of the structure.

Even the transport properties of semiconducting single-walled CNTs are modified when ssDNA wraps around them (Li et al. 2010b). At low temperatures, up to 80 K, the hybrid material displayed single-electron tunneling features explained by the formation of a series of quantum dots by wrapping with an ssDNA consisting of a sequence of 30 C bases. The size of the quantum dots is in the 25–30 nm range, and their Coulomb charging energies are about 0.1 eV, the wrapping length having no noticeable effect on the size of the quantum dots. At room temperature, the charge-transfer process between CNT and ssDNA modifies the threshold voltage of a FET structure with this material as channel from  $-30$  V for the pristine p-type CNT to 0 V for the wrapped nanotube.

Recently, it was found that when multiwalled CNTs were complexed with the cytoskeletal protein tubulin, the resulting hybrid assemblies had different nanotube morphologies depending on the concentration of tubulin: at low concentration, disorganized structures form, whereas petal-like and flower-like conformations are obtained at tubulin concentrations between 10 nM and 10  $\mu$ M, and 100  $\mu$ M, respectively (Dinu et al. 2009). The flower-like patterns are typically composed of 4–6 petals, the latter exhibiting on mica surfaces lengths of  $19 \pm 4.9$   $\mu$ m, widths of  $4.8 \pm 0.7$   $\mu$ m, and heights of  $0.3 \pm 0.1$   $\mu$ m.

It is instructing to specify that not only biological molecules wrap around CNTs, but CNTs with moderate flexibility (single-walled CNT and thin multiwalled CNT, with diameters of 30 nm) can also wound around bacteria such as *Streptococcus mutans* and immobilize them, having possible applications in eradicating oral pathogens at the nanoscale (Akasaka and Watari 2009). The CNT affinity toward bacteria originates in van der Waals forces.

DNA molecules not only change the electronic properties of CNTs but can also help to sort single-walled CNTs in a mixture according to their chirality (Tu et al. 2009). More than 20 short DNA sequences have been identified that bind selectively to and allow the chromatographic purification of a CNT with a specific chirality from a mixture containing 12 species. The periodic purine–pyrimidine pattern in the recognition sequences of the DNA forms a two-dimensional sheet resulting from hydrogen bonding between adjacent strands that encircle the nanotube, the resulting stable structure resembling a three-dimensional barrel. The selectivity is more pronounced in short DNA sequences, of about 10 mer, in which the contour length of the backbone becomes comparable to the van der Waals circumference of a single-walled CNT. Even low-abundant species can be purified with this method. For example, 90% purity of single-walled CNTs with chiralities (6,5), (7,5), (7,6), and (10,2) can be achieved by the DNA sequences (TAT)<sub>4</sub>, (ATT)<sub>4</sub>AT, (GTT)<sub>3</sub>G, and (TATT)<sub>2</sub>TAT, respectively, in a 0.1 M NaCl dispersion solution.

ssDNA molecules can also assist in the preparation of stable suspensions of graphene in water up to concentrations as high as 2.5 mg mL<sup>-1</sup> (Patil et al. 2009). As for CNTs, DNA binds to the graphene surface via  $\pi - \pi$  stacking interactions such that the sugar–phosphate backbone is positioned away from the surface and creates a hydrophilic outer layer that prevents sedimentation for several months.

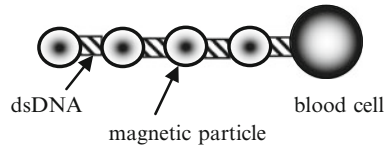
In contrast, graphene sheet suspensions obtained by reduction of graphene oxide aqueous suspensions in the absence of ssDNA aggregate within 30 min. The stable and highly negatively charged ssDNA-graphene sheets can be used for fabricating lamellar self-assembled bionanocomposite materials intercalating, for example, layers of the positively charged cytochrome *c* metalloprotein. A recent review on the strategies for biohybrid fabrication, including lamellar structures, can be found in [Ruiz et al. \(2010\)](#).

Biomolecules can also improve the performances of optoelectronic materials, in particular organic dyes. Organic dyes embedded in thin polymeric films are used in lasers, amplifiers, sensors, and displays due to their low cost, ease of fabrication, and wavelength control, but these advantages are hampered by the tendency of organic dyes to form nonfluorescent aggregates and to photodimerize and photooxidize after repeated excitation. A possible solution to increase the photostability of organic dyes is to encapsulate them in DNA thin films, as shown in [Ner et al. \(2009\)](#) for the nonlinear optical dye Hemi-22. DNA can become soluble in organic solvents if layers of DNA and the cationic surfactant hexadecyltrimethylammonium-chloride (CTMA) are assembled in a three-dimensional lamellar structure. Then, thin films are fabricated by spin coating from dye solutions containing DNA–CTMA assemblies. DNA–CTMA prevents the formation of H-type aggregates in thin films with dye loadings up to 10% (w/w) without altering the absorption spectrum of Hemi-22. The DNA–CTMA lamellar structure increases also the photophysical and photochemical properties of Hemi-22 films, enhancing in particular the stability at UV illumination. The reason is that DNA absorbs UV light but also that dye molecules in thin films bind with DNA base pairs in the polar microenvironment assured by the DNA groove, binding which explains the redshift of absorption and emission spectra compared to dye spectra in nonpolar solvents.

## 9.2 Nano-bio Mechanical Devices

An example of a hybrid nano-bio mechanical device is the nanomotor fabricated by attachment of flagella separated from the biflagellate *Chlamydomonas reinhardtii* unicellular alga to polystyrene microbeads ([Mori et al. 2010](#)). The flagella are in fact molecular motors with, in this case, dimensions of 12  $\mu\text{m}$  in length and 200 nm in diameter, which have controllable on/off states and are easier to prepare than artificial molecular motors. The flagella tips attach nonspecifically, and therefore, the surface of beads do not need to be functionalized in order to be propelled by flagella. Experiments showed that the beads perform a uniform rotation about their axes when one flagellum is attached to their surface and can advance if two flagella are attached. A flagellum imparts a torque to the bead, the resultant torque from two flagella vanishing, and hence, the resultant velocity becoming maximum, when the angle between flagella is 1.4 rad. This value is close to  $\pi/2$ , which represents the angle between the two flagella for which the theoretical probability of their attachment to the bead is maximum.

**Fig. 9.2** Nano-bio flagella with controlled direction of movement



Artificial flexible flagella able to propel nanoscale cargoes have been constructed (Dreyfus et al. 2005). The flagellum consists of a linear chain of streptavidin-coated micrometer-sized superparamagnetic colloids linked by 107-nm-long flexible dsDNA with biotin molecules at each end, and the cargo is a red blood cell, as shown in Fig. 9.2. A uniform magnetic field aligns the flagellum, while an oscillating transverse field actuates it. Reversible displacements do not move the cargo since the micrometer-scale fluid dynamics is governed by viscous and not by inertial terms. Therefore, swimming schemes that break the time-reversal invariance are needed to propel the blood cell. An oscillating magnetic field  $\mathbf{B}$  with a static and a time-varying sinusoidal components with comparable amplitudes,  $\mathbf{B}_s$  and  $\mathbf{B}_{osc}$ , respectively, acts as fuel and drives the flagellum, which follows the instantaneous magnetic field direction, bending, and reorienting in the process. A propelling force is generated for suitable flagellum flexibility and magnetic field, the artificial swimmer moving toward the free extremity of the flagellum, in the opposite direction compared to spermatozoa. The average velocity is oriented in the direction of  $\mathbf{B}_s$  and its maximum value is of about one blood-cell diameter per second.

Self-propelled bacteria such as *Escherichia coli*, when placed in asymmetric environments, can impart a rotary motion to nano- and microstructures immersed in a bacterial bath, as shown in Di Leonardo et al. (2010); the imparted motion is random in symmetric environments. Suspensions of motile cells from bacteria form a strong nonequilibrium fluid with an intrinsically irreversible dynamics. Collective action of these flagellar motors generates a propelling force that pushes against the drag force of the fluid, resulting in a nonconservative external force field. An asymmetric microstructure such as that represented in Fig. 9.3a, with a diameter of  $48 \mu\text{m}$ , can be rotated by a swimming cell, which aligns and slides parallel to the microstructure wall in a direction that depends on the contact angle, due to the repulsive contact force between cell and microstructure. In particular, bacterial population in a concentrated suspension tends to concentrate and order at the concave corners of the microstructure, generating a sufficient large torque to rotate the microgear at an average rotation frequency of approximately 1 rpm when the bacterial concentration becomes  $10^{10} \text{mL}^{-1}$ ; note that bacteria move at a speed of  $20 \mu\text{m s}^{-1}$ . In contrast, symmetric microgears, as those in Fig. 9.3b, rotate in a fluctuating direction, with a negligible average rotation angle. These cell-propelled microstructures rotate as long as nutrients are kept in sufficient supply and harmful metabolic by-products are removed. The number and shape of teeth do not influence significantly the rotation frequency, the configurations in Fig. 9.3a, c, displaying almost the same maximum angular speed in the bacterial bath. The angular speed increases, though, with the bacterial concentration. The directional motion that arises

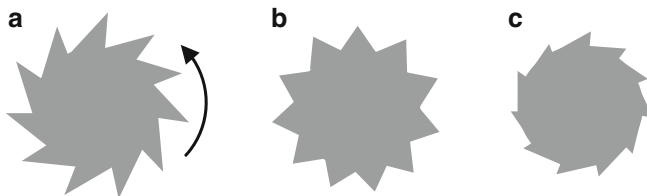
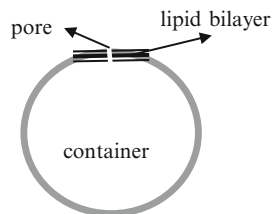


**Fig. 9.3** Configurations of rotary motors driven by bacteria

**Fig. 9.4** Hybrid lipid–polymer container with tunable permeability



from chaotic dynamics of small molecules in a nonequilibrium state and in an asymmetric environment is referred to as ratchet effect. A review on nanoscale ratchets can be found in [Hänggi and Marchesoni \(2009\)](#), whereas a theoretical approach to the rotary micromotor in a bacterial bath is presented in [Angelani et al. \(2009\)](#). The model supports the experimental finding that asymmetric objects can spontaneously rotate into the desired direction if pushed by biological micromotors.

Bioinorganic hybrids, fabricated by randomly incorporating elastin-like polypeptides into silica membranes by sol–gel synthesis, can be used as smart membranes, which exhibit molecular-level control of permeability in response to temperature changes and act as molecular weight cutoff filters ([Rama Rao et al. 2002](#)). The porosity of the membrane depends on the hydrophilic or hydrophobic nature of the polypeptides related to their conformations (the polypeptides are in a collapsed state if hydrophobic), the transition between these two states in aqueous environment taking place at the lower critical solution temperature (LCST). As a consequence, above the LCST, the 2.5- $\mu\text{m}$ -thick hybrid membranes are permeable only for molecules with weights less than 5,000 Da, whereas below LCST, the membranes are completely impermeable. The LCST takes place at different temperatures for different elastin-like polypeptides (e.g., at 34 °C for ELP-60 and at 45 °C for ELP-13), and the permeation properties are fully reversible upon cyclic changes of temperatures around the transition points.

A hybrid lipid–polymer nanocontainer with tunable permeability, illustrated in [Fig. 9.4](#), has been reported in [Dudia et al. \(2008\)](#). It was fabricated by drilling holes with a diameter of 1  $\mu\text{m}$  in an impermeable 100-nm-thick polystyrene scaffold by focused ion-beam lithography, sealing them with lipid bilayers and incorporating into these bilayers pore-forming channel proteins that can be remotely controlled.

The mechanosensitive channel protein, extracted from *E. coli*, allows passage of molecules with diameters smaller than 3 nm. Its conformation varies in response to the tension in the lipid membrane and forms a pore under severe hypoosmotic stress conditions induced by light and/or pH. Controlled opening of nanocontainers activated by adding a positively charged compound to the bulk solution could be monitored by the fluorescence of dyes introduced in the nanocontainers. This nanocontainer, filled with active molecules, could be used for smart drug delivery.

### 9.3 Nanobioelectronics and Optoelectronics

The integration of biological features and nanoelectronic devices is not an easy task since biomolecules are often soft materials, which operate in aqueous solutions, whereas nanotechnological processes require more robust and stiff materials. DNA is a versatile material for nanobioelectronics since it can not only influence the electrical conductivity of inorganic systems with which it interacts, but its own conduction depends on doping conditions. More precisely, the canonical Watson–Crick base pairs can be substituted by metal complexes, which influence the conductive or even magnetic properties of the metal–base pair molecules (Clever et al. 2007). In addition, DNA networks can be patterned on the Si/SiO<sub>2</sub> surface, which makes this biological molecule compatible with standard semiconductor nanotechnologies.

Nanobioelectronics implies ultimately the integration of biological systems with nanoelectronic devices. A successful integration implies that both components have comparable dimensions, which is only possible when networks or arrays of nanostructures are used. Such an integration of a purple cell membrane from *Halobacterium salinarum* and a nanotube network field-effect transistor, which consists of a dense network of randomly oriented carbon nanotubes contacted by electrodes, with the gate voltage assured by the buried substrate, is reported in Bradley et al. (2005). The purple cell membrane contains the bacteriorhodopsin protein, which is light-sensitive and has a permanent electric dipole moment that induces an electric field directed from the extracellular membrane side to the cytoplasmic side. Patches of the 5-nm-thick purple membranes were deposited on nanotube network field-effect transistors oriented with the cytoplasmic side or the extracellular side toward the nanotubes, as well as with a mixture of these orientations and the transfer characteristics (current vs. gate voltage) were measured. The reference devices, not covered with biological membranes, showed threshold voltages and significant hysteresis loops at left-moving and right-moving sweeps of the gate voltage, which narrowed considerably when purple membranes were present, irrespective of their orientations. The change of threshold voltages when the biological systems were deposited, however, depended on their orientations: shifts of 2.2 V and −0.4 V were measured, respectively, for the cytoplasmic and extracellular orientations, while for mixed orientations, the corresponding shift

was of 1 V. The asymmetry between the first two cases indicates that the dipole is closer to the cytoplasmic side of the membrane, the electrical characteristics indicating that both the nanoelectrical and the biological systems maintain their properties/functionalities and interact with one another. A true bionanoelectronic device was created.

In devices that use the whole cell behavior as opposed to the cell membrane patches referred to above, it is important to be able to introduce electrodes into cells without destroying them or inducing cell death (apoptosis). Such chip-based nanoscale electrodes consisting of a metallic post with a hydrophobic band have been fabricated (Verma and Melosh 2010). These electrodes can penetrate into the cell membrane of red blood cells and form tight seals, with a resistance of almost  $4\text{ G}\Omega$ . The stealth probe spontaneously fuses with the cell membrane because the 5–10-nm-wide hydrophobic band formed by self-assembly mimics the behavior of transmembrane proteins in the hydrophobic membrane core so that a bioinorganic lateral junction forms, accompanied by an impermeable gigaohm seal. Such Pt-tipped stealth probes with hydrophobic bands fabricated onto wider Ni bottom electrodes with a width of  $10\text{ }\mu\text{m}$  by electron-beam lithography induce membrane fusion, provide low-resistance electrical access to the tip for injection of redox-induced current in cells, and insulate the electrodes placed outside the cell. A stealth probe is illustrated in Fig. 9.5.

A quite common biomolecule in nanoelectronics is DNA. DNA field-effect transistors (FETs) with source and drain electrodes consisting of metallic multiwalled CNTs having a diameter of 50 nm have been reported in Sasaki et al. (2006). A schematic configuration of this DNA–FET is illustrated in Fig. 9.6. The CNTs make contact with 15/65 nm Ti/Au pads separated by 7–8  $\mu\text{m}$ , and the DNA

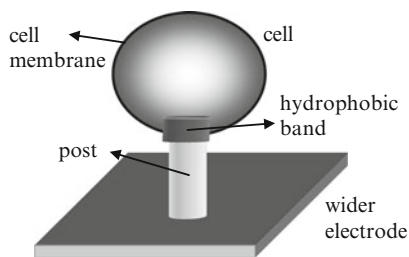


**Fig. 9.5** Penetration of a stealth probe into a biological cell

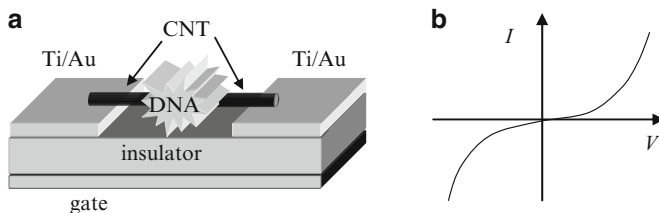
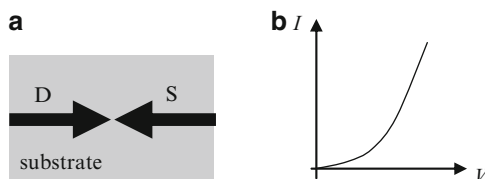


**Fig. 9.6** (a) DNA-based FET with CNT electrodes and (b) a typical current–voltage characteristic

**Fig. 9.7** (a) Arrow-shaped drain (D) and source (S) electrodes in a biological transistor and (b) a typical current–voltage characteristic



molecule is placed over the central part of the CNT, on which a 50-nm-wide channel is fabricated with the focused ion-beam bombardment technique. The poly(dG)–(dC) DNA molecule, placed using the electromagnetic trapping method, increases the electrical conductivity between CNT electrodes, acting as a p-type channel. The room-temperature current–voltage characteristic, which has a typical form as that in Fig. 9.6b, can be explained by the small polaron hopping model, the hopping transport mechanism being different for low- and high-bias voltage ranges. More specifically, the estimated hopping distance is 9.08 Å for biases between  $-10$  and  $10$  V; this parameter decreases to 3.8 Å if the whole  $-20$ – $20$  V bias range is taken into consideration. The latest value is comparable to the 3.4 Å distance between base pairs in the DNA molecule. Metallized DNA, consisting of arrays of  $\text{Co}^{2+}$ ,  $\text{Zn}^{2+}$ , or  $\text{Ni}^{2+}$  metal ions that substitute the imino protons of every base pair, can also be used as the active element of a FET, the rate of the phonon-assisted electron hopping between the localized states of metal ions being strongly influenced by a transverse electric field (Nokhrin et al. 2007).

Electrical transport between nanosized Cr/Au arrow-shaped source and drain electrodes bridged by self-assembled guanosine ribbons and placed above a back gate Ag electrode has been demonstrated in Maruccio et al. (2003). This FET, shown in Fig. 9.7, has a p-type channel consisting of ribbon-shaped supramolecular assemblies of deoxyguanosine derivatives that induce current rectification due to the intrinsic dipole moment oriented along the ribbon axis, which creates a preferential charge pathway. When the currents  $I$  are measured for both polarizations of the source–drain voltage  $V$ , the rectification ratio is found to be  $\text{RR}(V) = I(V)/I(-V) \cong 3$ . In fact, the current increases slowly, almost linearly with the source–drain voltage up to about 3 V, and shows an exponential increase above this threshold voltage, which depends slightly on the gate bias. In fact, although similar to a MOSFET, this biomolecular FET differs from the latter in that the current–gate voltage dependence does not saturate for a given source–drain voltage, indicating the presence of two transport mechanisms: energy band alignment and resonant transport in the molecular channel.

Biological organic FETs have been fabricated also from DNA-based polymers such as insulating DNA–CTMA thin films, but these devices often show large hysteresis caused by ionic charge migration, which limits their performances. In addition, DNA–CTMA films are soft and can be easily scratched. A significant improvement of both electrical and mechanical properties of DNA–CTMA FETs containing DNA purified from salmon waste occurs after cross-linking with poly(phenylisocyanate)-*co*-formaldehyde (PPIF) (Yumusak et al. 2009).

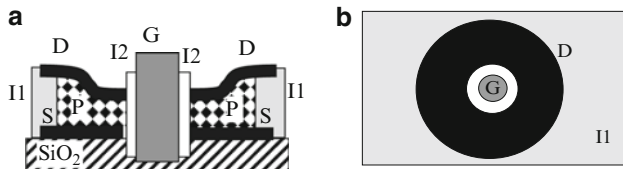


**Fig. 9.8** (a) Side view (cross-section) and (b) top view of an ambipolar central-gate vertical FET with biological channel

The n-channel FETs using 80-nm-thick  $C_{60}$  semiconductor channels in contact with 0.6/60-nm Cr/Au source and drain electrodes and separated from a bottom 60-nm Au electrode by a thin layer of DNA–CTMA–PPIF with a width of 0.5  $\mu\text{m}$ , displayed no hysteresis. Similarly, p-channel FETs with same dimensions but  $\alpha$ -sexithiophene as channel showed significantly reduced hysteresis due to ionic charge migration inhibition by cross-linking; the length and widths of the channels were 20 and 200  $\mu\text{m}$ , respectively.

In electrical DNA-based devices, high-yield DNA immobilization on anchor pads is an important issue. A technique describing the immobilization of individual DNA molecules on silicon substrates by binding to 3-aminopropyltriethoxysilane (APTES) anchoring pads is detailed (Gao et al. 2010). These pads were fabricated by electron-beam lithography, which defined the pad shapes by drilling holes in a poly(methyl methacrylate) (PMMA) layer, followed by APTES deposition by self-assembly from an aqueous solution, in the holes, and a final molecular lift-off in which the PMMA layer is removed. DNA rafts in solution bind with an 85% yield on the positively charged anchoring pads after a deposition time of 12–14 h.

Molecular transistors can even be mass produced. In particular, ambipolar central-gate vertical FETs with a cylindrical geometry, the cross-section of which is represented in Fig. 9.8, can be fabricated in parallel using photolithography and self-assembling (Mentovich et al. 2009). This FET has as channel the self-assembled monolayer of bovine serum albumin (BSA) protein P, with a length of 4 nm determined by the thickness of BSA, while the source, drain, and gate electrodes, denoted in Fig. 9.8 by S, D, and G, respectively, consist of thin layers of Au, Pd, and Ti. The source and drain electrodes are separated by the I1  $\text{Si}_3\text{N}_4$  dielectric layer, while the gate is isolated by an 8-nm-thin  $\text{TiO}_2$  oxide layer labeled as I2. The structure is grown on a Si wafer covered by a 100-nm-thick  $\text{SiO}_2$  layer. Arrays of such transistors with diameters between 800 and 1.5  $\mu\text{m}$  and showing n- or p-type conduction depending on the gate voltage were fabricated. The operating voltages are below 1 V. Transport in FET devices that include single molecules is expected to depend also on the strength of the electronic coupling between the molecule and the source and drain electrodes. This coupling can be weak, intermediate, or strong, each regime being characterized by specific phenomena (Moth-Poulsen and Bjørnholm 2009).

An example of a transistor based on a chemically modified graphene (CMG)/bacterial DNA and protein compound has been reported in Mohanty and

Berry (2008). The p-type semiconducting CMG sheets attach easily to microscale bacterial cells or proteins and allow hybridization of DNA on their surface, the interaction with these biological molecules modulating the electronic properties of CMG. For example, about 1,400 conducting holes are generated when a single bacterium attaches to the graphene-amine compound, while the hybridization of six complementary DNA strands on graphene oxide sheets produces one hole. DNA tethering on the latter material occurred predominantly on wrinkles and thicker parts of the sheets. The CMG/bacteria hybrids were fabricated by selectively assembling bacterial cells extracted from *Bacillus cereus*, which are negatively charged, on graphene-amine scaffolds, which are positively charged. Amazingly, most bacterial cells were alive after deposition but died after 4 h. Graphene-amine is obtained by aminization of graphene oxide sheets immobilized on silica substrates. The bacterial cells and proteins induced a sharp decrease of the resistance of a graphene-amine transistor with about two orders of magnitude, from 800 to 5.34 M $\Omega$  due to an increase in the number of holes of  $1.8 \times 10^{11} \text{ cm}^{-2}$ .

Engineered protein pores, which behave as diodes, can be inserted into interface bilayers between droplets in a droplet network that shows collective properties. Such networks can implement full- and half-wave current rectifiers or current limiters (Maglia et al. 2009). The protein diode-like pore is a modified staphylococcal  $\alpha$ -hemolysin, which can be introduced vectorially into lipid bilayers that form when two droplets enclosed in lipid monolayers are brought in contact (see Fig. 9.9), displaying full rectification of the ionic current in a 1 M KCl solution. The droplets are contacted by Ag/AgCl electrodes. More precisely, as shown in Fig. 9.9, the pore closes for negative voltages after an exponential time delay with a time constant of the order of 200 ms necessary for changing the conformation of the protein, and no ionic current is measured. In the absence of the nanopore, the current collected by the electrodes that penetrate the droplets simply follows the voltage signal. A measure of the rectification property is, for example, the ratio of conductance measured for the positive and negative polarities of the same applied bias; this rectification ratio at 50 mV is about 60.

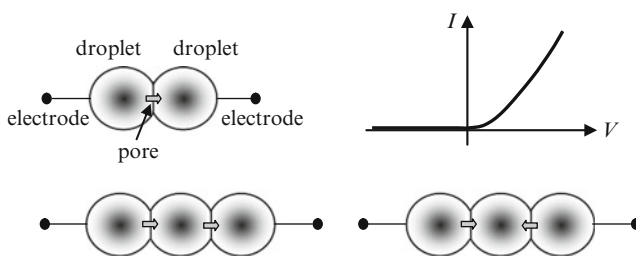


**Fig. 9.9** Top: engineered protein pores (left) with diode-like electrical behavior (right). Bottom: networks of engineered nanopores that act as a half-wave rectifier (left) and full-wave rectifier (right)

When a sinusoidal voltage is applied on this diode-like nanopore, it works as a half-wave rectifier, allowing the passage of applied voltages with positive polarity only. However, due to the decay time constant of the nanopore and the capacitance of the system, half-wave rectifier operation is possible only for voltage signals with frequencies below 0.2 Hz. In networks formed by chains of three touching droplets, the output current depends on the orientation of the pores that penetrate the two bilayers: the network acts as a half-wave rectifier if the two pores have the same orientation and as a full-wave rectifier when the pores are oriented in opposite directions, case in which the current is not allowed to pass through the device irrespective of its polarity. The orientation of the nanopore can be manipulated by selecting first the droplets that incorporate the protein and controlling the order in which the bilayers form. A more complicated, four-droplet network that acts as a bridge rectifier was also demonstrated. In reality, these devices are not ideal; brief current spikes appear, especially on closing and opening events of the nanopores.

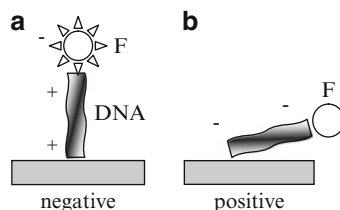
Optoelectronic devices can also benefit from the incorporation of biomolecules. The efficient photosynthesis properties of plants and bacteria, which can harvest photons with almost optimum yield, prompted the research of composites that could enhance the efficiency of photovoltaic cells and photodetectors. At least two biological photosynthetic complexes that fulfill this aim have been identified: a bacterial reaction center extracted from the purple bacteria *Rhodospirillum rubrum* and a larger complex isolated from spinach chloroplasts (Das et al. 2004). These complexes, after a careful processing, can be incorporated as interfacial materials in light-harvesting devices since they are able to sustain open circuit voltages of about 1 V without significant damage and can contribute to loss reduction by acting as a self-assembled insulating membrane. The hybrid devices have an internal quantum efficiency of about 12%.

Recently, another bioinspired conversion mechanism of light power into electricity in a hybrid solar cell based on proton transport across a membrane with smart-gating nanochannels, which mimic the ion channels in photosynthetic membranes in nature, has been reported in Wen et al. (2010) but showed extremely low efficiencies. The conical photon-driven channels had negatively charged DNA molecules attached on it, the conformation of which depends on the pH of a solution of the photo-acid molecule 8-hydroxypyrene-1,3,6-trisulfonate. This molecule releases protons when irradiated with UV light.

The fluorescence of hybrid bioinorganic surfaces can be modulated by an applied alternating electric field (Rant et al. 2004). As shown in Fig. 9.10, the polarity change of the applied bias switches the orientation of a dye-labeled biological molecule tethered on the surface between a standing and a lying state, which in turn modulates the fluorescence of the surface. The fluorescence in the case of the biological nano-electro-mechanical-optical system in Rant et al. (2004) is due to the Cy3 dye that binds to the 3' end of a DNA molecule (denoted by F in Fig. 9.10), the 5' end of which chemically grafts to gold surfaces.

In solution, the negatively charged DNA is driven away from the surface if the latter is negatively charged, adopting an upright position, and is pulled toward it if the surface is positively charged, case in which the DNA molecule is considerably

**Fig. 9.10** Electrically controlled fluorescent in a hybrid device



tilted. As a result, the nonradiative energy transfer from the dye molecule to the metal modulates the fluorescence intensity  $F$  according to the relation

$$F \propto \sigma(L_{\text{DNA}} \sin \theta)^3, \quad (9.1)$$

so that strong fluorescence is observed for the upright orientation and quenching occurs for the tilted DNA molecule. In (9.1),  $\sigma$  is the number of molecules per area,  $L_{\text{DNA}}$  is the effective length of DNA, and  $\theta$  is the angle between the molecule and the surface, which takes values of  $90^\circ$  and  $25^\circ$  for the upright and tilted DNA, the fluorescence decreasing ten times in the latter case compared to the former situation. Fluorescence modulation by an applied bias can only occur for sufficiently low packing densities of DNA molecules on the surface, such that these molecules can gyrate freely when the polarity of the electric field reverses. Fluorescence modulation can follow the electrical excitation for a large number of cycles only up to frequencies of 10 kHz, for higher frequencies the DNA molecule adopting an intermediate position between standing and lying. Although the device can work with both ssDNA and dsDNA, a higher cutoff frequency is observed in the latter case due to an increase in stiffness. The device works well in a solution with salt concentration of less than 10 mM since for higher concentrations, the dissolved ions in solution screen the electrode charge preventing the development of a high electric field at the surface of the gold electrodes.

Biological molecules are also used in miniature biofuel cells, as detailed in Heller (2004), consisting of carbon fibers with a diameter of  $7 \mu\text{m}$ , each coated with a distinct bioelectrocatalyst enzyme. Such cells deliver a power of  $4.3 \mu\text{W}$  when operated at 0.52 V in a physiological buffer solution at  $37^\circ\text{C}$ . Biofuel cells containing single-walled CNTs wrapped with DNA as bioelectrodes, glucose oxidase as the anode system, and laccase as cathode could even be implanted in vivo for power implants, for example (Lee et al. 2010). Glucose oxidase binds on the bioelectrodes by covalent bonds. This device delivers a maximum output power of  $442 \mu\text{W cm}^{-2}$  at a voltage of 0.46 V maintaining almost the same power level for 5 days. Biofuel cells can become an alternative for the conventional fuel cell since they can harvest energy from unusual sources, such as effluents of animal processes or carbohydrates from plants, or from unusual places. For example, microbial fuel cell can harvest energy from the interface between marine sediments and seawater. A review on microbial and enzymatic biofuel cells can be found in Calabrese Calabrese Barton et al. (2004).

## References

- Akasaka T, Watari F (2009) Capture of bacteria by flexible carbon nanotubes. *Acta Biomaterialia* 5:607–612
- Angelani L, Di Leonardo R, Ruocco G (2009) Self-starting micromotors in a bacterial bath. *Phys Rev Lett* 102:048104
- Bradley K, Davis A, Gabriel J-CP, Grüner G (2005) Integration of cell membranes and nanotube transistors. *Nano Lett* 5:841–845
- Calabrese Barton S, Gallaway J, Atanassov P (2004) Enzymatic biofuel cells for implantable and microscale devices. *Chem Rev* 104:4867–4886
- Cha M, Jung S, Cha M-H, Kim G, Ihm J, Lee J (2000) Reversible metal–semiconductor transition of ssDNA-decorated single-walled carbon nanotubes. *Nano Lett* 9:1345–1349
- Clever GH, Kaul C, Carell T (2007) DNA-metal base pairs. *Angew Chem Int Ed* 46:6226–6236
- Darder M, Aranda P, Ruiz-Hitzky E (2007) Bionanocomposites: a new concept of ecological, bioinspired, and functional hybrid materials. *Adv Mater* 19:1309–1319
- Das R, et al (2004) Integration of photosynthetic protein molecular complexes in solid-state electronic devices. *Nano Lett* 4:1079–1083
- Di Leonardo R, et al (2010) Bacterial ratchet motors. *Proc Natl Acad Sci* 107:9541–9545
- Dinu CZ, Bale SS, Zhu G, Dordick JS (2009) Tubulin encapsulation of carbon nanotubes into functional hybrid assemblies. *Small* 5:310–315
- Dreyfus R, Baudry J, Roper ML, Fermigier M, Stone HA, Bibette J (2005) Microscopic artificial swimmers. *Nature* 437:862–865
- Dudia A, Koçer A, Subramaniam V, Kanger JS (2008) Biofunctionalized lipid-polymer hybrid nanocontainers with controlled permeability. *Nano Lett* 8:1105–1110
- Gao B, Sarveswaran K, Bernstein GH, Lieberman M (2010) Guided deposition of individual DNA nanostructures on silicon substrates. *Langmuir* 26:12680–12683
- Hänggi P, Marchesoni F (2009) Artificial Brownian motors: controlling transport on the nanoscale. *Rev Mod Phys* 81:387–442
- Heller A (2004) Miniature biofuel cells. *Phys Chem Chem Phys* 6:209–216
- Kotov NA, et al (2009) Nanomaterials for neural interfaces. *Adv Mater* 21:3970–4004
- Lee JY, Shin HY, Kang SW, Park C, Kim SW (2010) Use of bioelectrode containing DNA-wrapped single-walled carbon nanotubes for enzyme-based biofuel cell. *J Power Sources* 195:750–755
- Li Y, Kaneko T, Hatakeyama R (2010a) Tailoring the electronic structure of double-walled carbon nanotubes by encapsulating single-stranded DNA. *Small* 6:729–732
- Li YF, Kaneko T, Hatakeyama R (2010b) Formation of quantum dots in single stranded DNA-wrapped single-walled carbon nanotubes. *Appl Phys Lett* 96:023104
- Maglia G, heron AJ, Hwang WL, Holden MA, Mikhailova E, Li Q, Cheley S, Bayley H (2009) Droplet networks with incorporated protein diodes show collective properties. *Nat Nanotechnol* 4:437–440
- Maruccio G, et al (2003) Field effect transistor based on a modified DNA base. *Nano Lett* 3:479–483
- Mentovich ED, Belgorodsky B, Kalifa I, Cohen H, Richter S, (2009) Large-scale fabrication of 4-nm-channel vertical protein-based ambipolar transistors. *Nano Lett* 9:1296–1300
- Mohanty N, Berry V (2008) Graphene-based single-bacterium resolution biodevice and DNA transistor: interfacing graphene derivatives with nanoscale and microscale biocomponents. *Nano Lett* 8:4469–4476
- Mori N, Kuribayashi K, Takeuchi S (2010) Artificial flagellates: analysis of advancing motions of biflagellate micro-objects. *Appl Phys Lett* 96:083701
- Moth-Poulsen K, Bjørnholm T (2000) Molecular electronics with single molecules in solid-state devices. *Nat Nanotechnol* 4:551–556
- Ner Y, Navarathne D, Niedzwiedzki DM, Grote JG, Dobrynin AV, Frank HA, Sotzing GA (2009) Stabilization of fluorophore in DNA thin films. *Appl Phys Lett* 95:263701

- Nokhrin S, Baru M, Lee JS (2007) A field-effect transistor from M-DNA. *Nanotechnology* 18:095205
- Patil AJ, Vickery JL, Scott TB, Mann S (2009) Aqueous stabilization and self-assembly of graphene sheets into layered bio-nanocomposites using DNA. *Adv Mater* 21:3159–3164
- Rama Rao GV, Balamurugan S, Meyer DE, Chilkoti A, López GP (2002) Hybrid bioinorganic smart membranes that incorporate protein-based molecular switches. *Langmuir* 18:1819–1824
- Rant U, Arinaga K, Fujita S, Yokoyama N, Abstreiter G, Tornow M (2004) Dynamic electrical switching of DNA layers on a metal surface. *Nano Lett* 4:2441–2445
- Ruiz-Hitzky E, Darder M, Aranda P, Ariga K (2010) Advances in biomimetic and nanostructured biohybrid materials. *Adv Mater* 22:323–336
- Sasaki TK, Ikegami A, Aoki N, Ochiai Y (2006) DNA-FET using carbon nanotube electrodes. *J Phys Conf Ser* 38:41–44 (2006)
- Tu X, Manohar S, Jagota A, Zheng M (2009) DNA sequence motifs for structure-specific recognition and separation of carbon nanotubes. *Nature* 460:250–253
- Verma P, Melosh NA (2010) Gigaohm resistance membrane seals with stealth probe electrodes. *Appl Phys Lett* 97:033704
- Wen L, Hou X, Tian, J, Zhai, Jiang L (2010) Bio-inspired photoelectric conversion based on smart-gating nanochannels. *Adv Funct Mater* 20:2636–2642
- Yumusak C, Singh ThB, Sariciftci NS, Grote JG (2009) Bio-organic field effect transistors based on crosslinked deoxyribonucleic acid (DNA) gate dielectric. *Appl Phys Lett* 95:263304

# Index

- AFM resolution, 111
- AM mode, 109
- Amplitude modulation (AM), 108
- AND gate, 195
- AND, OR, and AND-NOT, 194
- Anisotropic/directional wetting, 209
- Antireflection coatings, 215
- Antireflection effect, 216
- Antiwetting interfaces, 208
- Artificial molecular motors, 174
- Artificial muscles, 225
- Artificial organs, 148
- Artificial skin, 225
- Atomic force microscopy, 107
- Atomic lithographic technique, 23
- Autonomous DNA nanomotor, 178
  
- Ballistic conductor, 8
- Ballistic electrons, 12
- Ballistic regime, 7
- Ballistic semiconductor, 17
- Ballistic transport, 3
- Barrier, 10
- Bases of DNA, 36
- Beta cell at glucose, 228
- Biochip for controlled release of drugs, 140
- Bioinspired artificial bacterial flagella, 227
- Bioinspired compound lenses, 220
- Bioinspired devices, 207, 215
- Bioinspired lens with adjustable focus, 220
- Bioinspired self-pumping membrane, 228
- Bioinspired superhydrophobic surfaces, 208
- Bioinspired techniques, 222
- Biological materials, 35
- BioMEMS, 129
- Biomimetic nanopore, 221
  
- Biomimetic nanotechnology olfactory sensor (NOSE), 224
- Biomolecular computer, 204
- Biomolecular computing, 189, 192
- Biomolecular keypad, 196
- Biomolecular machines, 173
- Biomolecular memory, 202
- Biosilica, 222
- Biped walker, 181
- Born repulsive force, 107
- Bottom-up, 18
- Bottom-up approach, 24
- Bulk micromachining, 51
- Butterfly wings, 213
  
- Carbon nanotube aerogel, 225
- Carbon nanotubes, 3, 31, 120, 147
- Carrier transport, 2
- Chemical vapor deposition (CVD), 19
- Clausius–Mossotti factor, 117
- Codelivery, 128
- Coencapsulation, 128
- Coherent tunneling, 40
- Collect light, 217
- Contact, 109
- Controlled and tunable mechanical properties, 212
- Controlled dehybridization, 137
- Controlled drug delivery, 127
- Controlled polymer drug delivery system, 131
- Control of microtubule/kinesin interactions, 184
- Core/shell nanoparticles, 28
- Coulomb blockade, 16, 17
- Current density, 11, 12

- Debye length, 52
- Density of states (DOS), 114
  - of QD, 6
  - of QWR, 6
- Deposition techniques, 19
- Dielectric particle model, 118
- Dielectrophoresis, 117
- Diffusive, 2
- Digital biomolecular circuit, 195
- Dirac point, 34
- Discrete energy levels of the quantum well, 4
- Dispersion relation such as that in graphene, 34
- DNA, 35, 144
  - backbone, 36
  - based logic gates, 196
  - based walker, 182
  - bases, 1
  - chips, 144
  - conductance, 37
  - gates, 193
  - graph, 198
  - logic device, 203
  - nanotweezers, 177
  - patterned scaffolds, 199
  - template, 186
  - tweezer, 176
  - walker, 181
- Double-stranded DNA, 36
- Drug delivery, 204
- Drug delivery chip, 137
- Dyneins, 174
  
- Electrochemical deposition, 30
- Electron beam lithography (EBL), 22
- Electronic eye, 218
- Electronic signatures of the DNA bases, 116
- Electroosmosis, 53
- Electrostatic micropump, 140
- Electrostatic self-assembly, 25
- Electrostatic trapping, 38
- Electrowetting pump, 141
- Energy dispersion, 4, 15
- Energy dispersion relation in QWR, 5
- Enzymatic biomotors, 174
- Extracellular matrix, 146
  
- Fermi–Dirac distribution, 4, 9
- Fermi–Dirac function, 1
- Field-effect transistor (FET), 33, 53
- FM mode, 109
- Focused ion beam (FIB), 22
  
- Fractal memory, 202
- Frequency modulation (FM), 108
  
- Gecko-inspired synthetic materials, 210
- Gecko-inspired tipped fiber, 209
- Gradient index biological structures, 218
- Graphene, 3, 32
- Graphene nanoribbons, 35
- Growth, 30
  
- Hairpin DNA structure, 174
- Hollow microneedles, 143
- HOMO, 37, 39
- Hues, 214
- Hydrogel networks, 208
  
- Imaging, 107, 127
- Implantable controlled drug release system, 130
- Inductive stent antenna, 131
- Inorganic core/shell nanoparticles, 28
- Insect corneas, 223
- Integrated-ligand sensor, 180
  
- Kinesin motors, 174, 181
- Kinesins, 174
  
- Lab-on-chips, 50, 129, 145
- Landauer, 42
- Landauer formula, 8, 9
- Langmuir–Blodgett (LB), 24
- Lenses, 219
- Light modulation, 217
- Linear motors, 173
- Liposome, 128
- Logical deductions, 200
- Logic DNA computation, 200
- Logic gate, 204
- Logic operations, 197
- Lotus, 208
- Low energy consumption, 191
- LUMO, 37, 39
- Lungs, 226
  
- Main methods to produce graphene, 33
- Manipulate cells, 119
- Mask, 20
- Mean-free path, 2
- Messenger RNA (mRNA), 204

- Metal organic chemical vapor deposition (MOCVD), 19
- Micro, 128
- Microarray, 144
- Microelectromechanical systems, 51
- Microfluidic lenses, 221
- Microfluidic/nanofluidic, 140
- Microfluidics, 46
- Micromachining techniques, 51
- Microneedles, 142
- Micropumps, 140
- Microtubule, 183
- Microtubule/kinesin, 183
- Mixing of fluids, 49
- Mode, 109
- Molecular beam epitaxy (MBE), 19
- Molecular logic gates, 190
- Monolayer-protected clusters, 26
- Myosins, 174
- Nanoactuator, 178
- Nanofluidics, 52
- Nanofluidic transistors, 53
- Nanogap electrodes, 45
- Nanoimprint lithography, 23
- Nanolithography, 20
- Nanomachine, 176
- Nanomedicine, 127
- Nanomotor, 176
- Nanoneedles, 128
- Nanoparticles, 27
- Nanopatch, 143
- Nanopore tunneling, 116
- Nanoradio, 134
- Nanoscale, 1, 2
- Nanoscale lithographic, 37
- Nanowire fabrication, 29
- Nanowires, 28, 30
- Nanowire superlattices, 31
- Navier–Stokes equation, 47
- Negative differential resistance, 14, 31
- Network of synthetic peptides, 193
- Neural probes, 139
- Neuronal drug delivery, 138
- Noncontact, 112
- NOT gate, 193
- One-dimensional (1D) ballistic, 7
- Optical antennas, 137
- Optical lithography, 20
- Optical trapping, 122
- Optical tweezers, 121
- Organ-on-chip, 148
- Oxidation of silicon, 18
- Particle nanolithography, 22
- PCR lab-on-chip, 50
- Péclet number, 48
- Performances of various nanolithography techniques, 24
- Photon-driven switching of RNA, 175
- PIRE array, 119
- Plant-in-chip, 145
- Polymerase chain reaction (PCR), 50
- (Poly)methylmethacrylate (PMMA), 21
- Protein chip, 145
- Protein machines, 173
- Quantum computation, 190
- Quantum dot (QD), 6
- Quantum well (QW), 4, 5, 12, 14
- Quantum wire (QWR), 5
- Ratchet model, 174
- Reflection probabilities, 13
- Remotely control cellular processes by electrical means, 136
- Repulsive force, 108
- Resistance between contacts, 9
- Resonant tunneling, 12–14
- Reynolds number, 47
- RF implants, 133
- Ribozyme-based gates, 196
- Rotary motors, 174
- Scaffolds fabricated from bioactive nanotitanate, 212
- Scanning tunneling microscopy (STM), 11, 37, 114
- Schrödinger equations, 9, 11, 34
- Self-assembled monolayers, 26
- Self-assembly, 24, 37
- Semiconductor chemical doping, 18
- Sequencing, 116
- Sequential tunneling, 40
- Single-chip implantable RFID, 133
- Single-stranded DNA, 36
- Solar cells, 219
- Spin-degenerate density of states, 4
- State automaton, 201
- Static mode, 109
- Step-like conductance, 7

- Strong adhesive materials, 209
- Superlattices, 15, 30
- Surface micromachining, 52
- Switch, DNA, 176
- Switches, 175
- Synaptic transistor, 229
  
- Tapping mode, 110
- Template synthesis, 29
- Three-dimensional assemblies, 28
- Three-dimensional compound eye, 217
- Time-independent Schrödinger equation, 3
- Tip-sample force gradient, 112
- Tissue engineering, 127, 146
- Top-down, 18
- Transmission coefficient, 11
- Transmission probability, 8, 10, 11, 13
- Tunnel, 17
- Tunneling, 43
  - barriers, 16
  - currents, 116
  - devices, 11
  - nanoradio, 134
- Two-dimensional electron gas (2DEG), 5
- Two-dimensional nanoparticle arrays, 28
  
- Unidirectional DNA walker, 182
  
- Van der Waals, 108
- Vapor-liquid-solid, 30
- Vertical CNT arrays, 143
  
- Walker, 180
- Wings of the *Papilio blumei* butterfly, 223
- Wireless capsule endoscopy, 131

## About the Authors



**Mircea Dragoman** has been a senior researcher I at the National Research Institute in Microtechnology since 1996. In the period 1992–1994, he was the recipient of the Humboldt Fellowship award and he followed his postdoctoral studies at Duisburg University, Germany. He was an invited professor at CNR-Istituto di Electtronica dello Stato Solido-Roma (1993–1996), Univ. Saint-Etienne, France (1997), Univ. Mannheim (1998–1999, 2001–2002), Univ. Frankfurt (2003), and Univ. Darmstadt (2004). He was an invited professor at CNRS LAAS in the period 2005–2006 and 2008–2010.

He has published 205 scientific papers (114 in international journals and 91 communications at various national and international conferences). The papers are dedicated to the following areas: nanoelectronics, microwaves, MEMS, and optoelectronics. He is a coauthor of five books in prestigious international publishing houses.



**Daniela Dragoman** is a professor at the Physics Faculty of the University of Bucharest. In the period 1998–1999 and 2001–2002, she was the recipient of the Humboldt Fellowship award and followed her postdoctoral studies at the Mannheim University, Germany. She was an invited professor at Univ. Saint-Etienne, France (1997 and 2000), and at CNRS LAAS, Toulouse, in 2008, 2009, and 2010.

She is a coauthor of five monographs at prestigious international publishing houses and author or coauthor of 152 scientific papers in ISI-ranked international journals and 41 communications at national and international conferences. Her research areas of interest include nanostructures and nanodevices, quantum classical correspondence, and the foundations of quantum mechanics.